Spin-phonon interactions and spin decoherence from first principles

Thesis by

Jinsoo Park

In Partial Fulfillment of the Requirements for the
Degree of
Doctor of Philosophy

CALIFORNIA INSTITUTE OF TECHNOLOGY
Pasadena, California

2022
Defended May 27, 2022

ACKNOWLEDGEMENTS

First and foremost, I would like to express my sincere gratitude towards my advisor, Prof. Marco Bernardi, for his guidance, advice, and encouragement throughout my doctoral studies. If I had been able to become a better researcher, scientist, or communicator, it would be entirely due to the efforts of my wonderful advisor, Marco.

I would like to thank my thesis committee members, Prof. Stevan Nadj-Perge, Prof. Jason Alicea, and Prof. Nai-Chang Yeh, for their invaluable advice and helpful guidance.

I would like to thank the Korea Foundation for Advanced Studies for their kind support during my doctoral studies. I want to thank my collaborators, Dr. Iurii Timrov, Dr. Andrea Floris, Dr. Matteo Cococcioni, and Dr. Nicola Marzari, for whom I am grateful for the insights into correlated electron systems they have shared with me, and Dr. Cyrus E. Dreyer, for fruitful collaborations on quadrupole interactions. I thank Dr. Jin-Jian Zhou for sharing his vast knowledge of physics and computational techniques with me. I want to thank Dr. I-Te Lu for being both a friend and a patient mentor ever since our first meeting. I thank all members of the Bernardi group, including Dr. Luis Agapito, Dr. Vatsal Jhalani, Dr. Nien-En Lee, Dr. Hsiao-Yi Chen, Xiao Tong, Benjamin K. Chang, Dr. Raffaello Bianco, Dr. Shiyuan Gao, Dr. Ivan Maliyov, Dhruv Desai, Dr. Sergio Pineda Flores, Yao Luo, Kelly Yao, David Abramovitch, and other members who have overlapped with me.

I would like to thank Joy Kim and my relatives in Los Angeles for their warm company and kindly inviting me to Thanksgiving dinner every year. I would also like to thank my friends who helped to stay together in the uncertain times of the global pandemic. Last but not least, I would like to thank my family members, my father, mother, and my younger brothers, for their unconditional support and love.

ABSTRACT

Developing a microscopic understanding of spin decoherence is essential to advancing quantum technologies. Electron spin decoherence due to atomic vibrations (phonons) plays a special role as it sets an intrinsic limit to the performance of spin-based quantum devices. Two main sources of phonon-induced spin decoherence, the Elliott-Yafet (EY) and Dyakonov-Perel (DP) mechanisms, have distinct physical origins and theoretical treatments. First-principles calculations of electron-phonon (e-ph) interactions combined with many-body perturbation theory are promising to study phonon-induced spin decoherence. However, predicting the spin response in materials remains an open challenge; methods for quantifying spin-dependent e-ph interactions in materials, as well as a linear response framework for spins in the presence of e-ph interaction is missing. In this thesis, we provide a first-principles framework for computing the relativistic spin-dependent electron-phonon interactions. We develop a formalism that unifies the modeling of EY and DP spin decoherence, and provide a rigorous many-body perturbation theory for obtaining the spin-spin correlation function including the vertex corrections due to e-ph interactions. We compute the phonon-dressed vertex of the spin-spin correlation function with a treatment analogous to the calculation of the anomalous electron magnetic moment in QED. We find that the vertex correction provides a giant renormalization of the electron spin dynamics in solids, greater by many orders of magnitude than the corresponding correction from photons in vacuum. We further identify the long-range quadrupole e-ph interaction in materials, and demonstrate its importance in the description of phonon-induced spin decoherence. We show first-principle calculations of spin-dependent e-ph interactions in correlated electron systems, using the framework of Hubbard-corrected density functional theory. Lastly, we provide technical details in the implementation of *ab-initio* e-ph interaction in PERTURBO, a software package for first-principles calculations of charge transport, spin dynamics, and ultrafast carrier dynamics in materials. In summary, the thesis demonstrates a general approach for quantitative analysis of spin decoherence in materials, advancing the quest for spin-based quantum technologies.

PUBLISHED CONTENT AND CONTRIBUTIONS

[1] Dhruv C. Desai*, Jinsoo Park*, Jin-Jian Zhou, and Marco Bernardi. Transport in 3D topological Dirac semimetal Na$_3$Bi from first principles. *In Preparation.*, 2022.
J.P contributed to developing the theory and computational method, performed calculations, analyzed the data, and participated in the writing of the manuscript.
*These authors contributed equally to this work.

[2] Vatsal A. Jhalani*, Jin-Jian Zhou*, Jinsoo Park, Cyrus E. Dreyer, and Marco Bernardi. Piezoelectric electron-phonon interaction from ab initio dynamical quadrupoles: Impact on charge transport in wurtzite GaN. *Phys. Rev. Lett.*, 125(13):136602, 2020. doi: 10.1103/PhysRevLett.125.136602.
J.P contributed to developing the theory and computational method, performed calculations, analyzed the data, and participated in the writing of the manuscript.
*These authors contributed equally to this work.

[3] I-Te Lu, Jinsoo Park, Jin-Jian Zhou, and Marco Bernardi. Ab initio electron-defect interactions using Wannier functions. *npj Comput. Mater.*, 6(1):1–7, 2020. doi: 10.1038/s41524-020-0284-y.
J.P contributed to developing the theory and computational method and participated in the writing of the manuscript.

[4] I-Te Lu, Jin-Jian Zhou, Jinsoo Park, and Marco Bernardi. First-principles ionized-impurity scattering and charge transport in doped materials. *Phys. Rev. Mater.*, 6(1):L010801, 2022. doi: 10.1103/PhysRevMaterials.6.L010801.
J.P contributed to theory development and participated in the writing of the manuscript.

[5] Ivan Maliyov, Jinsoo Park, and Marco Bernardi. Ab initio electron dynamics in high electric fields: Accurate prediction of velocity-field curves. *Phys. Rev. B*, 104(10):L100303, 2021. doi: 10.1103/PhysRevB.104.L100303.
J.P contributed to performing calculations and participated in the writing of the manuscript.

[6] Jinsoo Park, Jin-Jian Zhou, and Marco Bernardi. Spin-phonon relaxation times in centrosymmetric materials from first principles. *Phys. Rev. B*, 101(4): 045202, 2020. doi: 10.1103/PhysRevB.101.045202.
J.P developed the theory and computational method, performed calculations, analyzed the data, and participated in the writing of the manuscript.

[7] Jinsoo Park, Jin-Jian Zhou, Vatsal A. Jhalani, Cyrus E. Dreyer, and Marco Bernardi. Long-range quadrupole electron-phonon interaction from first principles. *Phys. Rev. B*, 102(12):125203, 2020. doi: 10.1103/PhysRevB.102.

125203.
J.P contributed to developing the theory and computational method, performed calculations, analyzed the data, and participated in the writing of the manuscript.

[8] Jinsoo Park, Yao Luo, and Marco Bernardi. Many-body theory of phonon-induced spin relaxation and decoherence. *In Preparation.*, 2022.
J.P developed the theory and computational method, performed calculations, analyzed the data, and participated in the writing of the manuscript.

[9] Jinsoo Park, Jin-Jian Zhou, and Marco Bernardi. Predicting electron spin decoherence with a many-body first-principles approach. *arXiv preprint arXiv:2203.06401*, 2022.
J.P developed the theory and computational method, performed calculations, analyzed the data, and participated in the writing of the manuscript.

[10] Jin-Jian Zhou, Jinsoo Park, I-Te Lu, Ivan Maliyov, Xiao Tong, and Marco Bernardi. Perturbo: A software package for ab initio electron–phonon interactions, charge transport and ultrafast dynamics. *Comput. Phys. Commun.*, 264: 107970, 2021. doi: 10.1016/j.cpc.2021.107970.
J.P contributed in developing the PERTURBO code, the tutorial for the PERTURBO code, and participated in the writing of the manuscript.

[11] Jin-Jian Zhou*, Jinsoo Park*, Iurii Timrov, Andrea Floris, Matteo Cococcioni, Nicola Marzari, and Marco Bernardi. Ab initio electron-phonon interactions in correlated electron systems. *Phys. Rev. Lett.*, 127(12):126404, 2021. doi: 10.1103/PhysRevLett.127.126404.
J.P contributed to developing the computational method, performed calculations, analyzed the data, and participated in the writing of the manuscript.
*These authors contributed equally to this work.

TABLE OF CONTENTS

LIST OF ILLUSTRATIONS

Chapter 1

INTRODUCTION

1.1 Overview

Decoherence is a major unresolved challenge in quantum technology as it limits the manipulation of quantum information. Solid state devices based on the electron's spin, such as spin qubits and spintronic technologies, require long spin coherence times for optimal performance. There are various sources of spin decoherence in solids — noise, nuclear spins, etc. — but atomic thermal vibrations (phonons) are the only mechanism that is always present and that sets an intrinsic limit to the performance of any spin-based quantum technology.

Consequently, predicting spin decoherence due to phonons with a high accuracy remains a high priority for basic and applied quantum science. Previous work has identified two key mechanisms of phonon-induced spin decoherence in the presence of spin-orbit coupling. In the Elliott-Yafet (EY) mechanism, spin decoherence occurs as each e-ph collision has a finite probability to alter the spin direction. This mechanism dominates decoherence in centrosymmetric materials. In the Dyakonov-Perel (DP) mechanism, spin decoherence occurs as a result of spin precessions in-between electron scattering events. This mechanism dominates decoherence in materials which do not have inversion symmetry. The interplay between these two spin decoherence mechanisms is crucial in systems ranging from semiconductors for spintronics to defects for quantum technologies.

Despite decades of progress, theory and computational methods for quantitative predictions of spin decoherence remain an open problem. All existing approaches require empirical fitting of the spin interactions to construct the model, and of the dynamics to extract the spin relaxation times. Much research in this area has resorted to the momentum relaxation dynamics to indirectly estimate spin relaxation, usually by assuming a direct proportionality between the spin and momentum-scattering interactions or relaxation times for the EY theory, and an inverse proportionality between the two for the DP theory. A general scheme to compute spin-phonon interactions and spin relaxation times with quantitative accuracy is still missing; if developed, they could have significant impact and enable progress on many unresolved questions in spin physics and devices. Accurately predicting EY and DP spin decoherence can establish the intrinsic limit to the performance of spin-based devices and provide a detailed understanding of spin interactions.

1.2 First-Principles Computational Methods

Understanding the dynamical processes involving electrons, spins, and lattice vibrations (phonons) in the solid state is the key first step to investigate spin decoherence. Due to the increasing complexity of functional materials, there is a critical need for computational tools that can take into account the atomic and electronic structure of materials and make quantitative predictions on their physical properties. A generally applicable first-principles method to predict and microscopically understand spin-phonon interactions, and capture atomistic details such as the electronic wave function, spin texture, phonon modes and their mode-dependent spin-flip interactions, is necessary. We review the first-principles methods that have became a standard for calculating e-ph interactions in condensed matter.

Electrons, phonons, and e-ph interactions

Density functional theory (DFT) has become the mode widely accepted approach for computational modeling of the electronic structure in materials. DFT places its roots in the Hohenberg-Kohn theorem, which states that the total energy of a system is a unique functional of the electron density, and that the ground state energy can be obtained through a variational principle with respect to the electron density. Shortly after its introduction, Kohn and Sham proposed an effective Hamiltonian consisted of fictitious non-interacting particles to reproduce the original electron density of the interacting system. The corresponding Kohn-Sham (KS) Hamiltonian consists of the Kohn-Sham kinetic energy operator of the effective orbitals, the external potential, the Hartree potential, and the exchange-correlation potential.

The formalism of DFT has been extensively expanded since its initial introduction. It is implemented in numerous open-source codes such as Quantum ESPRESSO [1] and Abinit [2]. Modern research employing DFT focuses on excited state and microscopic electron interactions. For instance, the phonon dispersion is computed with density functional perturbation theory (DFPT), which is a linear response extension of DFT. In principle, the e-ph matrix elements can also be computed with these methods and used directly for carrier dynamics calculations. However, to converge transport and ultrafast dynamics, the e-ph matrix elements and the scattering processes need to be computed on ultra-dense $\boldsymbol{k}$- and $\boldsymbol{q}$-point BZ grids with roughly $100 \times 100 \times 100$ or more points. Therefore, the computational cost is prohibitive for direct DFPT calculations, and we resort to interpolation techniques to obtain the e-ph matrix elements and other relevant quantities on fine grids, starting from DFT and DFPT calculations on coarser BZ grids, typically of order 10×10×10.

Wannier interpolation of the electronic structure

We use Wannier interpolation to compute efficiently the electron energy and band velocity on ultra-fine $\boldsymbol{k}$-point grids [3]. We first perform DFT calculations on a regular coarse grid with points $\boldsymbol{k}_c$, and obtain the electron energies $\varepsilon_{n\boldsymbol{k}_c}$ and Bloch wavefunctions $|\psi_{n\boldsymbol{k}_c}\rangle$. We construct maximally localized Wannier functions $|n\boldsymbol{R}_e\rangle$, with index n and centered in the cell at $\boldsymbol{R}_e$, from the Bloch wavefunctions using the Wannier90 code [4, 5]:

$$|n\boldsymbol{R}_e\rangle = \frac{1}{N_e}\sum_{m\boldsymbol{k}_c} e^{-i\boldsymbol{k}_c\cdot\boldsymbol{R}_e}\mathcal{U}_{mn}(\boldsymbol{k}_c)\,|\psi_{m\boldsymbol{k}_c}\rangle, \tag{1.1}$$

where N_e is the number of $\boldsymbol{k}_c$-points in the coarse grid, and $\mathcal{U}(\boldsymbol{k}_c)$ are the unitary matrices transforming the Bloch wavefunctions to a Wannier gauge [6],

$$|\psi^{(W)}_{n\boldsymbol{k}_c}\rangle = \sum_{m}\mathcal{U}_{mn}(\boldsymbol{k}_c)\,|\psi_{m\boldsymbol{k}_c}\rangle. \tag{1.2}$$

For entangled band structures, $\mathcal{U}(\boldsymbol{k}_c)$ are not in general square matrices since they are also used to extract a smooth subspace from the original DFT Bloch eigenstates [7].

We compute the electron Hamiltonian in the Wannier function basis,

$$\begin{aligned} H_{nn'}(\boldsymbol{R}_e) &= \langle n0|\hat{H}|n'\boldsymbol{R}_e\rangle \\ &= \frac{1}{N_e}\sum_{\boldsymbol{k}_c} e^{-i\boldsymbol{k}_c\cdot\boldsymbol{R}_e}\left[\mathcal{U}^\dagger(\boldsymbol{k}_c)H(\boldsymbol{k}_c)\mathcal{U}(\boldsymbol{k}_c)\right]_{nn'}, \end{aligned} \tag{1.3}$$

where $H(\boldsymbol{k}_c)$ is the Hamiltonian in the DFT Bloch eigenstate basis, $H_{nm}(\boldsymbol{k}_c) = \varepsilon_{n\boldsymbol{k}_c}\delta_{nm}$. The Hamiltonian in the Wannier basis, $H_{nn'}(\boldsymbol{R}_e)$, can be seen as an *ab initio* tight-binding model, with hopping integrals from the Wannier orbital n' in the cell at $\boldsymbol{R}_e$ to the Wannier orbital n in the cell at the origin. Due to the localization of the Wannier orbitals, the hopping integrals decay rapidly with $|\boldsymbol{R}_e|$, so a small set of $\boldsymbol{R}_e$ vectors is sufficient to represent the electronic structure of the system.

Starting from $H_{nn'}(\boldsymbol{R}_e)$, we obtain the band energy $\varepsilon_{n\boldsymbol{k}}$ and band velocity $\boldsymbol{v}_{n\boldsymbol{k}}$ at any desired $\boldsymbol{k}$-point. We first compute the Hamiltonian matrix $H^{(W)}(\boldsymbol{k})$ in the basis of

Bloch sums of Wannier functions using an inverse discrete Fourier transform, and then diagonalize it through a unitary rotation matrix $U(\boldsymbol{k})$ satisfying

$$H^{(W)}(\boldsymbol{k}) = \sum_{\boldsymbol{R}_e} e^{i\boldsymbol{k}\cdot\boldsymbol{R}_e} H(\boldsymbol{R}_e) = U(\boldsymbol{k}) H^{(H)}(\boldsymbol{k}) U^{\dagger}(\boldsymbol{k}) \,, \tag{1.4}$$

where $H^{(H)}_{nm}(\boldsymbol{k}) = \varepsilon_{n\boldsymbol{k}}\delta_{nm}$, and $\varepsilon_{n\boldsymbol{k}}$ and $U(\boldsymbol{k})$ are the eigenvalues and eigenvectors of $H^{(W)}(\boldsymbol{k})$, respectively. One can also obtain the corresponding interpolated Bloch eigenstates as

$$|\psi_{n\boldsymbol{k}}\rangle = \sum_m U_{mn}(\boldsymbol{k})\, |\psi^{(W)}_{m\boldsymbol{k}}\rangle = \sum_m U_{mn}(\boldsymbol{k}) \sum_{\boldsymbol{R}_e} e^{i\boldsymbol{k}\cdot\boldsymbol{R}_e} |m\boldsymbol{R}_e\rangle. \tag{1.5}$$

The band velocity in the Cartesian direction α is computed as

$$\hbar \boldsymbol{v}^{\alpha}_{n\boldsymbol{k}} = [U^{\dagger}(\boldsymbol{k}) H^{(W)}_{\alpha}(\boldsymbol{k}) U(\boldsymbol{k})]_{nn}, \tag{1.6}$$

where $H^{(W)}_{\alpha}(\boldsymbol{k})$ is the $\boldsymbol{k}$-derivative of $H^{(W)}(\boldsymbol{k})$ in the α-direction, evaluated analytically using

$$H^{(W)}_{\alpha}(\boldsymbol{k}) = \partial_{\alpha} H^{(W)}(\boldsymbol{k}) = \sum_{\boldsymbol{R}_e} e^{i\boldsymbol{k}\cdot\boldsymbol{R}_e} H(\boldsymbol{R}_e) \cdot (iR^{\alpha}_{e}) \,. \tag{1.7}$$

An appropriate extension of Eq. (1.6) is used for degenerate states [8].

Interpolation of the phonon dispersion

The lattice dynamical properties are first obtained using DFPT on a regular coarse $\boldsymbol{q}_c$-point grid. Starting from the dynamical matrices $D(\boldsymbol{q}_c)$, we compute the interatomic force constants (IFCs) $D(\boldsymbol{R}_p)$ (here, without the mass factor) through a Fourier transform [9, 10],

$$D(\boldsymbol{R}_p) = \frac{1}{N_p} \sum_{\boldsymbol{q}_c} e^{-i\boldsymbol{q}_c\cdot\boldsymbol{R}_p} D(\boldsymbol{q}_c), \tag{1.8}$$

where N_p is the number of $\boldsymbol{q}_c$-points in the coarse grid. If the IFCs are short-ranged, a small set of $D(\boldsymbol{R}_p)$, obtained from dynamical matrices on a coarse $\boldsymbol{q}_c$-point grid, is sufficient to obtain the dynamical matrix at any desired $\boldsymbol{q}$-point with an inverse Fourier transform,

$$D(\boldsymbol{q}) = \sum_{\boldsymbol{R}_p} e^{i\boldsymbol{q}\cdot\boldsymbol{R}_p} D(\boldsymbol{R}_p). \tag{1.9}$$

We obtain the phonon frequencies $\omega_{\nu\boldsymbol{q}}$ and displacement eigenvectors $\boldsymbol{e}_{\nu\boldsymbol{q}}$ by diagonalizing $D(\boldsymbol{q})$.

Wannier interpolation of the e-ph matrix elements

The key quantities for e-ph scattering are the e-ph matrix elements $g_{mn\nu}\left(\boldsymbol{k},\boldsymbol{q}\right)$. They are given by

$$g_{mn\nu}\left(\boldsymbol{k},\boldsymbol{q}\right)=\sqrt{\frac{\hbar}{2\omega_{\nu\boldsymbol{q}}}}\sum_{\kappa\alpha}\frac{\boldsymbol{e}^{\kappa\alpha}_{\nu\boldsymbol{q}}}{\sqrt{M_\kappa}}\left\langle\psi_{m\boldsymbol{k}+\boldsymbol{q}}\left|\partial_{\boldsymbol{q},\kappa\alpha}V\right|\psi_{n\boldsymbol{k}}\right\rangle, \tag{1.10}$$

where $|\psi_{n\boldsymbol{k}}\rangle$ and $|\psi_{m\boldsymbol{k}+\boldsymbol{q}}\rangle$ are the wavefunctions of the initial and final Bloch states, respectively, and $\partial_{\boldsymbol{q},\kappa\alpha}V$ is the perturbation potential due to lattice vibrations, computed as the variation of the Kohn-Sham potential V with respect to the atomic displacement of atom κ (with mass M_κ) in the Cartesian direction α:

$$\partial_{\boldsymbol{q},\kappa\alpha}V=\sum_{\boldsymbol{R}_p}e^{i\boldsymbol{q}\cdot\boldsymbol{R}_p}\frac{\partial V}{\partial R_{p\kappa\alpha}}. \tag{1.11}$$

We obtain this perturbation potential as a byproduct of the DFPT lattice dynamical calculations at a negligible additional cost.

We compute the bra-ket in Eq. (1.10) directly, using the DFT Bloch states on a coarse $\boldsymbol{k}_c$-point grid and the perturbation potentials on a coarse $\boldsymbol{q}_c$-point grid,

$$\tilde{g}^{\kappa\alpha}_{mn}\left(\boldsymbol{k}_c,\boldsymbol{q}_c\right)=\left\langle\psi_{m\boldsymbol{k}_c+\boldsymbol{q}_c}\left|\partial_{\boldsymbol{q}_c,\kappa\alpha}V\right|\psi_{n\boldsymbol{k}_c}\right\rangle, \tag{1.12}$$

from which we obtain the e-ph matrix elements in the Wannier basis [11, 12], $\tilde{g}^{\kappa\alpha}_{ij}\left(\boldsymbol{R}_e,\boldsymbol{R}_p\right)$, by combining Eq. (1.1) and the inverse transformation of Eq. (1.11):

$$\begin{aligned}\tilde{g}^{\kappa\alpha}_{ij}\left(\boldsymbol{R}_e,\boldsymbol{R}_p\right)=&\left\langle i0\left|\frac{\partial V}{\partial R_{p,\kappa\alpha}}\right|j\boldsymbol{R}_e\right\rangle\\=&\frac{1}{N_eN_p}\sum_{\boldsymbol{k}_c,\boldsymbol{q}_c}e^{-i\left(\boldsymbol{k}_c\cdot\boldsymbol{R}_e+\boldsymbol{q}_c\cdot\boldsymbol{R}_p\right)}\tilde{\boldsymbol{g}}^{\kappa\alpha,(W)}_{ij}\left(\boldsymbol{k}_c,\boldsymbol{q}_c\right),\end{aligned} \tag{1.13}$$

where

$$\tilde{\boldsymbol{g}}^{\kappa\alpha,(W)}\left(\boldsymbol{k}_c,\boldsymbol{q}_c\right)=\mathcal{U}^\dagger(\boldsymbol{k}_c+\boldsymbol{q}_c)\tilde{\boldsymbol{g}}^{\kappa\alpha}\left(\boldsymbol{k}_c,\boldsymbol{q}_c\right)\mathcal{U}(\boldsymbol{k}_c)$$

are the matrix elements in the Wannier gauge. Similar to the electron Hamiltonian in the Wannier basis, $\tilde{g}^{\kappa\alpha}_{ij}\left(\boldsymbol{R}_e,\boldsymbol{R}_p\right)$ can be seen as a hopping integral between two localized Wannier functions, one at the origin and one at $\boldsymbol{R}_e$, due to a perturbation caused by an atomic displacement at $\boldsymbol{R}_p$. If the interactions are short-ranged in real space, $\tilde{g}$ decays rapidly with $|\boldsymbol{R}_e|$ and $|\boldsymbol{R}_p|$, and computing it on a small set of $\left(\boldsymbol{R}_e,\boldsymbol{R}_p\right)$ lattice vectors is sufficient to fully describe the coupling between electrons and lattice vibrations.

The e-ph matrix elements at any desired pair of $\boldsymbol{k}$- and $\boldsymbol{q}$-points can be computed efficiently using the inverse transformation in Eq. (1.13),

$$\begin{aligned} \tilde{g}^{\kappa\alpha}_{mn}(\boldsymbol{k},\boldsymbol{q}) = & \sum_{i,j} U^{\dagger}_{mi}(\boldsymbol{k}+\boldsymbol{q}) U_{jn}(\boldsymbol{k}) \\ & \times \sum_{\boldsymbol{R}_e,\boldsymbol{R}_p} e^{i(\boldsymbol{k}\cdot\boldsymbol{R}_e + \boldsymbol{q}\cdot\boldsymbol{R}_p)} \tilde{g}^{\kappa\alpha}_{ij}\left(\boldsymbol{R}_e,\boldsymbol{R}_p\right), \end{aligned} \tag{1.14}$$

where $U(\boldsymbol{k})$ is the matrix used to interpolate the Bloch states in Eq. (1.5).
The main requirement of this interpolation approach is that the e-ph interactions are short-ranged and the e-ph matrix elements in the local basis decay rapidly. Therefore, the e-ph interpolation works equally well with localized orbitals other than Wannier functions, as we have shown recently using atomic orbitals [13].

Polar corrections for phonons and e-ph interactions

The assumption that the IFCs and e-ph interactions are short-ranged does not hold for polar semiconductors and insulators. In polar materials, the displacement of ions with a non-zero Born effective charge creates dynamical dipoles, and the long-wavelength longitudinal optical (LO) phonon mode induces a macroscopic electric field [9]. The dipole-dipole interactions introduce long-range contributions to the IFCs and dynamical matrices [14], resulting in the well-known LO-TO splitting in the phonon dispersion at $\boldsymbol{q} \to 0$. For this reason, the dynamical matrix interpolation scheme in Eqs. (1.8)-(1.9) cannot provide correct phonon dispersions at small $\boldsymbol{q}$ for polar materials. To address this issue, a polar correction is typically used [10], in which the dynamical matrix is separated into two contributions: a short-range part that can be interpolated using the Fourier transformation in Eqs. (1.8)-(1.9), and a long-range part evaluated directly using an analytical formula involving the Born effective charges and the dielectric tensor [10].

Similar to the IFCs, the e-ph interactions possess both short-range and long-range components. A multipole expansion of the e-ph matrix elements by Vogl has shown that the long-range part consists of a dipole and a quadrupole contribution. The field due to the dynamical dipoles introduces long-range e-ph contributions — in particular, the Fröhlich interaction [15], a long-range coupling between electrons and LO phonons. The strength of the Fröhlich e-ph interaction diverges as $1/q$ for $\boldsymbol{q} \to 0$ in bulk materials. As a result, the Wannier interpolation is impractical and usually fails to correctly reproduce the DFPT e-ph matrix elements at small $\boldsymbol{q}$. Using a scheme analogous to the polar correction for phonon dispersion, one can split the e-ph matrix elements into a long-range part due to the dipole field and a short-range part [16, 17].

In this thesis, we first focus on a computational approach for the long-range e-ph matrix elements by replacing the perturbation potential in Eq. (1.12) with the potential of the dipole field,

$$\begin{aligned}\tilde{g}_{mn}^{\kappa\alpha,L}(\boldsymbol{k},\boldsymbol{q}) =& \frac{ie^2}{\epsilon_0\Omega}\sum_{\boldsymbol{G}\neq-\boldsymbol{q}}\frac{\left[(\boldsymbol{q}+\boldsymbol{G})\cdot\boldsymbol{Z}_\kappa^*\right]_\alpha e^{-i\boldsymbol{\tau}_\kappa\cdot(\boldsymbol{q}+\boldsymbol{G})}}{(\boldsymbol{q}+\boldsymbol{G})\cdot\boldsymbol{\epsilon}\cdot(\boldsymbol{q}+\boldsymbol{G})} \\ &\times\left\langle\psi_{m\boldsymbol{k}+\boldsymbol{q}}\middle|e^{i(\boldsymbol{q}+\boldsymbol{G})\cdot\boldsymbol{r}}\middle|\psi_{n\boldsymbol{k}}\right\rangle,\end{aligned} \tag{1.15}$$

where $\boldsymbol{Z}_\kappa^*$ and $\boldsymbol{\tau}_\kappa$ are the Born effective charge and position of atom κ in the unit cell, respectively, while Ω is the unit cell volume and $\boldsymbol{\epsilon}$ the dielectric tensor. In practice, the summation over $\boldsymbol{G}$ is performed using the Ewald method, by introducing a decay factor $e^{-(\boldsymbol{q}+\boldsymbol{G})\cdot\boldsymbol{\epsilon}\cdot(\boldsymbol{q}+\boldsymbol{G})/4\Lambda}$ with convergence parameter Λ, and multiplying each term in the summation by this factor. It is convenient to evaluate the bra-ket in Eq. (1.15) in the Wannier gauge, in which one can apply the smooth phase approximation $\langle u_{m\boldsymbol{k}+\boldsymbol{q}}|u_{n\boldsymbol{k}}\rangle^{(W)} = \delta_{mn}$, where $u_{n\boldsymbol{k}}$ is the periodic part of the Bloch function. Combining Eq. (1.2) and the smooth phase approximation in the Wannier gauge, we obtain

$$\left\langle\psi_{m\boldsymbol{k}+\boldsymbol{q}}\middle|e^{i(\boldsymbol{q}+\boldsymbol{G})\cdot\boldsymbol{r}}\middle|\psi_{n\boldsymbol{k}}\right\rangle = [\mathcal{U}(\boldsymbol{k}+\boldsymbol{q})\mathcal{U}^\dagger(\boldsymbol{k})]_{mn}. \tag{1.16}$$

Using the analytical formula in Eq. (1.15), with the bra-ket computed using Eq. (1.16), the long-range part of the e-ph matrix elements can be evaluated directly for any desired values of $\boldsymbol{k}$ and $\boldsymbol{q}$. Only the short-range part is computed using Wannier interpolation, and the full e-ph matrix elements are then obtained by adding together the short- and long-range contributions.

To extend the phonon and e-ph polar correction schemes to 2D materials, only small changes to the long-range parts are needed, as discussed in detail in Refs. [18–20]. In particular, the 2D extension of the long-range e-ph matrix elements is obtained by replacing in Eq. (1.15) the dielectric tensor $\boldsymbol{\epsilon}$ with the effective screening $\epsilon_{\text{eff}}(|\boldsymbol{q}|)$ of the 2D system and the unit cell volume Ω with $2A$, where A is the area of the 2D unit cell.

Limitations of the current approach

Note that the current *ab-initio* approach is incomplete as it lacks the quadrupole interaction, which is essential to accurately describe e-ph interactions in all materials — both polar and nonpolar — and is particularly important for piezoelectric materials. As a result, the e-ph interactions cannot be described correctly from first principles even in materials as simple as silicon, and currently e-ph calculations on piezoelectric materials (such as wurtzite and titanate crystals) lead to large errors.

The current approach also remains an open challenge in correlated electron systems (CES), where density functional theory fails to describe the ground state. As a result, reliable e-ph calculations remain out of reach for broad classes of strongly correlated materials such as high-temperature superconductors, Mott insulators, transition metal oxides, f-electron systems, planetary materials, and multiferroics. Widely used first-principles approaches to compute the ground state of CES include Hubbard-corrected DFT (DFT+U), hybrid functionals, and dynamical mean-field theory. Yet, calculations of e-ph interactions are currently not possible in any of these methods. Developing accurate e-ph calculations in CES and understanding their spin-dependent nature thus remains an important open challenge – if fulfilled, it would advance investigations of transport, high-temperature superconductivity, charge-density waves and metal-insulator transitions in broad classes of strongly correlated materials relevant for quantum technology.

1.3 Many-Body Perturbation Theory

First-principles approaches combined with many-body perturbation theory are particularly promising to tackle the problem of spin decoherence. Linear response theory is a powerful framework that can broaden our understanding of the microscopic correlation functions and the response of the system with respect to external perturbations [21–26]. Modern *ab-initio* microscopic electron interactions [11, 13, 27–31] complement linear response theory, allowing precise predictions of material properties without resorting to empirical fitting parameters. We provide a brief summary of the many-body techniques employed in this thesis.

Interacting Green's functions

We consider an unperturbed Hamiltonian H_0 diagonal in a Bloch basis, $\langle n'\boldsymbol{k}| H_0 |n\boldsymbol{k}\rangle = \varepsilon_{n\boldsymbol{k}}\delta_{nn'}$. The interacting imaginary-time Green's function $\mathcal{G}(i\omega_a)$ is written using the Dyson equation [21]

$$\mathcal{G}(i\omega_a)^{-1} = \mathcal{G}^{(0)}(i\omega_a)^{-1} - \Sigma(i\omega_a), \tag{1.17}$$

where ω_a is the fermionic Matsubara frequency of the electron, $\mathcal{G}^{(0)}(i\omega_a)$ is the non-interacting Green's function, and $\Sigma(i\omega_a)$ is the lowest order (Fan-Migdal) e-ph

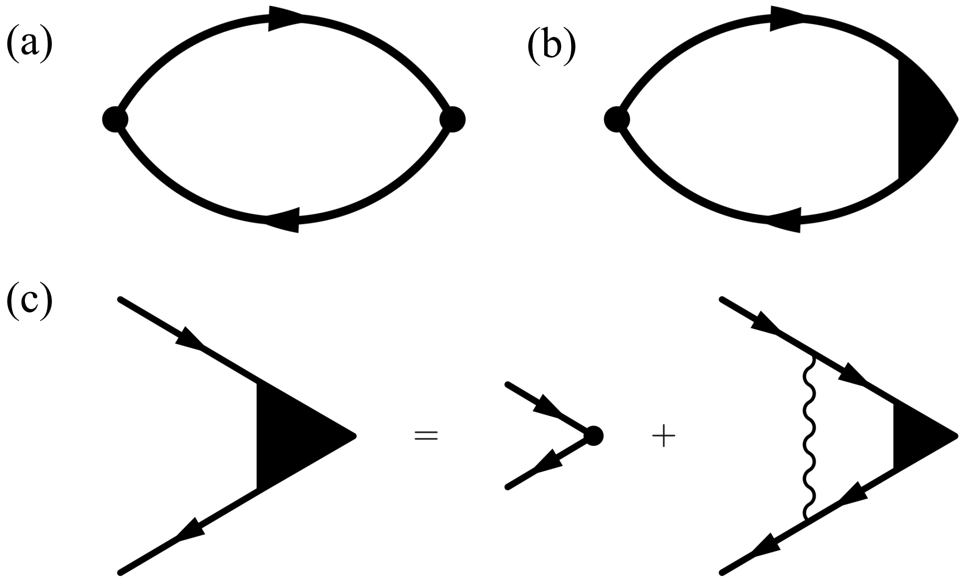

Figure 1.1: (a) Bare bubble diagram without the vertex correction. (b) Bubble diagram including the vertex correction. (c) Bethe-Salpeter equation for the vertex corrections Λ from electron-phonon interactions within the ladder approximation. The wavy line corresponds to the phonon propagator.

self-energy [21, 32, 33], whose band- and $\boldsymbol{k}$-dependent expression is

$$\Sigma_{nn'\boldsymbol{k}}(i\omega_a) = -\frac{1}{\beta N_q V} \sum_{mm'\boldsymbol{q}\nu, iq_c} [g_{n'm'\nu}(\boldsymbol{k},\boldsymbol{q})]^* \, g_{nm\nu}(\boldsymbol{k},\boldsymbol{q}) \mathcal{D}_{\nu\boldsymbol{q}}(iq_c) \mathcal{G}_{mm'\boldsymbol{k}+\boldsymbol{q}}(i\omega_a + iq_c). \tag{1.18}$$

Above, $\beta = 1/k_B T$ at temperature T, N_q is the number of $\boldsymbol{q}$-points, V is the volume of the unit cell, q_c is the bosonic Matsubara frequency of the phonon, and $\mathcal{D}_{\nu\boldsymbol{q}}(iq_c) = 2\omega_{\boldsymbol{q}\nu}/((iq_c)^2 - \omega^2_{\boldsymbol{q}\nu})$ is the non-interacting phonon Green's function for a phonon of mode index ν and wave-vector $\boldsymbol{q}$.

The key quantity is the e-ph matirx elements, $g_{nm\nu}(\boldsymbol{k},\boldsymbol{q})$, which quantify the probability amplitude for an electron in a Bloch state $|\psi_{n\boldsymbol{k}}\rangle$, with band index n and crystal momentum $\boldsymbol{k}$, to scatter into a final state $|\psi_{m\boldsymbol{k}+\boldsymbol{q}}\rangle$ by emitting or absorbing a phonon with mode index ν, wave-vector $\boldsymbol{q}$, and energy $\hbar\omega_{\nu\boldsymbol{q}}$ [21, 32],

$$g_{nm\nu}(\boldsymbol{k},\boldsymbol{q}) = \langle\psi_{m\boldsymbol{k}+\boldsymbol{q}}|\, d_{\boldsymbol{q}\nu}\hat{V}|\psi_{n\boldsymbol{k}}\rangle, \tag{1.19}$$

where $d_{\boldsymbol{q}\nu}\hat{V}$ is the e-ph perturbation due to the change of the potential acting on an electron from a phonon with mode index ν and crystal momentum $\boldsymbol{q}$.

Kubo formula and correlation function

One considers a complex vector operator $\hat{A}$, with matrix elements in the direction α given as $A^{\alpha}_{nm\boldsymbol{k}} = \langle m\boldsymbol{k}|\, \hat{A}^{\alpha}\, |n\boldsymbol{k}\rangle$.

Working in imaginary time coordinate and frequency, the retarded correlation function for the operator $\hat{A}$ can be obtained from the Kubo formula [21]

$$\chi_{\alpha\beta}(\boldsymbol{p}, i\nu_b) = \int_0^{\beta} d\tau e^{i\nu_b\tau} \left\langle T_\tau \hat{A}^{\alpha}(\boldsymbol{p},\tau)\hat{A}^{\beta}(-\boldsymbol{p},0)\right\rangle, \tag{1.20}$$

where $\boldsymbol{p}$ is the wave-vector, ν_b is the bosonic Matsubara frequency, τ is imaginary time ranging from 0 to $\beta = 1/k_B T$ at temperature T, and T_τ is the imaginary time ordering operator. Here we focus on the $\boldsymbol{p} \to 0$ limit, and thus drop $\boldsymbol{p}$ from the equations. This correlation function can be expressed as a sum of bubble diagrams P as

$$\chi_{\alpha\beta}(i\nu_b) = \frac{1}{\beta}\sum_{i\omega_a} P(i\omega_a, i\omega_a + i\nu_b). \tag{1.21}$$

For the simplest case, one considers the bare bubble diagram that includes electron self-energy only in the electron propagator $\mathcal{G}$ as shown Fig. 1.1(a):

$$\chi_{\alpha\beta}(i\nu_b) = \frac{1}{\beta V}\sum_{i\omega_a} \mathrm{Tr}\big[\mathcal{G}(i\omega_a)\hat{A}^{\alpha}\mathcal{G}(i\omega_a + i\nu_b)\hat{A}^{\beta}\big], \tag{1.22}$$

where the trace is evaluated over the band and momentum indices. In this expression, the operator $\hat{A}$ can be regarded as the bare vertex of the correlation function. For the velocity operator, Eq. (1.22) leads to the well-known Drude conductivity [21, 24].

In this work, the corrections to the vertex originates from e-ph interactions, which couple electronic states with different band and crystal momenta. Figure 1.1(b) shows the correlation function including the vertex correction Λ,

$$\chi_{\alpha\beta}(i\nu_b) = \frac{1}{\beta V}\sum_{i\omega_a} \mathrm{Tr}\big[\mathcal{G}(i\omega_a)\hat{A}^{\alpha}\mathcal{G}(i\omega_a + i\nu_b)\hat{A}^{\beta}\Lambda^{\beta}(i\omega_a, i\omega_a + i\nu_b)\big], \tag{1.23}$$

where $\hat{A}^{\beta}\Lambda^{\beta}(i\omega_a, i\omega_a + i\nu_b)$ is the phonon-dressed vertex for the operator $\hat{A}$ along the Cartesian direction β. Note that the vertex correction $\Lambda^{\beta}(i\omega_a, i\omega_a + i\nu_b)$ is a complex vector, and it contains information about the renormalized operator dynamics due to the e-ph interactions. In the ladder approximation, the vertex correction Λ satisfies a self-consistent Bethe-Salpeter equation (BSE), shown diagrammatically in Fig. 1.1(c).

1.4 Thesis Outline

In this thesis, we focus on three objectives: (i) developing a many-body framework for investigating phonon-induced spin decoherence, (ii) identifying and expanding the limitations of the first-principles e-ph interactions relevant for spin decoherence, and (iii) presenting an open-source software package for studying e-ph interactions from first principles.

In Chapter 2, we focus on spin-phonon interaction and relaxation. Spin-phonon interactions limit the performance of spin-based quantum technologies, but are challenging to compute with quantitative accuracy. We demonstrate a precise first-principles method to compute spin-phonon interactions and spin relaxation times. Our approach can predict spin relaxation times in silicon in excellent agreement with experiment, without using empirical or fitting parameters. We also predict intrinsic-limit spin relaxation times in diamond, a key material for spin-based quantum technologies. Our results further show that the widely used proportionality between spin and momentum relaxation times is inaccurate, highlighting the need for atomistic spin relaxation calculations.

In Chapter 3, we present a novel many-body first-principles approach for phonon-induced spin decoherence. Electron spin decoherence from atomic vibrations (phonons) limits the performance of spin-based quantum technologies but is challenging to model quantitatively. We present a many-body theory of phonon-induced spin decoherence that can capture both spin relaxation and precession. Our approach can predict with a high accuracy the intrinsic spin relaxation times in key materials for quantum devices — Si, GaAs, and WSe_2 — without using empirical or fitting parameters. Using this formalism, we find a colossal phonon-induced renormalization of the spin dynamics, and discover that spin decoherence times in condensed matter and the anomalous electron magnetic moment share a similar origin.

In Chapter 4, we develop a first-principles approach to model piezoelectric e-ph interaction, a long-range scattering mechanism due to acoustic phonon in noncentrosymmetric polar materials, which has not been accurately described at present. The accuracy of the approach is demonstrated by comparing with direct density functional perturbation theory calculations. We apply our method to silicon as a case of a nonpolar semiconductor and tetragonal $PbTiO_3$ as a case of a polar piezoelectric material. In both materials we find that the quadrupole term strongly impacts the e-ph matrix elements.

In Chapter 5, we demonstrate how spin-dependent e-ph interaction in correlated electron systems (CES) can be captured from first-principles calculations. Accurate studies of electron-phonon (e-ph) interactions in CES remain an open challenge as DFT often fails to describe their ground state. Here we show a broadly applicable and affordable approach for quantitative studies of e-ph interactions in CES, using the framework of Hubbard-corrected DFT. The accuracy of our approach is showcased on a prototypical Mott insulator, cobalt oxide (CoO), by carrying out a detailed investigation of its e-ph interactions and electron spectral functions. The new method enables investigations of transport, polarons, superconductivity, charge-density waves, and metal-insulator transitions in broad classes of strongly correlated materials.

In Chapter 6, we develop PERTURBO, a software package for first-principles calculations of charge transport, spin dynamics, and ultrafast carrier dynamics in materials. PERTURBO uses results from density functional theory and density functional perturbation theory calculations as input, and employs Wannier interpolation to reduce the computational cost. It supports norm-conserving and ultrasoft pseudopotentials, spin–orbit coupling, and polar electron–phonon interactions for bulk and 2D materials. Hybrid MPI plus OpenMP parallelization is implemented to enable efficient calculations on large systems (up to at least 50 atoms) using high-performance computing.

In Chapter 7, we summarize the main advancements made in this thesis and outline possible future research directions.

References

[1] Paolo Giannozzi, Stefano Baroni, Nicola Bonini, Matteo Calandra, Roberto Car, Carlo Cavazzoni, Davide Ceresoli, Guido L. Chiarotti, Matteo Cococcioni, Ismaila Dabo, Andrea Dal Corso, Stefano de Gironcoli, Stefano Fabris, Guido Fratesi, Ralph Gebauer, Uwe Gerstmann, Christos Gougoussis, Anton Kokalj, Michele Lazzeri, Layla Martin-Samos, Nicola Marzari, Francesco Mauri, Riccardo Mazzarello, Stefano Paolini, Alfredo Pasquarello, Lorenzo Paulatto, Carlo Sbraccia, Sandro Scandolo, Gabriele Sclauzero, Ari P. Seitsonen, Alexander Smogunov, Paolo Umari, and Renata M. Wentzcovitch. QUANTUM ESPRESSO: A modular and open-source software project for quantum simulations of materials. *J. Phys.: Condens. Matter*, 21(39):395502, 2009. doi: 10.1088/0953-8984/21/39/395502.

[2] Xavier Gonze, Bernard Amadon, Gabriel Antonius, Frédéric Arnardi, Lucas Baguet, Jean-Michel Beuken, Jordan Bieder, François Bottin, Johann Bouchet, Eric Bousquet, Nils Brouwer, Fabien Bruneval, Guillaume Brunin, Théo Cavignac, Jean-Baptiste Charraud, Wei Chen, Michel Côté, Stefaan Cottenier, Jules Denier, Grégory Geneste, Philippe Ghosez, Matteo Giantomassi, Yannick Gillet, Olivier Gingras, Donald R. Hamann, Geoffroy Hautier, Xu He, Nicole Helbig, Natalie Holzwarth, Yongchao Jia, François Jollet, William Lafargue-Dit-Hauret, Kurt Lejaeghere, Miguel A. L. Marques, Alexandre Martin, Cyril Martins, Henrique P. C. Miranda, Francesco Naccarato, Kristin Persson, Guido Petretto, Valentin Planes, Yann Pouillon, Sergei Prokhorenko, Fabio Ricci, Gian-Marco Rignanese, Aldo H. Romero, Michael Marcus Schmitt, Marc Torrent, Michiel J. van Setten, Benoit Van Troeye, Matthieu J. Verstraete, Gilles Zérah, and Josef W. Zwanziger. The Abinitproject: Impact, environment and recent developments. *Computer Physics Communications*, 248:107042, 2020. doi: 10.1016/j.cpc.2019.107042.

[3] Nicola Marzari, Arash A. Mostofi, Jonathan R. Yates, Ivo Souza, and David Vanderbilt. Maximally localized Wannier functions: Theory and applications. *Rev. Mod. Phys.*, 84(4):1419–1475, 2012. doi: 10.1103/RevModPhys.84.1419.

[4] Arash A. Mostofi, Jonathan R. Yates, Giovanni Pizzi, Young-Su Lee, Ivo Souza, David Vanderbilt, and Nicola Marzari. An updated version of wannier90: A tool for obtaining maximally-localised Wannier functions. *Comput. Phys. Commun.*, 185(8):2309–2310, 2014. doi: 10.1016/j.cpc.2014.05.003.

[5] Giovanni Pizzi, Valerio Vitale, Ryotaro Arita, Stefan Blügel, Frank Freimuth, Guillaume Géranton, Marco Gibertini, Dominik Gresch, Charles Johnson, Takashi Koretsune, Julen Ibañez-Azpiroz, Hyungjun Lee, Jae-Mo Lihm, Daniel Marchand, Antimo Marrazzo, Yuriy Mokrousov, Jamal I. Mustafa, Yoshiro Nohara, Yusuke Nomura, Lorenzo Paulatto, Samuel Poncé, Thomas Ponweiser, Junfeng Qiao, Florian Thöle, Stepan S. Tsirkin, Ma\lgorzata Wierzbowska, Nicola Marzari, David Vanderbilt, Ivo Souza, Arash A. Mostofi,

and Jonathan R. Yates. Wannier90 as a community code: New features and applications. *J. Phys. Condens. Matter*, 32(16):165902, 2020. doi: 10.1088/1361-648X/ab51ff.

[6] Xinjie Wang, Jonathan R. Yates, Ivo Souza, and David Vanderbilt. Ab initio calculation of the anomalous Hall conductivity by Wannier interpolation. *Phys. Rev. B*, 74(19):195118, 2006. doi: 10.1103/PhysRevB.74.195118.

[7] Ivo Souza, Nicola Marzari, and David Vanderbilt. Maximally localized wannier functions for entangled energy bands. *Phys. Rev. B*, 65:035109, 2001. doi: 10.1103/PhysRevB.65.035109. URL `https://link.aps.org/doi/10.1103/PhysRevB.65.035109`.

[8] Jonathan R. Yates, Xinjie Wang, David Vanderbilt, and Ivo Souza. Spectral and Fermi surface properties from Wannier interpolation. *Phys. Rev. B*, 75 (19):195121, 2007. doi: 10.1103/PhysRevB.75.195121.

[9] Max Born and Kun Huang. *Dynamical Theory of Crystal Lattices*. Oxford, 1954.

[10] Xavier Gonze and Changyol Lee. Dynamical matrices, born effective charges, dielectric permittivity tensors, and interatomic force constants from density-functional perturbation theory. *Phys. Rev. B*, 55:10355–10368, 1997. doi: 10.1103/PhysRevB.55.10355. URL `https://link.aps.org/doi/10.1103/PhysRevB.55.10355`.

[11] Feliciano Giustino, Marvin L. Cohen, and Steven G. Louie. Electron-phonon interaction using Wannier functions. *Phys. Rev. B*, 76(16):165108, 2007. doi: 10.1103/PhysRevB.76.165108.

[12] Matteo Calandra, Gianni Profeta, and Francesco Mauri. Adiabatic and nonadiabatic phonon dispersion in a Wannier function approach. *Phys. Rev. B*, 82 (16):165111, 2010. doi: 10.1103/PhysRevB.82.165111.

[13] Luis A. Agapito and Marco Bernardi. Ab initio electron-phonon interactions using atomic orbital wave functions. *Phys. Rev. B*, 97(23):235146, 2018. doi: 10.1103/PhysRevB.97.235146.

[14] X. Gonze, J.-C. Charlier, D.C. Allan, and M.P. Teter. Interatomic force constants from first principles: The case of α-quartz. *Phys. Rev. B*, 50: 13035–13038, 1994. doi: 10.1103/PhysRevB.50.13035. URL `https://link.aps.org/doi/10.1103/PhysRevB.50.13035`.

[15] H. Fröhlich. Electrons in lattice fields. *Advances in Physics*, 3(11):325–361, 1954. doi: 10.1080/00018735400101213.

[16] J. Sjakste, N. Vast, M. Calandra, and F. Mauri. Wannier interpolation of the electron-phonon matrix elements in polar semiconductors: Polar-optical

coupling in GaAs. *Phys. Rev. B*, 92(5):054307, 2015. doi: 10.1103/PhysRevB.92.054307.

[17] Carla Verdi and Feliciano Giustino. Fröhlich Electron-Phonon Vertex from First Principles. *Phys. Rev. Lett.*, 115(17):176401, 2015. doi: 10.1103/PhysRevLett.115.176401.

[18] Thibault Sohier, Matteo Calandra, and Francesco Mauri. Two-dimensional fröhlich interaction in transition-metal dichalcogenide monolayers: Theoretical modeling and first-principles calculations. *Phys. Rev. B*, 94(8):085415, 2016. doi: 10.1103/PhysRevB.94.085415.

[19] Thibault Sohier, Marco Gibertini, Matteo Calandra, Francesco Mauri, and Nicola Marzari. Breakdown of Optical Phonons' Splitting in Two-Dimensional Materials. *Nano Lett.*, 17(6):3758–3763, 2017. doi: 10.1021/acs.nanolett.7b01090.

[20] Thibault Sohier, Matteo Calandra, and Francesco Mauri. Density functional perturbation theory for gated two-dimensional heterostructures: Theoretical developments and application to flexural phonons in graphene. *Phys. Rev. B*, 96:075448, 2017. doi: 10.1103/PhysRevB.96.075448. URL `https://link.aps.org/doi/10.1103/PhysRevB.96.075448`.

[21] Gerald D. Mahan. *Many-Particle Physics*. Physics of Solids and Liquids. Third edition, 2000. ISBN 978-0-306-46338-9. doi: 10.1007/978-1-4757-5714-9.

[22] Michael Rohlfing and Steven G. Louie. Electron-hole excitations and optical spectra from first principles. *Phys. Rev. B*, 62(8):4927–4944, 2000. doi: 10.1103/PhysRevB.62.4927.

[23] Akihiko Sekine, Dimitrie Culcer, and Allan H. MacDonald. Quantum kinetic theory of the chiral anomaly. *Phys. Rev. B*, 96(23):235134, 2017. doi: 10.1103/PhysRevB.96.235134.

[24] Sunghoon Kim, Seungchan Woo, and Hongki Min. Vertex corrections to the dc conductivity in anisotropic multiband systems. *Phys. Rev. B*, 99(16):165107, 2019. doi: 10.1103/PhysRevB.99.165107.

[25] Jin-Jian Zhou and Marco Bernardi. Predicting charge transport in the presence of polarons: The beyond-quasiparticle regime in $SrTiO_3$. *Phys. Rev. Res.*, 1(3):033138, 2019. doi: 10.1103/PhysRevResearch.1.033138.

[26] Dhruv C. Desai, Bahdan Zviazhynski, Jin-Jian Zhou, and Marco Bernardi. Magnetotransport in semiconductors and two-dimensional materials from first principles. *Phys. Rev. B*, 103(16):L161103, 2021. doi: 10.1103/PhysRevB.103.L161103.

[27] Stefano Baroni, Stefano de Gironcoli, Andrea Dal Corso, and Paolo Giannozzi. Phonons and related crystal properties from density-functional perturbation theory. *Rev. Mod. Phys.*, 73(2):515–562, 2001. doi: 10.1103/RevModPhys.73.515.

[28] Vatsal A. Jhalani, Jin-Jian Zhou, Jinsoo Park, Cyrus E. Dreyer, and Marco Bernardi. Piezoelectric electron-phonon interaction from ab initio dynamical quadrupoles: Impact on charge transport in wurtzite GaN. *Phys. Rev. Lett.*, 125(13):136602, 2020. doi: 10.1103/PhysRevLett.125.136602.

[29] Guillaume Brunin, Henrique Pereira Coutada Miranda, Matteo Giantomassi, Miquel Royo, Massimiliano Stengel, Matthieu J. Verstraete, Xavier Gonze, Gian-Marco Rignanese, and Geoffroy Hautier. Electron-phonon beyond fröhlich: Dynamical quadrupoles in polar and covalent solids. *Phys. Rev. Lett.*, 125(13):136601, 2020. doi: 10.1103/PhysRevLett.125.136601.

[30] I.-Te Lu, Jinsoo Park, Jin-Jian Zhou, and Marco Bernardi. Ab initio electron-defect interactions using Wannier functions. *npj Comput. Mater.*, 6(1):1–7, 2020. doi: 10.1038/s41524-020-0284-y.

[31] Jin-Jian Zhou, Jinsoo Park, Iurii Timrov, Andrea Floris, Matteo Cococcioni, Nicola Marzari, and Marco Bernardi. Ab initio electron-phonon interactions in correlated electron systems. *Phys. Rev. Lett.*, 127(12):126404, 2021. doi: 10.1103/PhysRevLett.127.126404.

[32] Marco Bernardi. First-principles dynamics of electrons and phonons. *Eur. Phys. J. B*, 89(11):239, 2016. doi: 10.1140/epjb/e2016-70399-4.

[33] M. Cardona. Renormalization of the Optical Response of Semiconductors by Electron–Phonon Interaction. *Phys. Status Solidi A*, 188(4):1209–1232, 2001. doi: 10.1002/1521-396X(200112)188:4<1209::AID-PSSA1209>3.0.CO;2-2.

Chapter 2

SPIN-PHONON RELAXATION TIMES IN CENTROSYMMETRIC MATERIALS FROM FIRST PRINCIPLES

2.1 Introduction

Accurately predicting spin-phonon relaxation processes remains an open problem, particularly due to the challenge of quantifying spin-flip e-ph interactions [1]. Calculations of EY spin relaxation have mainly relied on empirical models [2, 3] and symmetry analysis [4–7], yet these approaches are laborious even for simple materials and not geared toward quantitative predictions. Attempts have also been made to study spin relaxation from first principles by assuming a direct proportionality between spin-flip and momentum-scattering e-ph interactions [8], or between spin-flip and momentum relaxation times [9]. However, these assumptions hold only for simple model potentials [10–12] as the spin-flip and momentum-scattering processes can differ greatly depending on the electronic wave function, spin texture, and phonon perturbation [7, 13].

Recently developed first-principles methods for computing e-ph interactions and relaxation times [14] are promising for studying EY spin-phonon relaxation. Their typical workflow [15] involves density functional theory (DFT) calculations of the ground state and electronic band structure, combined with density functional perturbation theory (DFPT) [16] to compute the phonon dispersions and e-ph perturbation potentials, followed by interpolation of the e-ph coupling matrix elements to fine Brillouin zone (BZ) grids. However, this workflow cannot be applied as is to investigate spin-flip e-ph interactions because the spin information is lost when one computes the e-ph matrix elements. For example, the electronic states in centrosymmetric crystals are at least two-fold degenerate, and their spin points in an arbitrary direction due to the freedom in describing the degenerate subspace. Computing spin-phonon interactions *ab initio*, especially in the presence of spin-orbit coupling (SOC) and spinor wave functions, remains an open challenge.

Here we present a first-principles method for computing the spin-flip e-ph coupling matrix elements and the T_1 spin-phonon relaxation times (SRTs). Our approach assumes no relationship between the matrix elements for spin-flip and momentum scattering, and treats spinor wave functions and SOC through fully-relativistic

DFT and DFPT calculations [17]. These advances enable accurate calculations of SRTs and shed light on microscopic details of spin-phonon interactions. We apply our method to investigate SRTs in two key materials for spintronic and quantum technologies, silicon and diamond. Our predicted SRTs in silicon are in excellent agreement with experiment between 50−300 K, while in diamond, where SRT measurements are missing, we predict intrinsic-limit SRTs of roughly 0.5 ms at 77 K and 2 μs at 300 K. In both materials, we find that spin-flip and momentum-scattering e-ph interactions differ widely and are not directly proportional, and the temperature dependence of the spin-flip and momentum relaxation times also differ greatly. Our work demonstrates a precise first-principles approach for computing SRTs, highlighting the limits of widely used simplified analyses and opening new avenues for microscopic understanding of spin dynamics.

2.2 Theoretical Framework

Spin-flip interactions

In centrosymmetric materials, the Bloch states with band index n and crystal momentum $\boldsymbol{k}$ can be decomposed into *effective* up and down spin states, denoted as $\Uparrow$ and $\Downarrow$, which diagonalize the spin operator $\hat{S}_\alpha$ (where α is the Cartesian direction of the spin quantization axis) in the Kramers degenerate subspace [1, 18, 19]:

$$\begin{aligned} \langle n\boldsymbol{k}\Uparrow|\hat{S}_\alpha|n\boldsymbol{k}\Uparrow\rangle &= -\langle n\boldsymbol{k}\Downarrow|\hat{S}_\alpha|n\boldsymbol{k}\Downarrow\rangle\,, \\ \langle n\boldsymbol{k}\Downarrow|\hat{S}_\alpha|n\boldsymbol{k}\Uparrow\rangle &= 0. \end{aligned} \tag{2.1}$$

The key ingredients for computing the SRTs are the spin-flip e-ph matrix elements [1],

$$g^{\text{flip}}_{mn\nu}(\boldsymbol{k},\boldsymbol{q}) = \langle m\boldsymbol{k}+\boldsymbol{q}\Downarrow|\Delta\hat{V}_{\nu\boldsymbol{q}}|n\boldsymbol{k}\Uparrow\rangle\,, \tag{2.2}$$

which quantify the probability amplitude to scatter from an initial Bloch state $|n\boldsymbol{k}\Uparrow\rangle$ to a final state $|m\boldsymbol{k}+\boldsymbol{q}\Downarrow\rangle$ with opposite effective spin, by emitting or absorbing a phonon with mode index ν and wave vector $\boldsymbol{q}$ due to the Kohn-Sham potential perturbation $\Delta\hat{V}_{\nu\boldsymbol{q}}$ [14], which is a 2×2 matrix in spin space in the presence of SOC.

To compute the SRTs, we obtain the effective spin states and from them the spin-flip e-ph matrix elements $g^{\text{flip}}_{mn\nu}(\boldsymbol{k},\boldsymbol{q})$ on fine BZ grids. We calculate the effective spin states from the spin matrix $S(\boldsymbol{k})$, which provides a matrix representation of the spin operator $\hat{S}_\alpha$ in the wave function basis [20], $S_{ms',ns}(\boldsymbol{k}) = \langle m\boldsymbol{k}s'|\hat{S}_\alpha|n\boldsymbol{k}s\rangle$, where s and s' denote the spin. We diagonalize separately each degenerate subspace in the spin matrix at each $\boldsymbol{k}$-point, obtaining the unitary matrices $D_{\boldsymbol{k}}$ that make each of the subspaces in $D_{\boldsymbol{k}} S(\boldsymbol{k}) D_{\boldsymbol{k}}^{\dagger}$ diagonal, with eigenvalues equal to the effective spin [1]. The spin-flip e-ph matrix elements, $g_{mn\nu}^{\text{flip}}(\boldsymbol{k}, \boldsymbol{q})$, are then computed using Eq. (2.2) for all pairs of states with opposite effective spin.

Interpolation

Since DFPT calculations of $\Delta \hat{V}_{\nu \boldsymbol{q}}$ on the fine BZ grids needed to converge the SRTs are prohibitively expensive, we interpolate the spin-flip e-ph matrix elements and spin matrices using Wannier functions [21–23]. To obtain $g_{mn\nu}^{\text{flip}}(\boldsymbol{k}', \boldsymbol{q}')$ at a desired pair of $\boldsymbol{k}'$ and $\boldsymbol{q}'$ points in the BZ, we first apply the usual Wannier interpolation workflow [15, 24] to obtain the e-ph matrix elements $g_{mn\nu}^{ss'}(\boldsymbol{k}', \boldsymbol{q}')$ between states with arbitrary spins s and s'. The e-ph matrix elements $g_{mn\nu}^{\sigma\sigma'}(\boldsymbol{k}', \boldsymbol{q}')$ coupling states with effective spins σ and σ' are then computed using the unitary matrix $D_{\boldsymbol{k}'}$ (the latter is obtained from Wannier interpolation of the spin matrix [20]):

$$g_{mn\nu}^{\sigma\sigma'}(\boldsymbol{k}', \boldsymbol{q}') = \left[D_{\boldsymbol{k}'+\boldsymbol{q}'}\right]_{m\sigma, ms} \left[g_{mn\nu}^{ss'}(\boldsymbol{k}', \boldsymbol{q}')\right] \left[D_{\boldsymbol{k}'}^{\dagger}\right]_{ns', n\sigma'} . \tag{2.3}$$

The spin-flip e-ph matrix elements are finally computed between all pairs of electronic states with opposite sign of the effective spin. Our interpolation scheme can accurately reproduce spin-flip e-ph matrix elements obtained by combining effective spin states with perturbation potentials computed directly with DFPT (see the Supplemental Material), thus enabling precise calculations of SRTs.

Spin relaxation times

The band- and $\boldsymbol{k}$-dependent spin-flip e-ph relaxation times, $\tau_{n\boldsymbol{k}}^{\text{flip}}$, are computed using lowest-order perturbation theory [1],

$$\begin{aligned} \frac{1}{\tau_{n\boldsymbol{k}}^{\text{flip}}} =& \frac{4\pi}{\hbar} \sum_{m\nu\boldsymbol{q}} \left| g_{mn\nu}^{\text{flip}}(\boldsymbol{k}, \boldsymbol{q}) \right|^2 \\ & [(N_{\nu\boldsymbol{q}} + 1 - f_{m\boldsymbol{k}\boldsymbol{q}}) \delta(\varepsilon_{n\boldsymbol{k}} - \varepsilon_{m\boldsymbol{k}\boldsymbol{q}} - \hbar\omega_{\nu\boldsymbol{q}}) \\ & + (N_{\nu\boldsymbol{q}} + f_{m\boldsymbol{k}\boldsymbol{q}}) \delta(\varepsilon_{n\boldsymbol{k}} - \varepsilon_{m\boldsymbol{k}\boldsymbol{q}} + \hbar\omega_{\nu\boldsymbol{q}})], \end{aligned} \tag{2.4}$$

where $\varepsilon_{n\boldsymbol{k}}$ and $\hbar\omega_{\nu\boldsymbol{q}}$ are the electron and phonon energies, respectively, and $f_{n\boldsymbol{k}}$ and $N_{\nu\boldsymbol{q}}$ the corresponding temperature-dependent occupations.

Converging the band- and $\boldsymbol{k}$-dependent spin-flip e-ph relaxation times, $\tau_{n\boldsymbol{k}}^{\text{flip}}$, is of paramount importance for precise predictions of T_1 spin-phonon relaxation times.

---

[1] When only the two-fold degeneracy due to time-reversal plus inversion symmetry is present, the diagonal elements of $S(\boldsymbol{k})$ naturally determine the effective spin value. For states with additional degeneracies, $D_{\boldsymbol{k}}$ diagonalizes the degenerate subspace, giving multiple pairs of states with opposite effective spin.

Computing $\tau_{n\boldsymbol{k}}^{\text{flip}}$ involves a sum over the $\boldsymbol{q}$-point grid, which is typically performed by random sampling of the BZ [25]. However, the spin-flip matrix elements $g_{mn\nu}^{\text{flip}}(\boldsymbol{k}, \boldsymbol{q})$ entering the summation vary by several orders of magnitude throughout the BZ, so converging $\tau_{n\boldsymbol{k}}^{\text{flip}}$ is challenging.

Here we develop and employ an importance sampling approach for efficiently converging the BZ $\boldsymbol{q}$-point summation in Eq. (2.4). We first sample on a regular $\boldsymbol{q}$-point BZ grid the quantity

$$\begin{aligned} P_{n\boldsymbol{k}}(\boldsymbol{q}) = \sum_{m\nu} &\left| g_{mn\nu}^{\text{flip}}(\boldsymbol{k}, \boldsymbol{q}) \right|^2 \\ &[(N_{\nu\boldsymbol{q}} + 1 - f_{m\boldsymbol{k}\boldsymbol{q}})\delta(\varepsilon_{n\boldsymbol{k}} - \varepsilon_{m\boldsymbol{k}\boldsymbol{q}} - \hbar\omega_{\nu\boldsymbol{q}}) \\ &+ (N_{\nu\boldsymbol{q}} + f_{m\boldsymbol{k}\boldsymbol{q}})\delta(\varepsilon_{n\boldsymbol{k}} - \varepsilon_{m\boldsymbol{k}\boldsymbol{q}} + \hbar\omega_{\nu\boldsymbol{q}})]. \end{aligned} \tag{2.5}$$

From $P_{n\boldsymbol{k}}(\boldsymbol{q})$, we construct a three-dimensional probability density function, $\tilde{P}_{n\boldsymbol{k}}(\boldsymbol{q})$, by nearest neighbor interpolation, and then perform an importance sampling integration for $\tau_{n\boldsymbol{k}}^{\text{flip}}$ by drawing samples from the probability density function $\tilde{P}_{n\boldsymbol{k}}(\boldsymbol{q})$. The convergence rate of the importance sampling approach is orders of magnitude faster than random sampling (see the Supplemental Material for the importance sampling approach used in Eq. (2.4), the states chosen for the comparison in Fig. 2.2, additional comparison of spin-flip and momentum-scattering matrix elements, momentum-scattering processes in diamond, and convergence of the interpolation scheme with respect to the coarse grid size). The considerable time-saving afforded by our importance sampling method allows us to fully converge the SRTs.

The temperature-dependent SRT, $\tau_s(T)$, is the main physical observable computed in this work. It is obtained as an ensemble average of the spin-flip relaxation times [1] by tetrahedron integration [31]:

$$\tau_s(T) = \left\langle \frac{1}{\tau_{n\boldsymbol{k}}^{\text{flip}}} \right\rangle_T^{-1} = \left(\frac{\sum_{n\boldsymbol{k}} \frac{1}{\tau_{n\boldsymbol{k}}^{\text{flip}}} \left(-\frac{df_{n\boldsymbol{k}}}{dE} \right) d\boldsymbol{k}}{\sum_{n\boldsymbol{k}} \left(-\frac{df_{n\boldsymbol{k}}}{dE} \right) d\boldsymbol{k}} \right)^{-1}. \tag{2.6}$$

Numerical methods

We apply our approach to investigate spin relaxation in silicon and diamond. We obtain their ground state and band structure using DFT with a plane-wave basis with the Quantum ESPRESSO code [32]. Briefly, we use relaxed lattice constants of 5.43 Å for silicon and 3.56 Å for diamond, together with a kinetic energy cutoff of 60 Ry

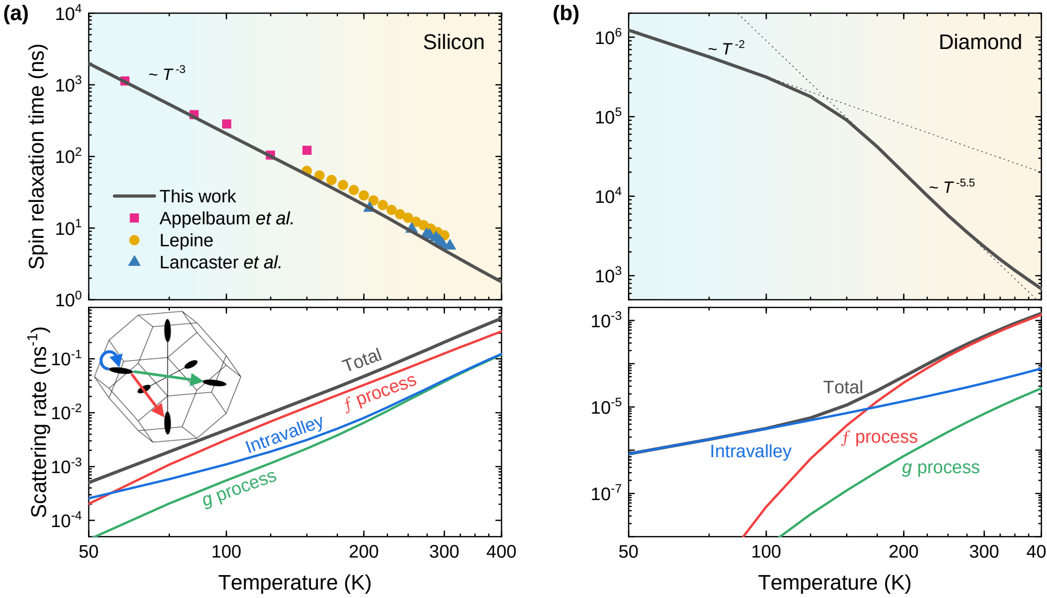

Figure 2.1: Computed spin-phonon relaxation times as a function of temperature in (a) silicon and (b) diamond. The experimental data in (a) are taken from Refs. [26–30]. The lower panels show the process-resolved spin-flip e-ph scattering rates, defined as the inverse of τ_s. Shown are the contributions from intravalley processes (blue line), f processes (red line) and g processes (green line), which add up to the total (gray line). The inset in (a) is a schematic of the intravalley and intervalley processes.

for silicon and 120 Ry for diamond. We employ the PBEsol exchange-correlation functional [33] and fully-relativistic norm-conserving pseudopotentials [17] from Pseudo Dojo [34], which correctly include the SOC. We use DFPT [16] to compute the phonon dispersions and the perturbation potential, $\Delta\hat{V}_{\nu\boldsymbol{q}}$ in Eq. (2.2), on coarse $\boldsymbol{q}$-point grids; our in-house developed Perturbo code (see Chapter 6) is employed to compute the spin-dependent e-ph matrix elements on coarse BZ grids [2]. The DFPT calculations are done only in the irreducible $\boldsymbol{q}$-point grid, following which we extend the coarse-grid e-ph matrix elements to the full $\boldsymbol{q}$-point grid in Perturbo by rotating the spinor wave functions with $SU(2)$ matrices. The Wannier functions and spin matrices are computed with the Wannier90 code [20] and employed in Perturbo to interpolate the spin-flip e-ph matrix elements on fine BZ grids with up to 200^3 $\boldsymbol{k}$-points to converge the SRTs. The spin quantization axis is chosen

---

[2] The DFPT calculations are carried out on an $8\times8\times8$ $\boldsymbol{q}$-point grid in diamond and a $10\times10\times10$ $\boldsymbol{q}$-point grid in silicon. The spin-flip e-ph matrix elements are computed on $16\times16\times16$ $\boldsymbol{k}$-point and $8\times8\times8$ $\boldsymbol{q}$-point grids in diamond and $10\times10\times10$ $\boldsymbol{k}$-point and $\boldsymbol{q}$-point grids in silicon.

as the [001] direction [3]. We employ a non-degenerate electron concentration of 7.4×10^{14} cm^{-3} for silicon, which is identical to the experimental value in Ref. [29], and 1.0×10^{17} cm^{-3} for diamond; in each case, the Fermi energy is computed from the carrier concentration. The carrier concentration dependence of the SRTs is negligible in this non-degenerate regime.

2.3 Results

Temperature-dependent spin relaxation times

Figure 2.1(a) shows our calculated SRT as a function of temperature in silicon, which is in excellent agreement with experiments [26–30] (see also Ref. [35]) at all temperatures between 50−300 K. For example, our calculated SRT at room-temperature is 4.9 ns, versus a 6.0 ns value measured by Lancaster *et al.* [4]. The SRT in silicon exhibits an approximate T^{-3} temperature dependence; to explain its origin, we analyze in Fig. 2.1(a) the contributions from the three valley-dependent scattering processes, including the intravalley and so-called g and f intervalley processes, which correspond to scattering between valleys along the same direction (g processes) or along different directions (f processes). We find that the SRTs are comparable in magnitude for the three processes at all temperatures. The intravalley processes govern spin relaxation below 60 K, while f intervalley scattering dominates at higher temperatures.

In the conventional theory of spin relaxation, the power-law temperature behavior of the SRT is typically attributed to a specific physical origin. For example, Yafet's prediction of a $T^{-2.5}$ temperature trend for the SRTs in silicon [1] took into account only acoustic phonons and intravalley processes. In our quantitative approach, all phonon modes and valley processes are taken into account on the same footing and enter the scattering rate in Eq. (2.4). Each phonon mode has its own energy dispersion and population factor, and the spin-flip coupling strength depends on the electronic states and phonon modes considered in the scattering process. As a result, the temperature trend emerges not from a unique origin, but due to a combination of factors due to all electronic-state and phonon-mode dependent quantities in Eq. (2.4). Therefore one cannot attribute a single physical origin to the approximate T^{-3} power

---

[3] Our computed SRTs are nearly independent of the choice of the spin quantization axis, which changes the SRTs by only 2−5% in our temperature range of interest, due to a symmetry breaking introduced by the Wannier interpolation.

[4] We have verified that the results are nearly unchanged when using a different exchange-correlation functional. Using the same settings, the calculated SRT at 300 K is 4.8 ns with PBE and 4.5 ns with LDA

law dependence of the SRTs.

Due to its weak SOC and correspondingly long SRT, diamond is a promising material for spintronics and spin-based quantum technologies. However, SRT measurements have not yet been reported in diamond due to challenges related to spin injection [36]. Figure 2.1(b) shows our computed SRT in diamond as a function of temperature. We find SRTs of 540 μs at 77 K and 2.3 μs at 300 K; these values set an intrinsic limit due to phonons to the SRTs in diamond. The SRT exhibits a T^{-2} temperature dependence below ~170 K and a stronger $T^{-5.5}$ trend above 170 K. This trend is in contrast with a previous prediction [8] of a T^{-5} temperature dependence throughout the entire temperature range and of an order-of-magnitude smaller SRT of 180 ns at room temperature. Ref. [8] assumed a direct proportionality between the spin-flip and momentum-scattering e-ph matrix elements, but, as we show below, this assumption is in general incorrect and can lead to inaccurate phonon contributions to the SRT. We analyze the valley scattering processes in diamond in Fig. 2.1(b), and find that the intravalley processes dominate below 170 K, while the intervalley f processes dominate above 170 K.

Spin-flip versus momentum scattering

Our quantitative approach reveals stark differences between the spin-flip and the momentum-scattering interactions. Figure 2.2 compares the spin-flip coupling matrix elements, $\left|g_{\nu}^{\text{flip}}(\boldsymbol{q})\right|$, with the spin-flip plus spin-conserving (i.e., momentum-scattering) e-ph matrix elements, $\left|g_{\nu}^{\text{tot}}(\boldsymbol{q})\right|$, and resolves their ratio for different phonon modes. Depending on the phonon branch, we find that the spin-flip and momentum matrix elements can differ by several orders of magnitude, as we find for the longitudinal acoustic (LA) and longitudinal optical (LO) branches along $\Gamma-$X and for the LO and for specific transverse optical (TO-1) and transverse acoustic (TA-2) branches along X$-$K$-\Gamma$. For other phonon modes and BZ directions, the two quantities exhibit smaller, yet quantitatively important, differences. Only in specific cases are the spin-flip and momentum-scattering interactions nearly identical, as we find for the TO-2, TA-1 and LA branches along X$-$K$-\Gamma$. These trends are common to silicon and diamond. Analogous results are found when analyzing various initial and final electronic states.

Lastly, we compare the spin-phonon and momentum relaxation times. The momentum relaxation time τ_p is defined as the usual (spin-independent) e-ph relaxation time [14], thermally averaged using Eq. (2.6) to make the comparison meaningful.

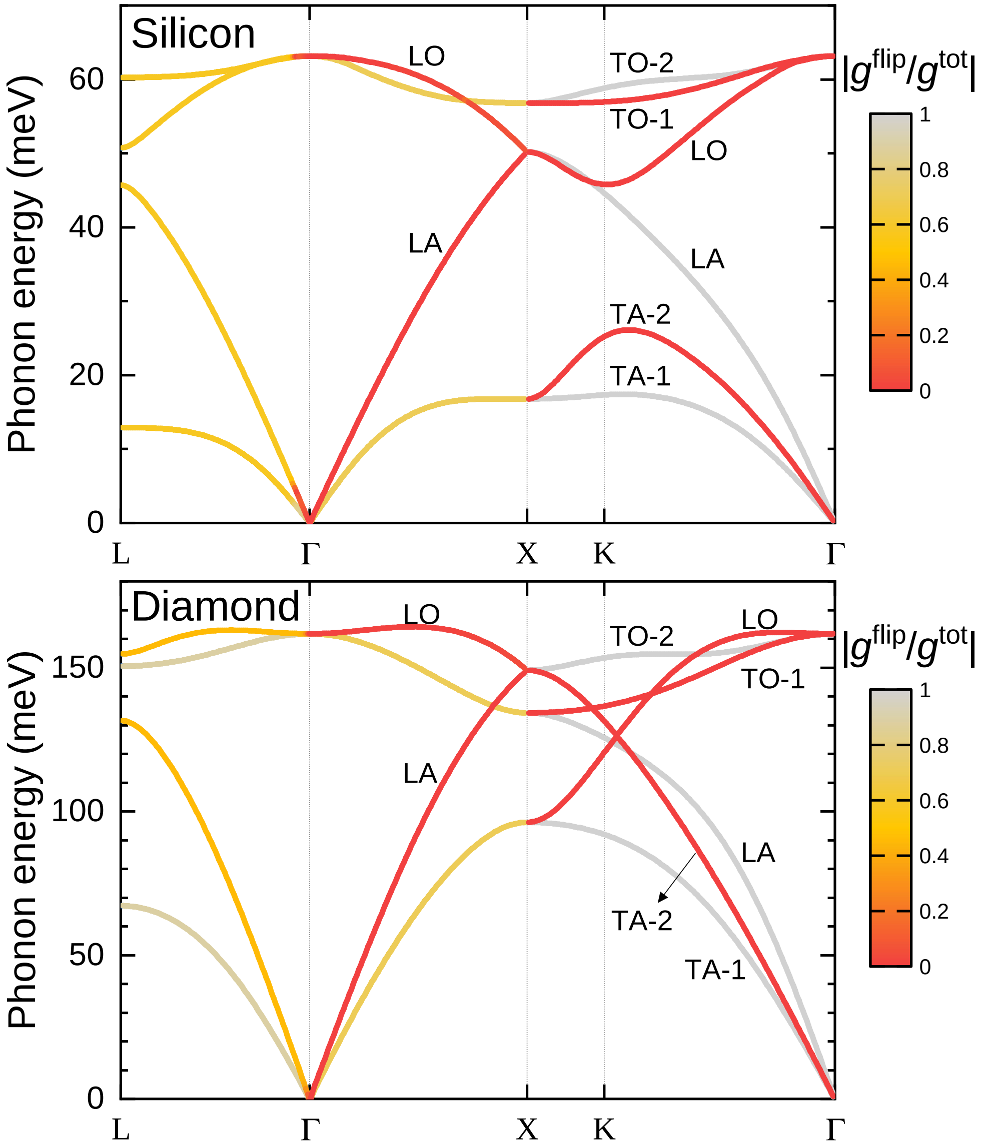

Figure 2.2: Phonon dispersions in silicon and diamond, overlaid with a color map of the ratio $\left|g_{\nu}^{\text{flip}}(\boldsymbol{q})/g_{\nu}^{\text{tot}}(\boldsymbol{q})\right|$ between the spin-flip and the momentum-scattering e-ph matrix elements. The two matrix elements differ by orders of magnitude for the branches shown in red. The data shown are the square root of the gauge-invariant trace of $|g|^2$ for a low-energy spin-degenerate conduction band. The initial electron momentum is set to the Γ point and we plot the ratio for phonon wave vectors $\boldsymbol{q}$ along a high-symmetry BZ line.

The conventional wisdom is that spin and momentum relaxation times are directly proportional [10, 18], an assumption that has been widely used to analyze spin relaxation mechanisms in experimental data [37–42]. Figure 2.3 shows the temperature dependent spin and momentum relaxation times in silicon and diamond. In silicon, the SRT follows a T^{-3} temperature dependence, whereas the momentum relaxation time follows a T^{-2} trend. In diamond, the SRT makes a sharp transition from a T^{-2} trend at low temperature to a stronger $T^{-5.5}$ trend above 170 K. In contrast, the momentum relaxation time exhibits a much weaker temperature dependence, roughly $T^{-1.5}$ at low temperature and $T^{-2.5}$ near room temperature.

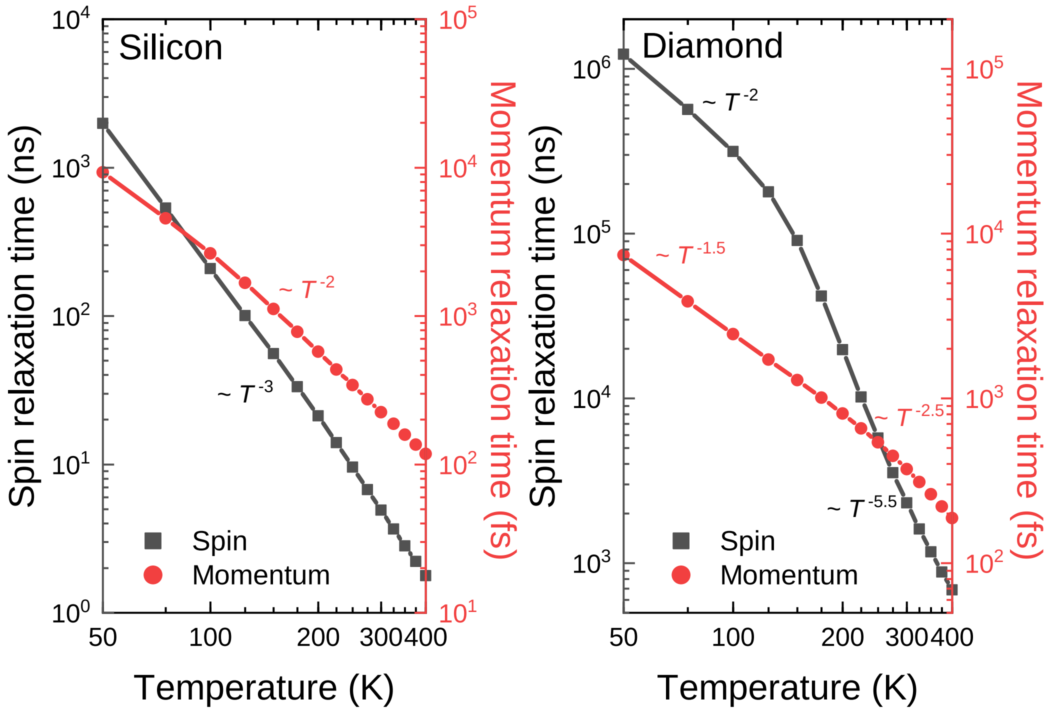

Figure 2.3: Comparison between the temperature dependence of the SRT (gray squares) and the momentum relaxation time (red circles) in silicon and diamond. The labels give the exponent n of the SRT temperature dependence, T^{-n}, separately for each of the spin and momentum relaxation times. Note that the SRTs are in ns units, and the momentum relaxation times in fs units.

There is no discernible direct proportionality between the spin and momentum relaxation times — rather, they both exhibit an approximate T^{-n} temperature dependence, but with different values of the exponent n (see Fig. 2.3). These differences originate from the different coupling strengths and phonon mode contributions, as we illustrate in Fig. 2.2. For example, we find that for momentum scattering in diamond the intravalley processes dominate over the entire temperature range up to 400 K, as opposed to just below 170 K as we show above for spin relaxation (see the Supplemental Material).

Simple formulas such as the Elliott approximation [18], $\tau_s = \tau_p/4\left\langle b^2\right\rangle_T$, where b^2 is the spin-mixing parameter [12, 43], also fail in both materials, as we show in Fig. 2.4. For silicon, the average spin-mixing parameter b^2 changes only by a small factor of 2 throughout the entire temperature range, whereas for diamond the change is less than 10 %. As a result, the temperature dependence of the SRTs from the Elliott approximation is weaker than the temperature dependence of the SRTs from first principles, and the SRTs computed with the Elliott approximation exhibit a trend similar to the momentum-relaxation times. We conclude that a reliable analysis of SRTs needs atomistic calculations that take into account the different nature of the spin-phonon and momentum-scattering e-ph interactions, by using accurate spin-flip e-ph matrix elements as we show in this work.

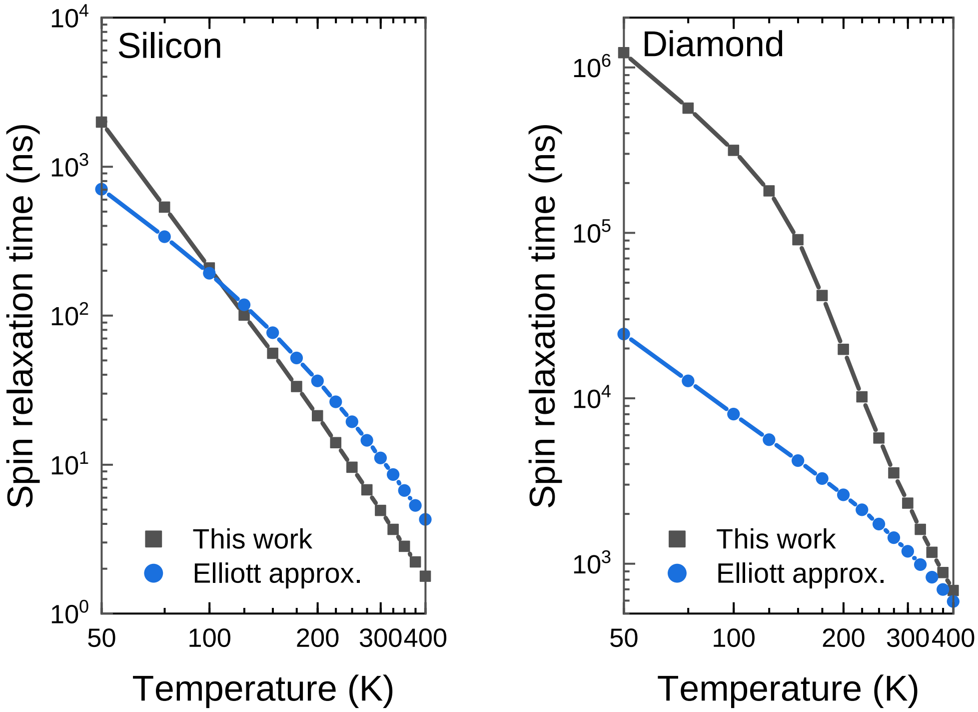

Figure 2.4: Comparison between the temperature dependence of the SRT from first principles (gray squares) and the Elliott approximation (blue circles) in silicon and diamond.

2.4 Discussion

Since SRT calculations involve a subtle interplay between spin-flip e-ph matrix elements and phonons and electronic states, the relative magnitude of the spin-phonon interactions for different phonon modes is of paramount importance for accurate predictions. Our results show that the widely used proportionality between spin and momentum relaxation times can be inaccurate, highlighting the need for atomistic details such as the electronic wave function, spin texture, phonon modes, and their mode-dependent spin-flip interactions. When these microscopic details are captured, as we have shown above, one can predict the SRTs within $\sim$10$-$20% of experiment over a wide temperature range, and predict which phonon modes govern spin relaxation. While computing e-ph interactions and carrier relaxation has become a main effort in first-principles calculations [25, 44–47], SRT calculations are still in their infancy, and more work is needed to expand their scope beyond the EY mechanism discussed here.

2.5 Conclusion

In summary, we have developed a quantitatively accurate approach for computing spin-flip e-ph interactions and SRTs due to the EY mechanism. Our calculations can predict accurately (within 10-20 of experiment) the measured spin relaxation times in silicon between 50-300 K, without using any empirical or fitting parameter. In diamond, where spin relaxation times have not yet been measured in spite of its wide use in spin-based qubits, we predict intrinsic-limit spin relaxation times over a wide temperature range, and reveal their microscopic origin. Our work further shows that the spin- and momentum-relaxation mechanisms are governed by distinct microscopic processes. We demonstrate that the widely used proportionality between spin and momentum relaxation times is inaccurate, highlighting the limits of simplified models and the need for atomistic spin relaxation calculations. Our work enables first-principles modeling of spin-phonon dynamics in broad classes of materials. It can advance microscopic understanding of spin dynamics in semiconductors, localized spins, ions, or quantum dots and other systems of fundamental and technological relevance.

2.6 Supplemental Material

Importance sampling approach for computing spin-flip relaxation times

Figure 2.5 compares the convergence of $\tau_{n\boldsymbol{k}}^{\text{flip}}$ with a random sampling approach and with our importance sampling method. The convergence rate of the importance sampling approach is orders of magnitude faster than random sampling. For example, the required number of $\boldsymbol{q}$-points to reach a 1% error for the importance sampling method is $30,000$, versus a much larger value of 65 million points for the random sampling method. The considerable time saving afforded by our importance sampling method allows us to fully converge the spin relaxation times.

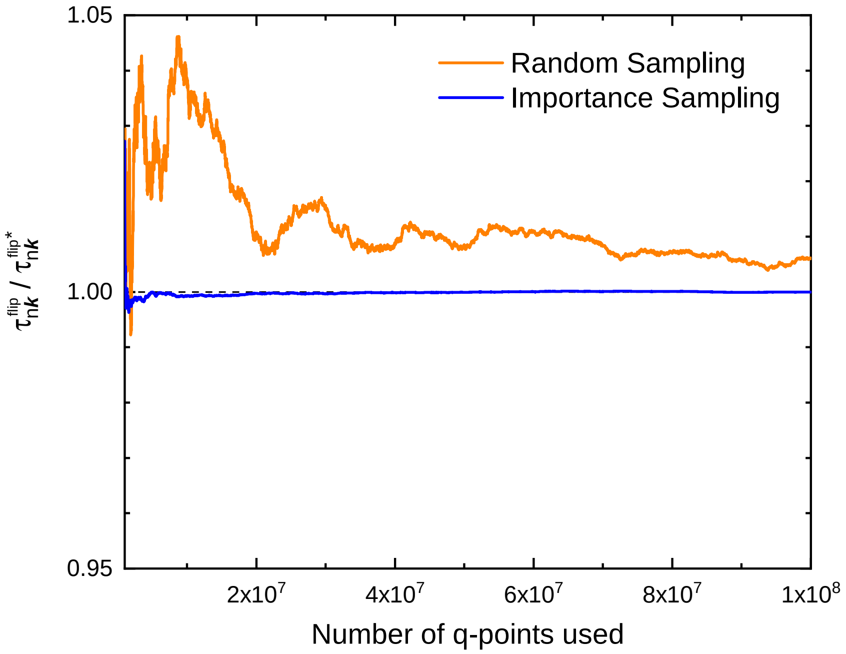

Figure 2.5: Comparison between the convergence of the random sampling method (orange line) and the importance sampling method (blue line). The initial electron band n and momentum $\boldsymbol{k}$ are set to the conduction band minimum, and only the f process is considered to illustrate the convergence trend. Shown is the ratio between the computed $\tau_{n\boldsymbol{k}}^{\text{flip}}$ and the converged value $\tau_{n\boldsymbol{k}}^{\text{flip}*}$, which is computed with a $1000 \times 1000 \times 1000$ $\boldsymbol{q}$-point BZ grid. The $P_{\boldsymbol{k}}(\boldsymbol{q})$ distribution used in the importance sampling method is computed using a $100 \times 100 \times 100$ $\boldsymbol{q}$-point grid.

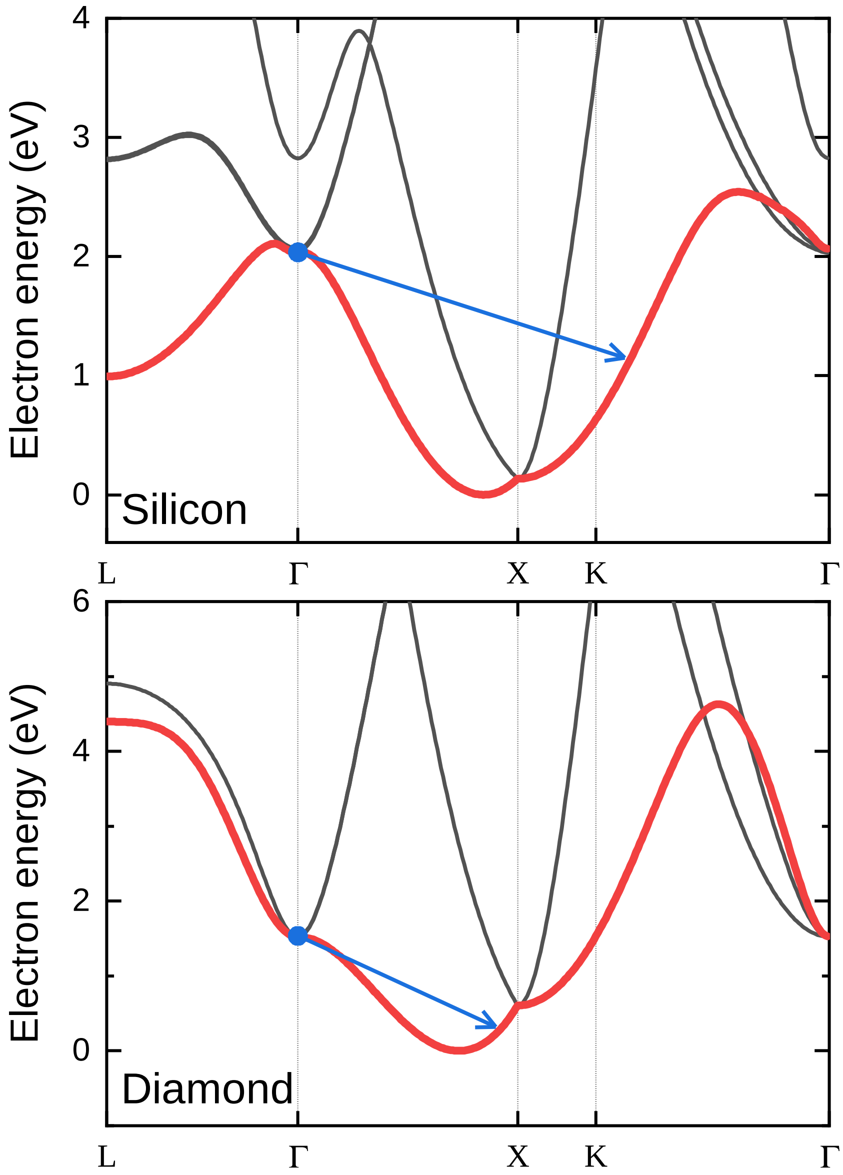

Figure 2.6: The low-energy spin-degenerate conduction band in silicon and diamond chosen to compute the ratio between the spin-flip and the momentum-scattering *e*-ph matrix elements in Fig. 2.2 of the main text. The blue circle is the initial electronic state.

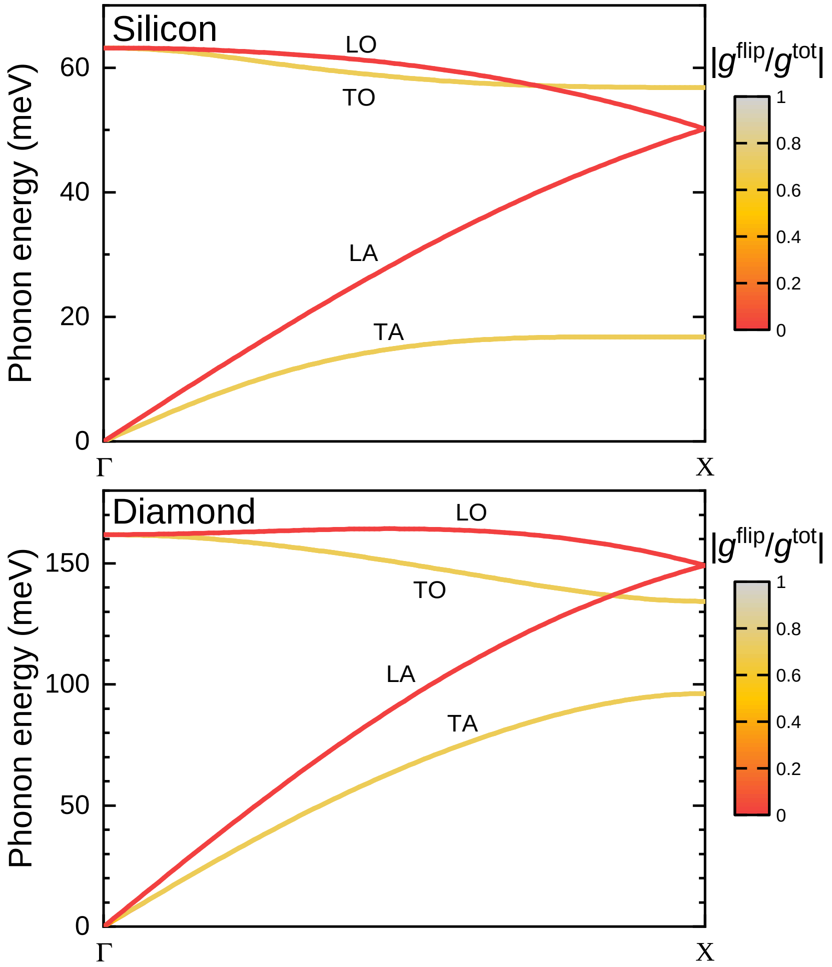

Figure 2.7: Phonon dispersions in silicon and diamond, overlaid with a color map of the ratio $\left|g_\nu^{\mathrm{flip}}(\boldsymbol{q})/g_\nu^{\mathrm{tot}}(\boldsymbol{q})\right|$ between the spin-flip and the total (i.e. momentum-scattering) e-ph matrix elements; the two matrix elements differ by orders of magnitude for the branches shown in red. The data shown are the square root of the gauge-invariant trace of $|g|^2$ over a low-energy spin-degenerate conduction band shown in Fig. 2.6. The initial electron momentum is set to the X point, which is different from the Γ point used in Fig. 2.2 of the main text, and we plot the ratio for phonon wave vectors $\boldsymbol{q}$ along Γ−X.

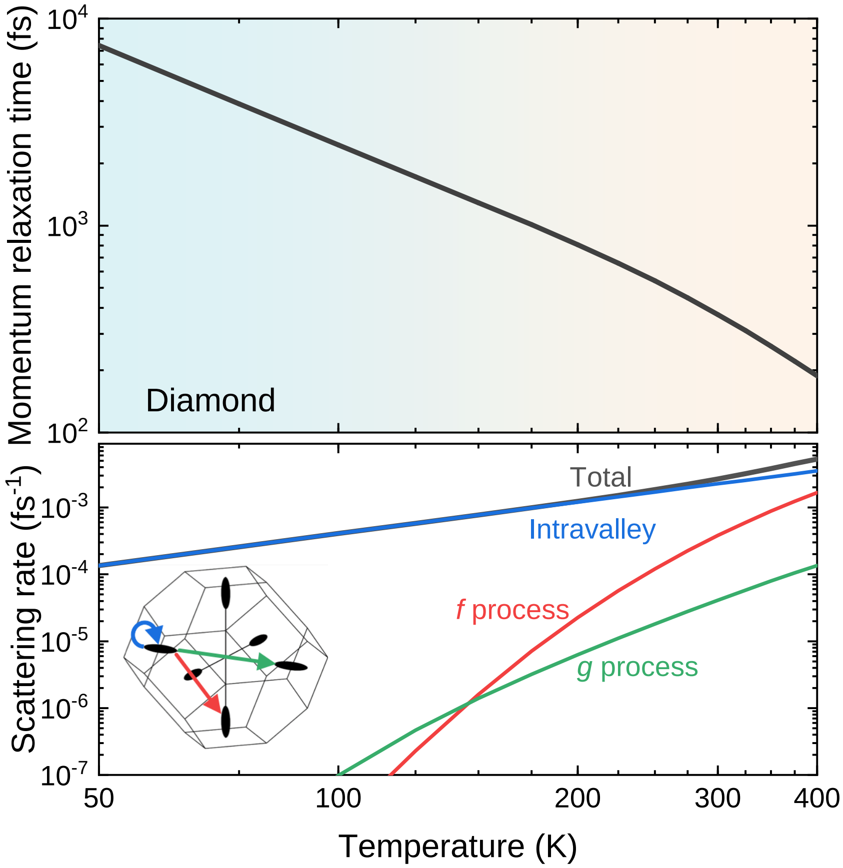

Figure 2.8: Computed momentum relaxation times as a function of temperature in diamond. The lower panel shows the process-resolved momentum-scattering *e*-ph scattering rates, defined as the inverse of the momentum relaxation time τ_p (see the main text). Shown are the contributions from intravalley processes (blue line), *f* processes (red line), and *g* processes (green line), which add up to the total (gray line). It is seen that for momentum scattering in diamond, intravalley scattering dominates over the entire temperature range, while for spin relaxation the intravalley processes are dominant only below 170 K (see the main text).

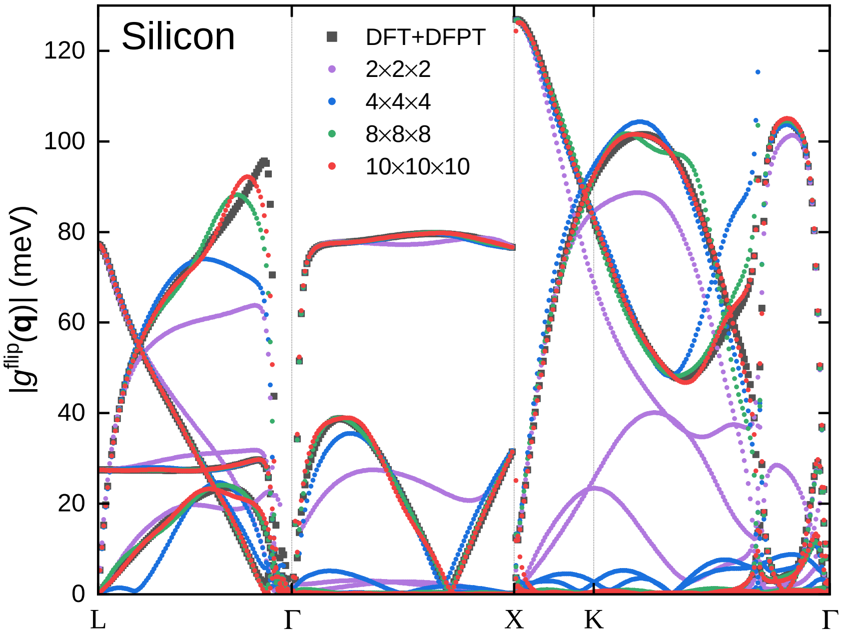

Figure 2.9: Comparison between the spin-flip e-ph matrix elements $\left|g_{\nu}^{\mathrm{flip}}(\boldsymbol{q})\right|$ computed with DFPT (gray squares) and those obtained from our Wannier interpolation scheme discussed in the main text. For the latter, we show results obtained with coarse $\boldsymbol{q}$-point grids of $2\times2\times2$ (purple dots), $4\times4\times4$ (blue dots), $8\times8\times8$ (green dots), and $10\times10\times10$ (red dots). It is seen that $8\times8\times8$ or finer $\boldsymbol{q}$-point grids, as we used in our work, are sufficient for accurately interpolating the DFPT e-ph matrix elements. The data shown are for silicon, and we plot the square root of the gauge-invariant trace of $|g|^2$ over the lowest spin-degenerate conduction band. The initial electron momentum is set to the Γ point and we plot the matrix elements for phonon wave vectors $\boldsymbol{q}$ along a high-symmetry BZ line.

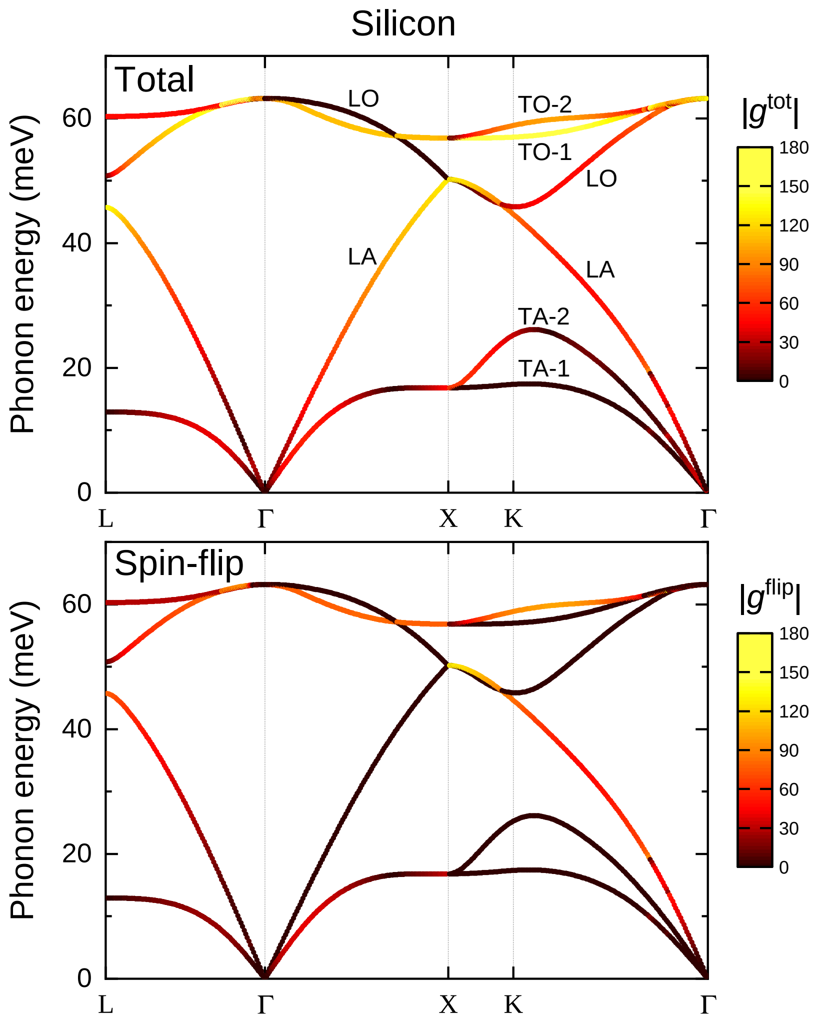

Figure 2.10: Phonon dispersions in silicon, overlaid with a color map of the total (i.e. momentum-scattering) e-ph matrix elements $\left|g_{\nu}^{\text{flip}}(\boldsymbol{q})\right|$ (upper panel) and the spin-flip e-ph matrix elements $\left|g_{\nu}^{\text{tot}}(\boldsymbol{q})\right|$ (lower panel). The data shown are the square root of the gauge-invariant trace of $|g|^2$ for a low-energy spin-degenerate conduction band (see Fig. 2.6). The initial electron momentum is set to the Γ point and we plot the values for phonon wave vectors $\boldsymbol{q}$ along a high-symmetry BZ line.

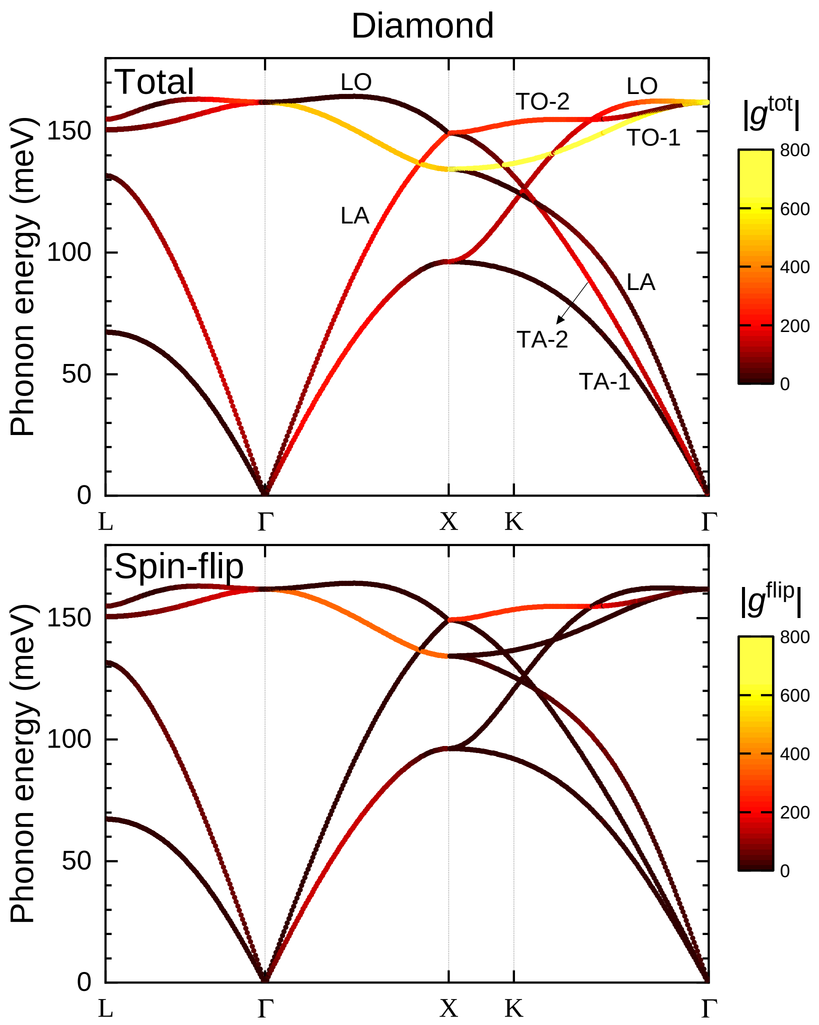

Figure 2.11: Phonon dispersions in diamond, overlaid with a color map of the total (i.e. momentum-scattering) e-ph matrix elements $\left|g_{\nu}^{\text{flip}}(\boldsymbol{q})\right|$ (upper panel) and the spin-flip e-ph matrix elements $\left|g_{\nu}^{\text{tot}}(\boldsymbol{q})\right|$ (lower panel). The data shown are the square root of the gauge-invariant trace of $|g|^2$ for a low-energy spin-degenerate conduction band (see Fig. 2.6). The initial electron momentum is set to the Γ point and we plot the values for phonon wave vectors $\boldsymbol{q}$ along a high-symmetry BZ line.

References

[1] Y. Yafet. G Factors and Spin-Lattice Relaxation of Conduction Electrons. In Frederick Seitz and David Turnbull, editors, *Solid State Physics*, volume 14, pages 1–98. Academic Press, 1963. doi: 10.1016/S0081-1947(08)60259-3.

[2] J. L. Cheng, M. W. Wu, and J. Fabian. Theory of the Spin Relaxation of Conduction Electrons in Silicon. *Phys. Rev. Lett.*, 104(1):016601, 2010. doi: 10.1103/PhysRevLett.104.016601.

[3] Annamária Kiss, Lénard Szolnoki, and Ferenc Simon. The Elliott-Yafet theory of spin relaxation generalized for large spin-orbit coupling. *Sci. Rep.*, 6:22706, 2016. ISSN 2045-2322. doi: 10.1038/srep22706.

[4] Jian-Ming Tang, Brian T. Collins, and Michael E. Flatté. Electron spin-phonon interaction symmetries and tunable spin relaxation in silicon and germanium. *Phys. Rev. B*, 85(4):045202, 2012. doi: 10.1103/PhysRevB.85.045202.

[5] Yang Song and Hanan Dery. Analysis of phonon-induced spin relaxation processes in silicon. *Phys. Rev. B*, 86(8):085201, 2012. doi: 10.1103/PhysRevB.86.085201.

[6] Pengke Li, Yang Song, and Hanan Dery. Intrinsic spin lifetime of conduction electrons in germanium. *Phys. Rev. B*, 86(8):085202, 2012. doi: 10.1103/PhysRevB.86.085202.

[7] Yang Song and Hanan Dery. Transport Theory of Monolayer Transition-Metal Dichalcogenides through Symmetry. *Phys. Rev. Lett.*, 111(2):026601, 2013. ISSN 0031-9007, 1079-7114. doi: 10.1103/PhysRevLett.111.026601.

[8] O. D. Restrepo and W. Windl. Full First-Principles Theory of Spin Relaxation in Group-IV Materials. *Phys. Rev. Lett.*, 109(16):166604, 2012. doi: 10.1103/PhysRevLett.109.166604.

[9] Marcin Kurpas, Martin Gmitra, and Jaroslav Fabian. Spin-orbit coupling and spin relaxation in phosphorene: Intrinsic versus extrinsic effects. *Phys. Rev. B*, 94(15):155423, 2016. doi: 10.1103/PhysRevB.94.155423.

[10] J. N. Chazalviel. Spin relaxation of conduction electrons in n-type indium antimonide at low temperature. *Phys. Rev. B*, 11(4):1555–1562, 1975. doi: 10.1103/PhysRevB.11.1555.

[11] Guy Fishman and Georges Lampel. Spin relaxation of photoelectrons in p-type gallium arsenide. *Phys. Rev. B*, 16(2):820–831, 1977. doi: 10.1103/PhysRevB.16.820.

[12] J. Fabian and S. Das Sarma. Spin Relaxation of Conduction Electrons in Polyvalent Metals: Theory and a Realistic Calculation. *Phys. Rev. Lett.*, 81 (25):5624–5627, 1998. doi: 10.1103/PhysRevLett.81.5624.

[13] Igor Žutić, Jaroslav Fabian, and S. Das Sarma. Spintronics: Fundamentals and applications. *Rev. Mod. Phys.*, 76:323–410, 2004. doi: 10.1103/RevModPhys.76.323. URL `https://link.aps.org/doi/10.1103/RevModPhys.76.323`.

[14] Marco Bernardi. First-principles dynamics of electrons and phonons. *Eur. Phys. J. B*, 89(11):239, 2016. ISSN 1434-6036. doi: 10.1140/epjb/e2016-70399-4.

[15] Luis A. Agapito and Marco Bernardi. Ab initio electron-phonon interactions using atomic orbital wave functions. *Phys. Rev. B*, 97(23):235146, 2018. doi: 10.1103/PhysRevB.97.235146.

[16] Stefano Baroni, Stefano de Gironcoli, Andrea Dal Corso, and Paolo Giannozzi. Phonons and related crystal properties from density-functional perturbation theory. *Rev. Mod. Phys.*, 73(2):515–562, 2001. doi: 10.1103/RevModPhys.73.515.

[17] Gerhard Theurich and Nicola A. Hill. Self-consistent treatment of spin-orbit coupling in solids using relativistic fully separable ab initio pseudopotentials. *Phys. Rev. B*, 64(7):073106, 2001. doi: 10.1103/PhysRevB.64.073106.

[18] R. J. Elliott. Theory of the Effect of Spin-Orbit Coupling on Magnetic Resonance in Some Semiconductors. *Phys. Rev.*, 96(2):266–279, 1954. doi: 10.1103/PhysRev.96.266.

[19] F. Pientka, M. Gradhand, D. V. Fedorov, I. Mertig, and B. L. Györffy. Gauge freedom for degenerate Bloch states. *Phys. Rev. B*, 86(5):054413, 2012. doi: 10.1103/PhysRevB.86.054413.

[20] Arash A. Mostofi, Jonathan R. Yates, Giovanni Pizzi, Young-Su Lee, Ivo Souza, David Vanderbilt, and Nicola Marzari. An updated version of wannier90: A tool for obtaining maximally-localised Wannier functions. *Comput. Phys. Commun.*, 185(8):2309–2310, 2014. ISSN 0010-4655. doi: 10.1016/j.cpc.2014.05.003.

[21] Nicola Marzari, Arash A. Mostofi, Jonathan R. Yates, Ivo Souza, and David Vanderbilt. Maximally localized Wannier functions: Theory and applications. *Rev. Mod. Phys.*, 84(4):1419–1475, 2012. doi: 10.1103/RevModPhys.84.1419.

[22] Xinjie Wang, Jonathan R. Yates, Ivo Souza, and David Vanderbilt. Ab initio calculation of the anomalous Hall conductivity by Wannier interpolation. *Phys. Rev. B*, 74(19):195118, 2006. doi: 10.1103/PhysRevB.74.195118.

[23] Jonathan R. Yates, Xinjie Wang, David Vanderbilt, and Ivo Souza. Spectral and Fermi surface properties from Wannier interpolation. *Phys. Rev. B*, 75(19):195121, 2007. doi: 10.1103/PhysRevB.75.195121.

[24] Feliciano Giustino, Marvin L. Cohen, and Steven G. Louie. Electron-phonon interaction using Wannier functions. *Phys. Rev. B*, 76(16):165108, 2007. doi: 10.1103/PhysRevB.76.165108.

[25] Jin-Jian Zhou and Marco Bernardi. Ab initio electron mobility and polar phonon scattering in GaAs. *Phys. Rev. B*, 94(20):201201(R), 2016. doi: 10.1103/PhysRevB.94.201201.

[26] Ian Appelbaum, Biqin Huang, and Douwe J. Monsma. Electronic measurement and control of spin transport in silicon. *Nature*, 447(7142):295–298, 2007. ISSN 1476-4687. doi: 10.1038/nature05803. URL `https://www.nature.com/articles/nature05803`.

[27] Biqin Huang and Ian Appelbaum. Spin dephasing in drift-dominated semiconductor spintronics devices. *Phys. Rev. B*, 77(16):165331, 2008. doi: 10.1103/PhysRevB.77.165331.

[28] Ian Appelbaum. Introduction to spin-polarized ballistic hot electron injection and detection in silicon. *Philos. Trans. Royal Soc. A*, 369 (1951):3554–3574, 2011. doi: 10.1098/rsta.2011.0137. URL `https://royalsocietypublishing.org/doi/abs/10.1098/rsta.2011.0137`.

[29] Daniel J. Lépine. Spin Resonance of Localized and Delocalized Electrons in Phosphorus-Doped Silicon between 20 and 30 K. *Phys. Rev. B*, 2(7):2429–2439, 1970. doi: 10.1103/PhysRevB.2.2429.

[30] G. Lancaster, J. A. van Wyk, and E. E. Schneider. Spin-lattice relaxation of conduction electrons in silicon. *Proc. Phys. Soc.*, 84(1):19–24, 1964. ISSN 0370-1328. doi: 10.1088/0370-1328/84/1/304.

[31] Peter E. Blöchl, O. Jepsen, and O. K. Andersen. Improved tetrahedron method for Brillouin-zone integrations. *Phys. Rev. B*, 49(23):16223–16233, 1994. doi: 10.1103/PhysRevB.49.16223.

[32] Paolo Giannozzi, Stefano Baroni, Nicola Bonini, Matteo Calandra, Roberto Car, Carlo Cavazzoni, Davide Ceresoli, Guido L. Chiarotti, Matteo Cococcioni, Ismaila Dabo, Andrea Dal Corso, Stefano de Gironcoli, Stefano Fabris, Guido Fratesi, Ralph Gebauer, Uwe Gerstmann, Christos Gougoussis, Anton Kokalj, Michele Lazzeri, Layla Martin-Samos, Nicola Marzari, Francesco Mauri, Riccardo Mazzarello, Stefano Paolini, Alfredo Pasquarello, Lorenzo Paulatto, Carlo Sbraccia, Sandro Scandolo, Gabriele Sclauzero, Ari P. Seitsonen, Alexander Smogunov, Paolo Umari, and Renata M. Wentzcovitch. QUANTUM ESPRESSO: A modular and open-source software project for quantum simulations of materials. *J. Phys.: Condens. Matter*, 21(39):395502, 2009. ISSN 0953-8984. doi: 10.1088/0953-8984/21/39/395502.

[33] John P. Perdew, Adrienn Ruzsinszky, Gábor I. Csonka, Oleg A. Vydrov, Gustavo E. Scuseria, Lucian A. Constantin, Xiaolan Zhou, and Kieron Burke.

Restoring the Density-Gradient Expansion for Exchange in Solids and Surfaces. *Phys. Rev. Lett.*, 100(13):136406, 2008. doi: 10.1103/PhysRevLett.100.136406.

[34] M. J. van Setten, M. Giantomassi, E. Bousquet, M. J. Verstraete, D. R. Hamann, X. Gonze, and G. M. Rignanese. The PseudoDojo: Training and grading a 85 element optimized norm-conserving pseudopotential table. *Comput. Phys. Commun.*, 226:39–54, 2018. ISSN 0010-4655. doi: 10.1016/j.cpc.2018.01.012.

[35] Jaroslav Fabian, Alex Matos-Abiague, Christian Ertler, Peter Stano, and Igor Žutić. Semiconductor spintronics. *Acta Phys. Slovaca*, 57(4-5):565–907, 2007. URL `https://www.degruyter.com/view/j/apsrt.2007.57.issue-4-5/v10155-010-0086-8/v10155-010-0086-8.xml`.

[36] M. W. Doherty, C. A. Meriles, A. Alkauskas, H. Fedder, M. J. Sellars, and N. B. Manson. Towards a Room-Temperature Spin Quantum Bus in Diamond via Electron Photoionization, Transport, and Capture. *Phys. Rev. X*, 6(4):041035, 2016. doi: 10.1103/PhysRevX.6.041035.

[37] Wei Han and R. K. Kawakami. Spin Relaxation in Single-Layer and Bilayer Graphene. *Phys. Rev. Lett.*, 107(4):047207, 2011. ISSN 0031-9007, 1079-7114. doi: 10.1103/PhysRevLett.107.047207.

[38] P. J. Zomer, M. H. D. Guimarães, N. Tombros, and B. J. van Wees. Long-distance spin transport in high-mobility graphene on hexagonal boron nitride. *Phys. Rev. B*, 86(16):161416(R), 2012. ISSN 1098-0121, 1550-235X. doi: 10.1103/PhysRevB.86.161416.

[39] Supriyo Bandyopadhyay. Dominant spin relaxation mechanism in compound organic semiconductors. *Phys. Rev. B*, 81(15):153202, 2010. ISSN 1098-0121, 1550-235X. doi: 10.1103/PhysRevB.81.153202.

[40] Wei Han, Jen-Ru Chen, Deqi Wang, Kathleen M. McCreary, Hua Wen, Adrian G. Swartz, Jing Shi, and Roland K. Kawakami. Spin Relaxation in Single-Layer Graphene with Tunable Mobility. *Nano Lett.*, 12(7):3443–3447, 2012. ISSN 1530-6984, 1530-6992. doi: 10.1021/nl301567n.

[41] Gordon Stecklein, Paul A. Crowell, Jing Li, Yoska Anugrah, Qun Su, and Steven J. Koester. Contact-Induced Spin Relaxation in Graphene Nonlocal Spin Valves. *Phys. Rev. Appl.*, 6(5):054015, 2016. ISSN 2331-7019. doi: 10.1103/PhysRevApplied.6.054015.

[42] Chinkhanlun Guite and V. Venkataraman. Temperature dependence of spin lifetime of conduction electrons in bulk germanium. *Appl. Phys. Lett.*, 101 (25):252404, 2012. ISSN 0003-6951, 1077-3118. doi: 10.1063/1.4772500.

[43] Bernd Zimmermann, Phivos Mavropoulos, Swantje Heers, Nguyen H Long, Stefan Blügel, and Yuriy Mokrousov. Anisotropy of spin relaxation in metals. *Phys. Rev. Lett.*, 109(23):236603, 2012. URL `https://journals.aps.org/prl/abstract/10.1103/PhysRevLett.109.236603`.

[44] Marco Bernardi, Derek Vigil-Fowler, Johannes Lischner, Jeffrey B. Neaton, and Steven G. Louie. Ab Initio Study of Hot Carriers in the First Picosecond after Sunlight Absorption in Silicon. *Phys. Rev. Lett.*, 112(25):257402, 2014. doi: 10.1103/PhysRevLett.112.257402.

[45] Vatsal A. Jhalani, Jin-Jian Zhou, and Marco Bernardi. Ultrafast Hot Carrier Dynamics in GaN and Its Impact on the Efficiency Droop. *Nano Lett.*, 17(8): 5012–5019, 2017. ISSN 1530-6984. doi: 10.1021/acs.nanolett.7b02212.

[46] Nien-En Lee, Jin-Jian Zhou, Luis A. Agapito, and Marco Bernardi. Charge transport in organic molecular semiconductors from first principles: The bandlike hole mobility in a naphthalene crystal. *Phys. Rev. B*, 97(11):115203, 2018. doi: 10.1103/PhysRevB.97.115203.

[47] Jin-Jian Zhou, Olle Hellman, and Marco Bernardi. Electron-Phonon Scattering in the Presence of Soft Modes and Electron Mobility in $SrTiO_3$ Perovskite from First Principles. *Phys. Rev. Lett.*, 121(22):226603, 2018. doi: 10.1103/PhysRevLett.121.226603.

Chapter 3

PREDICTING PHONON-INDUCED SPIN DECOHERENCE AND COLOSSAL SPIN RENORMALIZATION IN CONDENSED MATTER

3.1 Introduction

Spin decoherence from phonons is a pressing question in quantum technology – it governs spin transport [1–6] and limits the manipulation of quantum information [7–13] and the realization of reliable quantum devices [14–16]. Previous work has identified two key sources of phonon-induced spin decoherence in the presence of spin-orbit coupling (SOC): the Elliott-Yafet (EY) mechanism [17, 18], whereby electron-phonon (e-ph) collisions change the spin direction, and the Dyakonov-Perel (DP) mechanism [19] originating from spin precession between e-ph collisions. Historically, these two mechanisms have been described with distinct theoretical models [17–21], but significant efforts have been made to unify them, for example using real-time evolution of spin ensembles [22–24] or analyzing quasiparticle broadening in model systems [25–27].

However, formulating a theory that encompasses both the EY and DP mechanisms, and developing corresponding quantitative calculations of spin decoherence in real materials, are still outstanding challenges. Many-body approaches combined with density functional theory (DFT) and related first-principles calculations are particularly promising to tackle this problem. These *ab initio* methods have become a gold standard for calculations of e-ph interactions and transport phenomena in solids [28–36]. Recent work has extended this framework to compute spin-flip processes due to e-ph interactions, leading to predictions of EY spin decoherence within the spin relaxation time approximation (sRTA) [37]. It is widely accepted that the sRTA neglects spin precession, and thus a different formalism is needed to capture the DP mechanism [20, 24].

Inspired by the work of Kim et al. [38], which rigorously proved that the Boltzmann equation is equivalent to the ladder vertex correction to the conductivity, we ask if a similar many-body approach can be used to study spin dynamics. The development of this framework, and of corresponding first-principles calculations, would provide a viable tool to study phonon-induced spin decoherence, mimicking the progress of first-principles studies of charge transport [28–36]. In turn, accurate predictions of spin decoherence would advance both condensed matter theory and spin-based quantum technology.

Here we present a many-body theory of spin relaxation and develop precise *ab initio* calculations of phonon-induced spin decoherence in semiconductors. Our approach calculates the e-ph vertex corrections to the spin susceptibility, with an accurate account of electronic and vibrational states, SOC, and e-ph interactions. We compute the spin relaxation times (SRTs) of electron and hole carriers in Si and GaAs — two key candidates for spin-based quantum computing — and in monolayer WSe$_2$, a 2D semiconductor with strong SOC. Our predicted SRTs are in excellent agreement with experiments over a wide temperature range. We demonstrate that our formalism can calculate both spin relaxation and spin precession, and capture EY and DP decoherence on equal footing; we contrast these results with the sRTA, which lacks DP decoherence and gives unphysical SRTs near the band gap. Our analysis shows that the e-ph interactions lead to a colossal renormalization of the electron spin dynamics in solids, significantly modifying the SRTs and spin precession rates (SPRs). The theory and computational method developed in this work pave the way for a deeper understanding of electron spin decoherence, with broad implications for quantum materials and devices.

3.2 Methods

To describe phonon-induced spin decoherence, we consider the Kubo formula for the spin-spin correlation function [39], and include the ladder vertex correction [38] from e-ph interactions (see Fig. 3.1(a)). We derive a Bethe-Salpeter equation for the phonon-dressed spin vertex (in short, spin-phonon BSE), as discussed in the Supplemental Material. Our spin-phonon BSE is shown diagrammatically in Fig. 3.1(b), and can be written as:

$$\boldsymbol{s}\boldsymbol{\Lambda}_{\boldsymbol{k}}(\varepsilon) = \boldsymbol{s}_{\boldsymbol{k}} + \frac{1}{V}\sum_{\nu\boldsymbol{q}\pm} \mathbf{g}^{\dagger}_{\nu\boldsymbol{k}\boldsymbol{q}} \left[\mathbf{G}^{A}\boldsymbol{s}\boldsymbol{\Lambda}\mathbf{G}^{R}\right]_{\substack{\boldsymbol{k}+\boldsymbol{q},\\ \varepsilon\pm\omega_{\nu\boldsymbol{q}}}} \mathbf{g}_{\nu\boldsymbol{k}\boldsymbol{q}}\, F_{\pm}(T) \tag{3.1}$$

where all bolded quantities are matrices in Bloch basis. Above, $\boldsymbol{s}\boldsymbol{\Lambda}_{\boldsymbol{k}}(\varepsilon) = \boldsymbol{s}_{nn'\boldsymbol{k}}\boldsymbol{\Lambda}_{nn'\boldsymbol{k}}(\varepsilon)$ is the phonon-dressed spin vertex, $\Lambda^{\alpha}_{nn'\boldsymbol{k}}(\varepsilon)$ is the vertex correction at energy ε for the Cartesian direction α, and $\boldsymbol{s}_{nn'\boldsymbol{k}} = \langle n\boldsymbol{k}|\frac{\hbar}{2}\hat{\sigma}|n'\boldsymbol{k}\rangle$ is the bare spin vertex; $\mathbf{G}^{R/A}$ are the retarded/advanced interacting Green's functions [39], V is the system volume, $F_{\pm}(T)$ is a thermal occupation factor at temperature T, and $\left[\mathbf{g}_{\nu\boldsymbol{k}\boldsymbol{q}}\right]_{nm} = g_{nm\nu}(\boldsymbol{k},\boldsymbol{q})$ are e-ph matrix elements [29].

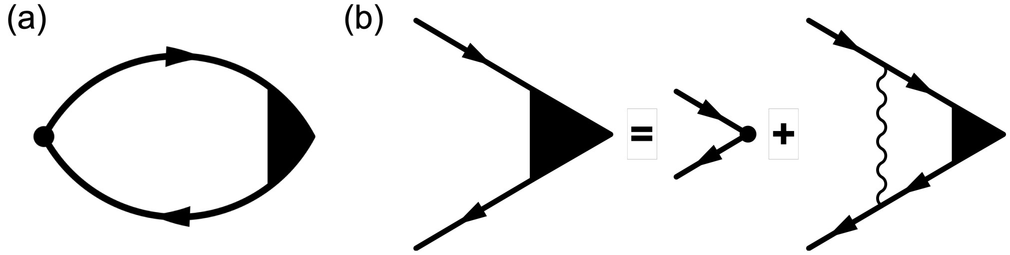

Figure 3.1: Feynman diagrams for spin decoherence. (a) Bubble diagram for the spin-spin correlation function including the vertex correction. (b) Bethe-Salpeter equation for the phonon-dressed spin vertex in the ladder approximation.

The vertex correction Λ governs the spin dynamics by renormalizing the microscopic SRTs and SPRs (see Supplemental Material). The macroscopic SRTs are obtained as the thermal average

$$\tau^{(s)}_{\alpha\beta} = \frac{\sum_{n\boldsymbol{k}} s^{\alpha}_{nn\boldsymbol{k}} s^{\beta}_{nn\boldsymbol{k}} \tau^{\text{e-ph}}_{n\boldsymbol{k}} \Lambda^{\beta}_{nn\boldsymbol{k}}(\varepsilon_{n\boldsymbol{k}})(-\frac{df_{n\boldsymbol{k}}}{d\varepsilon})}{\sum_{n\boldsymbol{k}} s^{\alpha}_{nn\boldsymbol{k}} s^{\beta}_{nn\boldsymbol{k}} \left(-\frac{df_{n\boldsymbol{k}}}{d\varepsilon}\right)}, \tag{3.2}$$

where $\tau^{\text{e-ph}}_{n\boldsymbol{k}}$ are e-ph collision times [28, 39]. For $\alpha = \beta$ along the external magnetic field, Eq. (3.2) gives the longitudinal SRT, usually called T_1. The renormalized microscopic SRTs ($\tau^{\alpha}_{nn'\boldsymbol{k}}$) and SPRs ($\omega^{\alpha}_{nn'\boldsymbol{k}}$), which are matrices in Bloch basis, are computed from the vertex correction using

$$\frac{1}{\frac{1}{\tau^{\alpha}_{nn'\boldsymbol{k}}(\varepsilon)} + i\omega^{\alpha}_{nn'\boldsymbol{k}}(\varepsilon)} \equiv \frac{\Lambda^{\alpha}_{nn'\boldsymbol{k}}(\varepsilon)}{i(\Sigma^{R}_{n\boldsymbol{k}} - \Sigma^{A}_{n'\boldsymbol{k}}) + i(\varepsilon_{n\boldsymbol{k}} - \varepsilon_{n'\boldsymbol{k}})}, \tag{3.3}$$

with $\Sigma^{A/R}$ the advanced/retarded e-ph self-energy [28]. The diagonal components with $n = n'$ give the renormalized microscopic SRTs, $\tau^{\beta}_{nn\boldsymbol{k}} = \tau^{\text{e-ph}}_{n\boldsymbol{k}} \Lambda^{\beta}_{nn\boldsymbol{k}}(\varepsilon_{n\boldsymbol{k}})$ entering Eq. (3.2). We implement and solve Eqs. (3.1)-(3.3) in our Perturbo code [29] (see Supplemental Material).

The ground state, band structures, and phonon dispersions are obtained using Quantum ESPRESSO [40]. We employ Perturbo [29] to compute and interpolate the e-ph matrix elements and spin matrices, using a method described in Ref. [37], starting from spinor Wannier functions from the wannier90 code [41]. We model all materials in the intrinsic (i.e., undoped) limit, and accordingly compare our results with experiments carried out on undoped samples.

3.3 Results

Using this formalism, in Fig. 3.2 we compute the *macroscopic* SRTs in Eq. (3.2) as a function of temperature for Si, GaAs, and monolayer WSe_2 (see Methods).

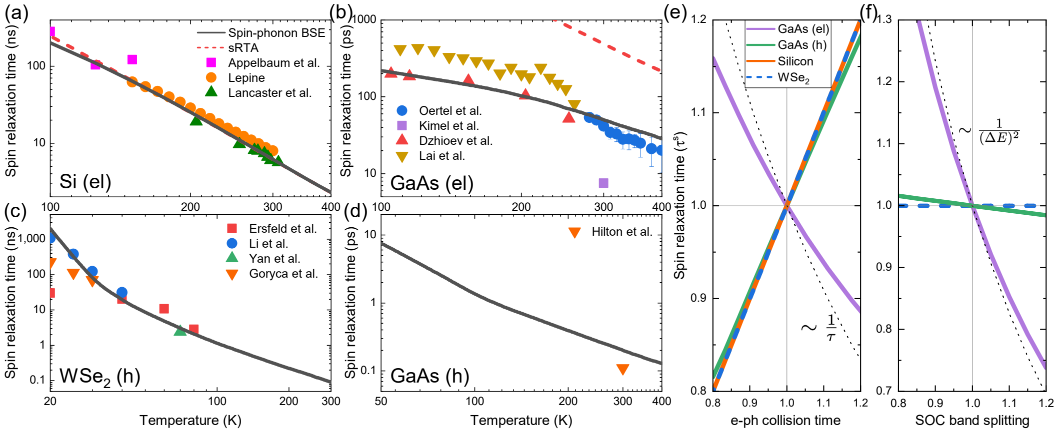

Figure 3.2: Spin relaxation times. (a)-(d) Computed spin relaxation times as a function of temperature, for (a) electrons in Si, (b) electrons in GaAs, (c) holes in monolayer WSe$_2$, and (d) holes in GaAs. Results obtained from the spin-phonon BSE (black solid line) are compared with sRTA calculations (red dashed line). Experimental results from Refs. [5, 42–51] are shown for comparison. (e)-(f) The SRTs at room temperature for these four cases are recomputed by artificially varying (e) the e-ph collision time and (f) the SOC band splitting entering the spin-phonon BSE. In all cases, the axes are referenced to the real system values. The conventional DP spin relaxation trend (black dotted line) is also shown for comparison.

In Si, a centrosymmetric material where spin decoherence is governed by the EY mechanism, the results are in excellent agreement with experiments [5, 42, 43] in the 100−300 K temperature range. For example, the SRT computed at 300 K is 6.1 ns, in remarkable agreement with the 6.0 ns value measured in Ref. [43]. Due to the dominant EY mechanism, in this case the sRTA, which neglects spin precession, also gives accurate SRTs.

In GaAs, the SOC induces a small (~1 meV) splitting in the conduction band, so spin relaxation is dominated by the DP mechanism [21]. Figure 3.2(b) shows our calculated SRTs for electrons in GaAs as function of temperature; the excellent agreement with experiments [44–47] is a strong evidence that the spin-phonon BSE describes correctly the DP mechanism. By contrast, the sRTA, which captures only the EY mechanism, clearly fails in GaAs, predicting SRTs an order of magnitude greater than experiments.

Our spin-phonon BSE achieves a similar accuracy for calculations on hole carriers. In Fig. 3.2(c), we compute the SRTs for hole spins in monolayer WSe$_2$, obtaining excellent agreement with all available experimental results between 20−90 K [48–51]. Note that the valence band of WSe$_2$ has a large (~0.4 eV) splitting due to SOC, leading to a precession rate far greater than the hole e-ph collision rates; in this strong precession regime, the spin dynamics is controlled by the diagonal part of the spin vertex and the DP mechanism becomes irrelevant, so EY spin decoherence dominates the SRTs. Conversely, for heavy holes in GaAs (see Fig. 3.2(d)) both EY and DP spin decoherence are important. The agreement with experiment is noteworthy in this regime where both mechanisms are relevant: our computed SRT for holes in GaAs at 300 K is 200 fs, versus a 110 fs value measured by Hilton et al. [52].

A key distinction between the EY and DP mechanisms is their dependence on the e-ph collision time, $\tau_{n\boldsymbol{k}}^{\text{e-ph}}$ in Eq. (3.2): the SRT is proportional to $\tau_{n\boldsymbol{k}}^{\text{e-ph}}$ for EY, and inversely proportional to $\tau_{n\boldsymbol{k}}^{\text{e-ph}}$ for DP. Our spin-phonon BSE can capture both of these trends, as we show in Fig. 3.2(e) by artificially increasing $\tau_{n\boldsymbol{k}}^{\text{e-ph}}$ (via the e-ph coupling strength $|g|^2$) and recomputing the SRTs at 300 K for all four cases. In Si and WSe$_2$, where EY spin decoherence is dominant, we find that the recomputed SRTs are directly proportional to the e-ph collision time, consistent with the EY mechanism [17, 18]. Conversely, for electron spins in GaAs, the SRTs are nearly inversely proportional to the e-ph collision time (see Fig. 3.2(e)), in agreement with the DP mechanism [19]. (Note that the computed trend slightly deviates from the conventional DP inverse proportionality because EY decoherence, although weak, is still present.) For hole spins in GaAs, the recomputed SRTs exhibit a trend intermediate between pure EY and DP, further supporting our conclusion that both mechanisms are important for hole spins in GaAs [24, 53].

Spin precession in the DP mechanism is induced by the SOC field, which is proportional to the band splitting for each electronic state. To examine the role of DP spin decoherence, we artificially vary the SOC band splitting ΔE and for each new value we recompute the SRTs (see Fig. 3.2(f)). For WSe$_2$, varying the SOC band splitting has no effect on the SRTs, showing that spin decoherence is controlled by the EY mechanism. For electrons in GaAs, the SRTs are highly sensitive to the SOC splitting, a clear evidence that our formalism can capture the dominant DP mechanism. This dependence is weaker than in the conventional trend for pure DP, $\tau^{(s)} \propto 1/(\Delta E)^2$, due to the coexistence of EY decoherence. For hole carriers in GaAs, the SRTs are less sensitive to the SOC splitting than for electrons, as the decoherence originates from a balanced combination of both EY and DP mechanisms. This analysis also shows that band structure calculations accurately describing the SOC band splitting are essential to predict spin precession and DP decoherence.

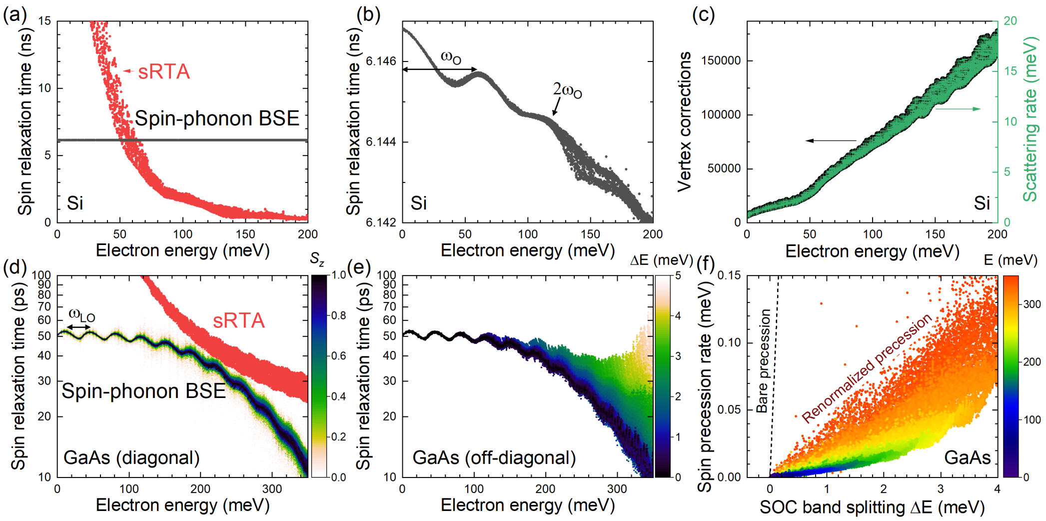

Figure 3.3: Microscopic spin decoherence. (a) Microscopic electron SRTs in Si as a function of conduction band energy, computed with the spin-phonon BSE (black) and sRTA (red). (b) Zoom-in of the spin-phonon BSE results in (a). (c) Vertex corrections $\Lambda_{nn\mathbf{k}}$ in Si (black dots) compared with the inverse e-ph collision times (green crosses). (d) Microscopic electron SRTs in GaAs from the spin-phonon BSE, shown as a function of conduction band energy and overlaid with a color map of the expectation value of S_z for each electronic state; the sRTA results (red) are given for comparison. (e) Microscopic off-diagonal SRTs, $\tau_{nn'\mathbf{k}}$ in Eq. (3.3), overlaid with a color map of the SOC band splitting ΔE. (f) Renormalized electron SPRs in GaAs, $\omega_{nn'\mathbf{k}}$ in Eq. (3.3), plotted as a function of SOC band splitting and overlaid with a color map of the conduction band energy; the bare electron SPRs (black dashed line) are given for comparison. All results are computed at 300 K, and the zero of the energy axis is the conduction band minimum.

The phonon-induced renormalization greatly modifies the microscopic spin dynamics. Figure 3.3(a) compares sRTA and spin-phonon BSE calculations of the *microscopic* electron SRTs, $\tau^{(s)}_{n\mathbf{k}} = \tau^{\text{e-ph}}_{n\mathbf{k}} \Lambda^{z}_{nn\mathbf{k}}(\varepsilon_{n\mathbf{k}})$ defined below Eq. (3.3), in Si at 300 K for energies near the conduction band minimum. The sRTA results are strongly energy dependent, with an unphysical divergence at low energy. By contrast, the results from the spin-phonon BSE are nearly energy independent. The vertex correction makes spins with similar energy relax on the same time scale (a constant value of 6.1 ns nearly equal to the macroscopic SRT) and overcomes the limitations of the sRTA. A closer examination of the SRTs from the spin-phonon BSE (see Fig. 3.3(b)) reveals an oscillatory pattern with a period of $\omega_O \approx 60$ meV, the energy of an optical phonon with strong e-ph coupling; this pattern disappears when optical phonons are neglected. This oscillation is a manifestation of the self-consistency of the spin-phonon BSE and its ability to capture strong coupling effects beyond lowest-order perturbation theory. We observe the same energy dependence and SRT oscillations due to optical phonons for hole spins in WSe_2.

Figure 3.3(c) shows the computed vertex correction $\Lambda^{z}_{nn\boldsymbol{k}}(\varepsilon_{n\boldsymbol{k}})$ as a function of energy in Si. The vertex correction from the e-ph interactions is colossal; relative to the bare spin, it is of order $\Lambda - 1 \approx 10^5$, and thus eight orders of magnitude greater than the corresponding vertex correction due to photons in vacuum [54, 55] (with value $\Lambda - 1 \approx 1.16 \cdot 10^{-3}$, which corrects the electron magnetic moment). The energy dependence of the vertex correction is nearly identical to that of the inverse e-ph collision times, thus explaining the origin of the constant trend with energy of the microscopic SRTs. We find large vertex correction values ($10^2 - 10^5$) also in GaAs and WSe_2. These giant values account for the large differences between e-ph collision times (femtoseconds) and SRTs (nanoseconds) in condensed matter, and are key to accurately predicting long spin coherence times of interest in quantum technologies.

In GaAs, due to the Dresselhaus SOC band splitting, the bare spin vertex $s_{nn'\boldsymbol{k}}$ acquires large off-diagonal ($n \neq n'$) components that precess in the effective SOC magnetic field with a *bare* SPR of $\varepsilon_{n\boldsymbol{k}}$–$\varepsilon_{n'\boldsymbol{k}}$. While the macroscopic SRTs in Eq. (3.2) are determined only by the band diagonal components $s_{nn\boldsymbol{k}}$, the spin-phonon BSE couples the diagonal and off-diagonal components via Eq. (3.1), so spin precession modifies the SRTs. The microscopic SRTs for electrons in GaAs (see Fig. 3.3(d)) exhibit trends similar to Si, with renormalized SRTs nearly energy independent near the band edge, in contrast with the rapidly varying SRTs predicted by the sRTA; an oscillating pattern is evident with period equal to the 30 meV longitudinal optical (LO) phonon energy, a signature of strong coupling with LO phonons [32]. Yet, due to the spin precession, we also observe unique trends not found in Si. The SRTs decrease at higher energies due to the increasing spin precession (the SOC band splitting increases with energy), a manifestation of DP spin decoherence. In addition, the SRTs are strongly state dependent as states with a smaller spin component along the quantization axis, shown with lighter colors in Fig. 3.3(d), are subject to stronger precession.

The relaxation of the off-diagonal spin components, quantified by the off-diagonal SRTs $\tau_{nn'\boldsymbol{k}}$ in Eq. (3.3), reveals additional signatures of the DP mechanism. Figure 3.3(e) shows these off-diagonal electron SRTs for GaAs and highlights their correlation with the SOC band splitting. When the band splitting is small (black), precession is negligible and the SRTs are identical to the diagonal SRTs in Fig. 3.3(d). However, for increasing values of the band splitting (lighter colors), spin precession significantly enhances the SRTs. These intriguing microscopic phenomena are encoded in the vertex correction Λ in Eq. (3.3), which suppresses the real part $1/\tau_{nn'\boldsymbol{k}}$ in the denominator, thus slowing down spin relaxation. Similarly, the vertex correction significantly slows down spin precession, as shown in Fig. 3.3(f) for GaAs. Electrons with a bare SPR of 1 meV drop to a $\sim 10^{-2}$ meV precession rate after renormalization due to phonons. These renormalized SPRs are strongly energy dependent, with higher electron energies leading to faster precession for spins with the same bare SPRs. This microscopic dynamics reveals the rich interplay between spin relaxation and precession in materials.

3.4 Conclusion

In conclusion, our findings highlight the dramatic effects of phonon-induced renormalization on electron spins in solids. Our spin-phonon BSE can capture renormalized spin dynamics beyond relaxation, shedding light on the interplay between the EY and DP spin decoherence mechanisms, and describing their diverse physics on the same footing. This formalism reveals that the long intrinsic spin coherence times in condensed matter are due to the colossal vertex correction from e-ph interactions.

3.5 Supplemental Material

Bethe-Salpeter equation for the phonon-dressed spin vertex

We provide a detailed derivation of the spin-phonon BSE, which computes the vertex correction to the spin operator due to e-ph interactions. We use atomic units and set $\hbar = 1$.

Interacting Green's function

We consider an unperturbed Hamiltonian H_0 diagonal in a Bloch basis, $\langle n'\boldsymbol{k}| H_0 |n\boldsymbol{k}\rangle = \varepsilon_{n\boldsymbol{k}}\, \delta_{nn'}$. The interacting imaginary-time Green's function $\mathcal{G}(i\omega_a)$ is written using the Dyson equation [39]

$$\mathcal{G}^{-1}(i\omega_a) = \mathcal{G}^{(0)-1}(i\omega_a) - \Sigma(i\omega_a), \tag{3.4}$$

where ω_a is the fermionic Matsubara frequency of the electron, $\mathcal{G}^{(0)}(i\omega_a)$ is the non-interacting Green's function, and $\Sigma(i\omega_a)$ is the lowest-order (Fan-Migdal) e-ph self-energy [28, 39, 56], whose band- and $\boldsymbol{k}$-dependent expression is

$$\Sigma_{nn'\boldsymbol{k}}(i\omega_a) = -\frac{1}{\beta V} \sum_{mm'\nu\boldsymbol{q},iq_c} [g_{n'm'\nu}(\boldsymbol{k},\boldsymbol{q})]^*\, g_{nm\nu}(\boldsymbol{k},\boldsymbol{q}) \mathcal{D}_{\nu\boldsymbol{q}}(iq_c)\, \mathcal{G}_{mm'\boldsymbol{k}+\boldsymbol{q}}(i\omega_a + iq_c). \tag{3.5}$$

Above, $\beta = 1/k_BT$ at temperature T, q_c is the bosonic Matsubara frequency of the phonon, V is the system volume, and $\mathcal{D}_{\nu\boldsymbol{q}}(iq_c) = 2\omega_{\boldsymbol{q}\nu}/((iq_c)^2 - \omega^2_{\boldsymbol{q}\nu})$ is the non-interacting phonon Green's function for a phonon with mode index ν and wave-vector $\boldsymbol{q}$.

Spin-spin correlation function

We consider the spin operator $\hat{s}$, with matrix elements in the direction α given by $s^{\alpha}_{nm\boldsymbol{k}} = \langle m\boldsymbol{k}|\,\hat{s}^{\alpha}\,|n\boldsymbol{k}\rangle$. We derive the spin-spin correlation function with a procedure analogous to the derivation of the dc electrical conductivity in the ladder approximation [38], where the operator of interest is the velocity operator $v_{n\boldsymbol{k}}$, which is diagonal in Bloch basis. Here, due to the spin-orbit coupling, the spin operator $\hat{s}$ is in general non-diagonal in the band index, leading to matrix elements $s_{nm\boldsymbol{k}}$, so the derivation for the diagonal case given in Ref. [38] needs to be extended to a non-diagonal operator and vertex correction.

The calculation of the spin-spin correlation function is first carried out in the imaginary time domain and then extended to real frequencies by analytic continuation. Working in imaginary time and frequency, the retarded spin-spin correlation function for the operator $\hat{s}$ can be obtained from the Kubo formula as [39]

$$\chi_{\alpha\beta}(\boldsymbol{p}, i\nu_b) = \int_0^{\beta} d\tau\, e^{i\nu_b\tau} \left\langle T_\tau \hat{s}^{\alpha}(\boldsymbol{p},\tau)\hat{s}^{\beta}(-\boldsymbol{p},0)\right\rangle, \tag{3.6}$$

where $\boldsymbol{p}$ is the wave-vector, ν_b is the bosonic Matsubara frequency, τ is imaginary time ranging from 0 to $\beta = 1/k_BT$ at temperature T, and T_τ is the imaginary time ordering operator. Here we focus on the $\boldsymbol{p} \rightarrow 0$ limit, and thus drop $\boldsymbol{p}$ from the equations. This correlation function can be expressed as a sum of bubble diagrams, where in the simplest case one considers the bare bubble diagram that includes the electron self-energy only in the electron propagator $\mathcal{G}$:

$$\chi_{\alpha\beta}(i\nu_b) = \frac{1}{\beta V_{\mathrm{uc}}} \sum_{i\omega_a} \mathrm{Tr}\big[\mathcal{G}(i\omega_a)\hat{s}^{\alpha}\mathcal{G}(i\omega_a + i\nu_b)\hat{s}^{\beta}\big], \tag{3.7}$$

where V_{uc} is the volume of the unit cell, and the trace is evaluated over the band and momentum indices. In this expression, the operator $\hat{s}$ can be regarded as the bare vertex of the correlation function (the left vertex of the diagram in Fig. 3.1(a) in the main text). For the velocity operator, Eq. (3.7) leads to the well-known Drude conductivity [38, 39].

In this work, the corrections to the spin vertex originate from the e-ph interactions, which couple electronic states with different bands and crystal momenta. Figure 3.1(a) in the main text shows the spin-spin correlation function including the vertex correction Λ,

$$\chi_{\alpha\beta}(i\nu_b) = \frac{1}{\beta V_{\mathrm{uc}}}\sum_{i\omega_a} \mathrm{Tr}\big[\mathcal{G}(i\omega_a)\hat{s}^{\alpha}\mathcal{G}(i\omega_a + i\nu_b)\hat{s}^{\beta}\Lambda^{\beta}(i\omega_a, i\omega_a + i\nu_b)\big], \tag{3.8}$$

where $\hat{s}^{\beta}\Lambda^{\beta}(i\omega_a, i\omega_a + i\nu_b)$ is the phonon-dressed vertex for the operator $\hat{s}$ along the cartesian direction β. Note that the vertex correction $\Lambda^{\beta}(i\omega_a, i\omega_a + i\nu_b)$ is a complex vector, and it contains information about the renormalized spin dynamics due to the e-ph interactions.

Bethe-Salpeter equation for the vertex correction

The leading correction to the spin vertex is obtained by summing over the ladder diagrams, which can be viewed as an abstract form of charge conservation during the e-ph scattering process [38, 39]. The vertex correction $\Lambda^{\alpha}_{nn'\boldsymbol{k}}$ satisfies a self-consistent Bethe-Salpeter equation (BSE), shown diagrammatically in Fig. 3.1(b) of the main text and written as

$$\begin{aligned} &s^{\alpha}_{nn'\boldsymbol{k}}\Lambda^{\alpha}_{nn'\boldsymbol{k}}(i\omega_a, i\omega_a + i\nu_b) \\ &\quad = s^{\alpha}_{nn'\boldsymbol{k}} - \frac{1}{\beta V}\sum_{mm'll'\nu\boldsymbol{q},iq_c} \left[\, g_{n'm'\nu}(\boldsymbol{k},\boldsymbol{q})\right]^{*} g_{nm\nu}(\boldsymbol{k},\boldsymbol{q})\mathcal{D}_{\nu\boldsymbol{q}}(iq_c) \\ &\quad \times \mathcal{G}_{ml\boldsymbol{k}+\boldsymbol{q}}(i\omega_a + iq_c)\mathcal{G}_{l'm'\boldsymbol{k}+\boldsymbol{q}}(i\omega_a + i\nu_b + iq_c)s^{\alpha}_{ll'\boldsymbol{k}}\Lambda^{\alpha}_{ll'\boldsymbol{k}+\boldsymbol{q}}(i\omega_a + iq_c, i\omega_a + i\nu_b + iq_c). \end{aligned} \tag{3.9}$$

The kernel of this BSE [57] is the e-ph interaction $g_{n'm'\nu}(\boldsymbol{k},\boldsymbol{q})^{*}g_{nm\nu}(\boldsymbol{k},\boldsymbol{q})\mathcal{D}_{\nu\boldsymbol{q}}(iq_c)$; this kernel is the origin of the Elliott-Yafet spin decoherence [37], whereas the electron propagators in Eq. (3.9), $\mathcal{G}_{ml\boldsymbol{k}+\boldsymbol{q}}(i\omega_a + iq_c)\mathcal{G}_{l'm'\boldsymbol{k}+\boldsymbol{q}}(i\omega_a + i\nu_b + iq_c)$, are the origin of the Dyakonov-Perel spin decoherence.

Following Mahan [39] and Ref. [38], we first sum over the bosonic Matsubara frequency iq_c in Eq. (3.9). This summation, defined as $S(i\omega_a, i\omega_a + i\nu_b)$, reads

$$\begin{aligned} &S(i\omega_a, i\omega_a + i\nu_b) \\ &\quad = \sum_{ll'} S_{ll'}(i\omega_a, i\omega_a + i\nu_b) \\ &\quad = \frac{1}{\beta}\sum_{ll'iq_c} \mathcal{D}_{\nu\boldsymbol{q}}(iq_c)\Lambda^{\alpha}_{ll'\boldsymbol{k}+\boldsymbol{q}}(i\omega_a + iq_c, i\omega_a + i\nu_b + iq_c)\mathcal{G}_{ml\boldsymbol{k}+\boldsymbol{q}}(i\omega_a + iq_c)\mathcal{G}_{l'm'\boldsymbol{k}+\boldsymbol{q}}(i\omega_a + i\nu_b + iq_c). \end{aligned} \tag{3.10}$$

As usual, the summation is done by a constructing a contour integral along a circle at infinity,

$$\oint \frac{dz}{2\pi i} n_B(z)\mathcal{D}_{\nu\boldsymbol{q}}(z)\Lambda^{\alpha}_{ll'\boldsymbol{k}+\boldsymbol{q}}(i\omega_a+z, i\omega_a+i\nu_b+z)\mathcal{G}_{ml\boldsymbol{k}+\boldsymbol{q}}(i\omega_a+z)\mathcal{G}_{l'm'\boldsymbol{k}+\boldsymbol{q}}(i\omega_a+i\nu_b+z). \tag{3.11}$$

The integrand has poles at $z = iq_c$ and $z = \pm\omega_{\nu\boldsymbol{q}}$, and branch cuts along $z = -i\omega_a$ and $z = -i\omega_a - i\nu_b$ [38, 39]. The leading contribution to $S_{ll'}(i\omega_a, i\omega_a + i\nu_b)$ comes from the combination of retarded and advanced Green's functions, G^R and G^A respectively, while terms of $O([G^R]^2, [G^A]^2)$ can be neglected at low electron density [38, 39]. Therefore, after the analytic continuations $i\omega_a \longrightarrow \varepsilon - i\eta$ and $i\omega_a + i\nu_b \longrightarrow \varepsilon + \nu + i\eta$, and using the identity $\frac{1}{x+i\eta} = \mathcal{P}\frac{1}{x} - i\pi\delta(x)$, we obtain $S_{ll'}(\varepsilon - i\eta, \varepsilon + i\eta)$ in the limit of $\nu \longrightarrow 0$:

$$\begin{aligned}
S_{ll'}(\varepsilon-&i\eta, \varepsilon+i\eta)\\
=&-[N_{\nu\boldsymbol{q}}+f(\varepsilon+\omega_{\nu\boldsymbol{q}})]\Lambda^{\alpha}_{ll'\boldsymbol{k}+\boldsymbol{q}}(\varepsilon+\omega_{\nu\boldsymbol{q}})G^R_{ml\boldsymbol{k}+\boldsymbol{q}}(\varepsilon+\omega_{\nu\boldsymbol{q}})G^A_{l'm'\boldsymbol{k}+\boldsymbol{q}}(\varepsilon+\omega_{\nu\boldsymbol{q}})\\
&-[N_{\nu\boldsymbol{q}}+1-f(\varepsilon-\omega_{\nu\boldsymbol{q}})]\Lambda^{\alpha}_{ll'\boldsymbol{k}+\boldsymbol{q}}(\varepsilon-\omega_{\nu\boldsymbol{q}})G^R_{ml\boldsymbol{k}+\boldsymbol{q}}(\varepsilon-\omega_{\nu\boldsymbol{q}})G^A_{l'm'\boldsymbol{k}+\boldsymbol{q}}(\varepsilon-\omega_{\nu\boldsymbol{q}}),
\end{aligned} \tag{3.12}$$

where R(A) stands for retarded (advanced) functions, $\Lambda^{\alpha}(\varepsilon) \equiv \Lambda^{\alpha}(\varepsilon - i\eta, \varepsilon + i\eta)$, $\omega_{\nu\boldsymbol{q}}$ are phonon energies, and $N_{\nu\boldsymbol{q}} \equiv n_B(\omega_{\nu\boldsymbol{q}})$ are the corresponding temperature-dependent Bose-Einstein occupations.

Using this result, we write the self-consistent BSE for the phonon-dressed vertex $\hat{s}\Lambda$ as

$$\begin{aligned}
s^{\alpha}_{nn'\boldsymbol{k}}&\Lambda^{\alpha}_{nn'\boldsymbol{k}}(\varepsilon)\\
=&s^{\alpha}_{nn'\boldsymbol{k}} + \frac{1}{V}\sum_{mm'll'\nu\boldsymbol{q}}[g_{n'm'\nu}(\boldsymbol{k},\boldsymbol{q})]^{*}\, g_{nm\nu}(\boldsymbol{k},\boldsymbol{q})s^{\alpha}_{ll'\boldsymbol{k}+\boldsymbol{q}}\\
&\times\Big[(N_{\nu\boldsymbol{q}}+f(\varepsilon+\omega_{\nu\boldsymbol{q}}))\Lambda^{\alpha}_{ll'\boldsymbol{k}+\boldsymbol{q}}(\varepsilon+\omega_{\nu\boldsymbol{q}})G^R_{ml\boldsymbol{k}+\boldsymbol{q}}(\varepsilon+\omega_{\nu\boldsymbol{q}})G^A_{l'm'\boldsymbol{k}+\boldsymbol{q}}(\varepsilon+\omega_{\nu\boldsymbol{q}})\\
&+(N_{\nu\boldsymbol{q}}+1-f(\varepsilon-\omega_{\nu\boldsymbol{q}}))\Lambda^{\alpha}_{ll'\boldsymbol{k}+\boldsymbol{q}}(\varepsilon-\omega_{\nu\boldsymbol{q}})G^R_{ml\boldsymbol{k}+\boldsymbol{q}}(\varepsilon-\omega_{\nu\boldsymbol{q}})G^A_{l'm'\boldsymbol{k}+\boldsymbol{q}}(\varepsilon-\omega_{\nu\boldsymbol{q}})\Big].
\end{aligned} \tag{3.13}$$

In matrix form and using a more compact notation, Eq. (3.13) becomes

$$\mathbf{s\Lambda}_{\boldsymbol{k}}(\varepsilon) = \mathbf{s}_{\boldsymbol{k}} + \frac{1}{V}\sum_{\nu\boldsymbol{q}\pm}\mathbf{g}^{\dagger}_{\nu\boldsymbol{k}\boldsymbol{q}}\left[\mathbf{G}^A\mathbf{s\Lambda}\mathbf{G}^R\right]_{\substack{\boldsymbol{k}+\boldsymbol{q},\\ \varepsilon\pm\omega_{\nu\boldsymbol{q}}}}\mathbf{g}_{\nu\boldsymbol{k}\boldsymbol{q}}\,F_{\pm}(T), \tag{3.14}$$

which is the spin-phonon BSE in Eq. (3.1) of the main text, with the thermal occupation factor defined as $F_{\pm}(T) = N_{\nu\boldsymbol{q}} + \frac{1}{2} \pm [f(\varepsilon \pm \omega_{\nu\boldsymbol{q}}) - \frac{1}{2}]$. By solving

Eq. (3.13), we obtain the phonon-dressed spin vertex $\mathbf{s}\boldsymbol{\Lambda}_{\boldsymbol{k}}(\varepsilon)$ and its dependence on band, crystal momentum $\boldsymbol{k}$ and energy ε.

In the weak scattering regime, where the electron spectral function has a well-defined quasiparticle peak [58] and the off-diagonal self-energy can be neglected [59, 60], the Green's function becomes band-diagonal and the self-energies are evaluated on-shell. The product of the retarded and advanced Green's functions, $G^R G^A$, can be recast [61] and approximated as

$$\begin{aligned}
&G^R_{m\boldsymbol{k}+\boldsymbol{q}}(\varepsilon) G^A_{m'\boldsymbol{k}+\boldsymbol{q}}(\varepsilon) \\
&= \frac{G^A_{m'\boldsymbol{k}+\boldsymbol{q}}(\varepsilon) - G^R_{m\boldsymbol{k}+\boldsymbol{q}}(\varepsilon)}{G^R_{m\boldsymbol{k}+\boldsymbol{q}}(\varepsilon)^{-1} - G^A_{m'\boldsymbol{k}+\boldsymbol{q}}(\varepsilon)^{-1}} \\
&\approx \frac{\pi\delta(\varepsilon - \varepsilon_{m'\boldsymbol{k}+\boldsymbol{q}}) + \pi\delta(\varepsilon - \varepsilon_{m\boldsymbol{k}+\boldsymbol{q}}) - i\mathcal{P}\frac{1}{\varepsilon - \varepsilon_{m'\boldsymbol{k}+\boldsymbol{q}}} + i\mathcal{P}\frac{1}{\varepsilon - \varepsilon_{m\boldsymbol{k}+\boldsymbol{q}}}}{i(\Sigma^R_{m\boldsymbol{k}+\boldsymbol{q}} - \Sigma^A_{m'\boldsymbol{k}+\boldsymbol{q}}) + i(\varepsilon_{m\boldsymbol{k}+\boldsymbol{q}} - \varepsilon_{m'\boldsymbol{k}+\boldsymbol{q}})},
\end{aligned} \tag{3.15}$$

a function that is strongly peaked at electron energies $\varepsilon = \varepsilon_{m\boldsymbol{k}+\boldsymbol{q}}$ and $\varepsilon = \varepsilon_{m'\boldsymbol{k}+\boldsymbol{q}}$. Therefore, we can further simplify the spin-phonon BSE from its full-frequency form in Eq. (3.13) to the following double-pole ansatz:

$$\begin{aligned}
&s^\alpha_{nn'\boldsymbol{k}} \Lambda^\alpha_{nn'\boldsymbol{k}}(\varepsilon) = s^\alpha_{nn'\boldsymbol{k}} + \frac{2\pi}{V} \sum_{mm'\nu\boldsymbol{q}} [g_{n'm'\nu}(\boldsymbol{k},\boldsymbol{q})]^* \, g_{nm\nu}(\boldsymbol{k},\boldsymbol{q}) s^\alpha_{mm'\boldsymbol{k}+\boldsymbol{q}} \\
&\times \frac{1}{2}\Bigg\{ [(N_{\nu\boldsymbol{q}} + f_{m\boldsymbol{k}+\boldsymbol{q}})(\delta(\varepsilon + \omega_{\nu\boldsymbol{q}} - \varepsilon_{m\boldsymbol{k}+\boldsymbol{q}}) - \frac{i}{\pi}\mathcal{P}\frac{1}{\varepsilon + \omega_{\nu\boldsymbol{q}} - \varepsilon_{m'\boldsymbol{k}+\boldsymbol{q}}}) \\
&+ (N_{\nu\boldsymbol{q}} + 1 - f_{m\boldsymbol{k}+\boldsymbol{q}})(\delta(\varepsilon - \omega_{\nu\boldsymbol{q}} - \varepsilon_{m\boldsymbol{k}+\boldsymbol{q}}) - \frac{i}{\pi}\mathcal{P}\frac{1}{\varepsilon - \omega_{\nu\boldsymbol{q}} - \varepsilon_{m'\boldsymbol{k}+\boldsymbol{q}}})] \times \frac{\Lambda^\alpha_{mm'\boldsymbol{k}+\boldsymbol{q}}(\varepsilon_{m\boldsymbol{k}+\boldsymbol{q}})}{i(\Sigma^R_{m\boldsymbol{k}+\boldsymbol{q}} - \Sigma^A_{m'\boldsymbol{k}+\boldsymbol{q}}) + i(\varepsilon_{m\boldsymbol{k}+\boldsymbol{q}} - \varepsilon_{m'\boldsymbol{k}+\boldsymbol{q}})} \\
&+ [(N_{\nu\boldsymbol{q}} + f_{m'\boldsymbol{k}+\boldsymbol{q}})(\delta(\varepsilon + \omega_{\nu\boldsymbol{q}} - \varepsilon_{m'\boldsymbol{k}+\boldsymbol{q}}) + \frac{i}{\pi}\mathcal{P}\frac{1}{\varepsilon + \omega_{\nu\boldsymbol{q}} - \varepsilon_{m\boldsymbol{k}+\boldsymbol{q}}}) \\
&+ (N_{\nu\boldsymbol{q}} + 1 - f_{m'\boldsymbol{k}+\boldsymbol{q}})(\delta(\varepsilon - \omega_{\nu\boldsymbol{q}} - \varepsilon_{m'\boldsymbol{k}+\boldsymbol{q}}) + \frac{i}{\pi}\mathcal{P}\frac{1}{\varepsilon - \omega_{\nu\boldsymbol{q}} - \varepsilon_{m\boldsymbol{k}+\boldsymbol{q}}})] \times \frac{\Lambda^\alpha_{mm'\boldsymbol{k}+\boldsymbol{q}}(\varepsilon_{m'\boldsymbol{k}+\boldsymbol{q}})}{i(\Sigma^R_{m\boldsymbol{k}+\boldsymbol{q}} - \Sigma^A_{m'\boldsymbol{k}+\boldsymbol{q}}) + i(\varepsilon_{m\boldsymbol{k}+\boldsymbol{q}} - \varepsilon_{m'\boldsymbol{k}+\boldsymbol{q}})} \Bigg\},
\end{aligned} \tag{3.16}$$

where ε stands for either $\varepsilon_{n\boldsymbol{k}}$ or $\varepsilon_{n'\boldsymbol{k}}$, and $f_{m\boldsymbol{k}+\boldsymbol{q}} \equiv f(\varepsilon_{m\boldsymbol{k}+\boldsymbol{q}})$. Note that the spin-phonon BSE in Eq. (3.16) should not be confused with the widely-used BSE for excitons and optical spectra [62], which is entirely unrelated.

The dressed vertex and its interpretation

We focus on the dressed spin operator divided by the band energy difference, which we introduced in Eq. (3.16):

$$\frac{s^\alpha_{mm'\boldsymbol{k}+\boldsymbol{q}} \Lambda^\alpha_{mm'\boldsymbol{k}+\boldsymbol{q}}(\varepsilon_{m'\boldsymbol{k}+\boldsymbol{q}})}{i(\Sigma^R_{m\boldsymbol{k}+\boldsymbol{q}} - \Sigma^A_{m'\boldsymbol{k}+\boldsymbol{q}}) + i(\varepsilon_{m\boldsymbol{k}+\boldsymbol{q}} - \varepsilon_{m'\boldsymbol{k}+\boldsymbol{q}})}. \tag{3.17}$$

This ratio describes the renormalized spin magnetization in the presence of e-ph interactions. The effective renormalized dynamics of the spin operator is obtained by dividing Eq. (3.17) by the bare spin expectation value $s^{\alpha}_{mm'\boldsymbol{k}+\boldsymbol{q}}$, which gives

$$\frac{\Lambda^{\alpha}_{mm'\boldsymbol{k}+\boldsymbol{q}}(\varepsilon_{m'\boldsymbol{k}+\boldsymbol{q}})}{i(\Sigma^{R}_{m\boldsymbol{k}+\boldsymbol{q}}-\Sigma^{A}_{m'\boldsymbol{k}+\boldsymbol{q}})+i(\varepsilon_{m\boldsymbol{k}+\boldsymbol{q}}-\varepsilon_{m'\boldsymbol{k}+\boldsymbol{q}})}. \tag{3.18}$$

The physical meaning of these ratios can be understood by analyzing the simpler case of the velocity operator, $v^{\alpha}_{mm'\boldsymbol{k}+\boldsymbol{q}} = v^{\alpha}_{m\boldsymbol{k}+\boldsymbol{q}}\delta_{mm'}$. As the velocity operator is band-diagonal, the band energy difference in the denominator vanishes, and the denominator is purely real because $\Sigma^{A}_{m'\boldsymbol{k}+\boldsymbol{q}} = (\Sigma^{R}_{m'\boldsymbol{k}+\boldsymbol{q}})^{*}$. Thus the analog of Eq. (3.17) for the velocity operator becomes

$$\frac{v^{\alpha}_{m\boldsymbol{k}+\boldsymbol{q}}\Lambda^{\alpha}_{mm\boldsymbol{k}+\boldsymbol{q}}(\varepsilon_{m\boldsymbol{k}+\boldsymbol{q}})}{i(\Sigma^{R}_{m\boldsymbol{k}+\boldsymbol{q}}-\Sigma^{A}_{m\boldsymbol{k}+\boldsymbol{q}})} = v^{\alpha}_{m\boldsymbol{k}+\boldsymbol{q}}\tau^{\text{e-ph}}_{m\boldsymbol{k}+\boldsymbol{q}}\Lambda^{\alpha}_{mm\boldsymbol{k}+\boldsymbol{q}}(\varepsilon_{m\boldsymbol{k}+\boldsymbol{q}}), \tag{3.19}$$

where we used $\tau^{\text{e-ph}}_{m\boldsymbol{k}+\boldsymbol{q}} = 1/|2\Im\Sigma_{m\boldsymbol{k}+\boldsymbol{q}}|$ for the e-ph collision time. Equation (3.19) gives the renormalized mean free path, and dividing by the bare velocity we obtain the renormalized relaxation time, also known as the transport relaxation time [38],

$$\tau^{\alpha(\text{tr})}_{m\boldsymbol{k}+\boldsymbol{q}} \equiv \tau^{\text{e-ph}}_{m\boldsymbol{k}+\boldsymbol{q}}\Lambda^{\alpha}_{mm\boldsymbol{k}+\boldsymbol{q}} = \frac{\Lambda^{\alpha}_{mm\boldsymbol{k}+\boldsymbol{q}}(\varepsilon_{m\boldsymbol{k}+\boldsymbol{q}})}{\frac{1}{\tau^{\text{e-ph}}_{m\boldsymbol{k}+\boldsymbol{q}}}}. \tag{3.20}$$

For a non-diagonal operator, both the vertex correction and the operator expectation value are complex, so the ratio in Eq. (3.18) cannot be represented by a single real quantity with units of time as in Eq. (3.20). We thus extend this formalism by defining the renormalized microscopic relaxation times $\tau^{\alpha}_{mm'\boldsymbol{k}+\boldsymbol{q}}(\varepsilon)$ and precession frequencies $\omega^{\alpha}_{mm'\boldsymbol{k}+\boldsymbol{q}}(\varepsilon)$:

$$\frac{\Lambda^{\alpha}_{mm'\boldsymbol{k}+\boldsymbol{q}}(\varepsilon)}{i(\Sigma^{R}_{m\boldsymbol{k}+\boldsymbol{q}}-\Sigma^{A}_{m'\boldsymbol{k}+\boldsymbol{q}})+i(\varepsilon_{m\boldsymbol{k}+\boldsymbol{q}}-\varepsilon_{m'\boldsymbol{k}+\boldsymbol{q}})} \equiv \frac{1}{\frac{1}{\tau^{\alpha}_{mm'\boldsymbol{k}+\boldsymbol{q}}(\varepsilon)}+i\omega^{\alpha}_{mm'\boldsymbol{k}+\boldsymbol{q}}(\varepsilon)}, \tag{3.21}$$

where ε stands for either $\varepsilon_{m\boldsymbol{k}+\boldsymbol{q}}$ or $\varepsilon_{m'\boldsymbol{k}+\boldsymbol{q}}$. This way, without the vertex correction the renormalized relaxation time reduces to the e-ph collision time, $\tau^{\text{e-ph}}_{mm'\boldsymbol{k}+\boldsymbol{q}} = 1/|\Im\Sigma_{m\boldsymbol{k}+\boldsymbol{q}} + \Im\Sigma_{m'\boldsymbol{k}+\boldsymbol{q}}|$, and the renormalized precession frequency reduces to the bare precession frequency, equal to the energy difference $(\varepsilon_{m\boldsymbol{k}+\boldsymbol{q}} + \Re\Sigma_{m\boldsymbol{k}+\boldsymbol{q}}) - (\varepsilon_{m'\boldsymbol{k}+\boldsymbol{q}} + \Re\Sigma_{m'\boldsymbol{k}+\boldsymbol{q}})$.

Renormalized spin relaxation times from linear response theory

We use linear response theory to derive the macroscopic spin relaxation times inclusive of vertex corrections. We focus on the spin magnetic moment $\hat{m} = g\mu_B \hat{s}$, where g is the electron Landé g-factor and μ_B is the Bohr magneton. The magnetic spin susceptibility χ^{M} is defined as the response function in

$$M^{\alpha}(\nu) = \chi^{\mathrm{M}}_{\alpha\beta}(\nu) B^{\beta}(\nu), \tag{3.22}$$

where B^{β} is the external magnetic field along the direction β, and M^{α} is the magnetization of the system along α generated in response to the applied magnetic field. Note that the magnetic susceptibility is proportional to the spin-spin correlation function χ introduced above, $\chi^{\mathrm{M}}_{\alpha\beta}(\nu) = (g\mu_B)^2 \chi_{\alpha\beta}(\nu)$. To study spin relaxation, we rewrite the magnetization as [63]

$$M^{\alpha}(\nu) = \sigma^{\mathrm{M}}_{\alpha\beta}(\nu) \dot{B}^{\beta}(\nu). \tag{3.23}$$

Thus, expressing it in terms of σ^{M}, the magnetic susceptibility to the spin injection field at frequency ν, $\dot{B}^{\beta}(\nu) = -i\nu B^{\beta}(\nu)$ [63]. This field produces a nonequilibrium spin density with a spin injection rate equal to the inverse spin relaxation time $1/\tau^{(s)}$ [63]. From Eqs. (3.22)-(3.23), we obtain

$$\sigma^{\mathrm{M}}_{\alpha\beta}(\nu) = \frac{\chi^{M}_{\alpha\beta}(\nu)}{-i\nu}. \tag{3.24}$$

We write the spin-spin correlation function with ladder vertex correction [see Eq. (3.8)] as a contour integral along a circle at infinity,

$$\chi_{\alpha\beta}(i\nu_b) = -\frac{1}{V_{\mathrm{uc}}} \oint \frac{dz}{2\pi i} f(z) \mathrm{Tr}\big[\mathcal{G}(z) \hat{s}^{\alpha} \mathcal{G}(z + i\nu_b) \hat{s}^{\beta} \Lambda^{\beta}(z, z + i\nu_b)\big], \tag{3.25}$$

which has branch cuts along $z = 0$ and $z = -i\nu_b$, and poles at $z = i\omega_a$, such that

$$\begin{aligned} \chi_{\alpha\beta}(i\nu_b) = \frac{1}{V_{\mathrm{uc}}} \int \frac{d\varepsilon}{2\pi i} f(\varepsilon) \mathrm{Tr}\Big[& -\mathcal{G}(\varepsilon + i\eta) \hat{s}^{\alpha} \mathcal{G}(\varepsilon + i\nu_b) \hat{s}^{\beta} \Lambda^{\beta}(\varepsilon + i\eta, \varepsilon + i\nu_b) \\ & + \mathcal{G}(\varepsilon - i\eta) \hat{s}^{\alpha} \mathcal{G}(\varepsilon + i\nu_b) \hat{s}^{\beta} \Lambda^{\beta}(\varepsilon - i\eta, \varepsilon + i\nu_b) \\ & - \mathcal{G}(\varepsilon - i\nu_b) \hat{s}^{\alpha} \mathcal{G}(\varepsilon + i\eta) \hat{s}^{\beta} \Lambda^{\beta}(\varepsilon - i\nu_b, \varepsilon + i\eta) \\ & + \mathcal{G}(\varepsilon - i\nu_b) \hat{s}^{\alpha} \mathcal{G}(\varepsilon - i\eta) \hat{s}^{\beta} \Lambda^{\beta}(\varepsilon - i\nu_b, \varepsilon - i\eta) \Big]. \end{aligned} \tag{3.26}$$

After the analytic continuation $i\nu_b \to \nu + i\eta$, we obtain the spin-spin correlation function to leading order by neglecting terms of order $O([G^R]^2, [G^A]^2)$ [38, 39]:

$$
\begin{aligned}
\chi_{\alpha\beta}(\nu) =& \frac{1}{V_{\mathrm{uc}}} \int \frac{d\varepsilon}{2\pi i}(f(\varepsilon) - f(\varepsilon+\nu))\mathrm{Tr}\big[G^R(\varepsilon)\hat{s}^\alpha G^A(\varepsilon+\nu)\hat{s}^\beta \Lambda^\beta(i\omega_a - i\eta, i\omega_a + i\nu_b + i\eta)\big] \\
\approx& \frac{1}{V}\sum_{nm\boldsymbol{k}} \int \frac{d\varepsilon}{2\pi i}(f(\varepsilon) - f(\varepsilon+\nu)) s^\alpha_{nm\boldsymbol{k}} s^\beta_{mn\boldsymbol{k}} \Lambda^\beta_{mn\boldsymbol{k}}(\varepsilon - i\eta, \varepsilon+\nu+i\eta) \\
&\times \frac{\pi\delta(\varepsilon - \varepsilon_{n\boldsymbol{k}}) + \pi\delta(\varepsilon+\nu-\varepsilon_{m\boldsymbol{k}})}{i(\varepsilon_{n\boldsymbol{k}} + \nu - \varepsilon_{m\boldsymbol{k}}) - i(\Sigma^A_{n\boldsymbol{k}} - \Sigma^R_{m\boldsymbol{k}})},
\end{aligned}
\tag{3.27}
$$

where we used Eq. (3.15) to obtain the second line. Equation (3.27) completely determines the frequency-dependent spin response of the system.

Using this result, we derive an analytic expression for the average macroscopic spin relaxation times. We focus on the dc limit $\nu \to 0$, where the external driving field is static, and compute the relaxation of the non-precessing (band-diagonal) spins by setting $m = n$ in Eq. (3.27). The the magnetic susceptibility to the spin injection field in the dc limit becomes

$$
\begin{aligned}
\lim_{\nu\to 0}\sigma^{\mathrm{M}}_{\alpha\beta}(\nu)|_{m=n} &= -(g\mu_B)^2 \lim_{\nu\to 0}\frac{1}{\nu}\Im\chi_{\alpha\beta}(\nu)\big|_{m=n} \\
&= \frac{(g\mu_B)^2}{V}\sum_{n\boldsymbol{k}} s^\alpha_{nn\boldsymbol{k}} s^\beta_{nn\boldsymbol{k}} \tau^{\text{e-ph}}_{n\boldsymbol{k}} \Lambda^\beta_{nn\boldsymbol{k}}(\varepsilon_{n\boldsymbol{k}})(-\frac{df_{n\boldsymbol{k}}}{d\varepsilon}),
\end{aligned}
\tag{3.28}
$$

which gives renormalized *microscopic* spin relaxation times $\tau^{\text{e-ph}}_{n\boldsymbol{k}}\Lambda^\beta_{nn\boldsymbol{k}}(\varepsilon_{n\boldsymbol{k}})$, consistent with Eq. (3.21) for non-precessing spins. The corresponding average *macroscopic* spin relaxation times are

$$
\tau^{(s)}_{\alpha\beta} = \frac{\sum_{n\boldsymbol{k}} s^\alpha_{nn\boldsymbol{k}} s^\beta_{nn\boldsymbol{k}} \tau^{\text{e-ph}}_{n\boldsymbol{k}} \Lambda^\beta_{nn\boldsymbol{k}}(\varepsilon_{n\boldsymbol{k}})(-\frac{df_{n\boldsymbol{k}}}{d\varepsilon})}{\sum_{n\boldsymbol{k}} s^\alpha_{nn\boldsymbol{k}} s^\beta_{nn\boldsymbol{k}}\big(-\frac{df_{n\boldsymbol{k}}}{d\varepsilon}\big)}.
\tag{3.29}
$$

References

[1] Gopalakrishnan Balasubramanian, I. Y. Chan, Roman Kolesov, Mohannad Al-Hmoud, Julia Tisler, Chang Shin, Changdong Kim, Aleksander Wojcik, Philip R. Hemmer, Anke Krueger, Tobias Hanke, Alfred Leitenstorfer, Rudolf Bratschitsch, Fedor Jelezko, and Jörg Wrachtrup. Nanoscale imaging magnetometry with diamond spins under ambient conditions. *Nature*, 455(7213): 648–651, 2008. doi: 10.1038/nature07278.

[2] Ron Jansen. Silicon spintronics. *Nat. Mater.*, 11(5):400–408, 2012. doi: 10.1038/nmat3293.

[3] Igor Žutić, Jaroslav Fabian, and S. Das Sarma. Spintronics: Fundamentals and applications. *Rev. Mod. Phys.*, 76(2):323–410, 2004. doi: 10.1103/RevModPhys.76.323.

[4] Wei Han, Roland K. Kawakami, Martin Gmitra, and Jaroslav Fabian. Graphene spintronics. *Nat. Nanotechnol.*, 9(10):794–807, 2014. doi: 10.1038/nnano.2014.214.

[5] Ian Appelbaum, Biqin Huang, and Douwe J. Monsma. Electronic measurement and control of spin transport in silicon. *Nature*, 447(7142):295–298, 2007. doi: 10.1038/nature05803.

[6] J. Železný, P. Wadley, K. Olejník, A. Hoffmann, and H. Ohno. Spin transport and spin torque in antiferromagnetic devices. *Nat. Phys.*, 14(3):220–228, 2018. doi: 10.1038/s41567-018-0062-7.

[7] M. Veldhorst, C. H. Yang, J. C. C. Hwang, W. Huang, J. P. Dehollain, J. T. Muhonen, S. Simmons, A. Laucht, F. E. Hudson, K. M. Itoh, A. Morello, and A. S. Dzurak. A two-qubit logic gate in silicon. *Nature*, 526(7573):410–414, 2015. doi: 10.1038/nature15263.

[8] X. Mi, M. Benito, S. Putz, D. M. Zajac, J. M. Taylor, Guido Burkard, and J. R. Petta. A coherent spin–photon interface in silicon. *Nature*, 555(7698): 599–603, 2018. doi: 10.1038/nature25769.

[9] Samuel J. Whiteley, Gary Wolfowicz, Christopher P. Anderson, Alexandre Bourassa, He Ma, Meng Ye, Gerwin Koolstra, Kevin J. Satzinger, Martin V. Holt, F. Joseph Heremans, Andrew N. Cleland, David I. Schuster, Giulia Galli, and David D. Awschalom. Spin–phonon interactions in silicon carbide addressed by Gaussian acoustics. *Nat. Phys.*, 15(5):490–495, 2019. doi: 10.1038/s41567-019-0420-0.

[10] Gary Wolfowicz, F. Joseph Heremans, Christopher P. Anderson, Shun Kanai, Hosung Seo, Adam Gali, Giulia Galli, and David D. Awschalom. Quantum guidelines for solid-state spin defects. *Nat. Rev. Mater.*, 6(10):906–925, 2021. doi: 10.1038/s41578-021-00306-y.

[11] Akito Noiri, Kenta Takeda, Takashi Nakajima, Takashi Kobayashi, Amir Sammak, Giordano Scappucci, and Seigo Tarucha. Fast universal quantum gate above the fault-tolerance threshold in silicon. *Nature*, 601(7893):338–342, 2022. doi: 10.1038/s41586-021-04182-y.

[12] Alexandre Bourassa, Christopher P. Anderson, Kevin C. Miao, Mykyta Onizhuk, He Ma, Alexander L. Crook, Hiroshi Abe, Jawad Ul-Hassan, Takeshi Ohshima, Nguyen T. Son, Giulia Galli, and David D. Awschalom. Entanglement and control of single nuclear spins in isotopically engineered silicon carbide. *Nat. Mater.*, 19(12):1319–1325, 2020. doi: 10.1038/s41563-020-00802-6.

[13] L. Petit, H. G. J. Eenink, M. Russ, W. I. L. Lawrie, N. W. Hendrickx, S. G. J. Philips, J. S. Clarke, L. M. K. Vandersypen, and M. Veldhorst. Universal quantum logic in hot silicon qubits. *Nature*, 580(7803):355–359, 2020. doi: 10.1038/s41586-020-2170-7.

[14] C. L. Degen, F. Reinhard, and P. Cappellaro. Quantum sensing. *Rev. Mod. Phys.*, 89(3):035002, 2017. doi: 10.1103/RevModPhys.89.035002.

[15] Denis Vasyukov, Yonathan Anahory, Lior Embon, Dorri Halbertal, Jo Cuppens, Lior Neeman, Amit Finkler, Yehonathan Segev, Yuri Myasoedov, Michael L. Rappaport, Martin E. Huber, and Eli Zeldov. A scanning superconducting quantum interference device with single electron spin sensitivity. *Nat. Nanotechnol.*, 8(9):639–644, 2013. doi: 10.1038/nnano.2013.169.

[16] John F. Barry, Jennifer M. Schloss, Erik Bauch, Matthew J. Turner, Connor A. Hart, Linh M. Pham, and Ronald L. Walsworth. Sensitivity optimization for NV-diamond magnetometry. *Rev. Mod. Phys.*, 92(1):015004, 2020. doi: 10.1103/RevModPhys.92.015004.

[17] R. J. Elliott. Theory of the effect of spin-orbit coupling on magnetic resonance in some semiconductors. *Phys. Rev.*, 96(2):266–279, 1954. doi: 10.1103/PhysRev.96.266.

[18] Y. Yafet. G factors and spin-lattice relaxation of conduction electrons. In Frederick Seitz and David Turnbull, editors, *Solid State Physics*, volume 14, pages 1–98. 1963. doi: 10.1016/S0081-1947(08)60259-3.

[19] MI Dyakonov and VI Perel. Spin relaxation of conduction electrons in noncentrosymmetric semiconductors. *Sov. Phys. Solid State USSR*, 13(12):3023–3026, 1972.

[20] Alexander Baral, Svenja Vollmar, Steffen Kaltenborn, and Hans Christian Schneider. Re-examination of the Elliott–Yafet spin-relaxation mechanism. *New J. Phys.*, 18(2):023012, 2016. doi: 10.1088/1367-2630/18/2/023012.

[21] Matthew D. Mower, G. Vignale, and I. V. Tokatly. Dyakonov-Perel spin relaxation for degenerate electrons in the electron-hole liquid. *Phys. Rev. B*, 83(15):155205, 2011. doi: 10.1103/PhysRevB.83.155205.

[22] M. W. Wu, J. H. Jiang, and M. Q. Weng. Spin dynamics in semiconductors. *Phys. Rep.*, 493(2):61–236, 2010. doi: 10.1016/j.physrep.2010.04.002.

[23] Junqing Xu, Adela Habib, Ravishankar Sundararaman, and Yuan Ping. Ab initio ultrafast spin dynamics in solids. *Phys. Rev. B*, 104(18):184418, 2021. doi: 10.1103/PhysRevB.104.184418.

[24] K. Shen and M. W. Wu. Hole spin relaxation in intrinsic and p-type bulk GaAs. *Phys. Rev. B*, 82(11):115205, 2010. doi: 10.1103/PhysRevB.82.115205.

[25] F. Simon, B. Dóra, F. Murányi, A. Jánossy, S. Garaj, L. Forró, S. Bud'ko, C. Petrovic, and P. C. Canfield. Generalized Elliott-Yafet theory of electron spin relaxation in metals: Origin of the anomalous electron spin lifetime in MgB_2. *Phys. Rev. Lett.*, 101(17):177003, 2008. doi: 10.1103/PhysRevLett.101.177003.

[26] Péter Boross, Balázs Dóra, Annamária Kiss, and Ferenc Simon. A unified theory of spin-relaxation due to spin-orbit coupling in metals and semiconductors. *Sci. Rep.*, 3(1):3233, 2013. doi: 10.1038/srep03233.

[27] Lénárd Szolnoki, Balázs Dóra, Annamária Kiss, Jaroslav Fabian, and Ferenc Simon. Intuitive approach to the unified theory of spin relaxation. *Phys. Rev. B*, 96(24):245123, 2017. doi: 10.1103/PhysRevB.96.245123.

[28] Marco Bernardi. First-principles dynamics of electrons and phonons. *Eur. Phys. J. B*, 89(11):239, 2016. doi: 10.1140/epjb/e2016-70399-4.

[29] Jin-Jian Zhou, Jinsoo Park, I-Te Lu, Ivan Maliyov, Xiao Tong, and Marco Bernardi. Perturbo: A software package for ab initio electron–phonon interactions, charge transport and ultrafast dynamics. *Comput. Phys. Commun.*, 264: 107970, 2021. doi: 10.1016/j.cpc.2021.107970.

[30] Thibault Sohier, Matteo Calandra, Cheol-Hwan Park, Nicola Bonini, Nicola Marzari, and Francesco Mauri. Phonon-limited resistivity of graphene by first-principles calculations: Electron-phonon interactions, strain-induced gauge field, and Boltzmann equation. *Phys. Rev. B*, 90(12):125414, 2014. doi: 10.1103/PhysRevB.90.125414.

[31] Wu Li. Electrical transport limited by electron-phonon coupling from Boltzmann transport equation: An ab initio study of Si, Al, and MoS_2. *Phys. Rev. B*, 92(7):075405, 2015. doi: 10.1103/PhysRevB.92.075405.

[32] Jin-Jian Zhou and Marco Bernardi. Ab initio electron mobility and polar phonon scattering in GaAs. *Phys. Rev. B*, 94(20):201201(R), 2016. doi: 10.1103/PhysRevB.94.201201.

[33] Samuel Poncé, Elena R. Margine, and Feliciano Giustino. Towards predictive many-body calculations of phonon-limited carrier mobilities in semiconductors. *Phys. Rev. B*, 97(12):121201, 2018. doi: 10.1103/PhysRevB.97.121201.

[34] Jin-Jian Zhou, Olle Hellman, and Marco Bernardi. Electron-phonon scattering in the presence of soft modes and electron mobility in $SrTiO_3$ perovskite from first principles. *Phys. Rev. Lett.*, 121(22):226603, 2018. doi: 10.1103/PhysRevLett.121.226603.

[35] Vatsal A. Jhalani, Jin-Jian Zhou, Jinsoo Park, Cyrus E. Dreyer, and Marco Bernardi. Piezoelectric electron-phonon interaction from ab initio dynamical quadrupoles: Impact on charge transport in wurtzite GaN. *Phys. Rev. Lett.*, 125(13):136602, 2020. doi: 10.1103/PhysRevLett.125.136602.

[36] Jin-Jian Zhou, Jinsoo Park, Iurii Timrov, Andrea Floris, Matteo Cococcioni, Nicola Marzari, and Marco Bernardi. Ab initio electron-phonon interactions in correlated electron systems. *Phys. Rev. Lett.*, 127(12):126404, 2021. doi: 10.1103/PhysRevLett.127.126404.

[37] Jinsoo Park, Jin-Jian Zhou, and Marco Bernardi. Spin-phonon relaxation times in centrosymmetric materials from first principles. *Phys. Rev. B*, 101(4): 045202, 2020. doi: 10.1103/PhysRevB.101.045202.

[38] Sunghoon Kim, Seungchan Woo, and Hongki Min. Vertex corrections to the dc conductivity in anisotropic multiband systems. *Phys. Rev. B*, 99(16):165107, 2019. doi: 10.1103/PhysRevB.99.165107.

[39] Gerald D. Mahan. *Many-Particle Physics*. Physics of Solids and Liquids. Third edition, 2000. ISBN 978-0-306-46338-9. doi: 10.1007/978-1-4757-5714-9.

[40] Paolo Giannozzi, Stefano Baroni, Nicola Bonini, Matteo Calandra, Roberto Car, Carlo Cavazzoni, Davide Ceresoli, Guido L. Chiarotti, Matteo Cococcioni, Ismaila Dabo, Andrea Dal Corso, Stefano de Gironcoli, Stefano Fabris, Guido Fratesi, Ralph Gebauer, Uwe Gerstmann, Christos Gougoussis, Anton Kokalj, Michele Lazzeri, Layla Martin-Samos, Nicola Marzari, Francesco Mauri, Riccardo Mazzarello, Stefano Paolini, Alfredo Pasquarello, Lorenzo Paulatto, Carlo Sbraccia, Sandro Scandolo, Gabriele Sclauzero, Ari P. Seitsonen, Alexander Smogunov, Paolo Umari, and Renata M. Wentzcovitch. QUANTUM ESPRESSO: A modular and open-source software project for quantum simulations of materials. *J. Phys.: Condens. Matter*, 21(39):395502, 2009. doi: 10.1088/0953-8984/21/39/395502.

[41] Giovanni Pizzi, Valerio Vitale, Ryotaro Arita, Stefan Blügel, Frank Freimuth, Guillaume Géranton, Marco Gibertini, Dominik Gresch, Charles Johnson, Takashi Koretsune, Julen Ibañez-Azpiroz, Hyungjun Lee, Jae-Mo Lihm, Daniel Marchand, Antimo Marrazzo, Yuriy Mokrousov, Jamal I. Mustafa, Yoshiro Nohara, Yusuke Nomura, Lorenzo Paulatto, Samuel Poncé, Thomas Ponweiser, Junfeng Qiao, Florian Thöle, Stepan S. Tsirkin, Ma\lgorzata

Wierzbowska, Nicola Marzari, David Vanderbilt, Ivo Souza, Arash A. Mostofi, and Jonathan R. Yates. Wannier90 as a community code: New features and applications. *J. Phys. Condens. Matter*, 32(16):165902, 2020. doi: 10.1088/1361-648X/ab51ff.

[42] Daniel J. Lépine. Spin resonance of localized and delocalized electrons in phosphorus-doped silicon between 20 and 30 °K. *Phys. Rev. B*, 2(7):2429–2439, 1970. doi: 10.1103/PhysRevB.2.2429.

[43] G. Lancaster, J. A. van Wyk, and E. E. Schneider. Spin-lattice relaxation of conduction electrons in silicon. *Proc. Phys. Soc.*, 84(1):19–24, 1964. doi: 10.1088/0370-1328/84/1/304.

[44] S. Oertel, J. Hübner, and M. Oestreich. High temperature electron spin relaxation in bulk GaAs. *Appl. Phys. Lett.*, 93(13):132112, 2008. doi: 10.1063/1.2993344.

[45] A. V. Kimel, F. Bentivegna, V. N. Gridnev, V. V. Pavlov, R. V. Pisarev, and Th. Rasing. Room-temperature ultrafast carrier and spin dynamics in GaAs probed by the photoinduced magneto-optical Kerr effect. *Phys. Rev. B*, 63(23): 235201, 2001. doi: 10.1103/PhysRevB.63.235201.

[46] R. I. Dzhioev, K. V. Kavokin, V. L. Korenev, M. V. Lazarev, N. K. Poletaev, B. P. Zakharchenya, E. A. Stinaff, D. Gammon, A. S. Bracker, and M. E. Ware. Suppression of Dyakonov-Perel spin relaxation in high-mobility n-GaAs. *Phys. Rev. Lett.*, 93(21):216402, 2004. doi: 10.1103/PhysRevLett.93.216402.

[47] Tianshu Lai, Xiaodong Liu, Haihong Xu, Zhongxing Jiao, Jinhui Wen, and Weizhu Lin. Temperature dependence of electron-spin coherence in intrinsic bulk GaAs. *Appl. Phys. Lett.*, 88(19):192106, 2006. doi: 10.1063/1.2202754.

[48] Manfred Ersfeld, Frank Volmer, Lars Rathmann, Luca Kotewitz, Maximilian Heithoff, Mark Lohmann, Bowen Yang, Kenji Watanabe, Takashi Taniguchi, Ludwig Bartels, Jing Shi, Christoph Stampfer, and Bernd Beschoten. Unveiling valley lifetimes of free charge carriers in monolayer WSe_2. *Nano Lett.*, 20(5): 3147–3154, 2020. doi: 10.1021/acs.nanolett.9b05138.

[49] Jing Li, M. Goryca, K. Yumigeta, H. Li, S. Tongay, and S. A. Crooker. Valley relaxation of resident electrons and holes in a monolayer semiconductor: Dependence on carrier density and the role of substrate-induced disorder. *Phys. Rev. Mater.*, 5(4):044001, 2021. doi: 10.1103/PhysRevMaterials.5.044001.

[50] Tengfei Yan, Siyuan Yang, Dian Li, and Xiaodong Cui. Long valley relaxation time of free carriers in monolayer WSe_2. *Phys. Rev. B*, 95(24):241406, 2017. doi: 10.1103/PhysRevB.95.241406.

[51] M. Goryca, N. P. Wilson, P. Dey, X. Xu, and S. A. Crooker. Detection of thermodynamic “valley noise” in monolayer semiconductors: Access to

intrinsic valley relaxation time scales. *Sci. Adv.*, 5(3):eaau4899, 2019. doi: 10.1126/sciadv.aau4899.

[52] D. J. Hilton and C. L. Tang. Optical orientation and femtosecond relaxation of spin-polarized holes in GaAs. *Phys. Rev. Lett.*, 89(14):146601, 2002. doi: 10.1103/PhysRevLett.89.146601.

[53] Michael Krauß, Martin Aeschlimann, and Hans Christian Schneider. Ultrafast spin dynamics including spin-orbit interaction in semiconductors. *Phys. Rev. Lett.*, 100(25):256601, 2008. doi: 10.1103/PhysRevLett.100.256601.

[54] Julian Schwinger. On quantum-electrodynamics and the magnetic moment of the electron. *Phys. Rev.*, 73(4):416–417, 1948. doi: 10.1103/PhysRev.73.416.

[55] D. Hanneke, S. Fogwell, and G. Gabrielse. New measurement of the electron magnetic moment and the fine structure constant. *Phys. Rev. Lett.*, 100:120801, 2008. doi: 10.1103/PhysRevLett.100.120801.

[56] M. Cardona. Renormalization of the Optical Response of Semiconductors by Electron–Phonon Interaction. *Phys. Status Solidi A*, 188(4):1209–1232, 2001. doi: 10.1002/1521-396X(200112)188:4<1209::AID-PSSA1209>3.0.CO;2-2.

[57] Gianluca Stefanucci and Robert van Leeuwen. *Nonequilibrium Many-Body Theory of Quantum Systems: A Modern Introduction*. Cambridge University Press, 2013. doi: 10.1017/CBO9781139023979.

[58] Jin-Jian Zhou and Marco Bernardi. Predicting charge transport in the presence of polarons: The beyond-quasiparticle regime in $SrTiO_3$. *Phys. Rev. Res.*, 1 (3):033138, 2019. doi: 10.1103/PhysRevResearch.1.033138.

[59] Jae-Mo Lihm and Cheol-Hwan Park. Phonon-induced renormalization of electron wave functions. *Phys. Rev. B*, 101(12):121102, 2020. doi: 10.1103/PhysRevB.101.121102.

[60] P. B. Allen and V. Heine. Theory of the temperature dependence of electronic band structures. *J. Phys. C: Solid State Phys.*, 9(12):2305–2312, 1976. doi: 10.1088/0022-3719/9/12/013.

[61] D. Vollhardt and P. Wölfle. Diagrammatic, self-consistent treatment of the Anderson localization problem in $d \leq 2$ dimensions. *Phys. Rev. B*, 22(10): 4666–4679, 1980. doi: 10.1103/PhysRevB.22.4666.

[62] Michael Rohlfing and Steven G. Louie. Electron-hole excitations and optical spectra from first principles. *Phys. Rev. B*, 62(8):4927–4944, 2000. doi: 10.1103/PhysRevB.62.4927.

[63] Ka Shen, G. Vignale, and R. Raimondi. Microscopic Theory of the Inverse Edelstein Effect. *Phys. Rev. Lett.*, 112(9):096601, 2014. doi: 10.1103/PhysRevLett.112.096601.

Chapter 4

LONG-RANGE QUADRUPOLE ELECTRON-PHONON INTERACTION FROM FIRST PRINCIPLES

4.1 Introduction

Electron-phonon (e-ph) interactions are key to understanding electrical transport, nonequilibrium dynamics, and superconductivity [1]. First-principles calculations can provide microscopic insight into e-ph scattering processes and are rapidly emerging as a quantitative tool for investigating charge transport and ultrafast carrier dynamics in materials [2–13]. The typical workflow combines density functional theory (DFT) [14] calculations of the ground state and band structure with density functional perturbation theory (DFPT) [15] for phonon dispersions and e-ph perturbation potentials. As DFPT can compute the electronic response to periodic lattice perturbations (phonons) with arbitrary wave-vector $\boldsymbol{q}$, the DFPT framework can capture both short- and long-range e-ph interactions.

However, a key challenge is that DFPT is too computationally demanding to be carried out on the fine Brillouin zone grids needed to compute electron scattering rates and transport properties. The established approach in first-principles e-ph studies [9] is to carry out DFPT calculations on coarse Brillouin zone grids with of order 10×10×10 $\boldsymbol{q}$-points, followed by interpolation of the e-ph matrix elements with a localized basis set such as Wannier functions or atomic orbitals [16]. As the perturbation potential can be non-analytic near $\boldsymbol{q} = 0$ [16] or even exhibit a divergence for certain phonon modes, interpolation is particularly challenging and less reliable in the region between $\boldsymbol{q} = 0$ and its nearest-neighbor $\boldsymbol{q}$-points in the coarse DFPT grid. This small-$\boldsymbol{q}$ region is critical as it is dominated by long-range e-ph interactions, whose treatment can affect the quality of the interpolation even at larger values of q in the Brillouin zone.

A multipole expansion of the e-ph perturbation potential shows that in the long-wavelenght limit (phonon wave-vector $\boldsymbol{q} \rightarrow 0$) the long-range dipole Fröhlich term diverges as $1/q$, the quadrupole term approaches a constant value and the short-range octopole and higher terms vanish [17, 18]. These trends in momentum space are due to the spatial decay of the e-ph interactions, with $1/r^2$ trend for the dipole, $1/r^3$ for the quadrupole, and $1/r^4$ or faster for the short-range part. The open question is how one can carry out the e-ph matrix element interpolation in the region near $\boldsymbol{q} = 0$ using analytical expressions for the long-range dipole and quadrupole terms. These expressions have been obtained by Vogl [18], but need to be rewritten in the *ab initio* formalism and computed with first-principles quantities such as the atomic dynamical dipoles [15] and quadrupoles [19–21] induced by lattice vibrations, which can be computed with DFPT. For each atom κ, one can obtain Born charge ($\mathbf{Z}_\kappa$) and dynamical quadrupole ($\mathbf{Q}_\kappa$) tensors, which, once contracted with the phonon eigenvector, give the atomic contributions to the dipole and quadrupole e-ph interactions.

The dipole Fröhlich term has been derived following this strategy [22, 23] and employed in electron scattering rate and transport calculations [4, 7]. The quadrupole term has not yet been derived or implemented in first-principles calculations and its important effect on the e-ph matrix elements has been overlooked. To understand the role of long-range dipole and quadrupole e-ph interactions, it is useful to consider separately the interactions for different phonon modes in the long-wavelength limit, discerning the effect of longitudinal and transverse, and acoustic and optical modes. Analytical models of e-ph interactions rely on such an intuition for the role of different phonon modes in various materials [24].

In ionic and polar covalent crystals (here and below, denoted as polar materials), the dipole Fröhlich term is dominant as $\boldsymbol{q} \rightarrow 0$ due to its $1/q$ trend. This e-ph interaction is due to longitudinal optical (LO) phonons and it dominates small-$\boldsymbol{q}$ scattering. For other phonon modes in polar materials, the dipole term vanishes, and the dominant long-range e-ph interaction is the quadrupole term, which is particularly important for acoustic phonons in piezoelectric (polar noncentrosymmetric) materials. In nonpolar semiconductors such as silicon and germanium, the dipole Fröhlich interaction vanishes and the quadrupole term is a key contribution for all modes in the long-wavelength limit. The quadrupole e-ph interaction is thus expected to play an important role in many classes of materials, making a compelling case for its inclusion in the first-principles framework.

Here we show *ab initio* calculations of the long-range quadrupole e-ph interaction and an approach to include it in the e-ph matrix elements. The accuracy of our method is confirmed by comparing the e-ph matrix elements with direct DFPT calculations. We find that the quadrupole contribution is significant for most phonon modes in both nonpolar and polar materials. In silicon, a nonpolar semiconductor, the quadrupole term has a large effect on the e-ph coupling for optical modes, but is negligible for acoustic modes in the long-wavelength limit. In tetragonal $\mathrm{PbTiO_3}$ (a polar piezoelectric material) the quadrupole corrections are substantial for all phonon modes and particularly important for acoustic modes, which contribute to the piezoelectric e-ph interaction. Including only the long-range Fröhlich interaction and neglecting the quadrupole term leads to large errors in $PbTiO_3$, while adding the quadrupole term leads to e-ph matrix elements that accurately reproduce the DFPT benchmark results for all phonon modes in the entire Brillouin zone. We investigate the impact of the quadrupole e-ph interaction on the electron scattering rates and mobility in silicon and $PbTiO_3$, finding mobility corrections of order 10% in silicon and 20% in $PbTiO_3$ at 100 K (and smaller corrections at 300 K) when the quadrupole term is included. The correction on the scattering rate at low electron energy in $PbTiO_3$ is substantial. Taken together, our results highlight the need to include the quadrupole term in all materials to correctly capture the long-range e-ph interactions. In turn, this development enables more precise calculations of electron dynamics and scattering processes from first principles.

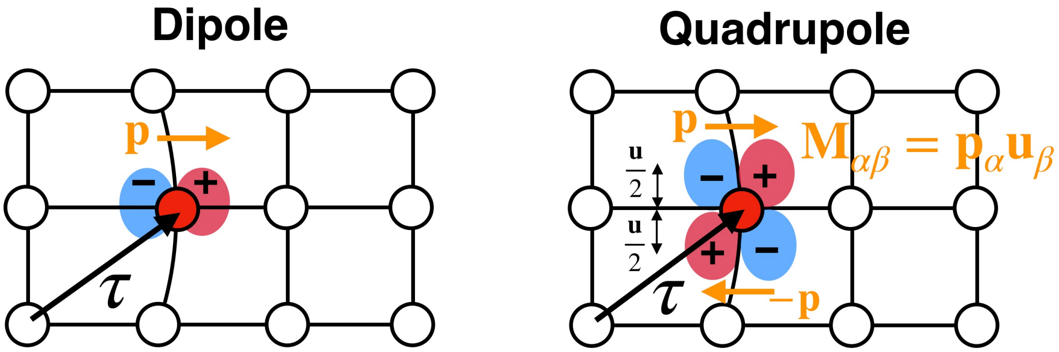

Figure 4.1: Schematic of the dipole and quadrupole charge configurations giving rise to long-range e-ph interactions.

4.2 Theory

The electron distribution changes in response to a displacement of an atom from its equilibrium position. The cell-integrated charge response to a displacement of atom κ due to a phonon with wave-vector $\boldsymbol{q} \to 0$ can be written as a multipole expansion [21]:

$$C^{\boldsymbol{q}}_{\kappa,\alpha} = -iZ_{\kappa,\alpha\beta}\, q_\beta - \frac{1}{2} Q_{\kappa,\alpha\beta\gamma}\, q_\beta q_\gamma + \dots, \tag{4.1}$$

where summation over the Cartesian indices β and γ is implied. This polarization response defines the Born effective charge $\mathbf{Z}_\kappa$, a rank-2 tensor associated with the dipole term, and the dynamical quadrupole $\mathbf{Q}_\kappa$, the rank-3 tensor in the quadrupole term; both tensors can be computed in the DFPT framework [15, 19]. Each of the dipole and quadrupole responses generates macroscopic electric fields and corresponding long-range e-ph interactions in semiconductors and insulators [18, 25], while in metals they are effectively screened out.

In a field-theoretic treatment of the e-ph interactions, one computes the dipole and quadrupole perturbation potentials $\Delta V_{\nu\boldsymbol{q}}$ due to a phonon with mode index ν and wave-vector $\boldsymbol{q}$, and the corresponding e-ph matrix elements [2]

$$g_{mn\nu}(\boldsymbol{k},\boldsymbol{q}) = \left(\frac{\hbar}{2\omega_{\nu\boldsymbol{q}}}\right)^{\frac{1}{2}} \langle m\boldsymbol{k}+\boldsymbol{q}|\, \Delta V_{\nu\boldsymbol{q}}\, |n\boldsymbol{k}\rangle\,, \tag{4.2}$$

which quantify the probability amplitude of an electron in a Bloch state $|n\boldsymbol{k}\rangle$ with band index n and crystal momentum $\boldsymbol{k}$ to scatter into a final state $|m\boldsymbol{k}+\boldsymbol{q}\rangle$ by emitting or absorbing a phonon with energy $\hbar\omega_{\nu\boldsymbol{q}}$.

Dipole and quadrupole e-ph interactions

To derive the dipole and quadrupole perturbation potentials, we consider a Born-von Karman (BvK) crystal [26] with N unit cells and volume $N\Omega$. The potential due to a dipole configuration with dipole moment $\mathbf{p}$ centered at position $\boldsymbol{\tau}$ in the crystal (see Fig. 4.1) can be written as [22, 23]

$$\Delta V^{\mathrm{dip}}(\mathbf{r};\boldsymbol{\tau}) = i\frac{e}{N\Omega\,\varepsilon_0}\sum_{\boldsymbol{q}}\sum_{\mathbf{G}\neq-\boldsymbol{q}} \frac{\mathbf{p}\cdot(\boldsymbol{q}+\mathbf{G})e^{i(\boldsymbol{q}+\mathbf{G})\cdot(\mathbf{r}-\boldsymbol{\tau})}}{(\boldsymbol{q}+\mathbf{G})\cdot\boldsymbol{\epsilon}\cdot(\boldsymbol{q}+\mathbf{G})}, \tag{4.3}$$

where $\boldsymbol{\epsilon}$ is the dielectric tensor of the material, the phonon wave-vector $\boldsymbol{q}$ belongs to a regular Brillouin zone grid with N points, and $\mathbf{G}$ are reciprocal lattice vectors. This result is derived by adding together the potentials generated in the crystal by two point charges of opposite sign with distance $\mathbf{u} \to 0$, resulting in a dipole $\mathbf{p}$ [4, 23]. The potential in Eq. (4.3) is readily extended to the case of an atomic dynamical dipole $\mathbf{p}_{\kappa,\mathbf{R}}$ from atom κ in the unit cell at Bravais lattice vector $\mathbf{R}$, due to the displacement induced by a phonon with mode index ν and wave-vector $\boldsymbol{q}$. The resulting atomic dynamical dipole is $\mathbf{p}_{\kappa,\mathbf{R}} = (e\mathbf{Z}_\kappa)\,\tilde{\mathbf{e}}^{(\kappa)}_{\nu\boldsymbol{q}} e^{i\mathbf{q}\cdot\mathbf{R}}$, where the phonon eigenvector projected on atom κ is defined as $\tilde{\mathbf{e}}^{(\kappa)}_{\nu\boldsymbol{q}} = \mathbf{e}^{(\kappa)}_{\nu\boldsymbol{q}}/\sqrt{M_\kappa}$, with $\mathbf{e}_{\nu\boldsymbol{q}}$ the eigenvector of the dynamical matrix at $\boldsymbol{q}$ and M_κ the mass of atom κ. Summing over the contributions from all atoms κ at lattice vectors $\mathbf{R}$ with positions $\boldsymbol{\tau}_{\kappa\mathbf{R}} = \boldsymbol{\tau}_\kappa + \mathbf{R}$ in the BvK supercell, the total e-ph dipole interaction due to the phonon mode is $\Delta V^{\mathrm{dip}}_{\nu\boldsymbol{q}}(\mathbf{r}) = \sum_{\kappa\mathbf{R}} \Delta V^{\mathrm{dip}}(\mathbf{r};\boldsymbol{\tau}_{\kappa\mathbf{R}})$. Using the identity $\frac{1}{N}\sum_{\mathbf{R}} e^{i\mathbf{q}\cdot\mathbf{R}} = \delta_{\mathbf{q},0}$, we obtain:

$$\Delta V^{\mathrm{dip}}_{\nu\mathbf{q}}(\mathbf{r}) = i\frac{e^2}{\Omega\varepsilon_0}\sum_{\kappa} M_\kappa^{-1/2} \sum_{\mathbf{G}\neq-\boldsymbol{q}} \frac{(\mathbf{Z}_\kappa \mathbf{e}^{(\kappa)}_{\nu\boldsymbol{q}})\cdot(\boldsymbol{q}+\mathbf{G})e^{i(\boldsymbol{q}+\mathbf{G})\cdot(\mathbf{r}-\boldsymbol{\tau})}}{(\boldsymbol{q}+\mathbf{G})\cdot\boldsymbol{\epsilon}\cdot(\boldsymbol{q}+\mathbf{G})}. \tag{4.4}$$

The *ab initio* Fröhlich e-ph coupling is obtained by evaluating the matrix elements with this potential:

$$g^{\mathrm{d}ip}_{mn\nu}(\boldsymbol{k},\boldsymbol{q}) = i\frac{e^2}{\Omega\varepsilon_0}\sum_{\kappa}\left(\frac{\hbar}{2\omega_{\nu\boldsymbol{q}}M_\kappa}\right)^{1/2}\sum_{\mathbf{G}\neq-\boldsymbol{q}}\frac{(\mathbf{Z}_\kappa\mathbf{e}^{(\kappa)}_{\nu\boldsymbol{q}})\cdot(\boldsymbol{q}+\mathbf{G})}{(\boldsymbol{q}+\mathbf{G})\cdot\boldsymbol{\epsilon}\cdot(\boldsymbol{q}+\mathbf{G})}\left\langle m\boldsymbol{k}+\boldsymbol{q}\right| e^{i(\boldsymbol{q}+\mathbf{G})\cdot(\mathbf{r}-\boldsymbol{\tau})}\left|n\boldsymbol{k}\right\rangle . \tag{4.5}$$

The potential due to the dynamical quadrupole response can be derived with a similar strategy. We first consider the potential generated by a quadrupole charge configuration consisting of two equal and oppositely oriented dipoles $\mathbf{p}$ and $-\mathbf{p}$, centered at positions $\boldsymbol{\tau} \pm \frac{\mathbf{u}}{2}$ respectively (see Fig. 4.1). The configuration, with quadrupole moment [27] $M_{\alpha\beta} = p_\alpha u_\beta$, gives a potential:

$$\begin{aligned}\Delta V^{\mathrm{quad}}(\mathbf{r};\boldsymbol{\tau}) &= \lim_{\mathbf{u}\to 0}\left[\Delta V^{\mathrm{dip}}\left(\mathbf{r};\boldsymbol{\tau}+\frac{\mathbf{u}}{2}\right)-\Delta V^{\mathrm{dip}}\left(\mathbf{r};\boldsymbol{\tau}-\frac{\mathbf{u}}{2}\right)\right]\\ &= \frac{e}{N\Omega\,\varepsilon_0}\sum_{\boldsymbol{q}}\sum_{\mathbf{G}\neq-\boldsymbol{q}}\frac{(\boldsymbol{q}+\mathbf{G})\cdot\mathbf{M}\cdot(\boldsymbol{q}+\mathbf{G})}{(\boldsymbol{q}+\mathbf{G})\cdot\boldsymbol{\epsilon}\cdot(\boldsymbol{q}+\mathbf{G})}\,e^{i(\boldsymbol{q}+\mathbf{G})\cdot(\mathbf{r}-\boldsymbol{\tau})},\end{aligned} \tag{4.6}$$

where to obtain the second line we used $\Delta V^{\mathrm{dip}}(\mathbf{r};\boldsymbol{\tau})$ in Eq. (4.3) and expanded the first line to first order in $\mathbf{u}$.

Similar to the dipole case, the potential from atomic quadrupoles $(\mathbf{M}_{\kappa,\mathbf{R}})_{\alpha\beta} = \frac{1}{2}(e\mathbf{Q}_\kappa)_{\alpha\beta\gamma}\,\mathbf{e}^{(\kappa)}_{\nu\boldsymbol{q},\gamma}\,e^{i\mathbf{q}\cdot\mathbf{R}}$ due to the displacement induced by a phonon is obtained as $\Delta V^{\mathrm{quad}}_{\nu\boldsymbol{q}}(\mathbf{r}) = \sum_{\kappa\mathbf{R}}\Delta V^{\mathrm{quad}}(\mathbf{r};\boldsymbol{\tau}_{\kappa\mathbf{R}})$. Following steps analogous to the dipole case, we find:

$$\begin{aligned}\Delta V^{\mathrm{quad}}_{\nu\boldsymbol{q}}(\mathbf{r}) = \frac{e^2}{\Omega\varepsilon_0}\sum_{\kappa}M_\kappa^{-1/2}\sum_{\mathbf{G}\neq-\boldsymbol{q}}\frac{1}{2}\frac{(\boldsymbol{q}+\mathbf{G})\cdot(\mathbf{Q}_\kappa\mathbf{e}^{(\kappa)}_{\nu\boldsymbol{q}})\cdot(\boldsymbol{q}+\mathbf{G})}{(\boldsymbol{q}+\mathbf{G})\cdot\boldsymbol{\epsilon}\cdot(\boldsymbol{q}+\mathbf{G})}\\ \times e^{i(\boldsymbol{q}+\mathbf{G})\cdot(\mathbf{r}-\boldsymbol{\tau}_\kappa)}.\end{aligned} \tag{4.7}$$

The corresponding e-ph matrix elements due to the quadrupole perturbation potential are:

$$g^{\mathrm{quad}}_{mn\nu}(\boldsymbol{k},\boldsymbol{q}) = \frac{e^2}{\Omega\varepsilon_0}\sum_{\kappa}\left(\frac{\hbar}{2\omega_{\nu\boldsymbol{q}}M_\kappa}\right)^{\frac{1}{2}}\sum_{\mathbf{G}\neq-\boldsymbol{q}}\frac{1}{2}\frac{(\boldsymbol{q}+\boldsymbol{G})_\alpha(Q_{\kappa,\alpha\beta\gamma}\mathrm{e}^{(\kappa)}_{\nu\boldsymbol{q},\gamma})(\boldsymbol{q}+\boldsymbol{G})_\beta}{(\boldsymbol{q}+\boldsymbol{G})_\alpha\epsilon_{\alpha\beta}(\boldsymbol{q}+\boldsymbol{G})_\beta}\left\langle m\boldsymbol{k}+\boldsymbol{q}\right| e^{i(\boldsymbol{q}+\mathbf{G})\cdot(\mathbf{r}-\boldsymbol{\tau}_\kappa)}\left|n\boldsymbol{k}\right\rangle . \tag{4.8}$$

Note that in the $\boldsymbol{q}\to 0$ limit the Fröhlich e-ph matrix elements are of order $1/q$ and the quadrupole matrix elements of order q^0, thus approaching a constant value; both quantities are non-analytic as $\boldsymbol{q} \to 0$. Octopole and higher electronic responses in Eq. (4.1) lead to potentials that vanish as $\boldsymbol{q}\to 0$ and can be grouped together into a short-range e-ph interaction, commonly referred to as the "deformation potential" in analytic e-ph theories [18].

Interpolation scheme for e-ph interactions

The total e-ph matrix elements g (here we omit the band and mode indices) can be formed by adding together the short-range part g^{S} and the dipole and quadrupole interactions, which can be combined into a long-range part g^{L}. Therefore,

$$\begin{aligned} g &= g^{\mathrm{S}} + g^{\mathrm{L}} \\ &= g^{\mathrm{S}} + g^{\mathrm{dip}} + g^{\mathrm{quad}}. \end{aligned} \tag{4.9}$$

We start from a set of e-ph matrix elements $g(\boldsymbol{k}, \boldsymbol{q})$ computed with DFPT on a regular coarse grid of $\boldsymbol{k}$- and $\boldsymbol{q}$-points [15]. The short-range part is obtained by subtracting the long-range terms on the coarse grid, $g^{\mathrm{S}}(\boldsymbol{k}, \boldsymbol{q}) = g(\boldsymbol{k}, \boldsymbol{q}) - g^{\mathrm{dip}}(\boldsymbol{k}, \boldsymbol{q}) - g^{\mathrm{quad}}(\boldsymbol{k}, \boldsymbol{q})$. The short-range e-ph matrix elements decay rapidly in real space, and thus are ideal for interpolation using a localized basis set such as Wannier functions [28] or atomic orbitals [16]. After interpolating the short-ranged part [9] on fine $\boldsymbol{k}$- and $\boldsymbol{q}$-point grids, we add back the long-range dipole and quadrupole matrix elements, computed using Eqs. (4.5) and (4.8) directly at the fine-grid $\boldsymbol{k}$ and $\boldsymbol{q}$-points.

As DFPT accurately captures the long-range dipole and quadrupole e-ph interactions [15], the matrix elements obtained from DFPT can be used as a benchmark for the interpolated results. For this comparison, following Ref. [22] we compute the gauge-invariant e-ph coupling strength, $D^{\nu}_{\mathrm{tot}}(\boldsymbol{q})$, which is proportional to the absolute value of the e-ph matrix elements:

$$D^{\nu}_{\mathrm{tot}}(\boldsymbol{q}) = \sqrt{\frac{2\omega_{\nu\boldsymbol{q}} M_{\mathrm{uc}}}{\hbar^2} \sum_{mn} \frac{|g_{mn\nu}(\boldsymbol{k} = \Gamma, \boldsymbol{q})|^2}{N_b}}, \tag{4.10}$$

where M_{uc} is the mass of the unit cell and the band indices n and m run over the N_b bands selected for the analysis.

Computational details

We investigate the effect of the quadrupole e-ph interaction in silicon, a nonpolar semiconductor, and tetragonal $\mathrm{PbTiO_3}$, a polar piezoelectric material. Calculations on GaN are shown in the companion work [29]. The ground state and band structure are obtained using DFT in the local density approximation with a plane-wave basis using the Quantum ESPRESSO code [30]. Kinetic energy cutoffs of 40 Ry for silicon and 76 Ry for $\mathrm{PbTiO_3}$ are employed, together with scalar-relativistic norm-conserving pseudopotentials from Pseudo Dojo [31]. We have verified that spin-orbit coupling has a negligible effect. The calculations employ relaxed lattice constants of 10.102 bohr for silicon and 7.275 bohr (with aspect ratio $c/a = 1.046$)

for $PbTiO_3$. We use the dynamical quadrupole tensors computed in Ref. [21] [32]. The phonon dispersions and e-ph perturbation potentials on coarse $\boldsymbol{q}$-point grids are computed with DFPT [15]. We employ the Perturbo code [9] to compute the e-ph matrix elements on coarse Brillouin zone grids with $10 \times 10 \times 10$ $\boldsymbol{k}$- and $\boldsymbol{q}$-points for silicon and $8 \times 8 \times 8$ $\boldsymbol{k}$- and $\boldsymbol{q}$-points for $PbTiO_3$. The Wannier functions are computed with the Wannier90 code [28] and employed in Perturbo [9] to interpolate the short-range e-ph matrix elements.

We compute the scattering rates and electron mobility using the Perturbo code [9]. Briefly, the band- and $\boldsymbol{k}$- dependent e-ph scattering rate $\Gamma_{n\boldsymbol{k}}$ is obtained as

$$\begin{aligned}\Gamma_{n\boldsymbol{k}} =& \frac{2\pi}{\hbar} \sum_{m\nu\boldsymbol{q}} |g_{mn\nu}(\boldsymbol{k},\boldsymbol{q})|^2 \\ & [(N_{\nu\boldsymbol{q}} + 1 - f_{m\mathbf{k+q}})\delta(\varepsilon_{n\boldsymbol{k}} - \varepsilon_{m\mathbf{k+q}} - \hbar\omega_{\nu\boldsymbol{q}}) \\ & + (N_{\nu\boldsymbol{q}} + f_{m\mathbf{k+q}})\delta(\varepsilon_{n\boldsymbol{k}} - \varepsilon_{m\mathbf{k+q}} + \hbar\omega_{\nu\boldsymbol{q}})],\end{aligned} \tag{4.11}$$

where $\varepsilon_{n\boldsymbol{k}}$ and $\hbar\omega_{\nu\boldsymbol{q}}$ are the electron and phonon energies, respectively, and $f_{n\boldsymbol{k}}$ and $N_{\nu\boldsymbol{q}}$ the corresponding temperature-dependent occupations. The scattering rate can be further divided into the long-range part [4], $\Gamma^L_{n\boldsymbol{k}}$, by replacing $|g|^2$ in Eq. (4.11) with $\left|g^{\mathrm{L}}\right|^2$. The carrier mobility is computed using $\mu = \sigma/(n_c e)$, where σ is the electrical conductivity and n_c is the carrier concentration. The electrical conductivity σ is computed within the relaxation time approximation of the Boltzmann transport equation [9, 33]:

$$\sigma_{\alpha\beta} = e^2 \int_{-\infty}^{+\infty} dE(-\partial f/\partial E)\Sigma_{\alpha\beta}(E,T), \tag{4.12}$$

where $\Sigma_{\alpha\beta}(E,T)$ is the transport distribution function at energy E,

$$\Sigma_{\alpha\beta}(E,T) = \frac{s}{\mathcal{N}_{\boldsymbol{k}}\Omega} \sum_{n\boldsymbol{k}} \tau_{n\boldsymbol{k}}(T) v^{\alpha}_{n\boldsymbol{k}} v^{\beta}_{n\boldsymbol{k}} \delta(E - \varepsilon_{n\boldsymbol{k}}), \tag{4.13}$$

which is computed in Perturbo using the tetrahedron integration method [34]. Above, s is the spin degeneracy, $\mathcal{N}_{\boldsymbol{k}}$ is the number of $\boldsymbol{k}$-points, $v_{n\boldsymbol{k}}$ is the band velocity, and $\tau_{n\boldsymbol{k}} = (\Gamma_{n\boldsymbol{k}})^{-1}$ is the relaxation time. The mobility is computed with non-degenerate electron concentrations of 10^{15} cm^{-3} for silicon and 10^{17} cm^{-3} for $PbTiO_3$. To fully converge the scattering rates and mobility, we use e-ph matrix elements evaluated on fine Brillouin zone grids with $200 \times 200 \times 200$ $\boldsymbol{k}$-points and 8×10^6 random $\boldsymbol{q}$-points [1].

---

[1] Uniform grids and random sampling can both be used to converge the scattering rate as long as a sufficiently large number of $\boldsymbol{q}$-points is employed. In our experience, random sampling, which

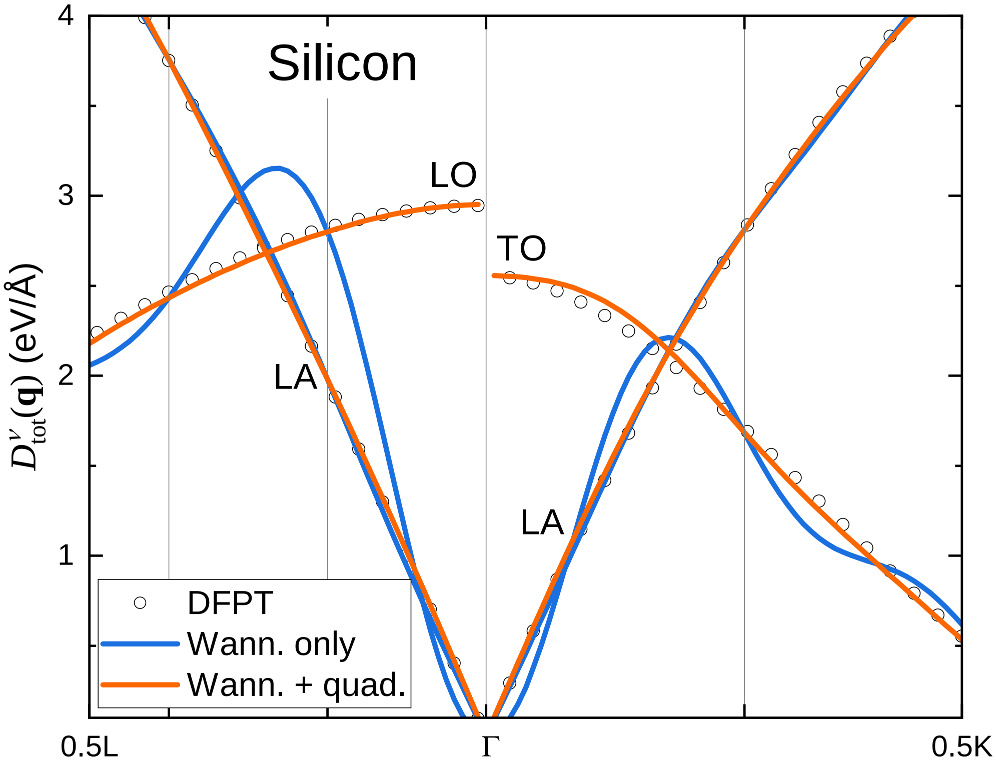

Figure 4.2: Mode-resolved e-ph coupling strength [see Eq. (4.10)] in silicon, computed using the lowest valence band. The electron momentum $\boldsymbol{k}$ is fixed at the Γ point and the phonon wave-vector $\boldsymbol{q}$ is varied along high-symmetry lines in the Brillouin zone. Benchmark results from DFPT (black circles) are compared with Wannier interpolation with the quadrupole e-ph interaction included (orange line) or neglected (blue line). The coarse-grid $\boldsymbol{q}$-points are indicated with vertical lines.

4.3 Results

Quadrupole effect on the e-ph matrix elements

The long-range quadrupole e-ph interaction is present in a wide range of semiconductors and insulators, where the atomic dynamical quadrupoles are in general non-zero. We illustrate this point by studying silicon, a simple nonpolar semiconductor in which the Born charges — and thus the Fröhlich interaction — vanish and the presence of long-range interactions is not immediately obvious. Figure 4.2 shows the e-ph coupling strength, $D^{\nu}_{\text{tot}}(\boldsymbol{q})$ in Eq. (4.10), computed directly using DFPT as a benchmark and compared with Wannier interpolation with and without

---

corresponds to Monte Carlo integration, usually leads to slightly faster convergence than uniform grids. It also has the advantage that one can systematically improve the convergence by running additional calculations, thus improving the sampling. For comparison, checking convergence with uniform grids requires using increasingly denser uniform meshes, which is computationally more expensive and inconvenient.

inclusion of the quadrupole term. The DFPT benchmark e-ph matrix elements for optical modes approach a constant value as $\boldsymbol{q} \rightarrow 0$, as we show for the LO mode in the $\Gamma - L$ direction and the transverse optical (TO) mode along $\Gamma - K$. This trend is distinctive of the quadrupole e-ph interaction, which is of order q^0 in the long-wavelength limit.

If the quadrupole term is neglected and all e-ph interactions are treated as short-ranged, the e-ph matrix elements for optical modes in silicon incorrectly vanish as $\boldsymbol{q} \rightarrow 0$. The interpolated values for optical modes are underestimated between the Γ point, where the error is greatest, and its nearest-neighbor $\boldsymbol{q}$-points in the coarse grid, where the error vanishes. Outside this $\boldsymbol{q}$-point region close to Γ, the interpolated matrix elements without the quadrupole interaction still deviate from the DFPT result, although the error is smaller than near Γ. When the quadrupole term is included, the long-range e-ph interactions for the optical modes are captured correctly, as can be seen for the Wannier plus quadrupole curves in Fig. 4.2. The root-mean-square deviation of $D^{\nu}_{\text{tot}}(\boldsymbol{q})$ from DFPT, for the optical branches shown in Fig. 4.2, is 0.78 eV/Å when the quadrupole term is neglected versus 0.03 eV/Å when the quadrupole term is included in the interpolation. This result highlights the importance of the quadrupole term to correctly capture long-range e-ph interactions in nonpolar semiconductors.

Observe also how for acoustic modes in silicon the quadrupole term has a nearly negligible effect, as we show for the longitudinal acoustic (LA) mode in Fig. 4.2. As contracting the dynamical quadrupoles $\mathbf{Q}_{\kappa}$ with a rigid shift of the lattice leads to a vanishing quadrupole contribution [18], one can obtain the quadrupole acoustic sum rule $\sum_{\alpha} Q_{\kappa,\alpha\beta\gamma} = 0$ for nonpolar materials [18]. This sum rule, which is satisfied by the dynamical quadrupole values we employ for silicon [21], leads to a negligible quadrupole correction for acoustic modes in the long-wavelength limit. Though we focus on silicon in this work, on the basis of our results we expect sizable quadrupole contributions for optical modes, and negligible for acoustic modes, in all nonpolar semiconductors.

The quadrupole e-ph interaction is particularly critical in piezoelectric materials, as discussed here for tetragonal PbTiO_3, a prototypical piezoelectric insulator. Piezoelectric materials are polar noncentrosymmetric systems with non-zero Born charges. As a result, the dipole Fröhlich interaction is dominant for LO modes near $\boldsymbol{q} \rightarrow 0$ due to its $1/q$ divergence. The quadrupole contribution is expected to be important for TO and acoustic modes (the quadrupole acoustic sum rule does not hold for polar noncentrosymmetric crystals).

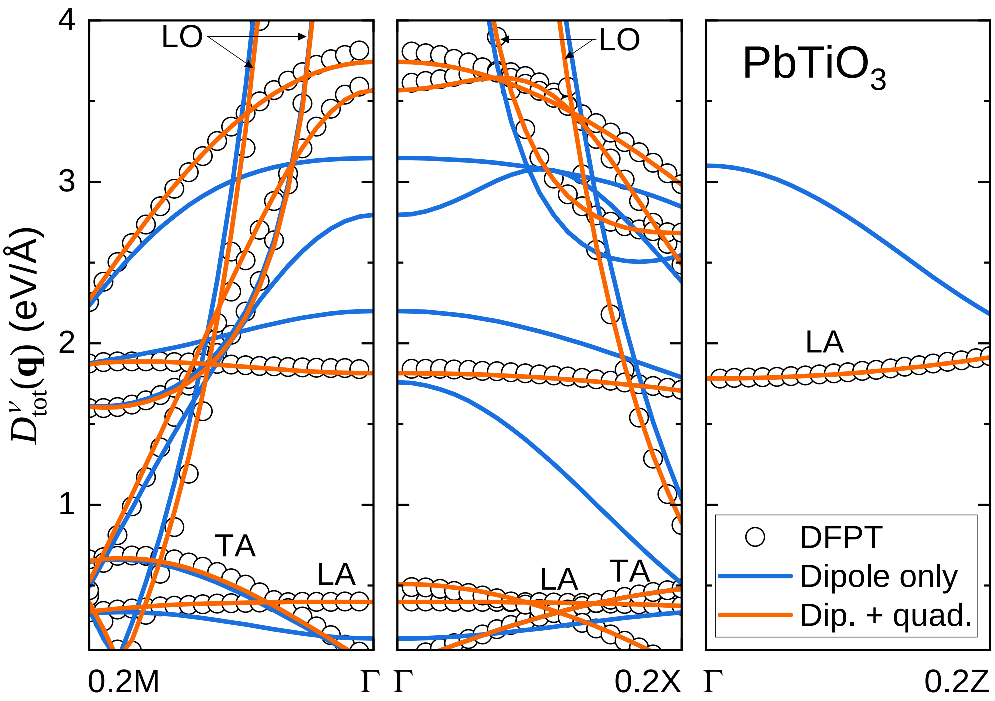

Figure 4.3: Mode-resolved e-ph coupling strength [see Eq. (4.10)] in tetragonal PbTiO$_3$, computed using the lowest conduction band. The initial electron momentum is fixed at the Γ point and the phonon wave-vector $\boldsymbol{q}$ is varied along high-symmetry lines in the Brillouin zone. Benchmark results from DFPT (black circles) are compared with Wannier interpolation plus the Fröhlich interaction (blue line) and Wannier interpolation plus the Fröhlich and quadrupole interactions (orange line). Note that two LO branches with coupling strength exceeding the y-axis limit are not shown.

Figure 4.3 shows the e-ph coupling strength, $D^{\nu}_{\text{tot}}(\boldsymbol{q})$ in Eq. (4.10), for the DFPT benchmark in tetragonal PbTiO$_3$, and compares it with interpolated results that include only the Fröhlich dipole interaction or both the Fröhlich and the quadrupole interactions. The short-range interactions are included through Wannier interpolation in both cases. When only the Fröhlich dipole interaction is included, the e-ph matrix elements deviate dramatically from the DFPT results. The values are either overestimated or underestimated depending on the phonon mode considered, with deviations from DFPT that depend strongly on the direction in which $\boldsymbol{q}$ approaches Γ due to the non-analytic character of the long-range e-ph interactions. When the quadrupole e-ph interaction is taken into account, the interpolated e-ph coupling strength matches the DFPT result very accurately for *all* phonon modes. For LO modes, the quadrupole correction is moderate due to the dominant Fröhlich term near $\boldsymbol{q} = 0$. For other optical and acoustic modes with a finite e-ph coupling at

$\boldsymbol{q} = 0$, the quadrupole term removes the large error in the dipole-only results (up to an order of magnitude) and gives e-ph matrix elements in nearly exact agreement with DFPT. For the branches shown in Fig. 4.3, the root-mean-square deviation of $D^{\nu}_{\mathrm{tot}}(\boldsymbol{q})$ from DFPT is 0.46 eV/Å for dipole-only results versus 0.03 eV/Å for our dipole plus quadrupole interpolation scheme. It is clear that the quadrupole term is essential in piezoelectric materials for all phonon modes.

Contrary to silicon and nonpolar materials, the quadrupole term has a large effect for acoustic modes in piezoelectric materials, where it is one of the two contributions to the so-called piezoelectric e-ph interaction [24]. Expanding the phonon eigenvectors at $\boldsymbol{q} \to 0$ as $\mathbf{e}_{\nu\boldsymbol{q}} \approx \mathbf{e}^{(0)}_{\nu\boldsymbol{q}} + i\mathbf{q} \cdot \mathbf{e}^{(1)}_{\nu\boldsymbol{q}}$, one finds two contributions of order q^0 [18]. One is from the Born charges, $\mathbf{Z}_{\kappa}\mathbf{e}^{(1)}_{\nu\boldsymbol{q}}$, and is a dipole-like interaction generated by atoms with a net charge experiencing different displacements due to strain from an acoustic mode. The other is from the dynamical quadrupoles, $\mathbf{Q}_{\kappa}\mathbf{e}^{(0)}_{\nu\boldsymbol{q}}$, and is associated with a clamped-ion electronic polarization [35]. The *ab initio* Fröhlich interaction includes only the former term, namely the strain component of the piezoelectric e-ph interaction, and thus the dipole-only scheme leads to large errors for acoustic phonons in $\mathrm{PbTiO_3}$ (see Fig. 4.3) as it neglects the important electronic quadrupole contribution. Until now, the *ab initio* Fröhlich term has been mistakenly thought to fully capture piezoelectric e-ph interactions. Our results demonstrate that both dipole and quadrupole terms are essential for accurate acoustic mode e-ph interactions in piezoelectric materials [36]. The relative magnitude of the strain and quadrupole contributions is material dependent; the two terms can nearly cancel each other out, as we have shown elsewhere for GaN [29], or their ratio can be mode and phonon wave-vector dependent, as we find in $\mathrm{PbTiO_3}$.

Quadrupole contribution to the scattering rate

Because the quadrupole interaction has a significant effect on the e-ph matrix elements, we expect that it also plays a role in calculations of the e-ph scattering rate and mobility. Figure 4.4(a) shows both the quadrupole contribution and the total e-ph scattering rate in silicon at 300 K for electron energies near the conduction band minimum. We find that the quadrupole contribution to the scattering rate is about 1% of the total scattering rate at temperatures between 100−400 K. At electron energies below the optical phonon emission threshold in silicon ($\hbar\omega_{\mathrm{O}} \approx 65$ meV relative to the conduction band minimum), absorption and emission of acoustic phonons dominate the scattering processes, and thus we find a small correction due

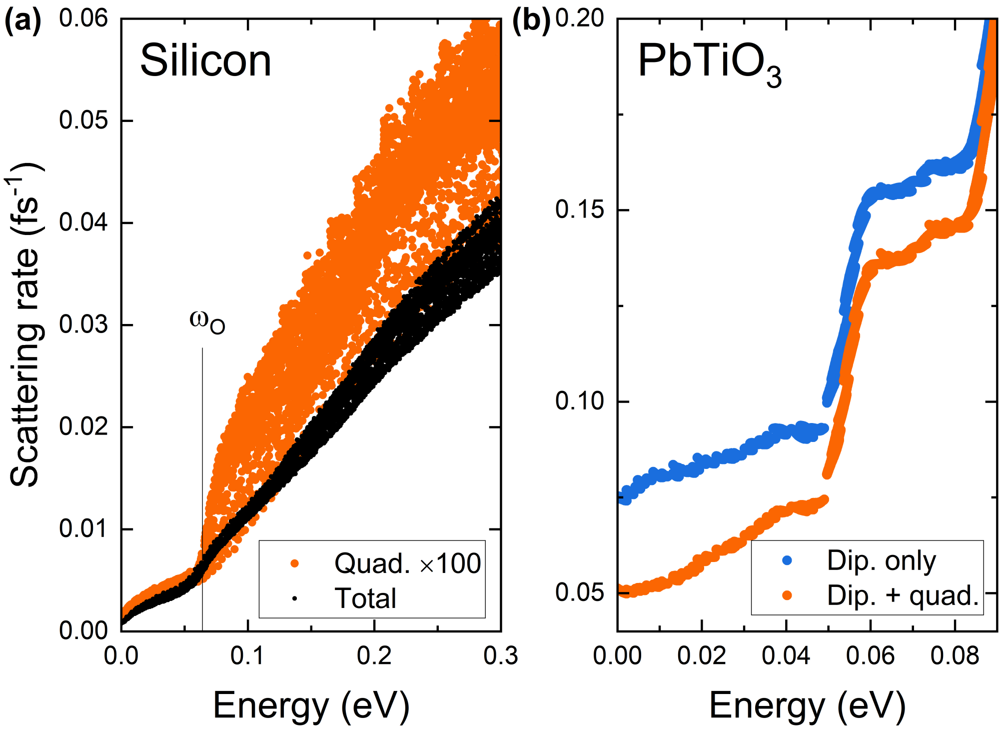

Figure 4.4: Room temperature scattering rate versus electron energy (referenced to the conduction band minimum) in (a) silicon and (b) PbTiO$_3$. For silicon, we plot the quadrupole contribution multiplied by 100 (orange) and the total scattering rate (black), which includes the short-range and the quadrupole contributions. For PbTiO$_3$, we show the long-range scattering rate computed using only the Fröhlich interaction (blue) or both the Fröhlich and quadrupole interactions (orange).

to the quadrupole interaction, which minimally affects acoustic modes in silicon. Since the quadrupole acoustic sum rule holds only in the long wavelength limit, the quadrupole interaction can still contribute to finite-$\boldsymbol{q}$ acoustic scattering, as is shown by the fact that the quadrupole scattering rate at energy below $\hbar\omega_{\mathrm{O}}$ is proportional to the total scattering rate. The quadrupole contribution increases sharply above the optical emission threshold because the quadrupole term is greater for optical modes in silicon. For the same reason, the relative contribution of the quadrupole term increases slightly with temperature in the 100−400 K range, varying from 1% of the total scattering rate at 100 K to 1.5% at 400 K.

The effect of the quadrupole interaction on the scattering rates is greater in PbTiO$_3$. Our analysis focuses on the e-ph scattering rate due to the long-range e-ph interactions, although similar conclusions hold for the total scattering rate. Figure 4.4(b) shows the long-range e-ph scattering rate in PbTiO$_3$ at 300 K as a function of electron energy, comparing results that include only the dipole Fröhlich interaction with results from our approach including both the dipole and quadrupole terms. The scattering rate from the long-range e-ph interactions is lower at all energies when the quadrupole term is taken into account. The difference is greatest near the band edge, where the scattering rate due to the dipole interaction alone is 0.075 fs^{-1} versus a 50% smaller value of 0.050 fs^{-1} for dipole plus quadrupole.

These trends can be understood on the basis of the e-ph matrix element analysis in Fig. 4.3. The errors found when neglecting the quadrupole term in $D^{\nu}_{\mathrm{tot}}(\boldsymbol{q})$, which is proportional to the absolute value of the matrix elements [see Eq. (4.10)], are amplified in calculations of the scattering rate, which is proportional to the square of the matrix elements. The largest errors we find for $D^{\nu}_{\mathrm{tot}}(\boldsymbol{q})$ are in the $\boldsymbol{q} \to 0$ limit, especially for the acoustic modes. For example, for the LA mode in the $\Gamma - M$ and $\Gamma - X$ directions, the value of $D^{\nu}_{\mathrm{tot}}(\boldsymbol{q})$ from the dipole-only calculation is 0.17 eV/Å compared to a twice-greater value of 0.40 eV/Å when the quadrupole term is included. This leads to a four-fold increase of the LA mode scattering rate upon including the quadrupole interaction. Opposite to the silicon case, in $\mathrm{PbTiO_3}$ the relative magnitude of the quadrupole correction is greater at lower temperatures because the quadrupole interaction is stronger for acoustic modes. Near the band edge, we find quadrupole corrections to the long-range scattering rate ranging from 97% at 100 K to 38% at 400 K. Given that low-energy electronic states near the band edge govern transport properties, including the quadrupole term is critical to accurately computing electronic transport.

Quadrupole contribution to the mobility

The effect of the quadrupole e-ph interaction on the mobility is noteworthy. Figure 4.5(a) shows the temperature dependent electron mobility in silicon computed with and without the quadrupole term. Including the quadrupole interaction reduces the computed mobility by approximately 5−10% due to the increased e-ph coupling strength and scattering rates. For example, the computed mobility at 300 K is 1390 cm^2/Vs when including the quadrupole interaction versus a value of 1473 cm^2/Vs with the conventional interpolation approach in which all e-ph interactions in silicon are treated as short-ranged. This discrepancy is due to the underestimation of the e-ph coupling strength for optical modes in the conventional approach, especially at small values of $\boldsymbol{q}$ as shown in Fig. 4.2.

In silicon, e-ph scattering mediates both intravalley and intervalley processes. The quadrupole interaction affects mainly small-$\boldsymbol{q}$ intravalley processes associated with

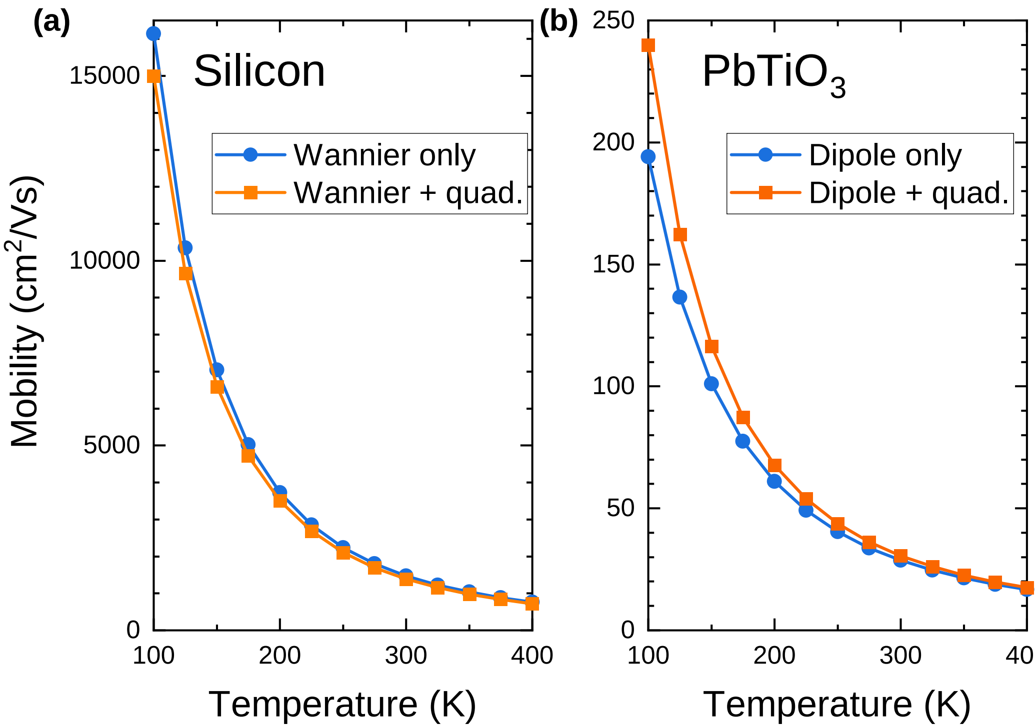

Figure 4.5: Computed temperature-dependent electron mobility in (a) silicon and (b) tetragonal $PbTiO_3$. The plot compares the mobility obtained when the quadrupole e-ph interaction is included (orange squares) or neglected (blue circles). The $PbTiO_3$ results are for transport in the basal xy plane.

optical phonons. However, intravalley processes — particularly those associated with acoustic phonons — are dominant only at low temperature, while at higher temperatures intervalley processes mediated by large-$\boldsymbol{q}$ phonons are dominant [37]. As a result, the intravalley optical phonon scattering processes mediated by the quadrupole interaction are active mainly at low temperature and are overall weaker than other scattering contributions in silicon, including acoustic intravalley scattering at low temperature. The contribution of the quadrupole correction to the mobility is thus maximal at low temperature and overall relatively small.

Although we focus on silicon, we expect that these trends apply in general to nonpolar semiconductors because small-$\boldsymbol{q}$ optical e-ph coupling will consistently be underestimated without the quadrupole term. The long-range quadrupole e-ph interaction is thus surprisingly manifest in the transport properties of nonpolar materials.

We find an opposite trend in $PbTiO_3$, in which including the quadrupole interaction increases the mobility by 10–25% between 100–400 K, as seen in Fig. 4.5(b). The quadrupole term gives a larger correction at lower temperatures, reaching values up to ~25% at 100 K. This result is due to the dominant acoustic mode contribution at low temperatures together with the large quadrupole correction for acoustic modes in piezoelectric materials. At higher temperatures, where optical mode scattering is dominant and acoustic scattering less important, the quadrupole contribution is smaller, only about 10% at 400 K. Due to differences in the quadrupole interaction for different phonon modes and to varying mode contributions to the mobility as a function of temperature, including the quadrupole term corrects the temperature dependence of the mobility [29] and is essential in piezoelectric materials.

4.4 Discussion

We briefly discuss a technical aspect of the e-ph matrix element interpolation. The treatment of long-wavelength perturbations with wave-vector $\boldsymbol{q} \to 0$ in DFPT is critical in semiconductors and insulators [16, 38]. The lattice-periodic part of the phonon perturbation potential, $\Delta v_{\boldsymbol{q}}(\mathbf{r})$, is the sum of a Coulomb and an exchange-correlation contribution,

$$\Delta v_{\boldsymbol{q}}(\mathbf{r}) = \Delta v_{\boldsymbol{q},C}(\mathbf{r}) + \Delta v_{\boldsymbol{q},XC}(\mathbf{r}). \tag{4.14}$$

The Coulomb contribution $\Delta v_{\boldsymbol{q},C}(\mathbf{r})$ combines the variation of the Hartree and electron-nuclei interactions. Its integral over the unit cell [38],

$$\Delta(\boldsymbol{q}) = \frac{1}{\Omega}\int_{\Omega} d\mathbf{r}\; v_{\boldsymbol{q},C}(\mathbf{r}), \tag{4.15}$$

is well-behaved for insulators (and semiconductors) at finite $\boldsymbol{q}$ values, but is ill-defined at $\boldsymbol{q} = 0$. First-principles codes such as Quantum ESPRESSO [30] subtract $\Delta(\boldsymbol{q})$ from the perturbation potential at $\boldsymbol{q}=0$, thus making it discontinuous at $\boldsymbol{q} = 0$. Therefore, due to both the discontinuity at $\boldsymbol{q} = 0$ and the non-analytic behavior near $\boldsymbol{q} = 0$, the e-ph matrix elements are challenging to interpolate in the long-wavelength limit.

In our scheme, we identify the quadrupole interaction as the key long-range term in nonpolar materials, and remove the non-analytic behavior near $\boldsymbol{q} = 0$ on the coarse grid by subtracting the quadrupole term. This strategy improves the interpolation near $\boldsymbol{q} = 0$ in nonpolar materials, at once capturing the correct physics and smoothing the coarse-grid matrix element to be interpolated. Due to the non-analytic behavior, denser DFPT grids cannot fully remove the interpolation error if the quadrupole term is not subtracted on the coarse grid. For polar materials such as $PbTiO_3$, the non-analytic behavior is due to both the dipole (Fröhlich) and quadrupole long-range e-ph interactions. By subtracting both terms in our scheme in polar materials, the coarse-grid matrix elements to be interpolated are made smooth and the interpolation approach more reliable. The non-analytic behavior of the Coulomb potential is correctly reconstructed by adding back the dipole (in polar materials) and quadrupole (in all insulators) contributions after interpolation.

4.5 Conclusion

In summary, we developed an accurate approach for computing the quadrupole e-ph interaction from first principles. This advance resolves the outstanding problem of correctly quantifying long-range e-ph interactions for all phonon modes in semiconductors and insulators. Our results clearly show that the quadrupole interactions are crucial for obtaining accurate e-ph matrix elements, scattering rates and electronic transport properties. The quadrupole effect is particularly apparent in piezoelectric materials such as wurtzite GaN [29] and $PbTiO_3$, in which neglecting the quadrupole interaction leads to large and uncontrolled errors. The method introduced in this work enables accurate calculations of electrical transport, thermoelectric properties, and superconductivity in a wide range of materials.

Note added. Recently, we became aware of a related work by another group that reaches similar conclusions about the importance of the dynamical quadrupole term to obtain an accurate physical description of e-ph interactions [39, 40].

References

[1] J. M. Ziman. *Electrons and Phonons: The Theory of Transport Phenomena in Solids*. Oxford University Press, 2001. ISBN 978-0-19-850779-6.

[2] Marco Bernardi. First-principles dynamics of electrons and phonons. *Eur. Phys. J. B*, 89(11):239, 2016. ISSN 1434-6036. doi: 10.1140/epjb/e2016-70399-4.

[3] Marco Bernardi, Derek Vigil-Fowler, Johannes Lischner, Jeffrey B. Neaton, and Steven G. Louie. Ab Initio Study of Hot Carriers in the First Picosecond after Sunlight Absorption in Silicon. *Phys. Rev. Lett.*, 112(25):257402, 2014. doi: 10.1103/PhysRevLett.112.257402.

[4] Jin-Jian Zhou and Marco Bernardi. Ab initio electron mobility and polar phonon scattering in GaAs. *Phys. Rev. B*, 94(20):201201(R), 2016. doi: 10.1103/PhysRevB.94.201201.

[5] Vatsal A. Jhalani, Jin-Jian Zhou, and Marco Bernardi. Ultrafast Hot Carrier Dynamics in GaN and Its Impact on the Efficiency Droop. *Nano Lett.*, 17(8): 5012–5019, 2017. ISSN 1530-6984. doi: 10.1021/acs.nanolett.7b02212.

[6] Nien-En Lee, Jin-Jian Zhou, Luis A. Agapito, and Marco Bernardi. Charge transport in organic molecular semiconductors from first principles: The bandlike hole mobility in a naphthalene crystal. *Phys. Rev. B*, 97(11):115203, 2018. doi: 10.1103/PhysRevB.97.115203.

[7] Jin-Jian Zhou, Olle Hellman, and Marco Bernardi. Electron-Phonon Scattering in the Presence of Soft Modes and Electron Mobility in $SrTiO_3$ Perovskite from First Principles. *Phys. Rev. Lett.*, 121(22):226603, 2018. doi: 10.1103/PhysRevLett.121.226603.

[8] Jin-Jian Zhou and Marco Bernardi. Predicting charge transport in the presence of polarons: The beyond-quasiparticle regime in $SrTiO_3$. *Phys. Rev. Res.*, 1 (3):033138, 2019. doi: 10.1103/PhysRevResearch.1.033138.

[9] Jin-Jian Zhou, Jinsoo Park, I.-Te Lu, Ivan Maliyov, Xiao Tong, and Marco Bernardi. Perturbo: A software package for ab initio electron-phonon interactions, charge transport and ultrafast dynamics.

[10] Wu Li. Electrical transport limited by electron-phonon coupling from Boltzmann transport equation: An ab initio study of Si, Al, and MoS_2. *Phys. Rev. B*, 92(7):075405, 2015. doi: 10.1103/PhysRevB.92.075405.

[11] Te-Huan Liu, Jiawei Zhou, Bolin Liao, David J. Singh, and Gang Chen. First-principles mode-by-mode analysis for electron-phonon scattering channels and mean free path spectra in GaAs. *Phys. Rev. B*, 95(7):075206, 2017. ISSN 2469-9950, 2469-9969. doi: 10.1103/PhysRevB.95.075206.

[12] Jinlong Ma, Arun S. Nissimagoudar, and Wu Li. First-principles study of electron and hole mobilities of Si and GaAs. *Phys. Rev. B*, 97(4):045201, 2018. ISSN 2469-9950, 2469-9969. doi: 10.1103/PhysRevB.97.045201.

[13] Thibault Sohier, Davide Campi, Nicola Marzari, and Marco Gibertini. Mobility of two-dimensional materials from first principles in an accurate and automated framework. *Phys. Rev. Mater.*, 2(11):114010, 2018. ISSN 2475-9953. doi: 10.1103/PhysRevMaterials.2.114010.

[14] Richard M. Martin. *Electronic Structure: Basic Theory and Practical Methods*. Cambridge University Press, Cambridge, UK ; New York, 2004. ISBN 978-0-521-78285-2.

[15] Stefano Baroni, Stefano de Gironcoli, Andrea Dal Corso, and Paolo Giannozzi. Phonons and related crystal properties from density-functional perturbation theory. *Rev. Mod. Phys.*, 73(2):515–562, 2001. doi: 10.1103/RevModPhys.73.515.

[16] Luis A. Agapito and Marco Bernardi. Ab initio electron-phonon interactions using atomic orbital wave functions. *Phys. Rev. B*, 97(23):235146, 2018. doi: 10.1103/PhysRevB.97.235146.

[17] P. Lawaetz. Long-wavelength phonon scattering in nonpolar semiconductors. *Phys. Rev.*, 183:730–739, 1969. doi: 10.1103/PhysRev.183.730. URL `https://link.aps.org/doi/10.1103/PhysRev.183.730`.

[18] P. Vogl. Microscopic theory of electron-phonon interaction in insulators or semiconductors. *Phys. Rev. B*, 13(2):694–704, 1976. doi: 10.1103/PhysRevB.13.694.

[19] Massimiliano Stengel. Flexoelectricity from density-functional perturbation theory. *Phys. Rev. B*, 88:174106, 2013. doi: 10.1103/PhysRevB.88.174106. URL `https://link.aps.org/doi/10.1103/PhysRevB.88.174106`.

[20] Cyrus E. Dreyer, Massimiliano Stengel, and David Vanderbilt. Current-density implementation for calculating flexoelectric coefficients. *Phys. Rev. B*, 98: 075153, 2018. doi: 10.1103/PhysRevB.98.075153. URL `https://link.aps.org/doi/10.1103/PhysRevB.98.075153`.

[21] Miquel Royo and Massimiliano Stengel. First-principles theory of spatial dispersion: Dynamical quadrupoles and flexoelectricity. *Phys. Rev. X*, 9: 021050, 2019. doi: 10.1103/PhysRevX.9.021050. URL `https://link.aps.org/doi/10.1103/PhysRevX.9.021050`.

[22] J. Sjakste, N. Vast, M. Calandra, and F. Mauri. Wannier interpolation of the electron-phonon matrix elements in polar semiconductors: Polar-optical coupling in GaAs. *Phys. Rev. B*, 92(5):054307, 2015. doi: 10.1103/PhysRevB.92.054307.

[23] Carla Verdi and Feliciano Giustino. Fröhlich Electron-Phonon Vertex from First Principles. *Phys. Rev. Lett.*, 115(17):176401, 2015. doi: 10.1103/PhysRevLett.115.176401.

[24] Gerald D. Mahan. *Condensed Matter in a Nutshell.* Princeton University Press, 2011. ISBN 978-0-691-14016-2.

[25] H. Fröhlich. Electrons in lattice fields. *Advances in Physics*, 3(11):325–361, 1954. ISSN 0001-8732, 1460-6976. doi: 10.1080/00018735400101213.

[26] Max Born and Kun Huang. *Dynamical Theory of Crystal Lattices.* Oxford University Press, Oxford, 1954.

[27] David J Griffiths. *Introduction to Electrodynamics.* Cambridge University Press, 2017.

[28] Giovanni Pizzi, Valerio Vitale, Ryotaro Arita, Stefan Blügel, Frank Freimuth, Guillaume Géranton, Marco Gibertini, Dominik Gresch, Charles Johnson, Takashi Koretsune, Julen Ibañez-Azpiroz, Hyungjun Lee, Jae-Mo Lihm, Daniel Marchand, Antimo Marrazzo, Yuriy Mokrousov, Jamal I. Mustafa, Yoshiro Nohara, Yusuke Nomura, Lorenzo Paulatto, Samuel Poncé, Thomas Ponweiser, Junfeng Qiao, Florian Thöle, Stepan S. Tsirkin, Ma\lgorzata Wierzbowska, Nicola Marzari, David Vanderbilt, Ivo Souza, Arash A. Mostofi, and Jonathan R. Yates. Wannier90 as a community code: New features and applications. *J. Phys.: Condens. Matter*, 32(16):165902, 2020. ISSN 0953-8984. doi: 10.1088/1361-648X/ab51ff.

[29] Vatsal A. Jhalani, Jin-Jian Zhou, Jinsoo Park, Cyrus E. Dreyer, and Marco Bernardi. Piezoelectric electron-phonon interaction from ab initio dynamical quadrupoles: Impact on charge transport in wurtzite GaN. *Phys. Rev. Lett.*, 125(13):136602, 2020. doi: 10.1103/PhysRevLett.125.136602.

[30] Paolo Giannozzi, Stefano Baroni, Nicola Bonini, Matteo Calandra, Roberto Car, Carlo Cavazzoni, Davide Ceresoli, Guido L. Chiarotti, Matteo Cococcioni, Ismaila Dabo, Andrea Dal Corso, Stefano de Gironcoli, Stefano Fabris, Guido Fratesi, Ralph Gebauer, Uwe Gerstmann, Christos Gougoussis, Anton Kokalj, Michele Lazzeri, Layla Martin-Samos, Nicola Marzari, Francesco Mauri, Riccardo Mazzarello, Stefano Paolini, Alfredo Pasquarello, Lorenzo Paulatto, Carlo Sbraccia, Sandro Scandolo, Gabriele Sclauzero, Ari P. Seitsonen, Alexander Smogunov, Paolo Umari, and Renata M. Wentzcovitch. QUANTUM ESPRESSO: A modular and open-source software project for quantum simulations of materials. *J. Phys.: Condens. Matter*, 21(39):395502, 2009. ISSN 0953-8984. doi: 10.1088/0953-8984/21/39/395502.

[31] M. J. van Setten, M. Giantomassi, E. Bousquet, M. J. Verstraete, D. R. Hamann, X. Gonze, and G. M. Rignanese. The PseudoDojo: Training and grading a 85 element optimized norm-conserving pseudopotential table. *Comput. Phys.*

Commun., 226:39–54, 2018. ISSN 0010-4655. doi: 10.1016/j.cpc.2018.01.012.

[32] Xavier Gonze, Bernard Amadon, Gabriel Antonius, Frédéric Arnardi, Lucas Baguet, Jean-Michel Beuken, Jordan Bieder, François Bottin, Johann Bouchet, Eric Bousquet, Nils Brouwer, Fabien Bruneval, Guillaume Brunin, Théo Cavignac, Jean-Baptiste Charraud, Wei Chen, Michel Côté, Stefaan Cottenier, Jules Denier, Grégory Geneste, Philippe Ghosez, Matteo Giantomassi, Yannick Gillet, Olivier Gingras, Donald R. Hamann, Geoffroy Hautier, Xu He, Nicole Helbig, Natalie Holzwarth, Yongchao Jia, François Jollet, William Lafargue-Dit-Hauret, Kurt Lejaeghere, Miguel A. L. Marques, Alexandre Martin, Cyril Martins, Henrique P. C. Miranda, Francesco Naccarato, Kristin Persson, Guido Petretto, Valentin Planes, Yann Pouillon, Sergei Prokhorenko, Fabio Ricci, Gian-Marco Rignanese, Aldo H. Romero, Michael Marcus Schmitt, Marc Torrent, Michiel J. van Setten, Benoit Van Troeye, Matthieu J. Verstraete, Gilles Zérah, and Josef W. Zwanziger. The Abinitproject: Impact, environment and recent developments. *Computer Physics Communications*, 248:107042, 2020. ISSN 0010-4655. doi: 10.1016/j.cpc.2019.107042.

[33] Gerald D. Mahan. *Many-Particle Physics*. Springer US, 3 edition, 2000. ISBN 978-0-306-46338-9. doi: 10.1007/978-1-4757-5714-9.

[34] Peter E. Blöchl, O. Jepsen, and O. K. Andersen. Improved tetrahedron method for Brillouin-zone integrations. *Phys. Rev. B*, 49(23):16223–16233, 1994. doi: 10.1103/PhysRevB.49.16223.

[35] Fabio Bernardini, Vincenzo Fiorentini, and David Vanderbilt. Spontaneous polarization and piezoelectric constants of iii-v nitrides. *Phys. Rev. B*, 56: R10024–R10027, 1997. doi: 10.1103/PhysRevB.56.R10024. URL `https://link.aps.org/doi/10.1103/PhysRevB.56.R10024`.

[36] Gotthard Sághi-Szabó, Ronald E. Cohen, and Henry Krakauer. First-Principles Study of Piezoelectricity in PbTiO 3. *Phys. Rev. Lett.*, 80(19):4321–4324, 1998. ISSN 0031-9007, 1079-7114. doi: 10.1103/PhysRevLett.80.4321.

[37] Jinsoo Park, Jin-Jian Zhou, and Marco Bernardi. Spin-phonon relaxation times in centrosymmetric materials from first principles. *Phys. Rev. B*, 101(4): 045202, 2020. ISSN 2469-9950, 2469-9969. doi: 10.1103/PhysRevB.101.045202.

[38] Matteo Calandra, Gianni Profeta, and Francesco Mauri. Adiabatic and nonadiabatic phonon dispersion in a Wannier function approach. *Phys. Rev. B*, 82 (16):165111, 2010. doi: 10.1103/PhysRevB.82.165111.

[39] Guillaume Brunin, Henrique Pereira Coutada Miranda, Matteo Giantomassi, Miquel Royo, Massimiliano Stengel, Matthieu J. Verstraete, Xavier Gonze, Gian-Marco Rignanese, and Geoffroy Hautier. Electron-phonon beyond fröhlich: Dynamical quadrupoles in polar and covalent solids. *Phys. Rev.*

Lett., 125:136601, 2020. doi: 10.1103/PhysRevLett.125.136601. URL `https://link.aps.org/doi/10.1103/PhysRevLett.125.136601`.

[40] Guillaume Brunin, Henrique Pereira Coutada Miranda, Matteo Giantomassi, Miquel Royo, Massimiliano Stengel, Matthieu J. Verstraete, Xavier Gonze, Gian-Marco Rignanese, and Geoffroy Hautier. Phonon-limited electron mobility in si, gaas, and gap with exact treatment of dynamical quadrupoles. *Phys. Rev. B*, 102:094308, 2020. doi: 10.1103/PhysRevB.102.094308. URL `https://link.aps.org/doi/10.1103/PhysRevB.102.094308`.

Chapter 5

AB INITIO ELECTRON-PHONON INTERACTIONS IN CORRELATED ELECTRON SYSTEMS

5.1 Introduction

Strongly correlated materials are at the center of exciting advances in condensed matter physics. These correlated electron systems (CES) can host states of matter ranging from high-temperature superconductivity [1] to Mott transitions [2, 3], colossal magnetoresistance [4] and multiferroicity [5]. Electron-phonon (e-ph) interactions play an important role in these phenomena, often governing their origin and temperature dependence. A promising direction to study quantitatively e-ph interactions in CES is using first-principles calculations, where one employs density functional theory (DFT) to compute the electronic structure, density functional perturbation theory [6] (DFPT) for the lattice dynamics, and their combination to obtain the e-ph coupling [7, 8]. This approach can successfully describe e-ph interactions and electron dynamics in a wide range of materials [7–20]. Recent work has extended this framework by combining the GW and DFPT approaches to reveal correlation-enhanced e-ph interactions in metallic systems [21, 22].

However, computing e-ph interactions in CES remains challenging as standard DFT usually fails to describe their ground state, mainly due to self-interaction errors in open subshells of localized d or f electrons. In addition, correlated transition metal oxides (TMOs) often exhibit strong e-ph coupling and polaron effects, requiring treatments beyond lowest-order perturbation theory [12]. Widely used first-principles approaches to compute the ground state of CES include DFT+U [23–26], hybrid functionals [27], and dynamical mean-field theory [28, 29]. Developing accurate e-ph calculation in any of these frameworks is an important open challenge; if fulfilled, it would advance investigations of the rich physics of CES and significantly expand the scope of first-principles studies of e-ph interactions.

The DFT+U method [23–26] is particularly promising to mitigate the self-interaction error of DFT, using the Hubbard correction to better capture the physics of localized d electrons [30, 31]. It can predict the ground state of various families of correlated TMOs, including Mott insulators [23], high-temperature superconductors [32] and multiferroics [33, 34]. Its linear response variant, DFPT+U, has been employed successfully to study the lattice dynamics of TMOs [35–38]. As the Hubbard-U

value can be computed *ab initio* [39], as we do here, the framework is entirely free of empirical parameters.

In this chapter, we show calculations of e-ph interactions in the framework of DFT+U, focusing on a prototypical Mott insulator, cobalt oxide (CoO), as a case study. While DFT predicts CoO to be a dynamically unstable metal, DFT+U correctly predicts its antiferromagnetic insulating ground state [36, 40, 41]. We thus find that the long-range Fröhlich e-ph interaction is restored in DFPT+U, and unphysical divergences of the e-ph coupling due to spurious soft modes are removed. With the correct Fröhlich interaction in hand, we study the electron spectral function with a cumulant approach, revealing the formation of a polaron state with sharp quasiparticle and satellite peaks at low temperature that broaden and disappear entirely at room temperature. The Hubbard U-derived e-ph perturbation, missing in DFPT, is found to act primarily on the partially filled d bands of each spin channel, showing the impact of the d electron Coulomb repulsion on e-ph interactions. The DFT+U e-ph calculations developed in this work are poised to advance the understanding of e-ph coupling, transport and superconductivity in strongly correlated materials.

5.2 Methods

For quantitative studies of e-ph interactions, of key interest are the e-ph matrix elements, $g^{\sigma}_{mn\nu}(\boldsymbol{k},\boldsymbol{q})$, which quantify the probability amplitude for an electron in a Bloch state $|\psi_{n\boldsymbol{k}\sigma}\rangle$, with band index n, spin σ and crystal momentum $\boldsymbol{k}$, to scatter into a final state $|\psi_{m\boldsymbol{k}+\boldsymbol{q}\sigma}\rangle$ by emitting or absorbing a phonon with mode index ν, wave-vector $\boldsymbol{q}$, energy $\hbar\omega_{\nu\boldsymbol{q}}$, and displacement eigenvector $\mathbf{e}_{\nu\boldsymbol{q}}$ [7, 42, 43],

$$g^{\sigma}_{mn\nu}(\boldsymbol{k},\boldsymbol{q}) = \left(\frac{\hbar}{2\omega_{\nu\boldsymbol{q}}}\right)^{\frac{1}{2}} \sum_{I} \frac{\mathbf{e}^{I}_{\nu\boldsymbol{q}}}{\sqrt{M_I}} \langle\psi_{m\boldsymbol{k}+\boldsymbol{q}\sigma}|\, d_{\boldsymbol{q}I}\hat{V}^{\sigma}|\psi_{n\boldsymbol{k}\sigma}\rangle, \tag{5.1}$$

where $d_{\boldsymbol{q}I}\hat{V}^{\sigma} \equiv \sum_p e^{i\boldsymbol{q}\cdot\mathbf{R}_p} d_{pI}\hat{V}^{\sigma}$ is the e-ph perturbation due to the change of the potential acting on an electron with spin σ from a unit displacement of atom I (with mass M_I and located in the unit cell at $\mathbf{R}_p$).

In DFPT+U, besides the usual Kohn-Sham (KS) perturbation potential [42], there is an additional term from the perturbation of the Hubbard potential [36]:

$$d\hat{V}^{\sigma} = d\hat{V}^{\sigma}_{\mathrm{KS}} + d\hat{V}^{\sigma}_{\mathrm{Hub}}. \tag{5.2}$$

This Hubbard perturbation potential is the sum of projector and occupation-matrix derivative terms [36],

$$\begin{aligned} d\hat{V}^{\sigma}_{\mathrm{Hub}} = &\sum_{Im_1m_2} U^I \left(\frac{\delta_{m_1m_2}}{2} - n^{I\sigma}_{m_1m_2}\right) \partial \hat{P}^I_{m_1m_2} \\ &- \sum_{Im_1m_2} U^I (dn^{I\sigma}_{m_1m_2}) \hat{P}^I_{m_1m_2}, \end{aligned} \tag{5.3}$$

where m_1 and m_2 are magnetic quantum numbers of the $3d$ orbitals, U^I is the effective Hubbard parameter for atom I, and $n^{I\sigma}_{m_1m_2}$ is the occupation matrix for orbitals with magnetic quantum numbers m_1 and m_2 on atom I,

$$n^{I\sigma}_{m_1m_2} = \sum_{n\boldsymbol{k}} \langle \psi_{n\boldsymbol{k}\sigma} | \, \hat{P}^I_{m_2m_1} \, | \psi_{n\boldsymbol{k}\sigma} \rangle \, . \tag{5.4}$$

Here, $\hat{P}$ is the generalized projector on the space of the localized atomic orbitals φ^I_m,

$$\hat{P}^I_{m_2m_1} = \hat{S} \, |\varphi^I_{m_2}\rangle \, \langle \varphi^I_{m_1}| \, \hat{S}, \tag{5.5}$$

and $\hat{S}$ is the overlap operator of the ultrasoft pseudopotential [44]. In Eq. 5.3, the projector derivative term is efficiently computed with an analytical formula [36] while the occupation-matrix derivative $dn^{I\sigma}_{m_1m_2}$ is computed with DFPT and includes contributions from the response of the wave functions to the atomic displacements [36]:

$$\begin{aligned} dn^{I\sigma}_{m_1m_2} = &\sum_{n\boldsymbol{k}} \langle \psi_{n\boldsymbol{k}\sigma} | \, \partial \hat{P}^I_{m_2m_1} \, | \psi_{n\boldsymbol{k}\sigma} \rangle \\ &+ \sum_{n\boldsymbol{k}} \left[\langle d\psi_{n\boldsymbol{k}\sigma} | \, \hat{P}^I_{m_2m_1} \, | \psi_{n\boldsymbol{k}\sigma} \rangle + \langle \psi_{n\boldsymbol{k}\sigma} | \, \hat{P}^I_{m_2m_1} \, | d\psi_{n\boldsymbol{k}\sigma} \rangle \right]. \end{aligned} \tag{5.6}$$

We apply this framework to investigate the e-ph interactions and electron spectral functions in CoO, focusing on the effects of the Hubbard U correction. The ground state electronic structure of CoO is obtained with collinear spin-polarized DFT+U calculations in a plane-wave basis using the Quantum ESPRESSO code [45]. We use the PBEsol exchange-correlation functional [46] and ultrasoft pseudopotentials [44] from the GBRV library [47]. We employ a 4-atom rhombohedral unit cell with relaxed lattice constants (a = 5.206 Å, b = 3.019 Å, c = 3.009 Å and angle $\beta = 125.05°$) and kinetic energy cutoffs of 60 Ry for the wave functions and 720 Ry for the charge density. Results for the 4-atom rhombohedral and 8-atom monoclinic unit cells [36] are nearly identical, as we have verified, so we choose the 4-atom unit cell for simplicity. Leveraging a recent implementation of DFPT+U [36, 43], we compute the lattice dynamics and e-ph perturbation potentials on coarse irreducible

$\boldsymbol{q}$-point grids. We then rotate the KS and Hubbard perturbation potentials with the Perturbo code to obtain the e-ph matrix elements in the full Brillouin zone (BZ), using coarse grids with $8 \times 8 \times 8$ $\boldsymbol{k}$ and $\boldsymbol{q}$ points. The Wannier functions are obtained with the Wannier90 code [48] and used in Perturbo [42] to interpolate the e-ph matrix elements to finer grids. We use atomic orbitals as the basis for the Hubbard manifold. Our method is free of adjustable parameters, including the Hubbard U value, $U = 4.55$ eV for Co $3d$ states, which is determined *ab initio* with a linear response approach [36, 39, 49].

Using these quantities, we compute the lowest-order (Fan-Migdal) e-ph self-energy, $\Sigma_{n\boldsymbol{k}\sigma}(\omega, T)$, at temperature T and electron energy ω, as implemented in Perturbo [12, 42]; the imaginary part is computed off-shell on a fine energy grid while the real part is evaluated on-shell at the band energy $\varepsilon_{n\boldsymbol{k}\sigma}$. To capture strong e-ph interactions beyond the lowest-order, we use the finite-temperature cumulant approach described in Ref. [12]. The latter allows us to obtain the temperature-dependent retarded Green's function $G^R_{n\boldsymbol{k}\sigma}(\omega)$ and the resulting electron spectral function, $A_{n\boldsymbol{k}\sigma}(\omega) = -\mathrm{Im}G^R_{n\boldsymbol{k}\sigma}(\omega)/\pi$, which includes polaron effects such as band renormalization and satellite peaks [12, 50–52]. Our framework therefore captures two key aspects of the physics of correlated TMOs, the effects of the localized Coulomb repulsion through DFT+U and the strong e-ph coupling and its temperature dependence with the finite-temperature cumulant approach.

5.3 Results and discussion

The e-ph matrix elements from DFPT+U, which include effects from both the KS and Hubbard perturbations, are computed for the d bands of CoO in Fig. 5.1(a) and compared with results from standard DFPT [53]. The Hubbard U correction has a dramatic effect: the two sets of d band e-ph matrix elements differ widely, for all phonon modes and everywhere in the BZ. The largest difference occurs near the zone center, where the DFPT+U results show the presence of the Fröhlich interaction [54], whereby the e-ph matrix elements diverge as $q \to 0$ for the longitudinal optical (LO) modes [10], whereas in plain DFPT they approach a finite value. The reason for this difference is subtle: although CoO is a semiconductor with a 2.5 eV band gap [55], DFT fails to properly describe its d electrons due to self-interaction errors and incorrectly predicts CoO to be a metal, so the Born effective charges and the Fröhlich interaction vanish in DFPT. When the Hubbard U correction is included, the self-interaction errors are mitigated and CoO is correctly predicted to

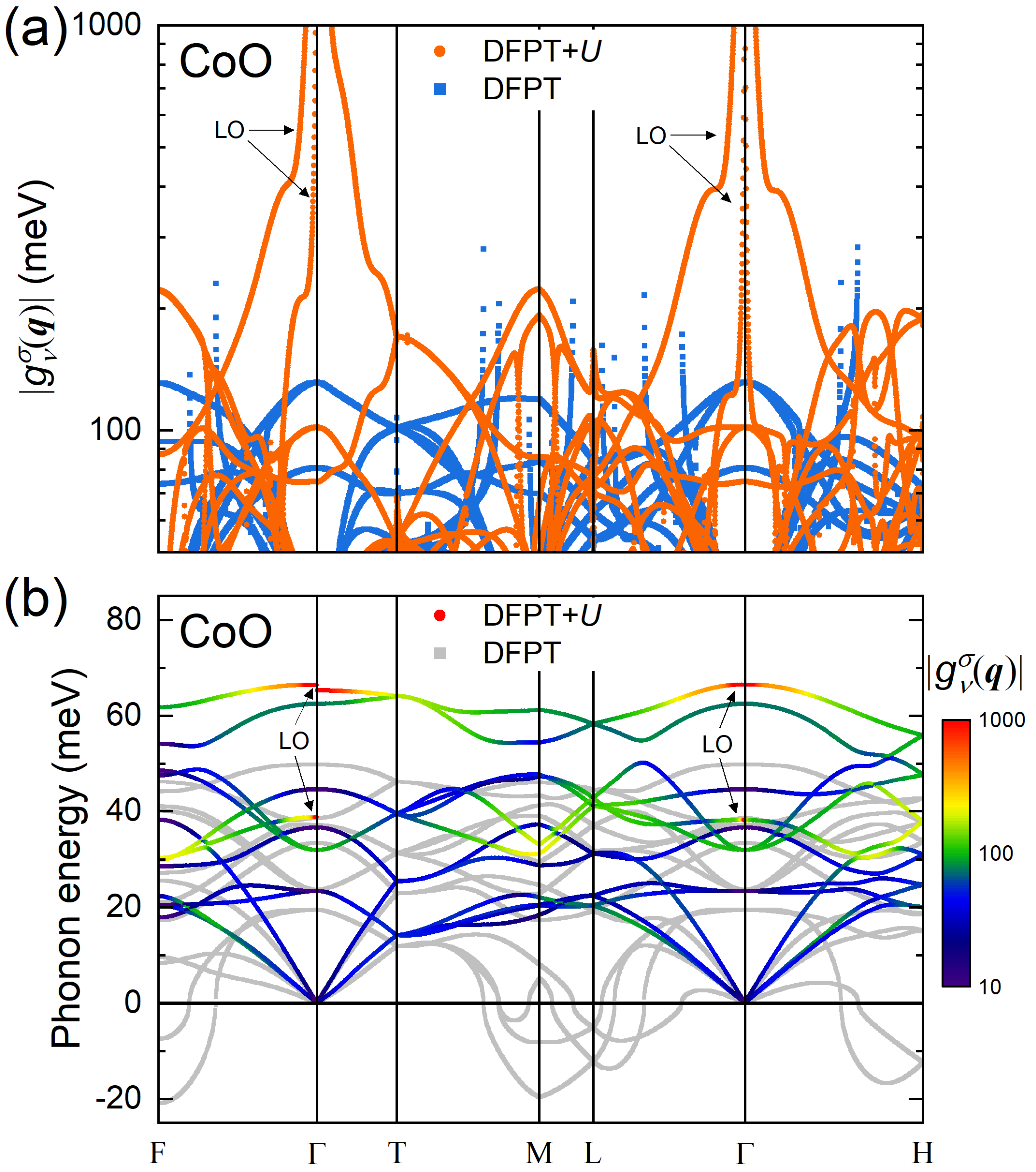

Figure 5.1: (a) Comparison between the e-ph matrix elements in CoO computed with DFPT+U (orange) and standard DFPT (blue). Shown is $\left|g^{\sigma}_{\nu}(\boldsymbol{q})\right| \equiv \left(\sum_{mn}\left|g^{\sigma}_{mn\nu}(\boldsymbol{k}=0,\boldsymbol{q})\right|^{2}/N_b\right)^{1/2}$ for all phonon modes ν, where the phonon wavevector $\boldsymbol{q}$ is varied along high-symmetry BZ lines and the summation runs over the $N_b = 10$ spin-up Co $3d$ bands [53]. (b) CoO phonon dispersions overlaid with a log-scale color map of $\left|g^{\sigma}_{\nu}(\boldsymbol{q})\right|$ computed with DFPT+U (colored line). The CoO phonon dispersions from standard DFPT (gray line) are given for comparison, with imaginary frequencies shown as negative values.

be a polar semiconductor with divergent e-ph coupling for LO phonons near the zone center. This hallmark of the Fröhlich interaction is of critical importance for studies of transport and carrier dynamics in polar materials [10–12].

Figure 5.1(b) highlights the dramatic differences in the phonon dispersions computed with DFPT+U and plain DFPT [36]. In the latter, the ground state is dynamically unstable and the phonon dispersions exhibit soft phonon modes with imaginary frequencies. These errors are propagated to the e-ph interactions, resulting in e-ph matrix elements with unphysical divergences — near the F, M, L, and H points of the BZ in Fig. 5.1(a) — corresponding to zero-frequency phonon modes [11]. In DFPT+U, the ground state is stabilized to the correct antiferromagnetic phase, and the phonon dispersions are significantly improved [36] and in very good agreement with experiments (see Supplemental Material); the soft phonon modes are removed entirely and the e-ph matrix elements are well behaved throughout the BZ, without spurious divergences. These results underscore the importance of the Hubbard U correction for describing the electronic ground state and the resulting e-ph interactions in correlated TMOs.

In CoO, correcting the wave functions and charge density with DFT+U provides the main improvement to the e-ph coupling. To illustrate this point, Fig. 5.2 shows that the e-ph matrix elements computed with the KS perturbation alone but with DFT+U wave functions, $\tilde{g}_{\text{KS}} \propto \langle \psi_{\text{H}ub} | \, d\hat{V}_{\text{KS}} \, | \psi_{\text{H}ub} \rangle$, can capture both the Fröhlich interaction and the main trends in the e-ph coupling. Yet, the Hubbard perturbation potential $d\hat{V}_{\text{Hub}}$, which describes the effect of the lattice dynamics on the Hubbard U correction, also gives an important contribution. Figure 5.2 compares $\tilde{g}_{\text{K}S}$ with the total DFPT+U e-ph matrix elements, $g_{tot} \propto \langle \psi_{\text{H}ub} | \, d\hat{V}_{\text{KS}} + d\hat{V}_{\text{Hub}} \, | \psi_{\text{H}ub} \rangle$, showing that both the KS and Hubbard terms are needed for quantitative accuracy. Direct DFPT+U calculations, shown in Fig. 5.2 as a benchmark, confirm this point and also validate our interpolation procedure.

Further analysis reveals that the contribution of the Hubbard e-ph perturbation is strongly band dependent and acts primarily on the partially filled $3d$ states of each spin channel [56]. To demonstrate this result, we compute the imaginary part of the e-ph self-energy [42] with contribution from only the Hubbard e-ph perturbation, and map it on the electronic spin-up band structure in Fig. 5.3(a). The plot shows the selective contribution of the Hubbard perturbation to e-ph processes in the partially filled $3d$ bands and the nearly negligible contribution in the completely filled $3d$ bands. The situation is analogous for the spin-down bands.

This trend is confirmed by studying the e-ph matrix elements in the Wannier basis, $g_{ij}(\mathbf{r}_p) \propto \langle \phi_i(0) | \, d\hat{V}(\mathbf{r}_p) \, | \phi_j(0) \rangle$ [42], computed using Co $3d$ Wannier functions ϕ_i and ϕ_j located on the same Co atom. These e-ph matrix elements decay exponentially with perturbation distance $|\mathbf{r}_p|$ due to the localized nature of the $3d$

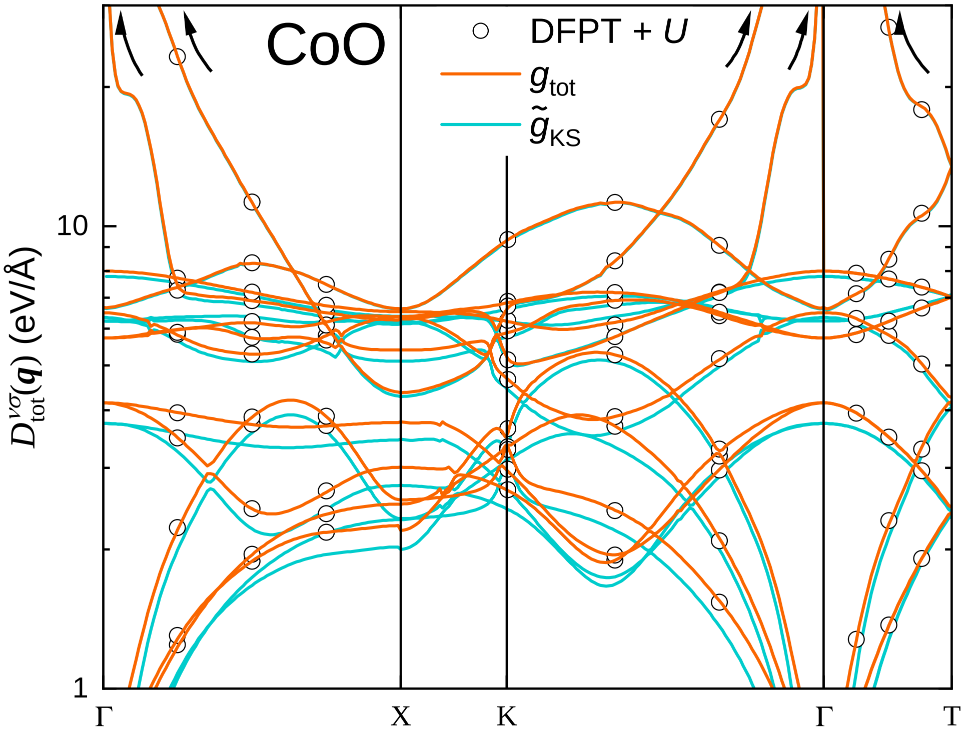

Figure 5.2: Comparison between the e-ph coupling from the KS potential contribution alone (cyan line) and the total result including the Hubbard correction (orange line). In each case, we show the gauge-invariant e-ph coupling strength [42], $D^{\nu\sigma}_{\mathrm{tot}}(\boldsymbol{q}) = (2\omega_{\nu\boldsymbol{q}} M_{\mathrm{uc}} \sum_{nm} \left| g^{\sigma}_{nm\nu}(\boldsymbol{k}=0,\boldsymbol{q}) \right|^2 / N_b)^{1/2}$, computed respectively with e-ph matrix elements $\tilde{g}_{KS}$ and g_{tot}, summing over all $N_b = 13$ spin-up valence bands. The BZ labeling refers to an equivalent (distorted) rocksalt structure [36]. Direct DFPT+U calculations (circles), shown as a benchmark, validate the Wannier interpolation. The arrows indicate the divergence due to the Fröhlich interaction.

Wannier functions. For these local e-ph interactions, we find that the KS and Hubbard contributions are nearly identical for the Co atom with partially filled spin-up $3d$ orbitals [Fig. 5.3(b)], whereas for the Co atom with completely filled spin-up $3d$ orbitals the Hubbard contribution is orders of magnitude smaller than the KS contribution [Fig. 5.3(c)] [56].

In TMOs, due to the polar bonds, electrons typically couple strongly with LO phonons via the Fröhlich interaction. In this common scenario, the e-ph interactions are strong enough to form large polarons, which can dominate transport and electron dynamical processes. The dominant coupling of electrons with LO phonons is clearly seen in Fig. 5.1(b), and thus we expect significant polaron effects in CoO. To investigate them, we compute the electron spectral function with our recently developed finite-temperature cumulant approach, using the DFPT+U e-ph matrix

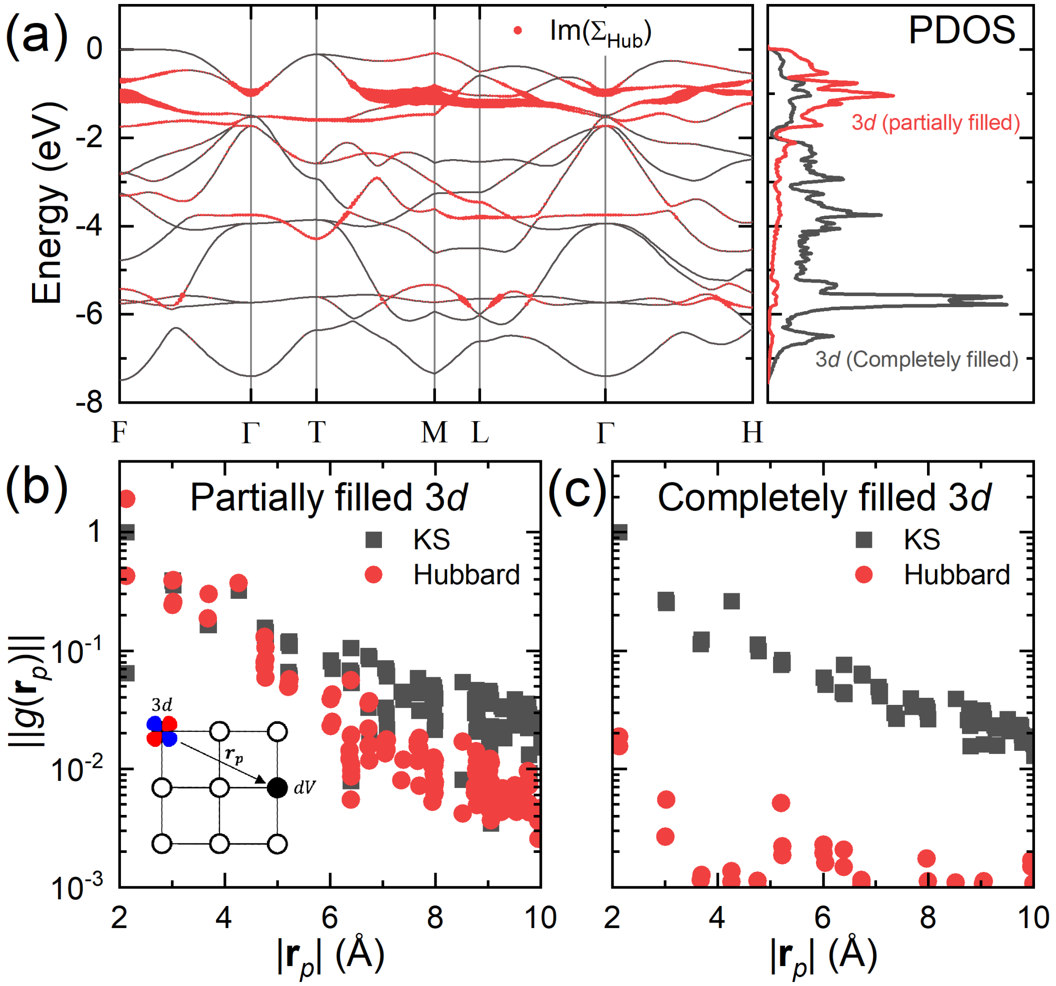

Figure 5.3: (a) Band structure of CoO overlaid with the Hubbard contribution to the imaginary part of the e-ph self-energy, $\text{Im}(\Sigma_{\text{Hub}})$, for the representative case of the spin-up bands. The right panel shows the projected density of states (PDOS) of the partially and completely filled 3d orbitals. (b),(c) Comparison between the spatial decay of the real-space e-ph matrix elements for (b) the partially filled and (c) the completely filled 3d orbitals. Shown are the contributions from the KS (black squares) and Hubbard (red circles) e-ph perturbations [see Eq. (5.2)] to the maximum value of the Wannier basis matrix elements [8], $\left\|g(\mathbf{r}_p)\right\| = \max_{ij}\left|g_{ij}(\mathbf{r}_p)\right|$, normalized using the KS contribution. The inset in (b) is a schematic of the e-ph matrix elements in the Wannier basis, showing the atomic displacement perturbation at distance $|\mathbf{r}_p|$.

elements as input [12].

Figure 5.4 shows the computed electron spectral functions at three temperatures between 100 – 300 K, for an electronic state near the top of the valence band. The spectral function at 100 K shows a sharp quasiparticle (QP) peak and two promi-

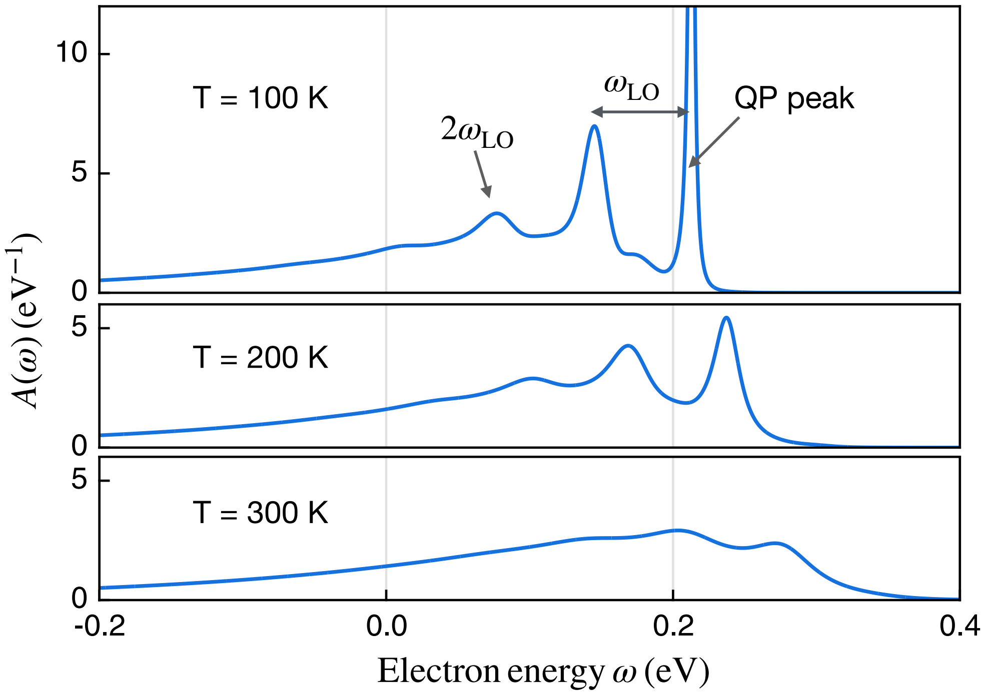

Figure 5.4: Electron spectral function in CoO, computed at three temperatures from 100 K to 300 K, for the highest valence band at crystal momentum $\boldsymbol{k} = \mathbf{F}$. In each panel, the zero of the electron energy ω is set to the band energy obtained from DFT+U calculations.

nent sideband peaks, respectively at energies $\omega_{\mathrm{L}O}$ and $2\omega_{\mathrm{L}O}$ below the QP peak, where $\omega_{\mathrm{L}O} \approx 65$ meV is the energy of the zone center LO phonon with strongest e-ph coupling [see Fig. 5.1(b)]. These phonon sidebands are a hallmark of strong e-ph coupling and polaron effects [12]. Note that our calculations are performed with the Fermi energy lying above the valence band edge (a situation corresponding to lightly p-doped CoO) so the QP peak corresponds to a holelike QP excitation. Accordingly, the phonon sidebands appear at energy lower than the QP peak [57] and are associated with the simultaneous excitation of a holelike QP plus one or two LO phonons, respectively.

Due to a well-known sum rule, the spectral function integrates to one over energy, and thus the phonon sidebands transfer spectral weight from the QP peak. In CoO, the QP spectral weight is strongly renormalized to a value of 0.2 at 100 K, with significant weight transfer to the phonon sidebands due to the strong e-ph interactions. As the temperature increases from 100 to 200 K, the QP peak becomes broader and overlaps with the phonon sidebands. At 300 K and higher temperatures, the peaks merge into a continuous background and the QP peak representing the original electronic state melts entirely into a polaron excitation. As the Fröhlich interaction making up the large polaron is entirely missing in DFT, our study of polaron effects in TMOs is enabled by the correct account of e-ph interactions in the DFT+U framework developed in this work.

5.4 Conclusion

In summary, we introduced an *ab initio* approach enabling quantitative calculations of e-ph interactions and polarons in correlated systems. Our method can be applied broadly to various families of strongly correlated materials with localized d or f electrons, leveraging the framework of parameter-free DFT+U. As shown in this work, our formalism can capture the strong coupling of electron, spin, and lattice degrees of freedom in CES and their combined effect on the e-ph interactions, paving the way for quantitative studies of the rich physics of various families of strongly correlated materials.

5.5 Supplemental Material

Additional derivations on the projector derivatives

The generalized projector $\hat{P}$ on the space of the localized atomic orbitals φ^I_m is defined as

$$\hat{P}^I_{m_2 m_1} = \hat{S}|\varphi^I_{m_2}\rangle\langle\varphi^I_{m_1}|\hat{S}, \tag{5.7}$$

where m_1 and m_2 are magnetic quantum numbers, I is the atomic index, and $\hat{S}$ is the overlap operator in the ultrasoft (US) or projector-augmented-wave (PAW) framework, which is defined as

$$\hat{S} = 1 + \sum_{J\mu\nu} q^J_{\mu\nu}|\beta^J_\mu\rangle\langle\beta^J_\nu|. \tag{5.8}$$

In Eq. (5.8), β^J_μ and β^J_ν are the localized atom-centered projector functions for the US or PAW schemes, labeled by an atomic (J) and a state (greek letter) index, and the coefficients $q^J_{\mu\nu}$ are integrals of the augmentation functions $Q^J_{\mu\nu}(\mathbf{r})$:

$$q^J_{\mu\nu} = \int Q^J_{\mu\nu}(\mathbf{r})d\mathbf{r}. \tag{5.9}$$

The bare derivative of the generalized projector $\partial_{I\alpha}\hat{P}^I_{m_2 m_1}$ with respect to a unit displacement of atom I in the direction α becomes [36]

$$\partial_{I\alpha}\hat{P}^I_{m_2 m_1} = |\partial_{I\alpha}(\hat{S}\varphi^I_{m_2})\rangle\langle\varphi^I_{m_1}|\hat{S} + \hat{S}|\varphi^I_{m_2}\rangle\langle\partial_{I\alpha}(\hat{S}\varphi^I_{m_1})|. \tag{5.10}$$

In Eq. (5.10), the derivatives $\partial_{I\alpha}(\hat{S}\varphi^I_{m_2})$ can be further expanded as

$$|\partial_{I\alpha}(\hat{S}\varphi^I_{m_2})\rangle = \partial_{I\alpha}(\hat{S})\,|\varphi^I_{m_2}\rangle + \hat{S}\,|\partial_{I\alpha}(\varphi^I_{m_2})\rangle, \tag{5.11}$$

where [see Eq. (5.8)]

$$\partial_{I\alpha}(\hat{S}) = \sum_{\mu\nu} q^J_{\mu\nu}\Big[|\partial_{I\alpha}(\beta^J_\mu)\rangle\langle\beta^J_\nu| + |\beta^J_\mu\rangle\langle\partial_{I\alpha}(\beta^J_\nu)|\Big]. \tag{5.12}$$

The derivatives $\partial_{I\alpha}(\varphi^I_{m_2})$ and $\partial_{I\alpha}(\beta^J_\mu)$ can be computed efficiently in reciprocal space, as discussed in Ref. [36].

In the case of norm-conserving pseudopotentials, $\hat{S} = 1$ and thus Eqs. (5.7) and (5.10) simplify to

$$\hat{P}^I_{m_2m_1} = |\varphi^I_{m_2}\rangle\langle\varphi^I_{m_1}|, \tag{5.13}$$

and

$$\partial_{I\alpha}\hat{P}^I_{m_2m_1} = |\partial_{I\alpha}(\varphi^I_{m_2})\rangle\langle\varphi^I_{m_1}| + |\varphi^I_{m_2}\rangle\langle\partial_{I\alpha}(\varphi^I_{m_1})|. \tag{5.14}$$

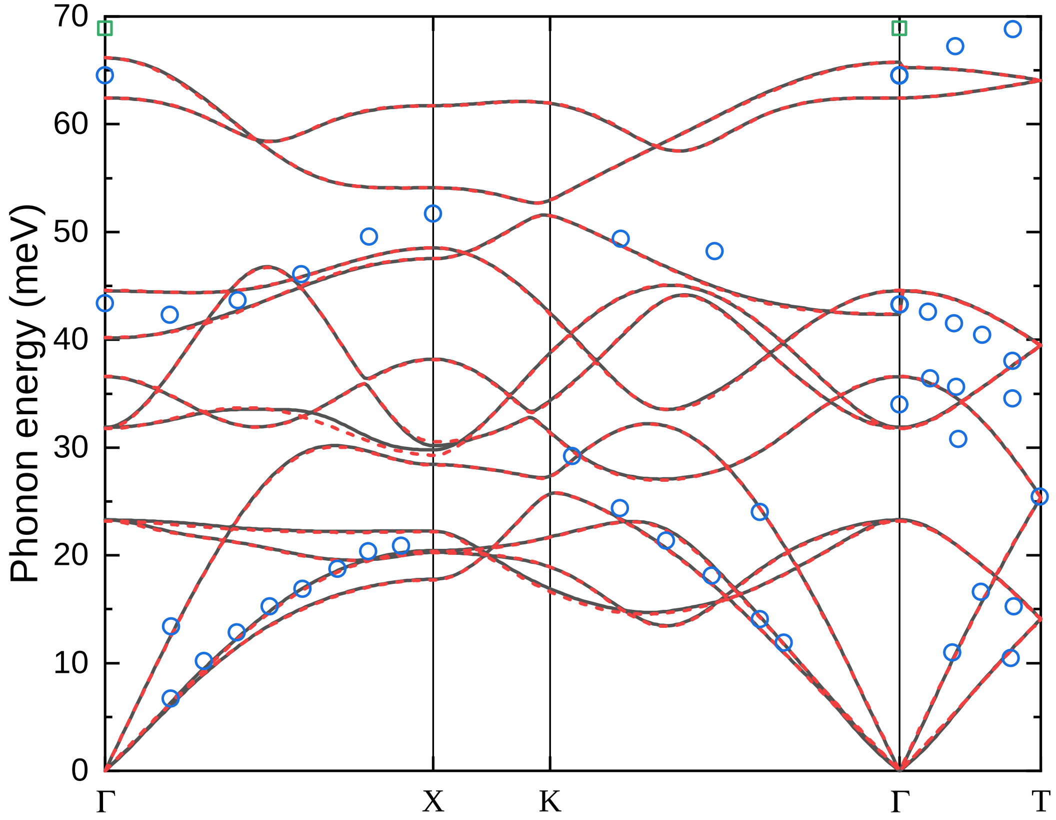

Figure 5.5: CoO phonon dispersion in an equivalent (distorted) rock-salt cell. Shown are the DFPT+U results from our work (black solid line, $8 \times 8 \times 8$ coarse $\boldsymbol{q}$-point grid), DFPT+U results from Ref. [36] (red dashed line, $4\times4\times4$ coarse $\boldsymbol{q}$-point grid), and experimental results from Ref. [58] (blue circles) and Ref. [59] (green squares). Experimental data along the Γ-T direction were folded to account for the doubled periodicity of the four-atoms rhombohedral unit cell along the [111] direction [36].

References

[1] Warren E. Pickett. Electronic structure of the high-temperature oxide superconductors. *Rev. Mod. Phys.*, 61(2):433–512, 1989. doi: 10.1103/RevModPhys.61.433.

[2] N. F. Mott. The Basis of the Electron Theory of Metals, with Special Reference to the Transition Metals. *Proc. Phys. Soc. A*, 62(7):416–422, 1949. ISSN 0370-1298. doi: 10.1088/0370-1298/62/7/303.

[3] N. F. Mott. Metal-Insulator Transition. *Rev. Mod. Phys.*, 40(4):677–683, 1968. doi: 10.1103/RevModPhys.40.677.

[4] A. P. Ramirez. Colossal magnetoresistance. *J. Phys.: Condens. Matter*, 9(39): 8171–8199, 1997. ISSN 0953-8984. doi: 10.1088/0953-8984/9/39/005.

[5] Hans Schmid. Multi-ferroic magnetoelectrics. *Ferroelectrics*, 162(1):317–338, 1994. ISSN 0015-0193. doi: 10.1080/00150199408245120.

[6] Stefano Baroni, Stefano de Gironcoli, Andrea Dal Corso, and Paolo Giannozzi. Phonons and related crystal properties from density-functional perturbation theory. *Rev. Mod. Phys.*, 73(2):515–562, 2001. doi: 10.1103/RevModPhys.73.515.

[7] Marco Bernardi. First-principles dynamics of electrons and phonons. *Eur. Phys. J. B*, 89(11):239, 2016. ISSN 1434-6036. doi: 10.1140/epjb/e2016-70399-4.

[8] Luis A. Agapito and Marco Bernardi. Ab initio electron-phonon interactions using atomic orbital wave functions. *Phys. Rev. B*, 97(23):235146, 2018. doi: 10.1103/PhysRevB.97.235146.

[9] Marco Bernardi, Derek Vigil-Fowler, Johannes Lischner, Jeffrey B. Neaton, and Steven G. Louie. Ab Initio Study of Hot Carriers in the First Picosecond after Sunlight Absorption in Silicon. *Phys. Rev. Lett.*, 112(25):257402, 2014. doi: 10.1103/PhysRevLett.112.257402.

[10] Jin-Jian Zhou and Marco Bernardi. Ab initio electron mobility and polar phonon scattering in GaAs. *Phys. Rev. B*, 94(20):201201(R), 2016. doi: 10.1103/PhysRevB.94.201201.

[11] Jin-Jian Zhou, Olle Hellman, and Marco Bernardi. Electron-Phonon Scattering in the Presence of Soft Modes and Electron Mobility in $SrTiO_3$ Perovskite from First Principles. *Phys. Rev. Lett.*, 121(22):226603, 2018. doi: 10.1103/PhysRevLett.121.226603.

[12] Jin-Jian Zhou and Marco Bernardi. Predicting charge transport in the presence of polarons: The beyond-quasiparticle regime in $SrTiO_3$. *Phys. Rev. Res.*, 1 (3):033138, 2019. doi: 10.1103/PhysRevResearch.1.033138.

[13] Cheol-Hwan Park, Feliciano Giustino, Marvin L. Cohen, and Steven G. Louie. Velocity renormalization and carrier lifetime in graphene from the electron-phonon interaction. *Phys. Rev. Lett.*, 99:086804, 2007. URL `https://link.aps.org/doi/10.1103/PhysRevLett.99.086804`.

[14] A Floris, Antonio Sanna, S Massidda, and E.K.U. Gross. Two-band superconductivity in pb from ab initio calculations. *Phys. Rev. B*, 75(5): 054508, 2007. URL `https://journals.aps.org/prb/abstract/10.1103/PhysRevB.75.054508`.

[15] Jelena Sjakste, Iurii Timrov, Paola Gava, Natalio Mingo, and Nathalie Vast. First-principles calculations of electron-phonon scattering. *Annual Rev. Heat Transfer*, 17, 2014. URL `http://dl.begellhouse.com/ru/references/5756967540dd1b03,7deb9f2f1087a9e3,7c2384aa250f0b1f.html`.

[16] Wu Li. Electrical transport limited by electron-phonon coupling from Boltzmann transport equation: An ab initio study of Si, Al, and MoS_2. *Phys. Rev. B*, 92(7):075405, 2015. doi: 10.1103/PhysRevB.92.075405.

[17] Te-Huan Liu, Jiawei Zhou, Bolin Liao, David J. Singh, and Gang Chen. First-principles mode-by-mode analysis for electron-phonon scattering channels and mean free path spectra in GaAs. *Phys. Rev. B*, 95(7):075206, 2017. ISSN 2469-9950, 2469-9969. doi: 10.1103/PhysRevB.95.075206.

[18] Jinlong Ma, Arun S. Nissimagoudar, and Wu Li. First-principles study of electron and hole mobilities of Si and GaAs. *Phys. Rev. B*, 97(4):045201, 2018. ISSN 2469-9950, 2469-9969. doi: 10.1103/PhysRevB.97.045201.

[19] Samuel Poncé, Elena R. Margine, and Feliciano Giustino. Towards predictive many-body calculations of phonon-limited carrier mobilities in semiconductors. *Phys. Rev. B*, 97:121201(R), 2018. URL `https://link.aps.org/doi/10.1103/PhysRevB.97.121201`.

[20] Jinsoo Park, Jin-Jian Zhou, and Marco Bernardi. Spin-phonon relaxation times in centrosymmetric materials from first principles. *Phys. Rev. B*, 101(4): 045202, 2020. ISSN 2469-9950, 2469-9969. doi: 10.1103/PhysRevB.101.045202.

[21] Zhenglu Li, Gabriel Antonius, Meng Wu, Felipe H. da Jornada, and Steven G. Louie. Electron-phonon coupling from ab initio linear-response theory within the *GW* method: Correlation-enhanced interactions and superconductivity in $Ba_{1-x}K_xBiO_3$. *Phys. Rev. Lett.*, 122:186402, 2019. doi: 10.1103/PhysRevLett.122.186402. URL `https://link.aps.org/doi/10.1103/PhysRevLett.122.186402`.

[22] Zhenglu Li, Meng Wu, Yang-Hao Chan, and Steven G. Louie. Unmasking the origin of kinks in the photoemission spectra of cuprate superconductors. *Phys. Rev. Lett.*, 126:146401, 2021. doi: 10.1103/PhysRevLett.126.146401. URL `https://link.aps.org/doi/10.1103/PhysRevLett.126.146401`.

[23] Vladimir I. Anisimov, Jan Zaanen, and Ole K. Andersen. Band theory and Mott insulators: Hubbard U instead of Stoner I. *Phys. Rev. B*, 44(3):943–954, 1991. doi: 10.1103/PhysRevB.44.943.

[24] V. I. Anisimov, I. S. Elfimov, N. Hamada, and K. Terakura. Charge-ordered insulating state of Fe_3O_4 from first-principles electronic structure calculations. *Phys. Rev. B*, 54(7):4387–4390, 1996. doi: 10.1103/PhysRevB.54.4387.

[25] Vladimir I. Anisimov, F. Aryasetiawan, and A. I. Lichtenstein. First-principles calculations of the electronic structure and spectra of strongly correlated systems: the LDA+U method. *J. Phys.: Condens. Matter*, 9(4):767–808, 1997. ISSN 0953-8984. doi: 10.1088/0953-8984/9/4/002.

[26] S. L. Dudarev, G. A. Botton, S. Y. Savrasov, C. J. Humphreys, and A. P. Sutton. Electron-energy-loss spectra and the structural stability of nickel oxide: An LSDA+U study. *Phys. Rev. B*, 57(3):1505–1509, 1998. doi: 10.1103/PhysRevB.57.1505.

[27] Jochen Heyd, Gustavo E. Scuseria, and Matthias Ernzerhof. Hybrid functionals based on a screened Coulomb potential. *J. Chem. Phys.*, 118(18):8207–8215, 2003. ISSN 0021-9606. doi: 10.1063/1.1564060.

[28] Antoine Georges, Gabriel Kotliar, Werner Krauth, and Marcelo J. Rozenberg. Dynamical mean-field theory of strongly correlated fermion systems and the limit of infinite dimensions. *Rev. Mod. Phys.*, 68(1):13–125, 1996. doi: 10.1103/RevModPhys.68.13.

[29] G. Kotliar, S. Y. Savrasov, K. Haule, V. S. Oudovenko, O. Parcollet, and C. A. Marianetti. Electronic structure calculations with dynamical mean-field theory. *Rev. Mod. Phys.*, 78(3):865–951, 2006. doi: 10.1103/RevModPhys.78.865.

[30] Heather J Kulik, Matteo Cococcioni, Damian A Scherlis, and Nicola Marzari. Density functional theory in transition-metal chemistry: A self-consistent hubbard u approach. *Phys. Rev. Lett.*, 97:103001, 2006. URL `https://journals.aps.org/prl/abstract/10.1103/PhysRevLett.97.103001`.

[31] Heather J Kulik. Perspective: Treating electron over-delocalization with the dft+ u method. *J. Chem. Phys.*, 142(24):240901, 2015. URL `https://aip.scitation.org/doi/full/10.1063/1.4922693`.

[32] Simon Pesant and Michel Côté. DFT + U study of magnetic order in doped La_2CuO_4 crystals. *Phys. Rev. B*, 84(8):085104, 2011. doi: 10.1103/PhysRevB.84.085104.

[33] Pio Baettig, Claude Ederer, and Nicola A. Spaldin. First principles study of the multiferroics $BiFeO_3$, Bi_2FeCrO_6, and $BiCrO_3$: Structure, polarization, and magnetic ordering temperature. *Phys. Rev. B*, 72(21):214105, 2005. doi: 10.1103/PhysRevB.72.214105.

[34] James M. Rondinelli, Aaron S. Eidelson, and Nicola A. Spaldin. Non-d^0 Mn-driven ferroelectricity in antiferromagnetic $BaMnO_3$. *Phys. Rev. B*, 79(20): 205119, 2009. doi: 10.1103/PhysRevB.79.205119.

[35] A. Floris, S. de Gironcoli, E. K. U. Gross, and M. Cococcioni. Vibrational properties of MnO and NiO from DFT+*U*-based density functional perturbation theory. *Phys. Rev. B*, 84(16):161102(R), 2011. doi: 10.1103/PhysRevB.84.161102.

[36] A. Floris, I. Timrov, B. Himmetoglu, N. Marzari, S. de Gironcoli, and M. Cococcioni. Hubbard-corrected density functional perturbation theory with ultrasoft pseudopotentials. *Phys. Rev. B*, 101(6):064305, 2020. doi: 10.1103/PhysRevB.101.064305.

[37] Marc Blanchard, Etienne Balan, Paola Giura, Keevin Béneut, Haohao Yi, Guillaume Morin, Carlos Pinilla, Michele Lazzeri, and Andrea Floris. Infrared spectroscopic properties of goethite: anharmonic broadening, long-range electrostatic effects and al substitution. *Phys. Chem. Miner.*, 41:289, 2014. URL `https://link.springer.com/article/10.1007/s00269-013-0648-7`.

[38] Kazutoshi Miwa. Prediction of Raman spectra with DFT+*U* method. *Phys. Rev. B*, 97(7):075143, 2018. doi: 10.1103/PhysRevB.97.075143.

[39] Iurii Timrov, Nicola Marzari, and Matteo Cococcioni. Hubbard parameters from density-functional perturbation theory. *Phys. Rev. B*, 98(8):085127, 2018. doi: 10.1103/PhysRevB.98.085127.

[40] U. D. Wdowik and K. Parlinski. Lattice dynamics of coo from first principles. *Phys. Rev. B*, 75:104306, 2007. doi: 10.1103/PhysRevB.75.104306. URL `https://link.aps.org/doi/10.1103/PhysRevB.75.104306`.

[41] U. D. Wdowik and K. Parlinski. Lattice dynamics of cobalt-deficient coo from first principles. *Phys. Rev. B*, 78:224114, 2008. doi: 10.1103/PhysRevB.78.224114. URL `https://link.aps.org/doi/10.1103/PhysRevB.78.224114`.

[42] Jin-Jian Zhou, Jinsoo Park, I-Te Lu, Ivan Maliyov, Xiao Tong, and Marco Bernardi. Perturbo: A software package for ab initio electron–phonon interactions, charge transport and ultrafast dynamics. *Comput. Phys. Commun.*, 264:107970, 2021. ISSN 0010-4655. doi: 10.1016/j.cpc.2021.107970. URL `https://www.sciencedirect.com/science/article/pii/S0010465521000837`.

[43] P Giannozzi, O Andreussi, T Brumme, O Bunau, M Buongiorno Nardelli, M Calandra, R Car, C Cavazzoni, D Ceresoli, M Cococcioni, N Colonna, I Carnimeo, A Dal Corso, S de Gironcoli, P Delugas, R A DiStasio, A Ferretti, A Floris, G Fratesi, G Fugallo, R Gebauer, U Gerstmann, F Giustino,

T Gorni, J Jia, M Kawamura, H-Y Ko, A Kokalj, E Küçükbenli, M Lazzeri, M Marsili, N Marzari, F Mauri, N L Nguyen, H-V Nguyen, A Otero dela Roza, L Paulatto, S Poncé, D Rocca, R Sabatini, B Santra, M Schlipf, A P Seitsonen, A Smogunov, I Timrov, T Thonhauser, P Umari, N Vast, X Wu, and S Baroni. Advanced capabilities for materials modelling with quantum ESPRESSO. *J. Phys.: Condens. Matter*, 29(46):465901, 2017. doi: 10.1088/1361-648x/aa8f79. URL `https://doi.org/10.1088/1361-648x/aa8f79`.

[44] David Vanderbilt. Soft self-consistent pseudopotentials in a generalized eigenvalue formalism. *Phys. Rev. B*, 41(11):7892–7895, 1990. doi: 10.1103/PhysRevB.41.7892.

[45] Paolo Giannozzi, Stefano Baroni, Nicola Bonini, Matteo Calandra, Roberto Car, Carlo Cavazzoni, Davide Ceresoli, Guido L. Chiarotti, Matteo Cococcioni, Ismaila Dabo, Andrea Dal Corso, Stefano de Gironcoli, Stefano Fabris, Guido Fratesi, Ralph Gebauer, Uwe Gerstmann, Christos Gougoussis, Anton Kokalj, Michele Lazzeri, Layla Martin-Samos, Nicola Marzari, Francesco Mauri, Riccardo Mazzarello, Stefano Paolini, Alfredo Pasquarello, Lorenzo Paulatto, Carlo Sbraccia, Sandro Scandolo, Gabriele Sclauzero, Ari P. Seitsonen, Alexander Smogunov, Paolo Umari, and Renata M. Wentzcovitch. QUANTUM ESPRESSO: A modular and open-source software project for quantum simulations of materials. *J. Phys.: Condens. Matter*, 21(39):395502, 2009. ISSN 0953-8984. doi: 10.1088/0953-8984/21/39/395502.

[46] John P. Perdew, Adrienn Ruzsinszky, Gábor I. Csonka, Oleg A. Vydrov, Gustavo E. Scuseria, Lucian A. Constantin, Xiaolan Zhou, and Kieron Burke. Restoring the Density-Gradient Expansion for Exchange in Solids and Surfaces. *Phys. Rev. Lett.*, 100(13):136406, 2008. doi: 10.1103/PhysRevLett.100.136406.

[47] Kevin F. Garrity, Joseph W. Bennett, Karin M. Rabe, and David Vanderbilt. Pseudopotentials for high-throughput DFT calculations. *Comput. Mater. Sci.*, 81:446, 2014. URL `https://www.sciencedirect.com/science/article/abs/pii/S0927025613005077`.

[48] Giovanni Pizzi, Valerio Vitale, Ryotaro Arita, Stefan Blügel, Frank Freimuth, Guillaume Géranton, Marco Gibertini, Dominik Gresch, Charles Johnson, Takashi Koretsune, Julen Ibañez-Azpiroz, Hyungjun Lee, Jae-Mo Lihm, Daniel Marchand, Antimo Marrazzo, Yuriy Mokrousov, Jamal I. Mustafa, Yoshiro Nohara, Yusuke Nomura, Lorenzo Paulatto, Samuel Poncé, Thomas Ponweiser, Junfeng Qiao, Florian Thöle, Stepan S. Tsirkin, Ma\lgorzata Wierzbowska, Nicola Marzari, David Vanderbilt, Ivo Souza, Arash A. Mostofi, and Jonathan R. Yates. Wannier90 as a community code: New features and applications. *J. Phys.: Condens. Matter*, 32(16):165902, 2020. ISSN 0953-8984. doi: 10.1088/1361-648X/ab51ff.

[49] Iurii Timrov, Nicola Marzari, and Matteo Cococcioni. Self-consistent hubbard parameters from density-functional perturbation theory in the ultrasoft and projector-augmented wave formulations. *Phys. Rev. B*, 103: 045141, 2021. URL `https://journals.aps.org/prb/abstract/10.1103/PhysRevB.103.045141`.

[50] F. Aryasetiawan, L. Hedin, and K. Karlsson. Multiple plasmon satellites in Na and Al spectral functions from ab initio cumulant expansion. *Phys. Rev. Lett.*, 77(11):2268–2271, 1996. doi: 10.1103/PhysRevLett.77.2268. URL `https://link.aps.org/doi/10.1103/PhysRevLett.77.2268`.

[51] S. M. Story, J. J. Kas, F. D. Vila, M. J. Verstraete, and J. J. Rehr. Cumulant expansion for phonon contributions to the electron spectral function. *Phys. Rev. B*, 90(19):195135, 2014. doi: 10.1103/PhysRevB.90.195135. URL `https://link.aps.org/doi/10.1103/PhysRevB.90.195135`.

[52] Jean Paul Nery, Philip B. Allen, Gabriel Antonius, Lucia Reining, Anna Miglio, and Xavier Gonze. Quasiparticles and phonon satellites in spectral functions of semiconductors and insulators: Cumulants applied to the full first-principles theory and the Fröhlich polaron. *Phys. Rev. B*, 97(11):115145, 2018. doi: 10.1103/PhysRevB.97.115145. URL `https://link.aps.org/doi/10.1103/PhysRevB.97.115145`.

[53] . As the Hubbard U correction reorders the band energies, to make a meaningful comparison in Fig. 5.1(a) we average the e-ph coupling over the entire set of 10 3d bands, for both the DFPT and DFPT+U calculations.

[54] H. Fröhlich. Electrons in lattice fields. *Adv. Phys.*, 3(11):325–361, 1954. ISSN 0001-8732, 1460-6976. doi: 10.1080/00018735400101213.

[55] J. van Elp, J. L. Wieland, H. Eskes, P. Kuiper, G. A. Sawatzky, F. M. F. de Groot, and T. S. Turner. Electronic structure of CoO, Li-doped CoO, and $LiCoO_2$. *Phys. Rev. B*, 44(12):6090–6103, 1991. doi: 10.1103/PhysRevB.44.6090.

[56] . Note that there are two Co atoms in the unit cell of CoO, each generating a set of 3d bands in the solid; for each spin channel, due to the antiferromagnetic ground state of CoO, one set of 3d bands is completely filled and the other is partially filled.

[57] Andrea Damascelli, Zahid Hussain, and Zhi-Xun Shen. Angle-resolved photoemission studies of the cuprate superconductors. *Rev. Mod. Phys.*, 75:473–541, 2003. URL `https://link.aps.org/doi/10.1103/RevModPhys.75.473`.

[58] J. Sakurai, W. J. L. Buyers, R. A. Cowley, and G. Dolling. Crystal dynamics and magnetic excitations in cobaltous oxide. *Phys. Rev.*, 167:510–518, 1968. doi: 10.1103/PhysRev.167.510. URL `https://link.aps.org/doi/10.1103/PhysRev.167.510`.

[59] M. H. Nassir and M. A. Langell. CoO(100) Fuchs-Kliewer phonon spectrum by high resolution electron energy loss spectroscopy. *Solid State Commun.*, 92(10):791–795, 1994. ISSN 0038-1098. doi: https://doi.org/10.1016/0038-1098(94)90314-X.

Chapter 6

PERTURBO: A SOFTWARE PACKAGE FOR *AB INITIO* ELECTRON-PHONON INTERACTIONS, CHARGE TRANSPORT AND ULTRAFAST DYNAMICS

6.1 Introduction

PERTURBO is a software package for first-principles calculations of charge transport, spin dynamics, and ultrafast carrier dynamics in materials [1, 2]. The vision behind PERTURBO is to provide a unified platform and a validated code that can be applied broadly to compute the interactions, transport and ultrafast dynamics of electrons and excited states in materials [3]. The goal is to facilitate basic scientific discoveries in materials and devices by advancing microscopic understanding of carrier dynamics, while creating a sustainable software element able to address the demands of the computational physics community.

PERTURBO builds on established first-principles methods. It uses density functional theory (DFT) and density functional perturbation theory (DFPT) [4] as a starting point for computing electron dynamics. It reads the output of DFT and DFPT calculations, for now from the Quantum ESPRESSO (QE) code [5, 6], and uses this data to compute electron interactions, charge transport and ultrafast dynamics. The current distribution focuses on electron-phonon (e-ph) interactions and the related phonon-limited transport properties [7], including the electrical conductivity, mobility and the Seebeck coefficient. It can also simulate the ultrafast nonequilibrium electron dynamics in the presence of e-ph interactions. The developer branch, which is not publicly available yet, also includes routines for computing spin [8], electron-defect [9, 10], and electron-photon interactions [11], as well as advanced methods to compute the ultrafast dynamics of electrons and phonons in the presence of electric and magnetic fields. These additional features will be made available in future releases.

The transport module of PERTURBO enables accurate calculations of charge transport in a wide range of functional materials. In its most basic workflow, PERTURBO computes the conductivity and mobility as a function of temperature and carrier concentration, either within the relaxation time approximation (RTA) or with an iterative solution of the linearized Boltzmann transport equation (BTE) [12, 13]. The ultrafast dynamics module explicitly evolves in time the electron BTE (while keeping the phonon occupations fixed), enabling investigations of the ultrafast electron dynamics starting from a given initial electron distribution [14]. Our routines can carry out these calculations in metals, semiconductors, insulators, and 2D materials. An efficient implementation of long-range e-ph interactions is employed for polar bulk and 2D materials. Materials with spin-orbit coupling (SOC) are treated using fully relativistic pseudopotentials [8, 13]. Both norm-conserving and ultrasoft pseudopotentials are supported. Quantities related to e-ph interactions can be easily obtained, stored and analyzed.

PERTURBO is implemented in modern Fortran with a modular code design. All calculations employ intuitive workflows. The code is highly efficient thanks to its hybrid MPI (Message Passing Interface) and OpenMP (Open Multi-Processing) parallelization. It can run on record-large unit cells with up to at least 50 atoms [15], and its performance scales up to thousands of CPU cores. It conveniently writes files using the HDF5 format, and is suitable for both high-performance supercomputers and smaller computer clusters.

Target users include both experts in first-principles calculations and materials theory as well as experimental researchers and teams in academic or national laboratories investigating charge transport, ultrafast spectroscopy, advanced functional materials, and semiconductor or solid-state devices. PERTURBO will equip these users with an efficient quantitative tool to investigate electron interactions and dynamics in broad families of materials, filling a major void in the current software ecosystem.

The chapter is organized as follows: Sec. 6.2 discusses the theory and numerical methods implemented in the code; Sec. 6.3 describes the code capabilities and workflows; Sec. 6.4 delves deeper into selected technical aspects; Sec. 6.5 shows several example calculations provided as tutorials in the code; and Sec. 6.6 discusses the parallelization strategy and the scaling of the code on high performance supercomputers. We conclude in Sec. 6.7 by summarizing the main features of PERTURBO.

6.2 Methodology

Boltzmann transport equation

The current release of PERTURBO can compute charge transport and ultrafast dynamics in the framework of the semiclassical BTE. The BTE describes the flow of the electron occupations $f_{n\boldsymbol{k}}(\boldsymbol{r}, t)$ in the phase-space variables of relevance in a periodic system, the crystal momentum $\boldsymbol{k}$ and spatial coordinate $\boldsymbol{r}$:

$$\begin{aligned}\frac{\partial f_{n\boldsymbol{k}}(\boldsymbol{r},t)}{\partial t} =& - \left[\nabla_{\boldsymbol{r}} f_{n\boldsymbol{k}}(\boldsymbol{r},t)\cdot \boldsymbol{v}_{n\boldsymbol{k}} + \hbar^{-1}\nabla_{\boldsymbol{k}} f_{n\boldsymbol{k}}(\boldsymbol{r},t)\cdot \boldsymbol{F}\right] \\ &+ \mathcal{I}\left[f_{n\boldsymbol{k}}\right],\end{aligned} \tag{6.1}$$

where n is the band index and $v_{n\boldsymbol{k}}$ are band velocities. The time evolution of the electron occupations is governed by the so-called drift term due to external fields $\boldsymbol{F}$ and the collision term $\mathcal{I}\left[f_{n\boldsymbol{k}}\right]$, which captures electron scattering processes due to phonons or other mechanisms [16]. In PERTURBO, the fields are assumed to be slowly varying and the material homogeneous, so $f_{n\boldsymbol{k}}$ does not depend on the spatial coordinates and its spatial dependence is not computed explicitly.

The collision integral $\mathcal{I}\left[f_{n\boldsymbol{k}}\right]$ is a sum over a large number of scattering processes in momentum space, and it is very computationally expensive because it involves Brillouin zone (BZ) integrals on fine grids. Most analytical and computational treatments simplify the scattering integral with various approximations. A common one is the RTA, which assumes that the scattering integral is proportional to the deviation $\delta f_{n\boldsymbol{k}}$ of the electron occupations from the equilibrium Fermi-Dirac distribution, $\mathcal{I}\left[f_{n\boldsymbol{k}}\right] = -\delta f_{n\boldsymbol{k}}/\tau$; the relaxation time τ is either treated as a constant empirical parameter [17, 18] or as a state-dependent quantity, $\tau_{n\boldsymbol{k}}$.

PERTURBO implements the first-principles formalism of the BTE, which employs materials properties obtained with quantum mechanical approaches, using the atomic structure of the material as the only input. The electronic structure is computed using DFT and the lattice dynamical properties using DFPT. The scattering integral is computed only for e-ph processes in the current release, while other scattering mechanisms, such as electron-defect and electron-electron scattering, are left for future releases. The scattering integral due to e-ph processes can be written as

$$\begin{aligned}\mathcal{I}^{e-\mathrm{ph}}\left[f_{n\boldsymbol{k}}\right] =& -\frac{2\pi}{\hbar}\frac{1}{\mathcal{N}_{\boldsymbol{q}}}\sum_{m\boldsymbol{q}\nu}\left|g_{mn\nu}(\boldsymbol{k},\boldsymbol{q})\right|^2 \\ &\times\left[\delta\left(\varepsilon_{n\boldsymbol{k}} - \hbar\omega_{\nu\boldsymbol{q}} - \varepsilon_{m\boldsymbol{k}+\boldsymbol{q}}\right)\times F_{\mathrm{em}}\right. \\ &\left.+\,\delta\left(\varepsilon_{n\boldsymbol{k}} + \hbar\omega_{\nu\boldsymbol{q}} - \varepsilon_{m\boldsymbol{k}+\boldsymbol{q}}\right)\times F_{\mathrm{abs}}\right],\end{aligned} \tag{6.2}$$

where $\mathcal{N}_{\boldsymbol{q}}$ is the number of $\boldsymbol{q}$-points used in the summation, and $g_{mn\nu}(\boldsymbol{k},\boldsymbol{q})$ are e-ph matrix elements (see Sec. 1.2) quantifying the probability amplitude for an electron to scatter from an initial state $|n\boldsymbol{k}\rangle$ to a final state $|m\boldsymbol{k}+\boldsymbol{q}\rangle$, by emitting or absorbing a phonon with wavevector $\boldsymbol{q}$ and mode index ν; here and below, $\varepsilon_{n\boldsymbol{k}}$ and $\hbar\omega_{\nu\boldsymbol{q}}$ are the energies of electron quasiparticles and phonons, respectively. The phonon absorption (F_{abs}) and emission (F_{em}) terms are defined as

$$\begin{aligned} F_{\text{abs}} &= f_{n\boldsymbol{k}}\left(1 - f_{m\boldsymbol{k}+\boldsymbol{q}}\right) N_{\nu\boldsymbol{q}} - f_{m\boldsymbol{k}+\boldsymbol{q}}\left(1 - f_{n\boldsymbol{k}}\right)\left(N_{\nu\boldsymbol{q}} + 1\right), \\ F_{\text{em}} &= f_{n\boldsymbol{k}}\left(1 - f_{m\boldsymbol{k}+\boldsymbol{q}}\right)\left(N_{\nu\boldsymbol{q}} + 1\right) - f_{m\boldsymbol{k}+\boldsymbol{q}}\left(1 - f_{n\boldsymbol{k}}\right) N_{\nu\boldsymbol{q}} \end{aligned} \tag{6.3}$$

where $N_{\nu\boldsymbol{q}}$ are phonon occupations.

Ultrafast carrier dynamics

PERTURBO can solve the BTE numerically to simulate the evolution in time t of the electron occupations $f_{n\boldsymbol{k}}(t)$ due to e-ph scattering processes, starting from an initial nonequilibrium distribution. In the presence of a slowly varying external electric field, and assuming the material is homogeneous, we rewrite the BTE in Eq. (6.1) as

$$\frac{\partial f_{n\boldsymbol{k}}(t)}{\partial t} = \frac{e\boldsymbol{E}}{\hbar} \cdot \nabla_{\boldsymbol{k}} f_{n\boldsymbol{k}}(t) + \mathcal{I}^{e-\text{ph}}\left[f_{n\boldsymbol{k}}\right], \tag{6.4}$$

where e is the electron charge and $\boldsymbol{E}$ the external electric field. We solve this non-linear integro-differential equation numerically (in the current release, only for $\boldsymbol{E} = 0$), using explicit time-stepping with the 4th-order Runge-Kutta (RK4) or Euler methods. The RK4 solver is used by default due to its superior accuracy. The Euler method is much faster than RK4, but it is only first-order accurate in time, so it should be tested carefully and compared against RK4.

Starting from an initial nonequilibrium electron distribution $f_{n\boldsymbol{k}}(t_0)$, we evolve in time Eq. (6.4) with a small time step (typically in the order of 1 fs) to obtain $f_{n\boldsymbol{k}}(t)$ as a function of time. One application of this framework is to simulate the equilibration of excited electrons [14, 19], in which we set $\boldsymbol{E} = 0$ and simulate the time evolution of the excited electron distribution as it approaches its equilibrium Fermi-Dirac value through e-ph scattering processes. The phonon occupations are kept fixed (usually, to their equilibrium value at a given temperature) in the current version of the code. Another application, which is currently under development, is charge transport in high electric fields.

Charge transport

In an external electric field, the drift and collision terms in the BTE balance out at long enough times; the field drives the electron distribution out of equilibrium, while the collisions tend to restore equilibrium. At steady state, a nonequilibrium electron distribution is reached, for which $\partial f_{n\boldsymbol{k}}/\partial t = 0$. The BTE for transport at steady state becomes

$$-\frac{e\boldsymbol{E}}{\hbar}\cdot\nabla_{\boldsymbol{k}}f_{n\boldsymbol{k}}(t)=\mathcal{I}^{e\text{-ph}}\left[f_{n\boldsymbol{k}}\right]. \tag{6.5}$$

When the electric field is relatively weak, the steady-state electron distribution deviates only slightly from its equilibrium value. As is usual, we expand $f_{n\boldsymbol{k}}$ around the equilibrium Fermi-Dirac distribution, $f^0_{n\boldsymbol{k}}$, and keep only terms linear in the electric field:

$$\begin{aligned} f_{n\boldsymbol{k}} &= f^0_{n\boldsymbol{k}}+f^1_{n\boldsymbol{k}}+O\left(E^2\right) \\ &= f^0_{n\boldsymbol{k}}+e\boldsymbol{E}\cdot\boldsymbol{F}_{n\boldsymbol{k}}\frac{\partial f^0_{n\boldsymbol{k}}}{\partial\varepsilon_{n\boldsymbol{k}}}+O\left(E^2\right), \end{aligned} \tag{6.6}$$

where $\boldsymbol{F}_{n\boldsymbol{k}}$ characterizes the first-order deviation from equilibrium of the electron distribution. We substitute Eq. (6.6) into both sides of Eq. (6.5), and obtain a linearized BTE for the distribution deviation $\boldsymbol{F}_{n\boldsymbol{k}}$ keeping only terms up to first-order in the electric field:

$$\boldsymbol{F}_{n\boldsymbol{k}}=\tau_{n\boldsymbol{k}}\boldsymbol{v}_{n\boldsymbol{k}}+\frac{\tau_{n\boldsymbol{k}}}{\mathcal{N}_{\boldsymbol{q}}}\sum_{m,\nu\boldsymbol{q}}\boldsymbol{F}_{m\boldsymbol{k}+\boldsymbol{q}}W^{\nu\boldsymbol{q}}_{n\boldsymbol{k},m\boldsymbol{k}+\boldsymbol{q}}, \tag{6.7}$$

where $\tau_{n\boldsymbol{k}}$ is the electron relaxation time, computed as the inverse of the scattering rate, $\tau_{n\boldsymbol{k}}=\Gamma^{-1}_{n\boldsymbol{k}}$. The scattering rate $\Gamma_{n\boldsymbol{k}}$ is given by

$$\Gamma_{n\boldsymbol{k}}=\frac{1}{\mathcal{N}_{\boldsymbol{q}}}\sum_{m,\nu\boldsymbol{q}}W^{\nu\boldsymbol{q}}_{n\boldsymbol{k},m\boldsymbol{k}+\boldsymbol{q}}. \tag{6.8}$$

The scattering probability $W^{\nu\boldsymbol{q}}_{n\boldsymbol{k},m\boldsymbol{k}+\boldsymbol{q}}$ involves both phonon emission and absorption processes:

$$\begin{aligned} W^{\nu\boldsymbol{q}}_{n\boldsymbol{k},m\boldsymbol{k}+\boldsymbol{q}} = &\frac{2\pi}{\hbar}\left|g_{mn\nu}(\boldsymbol{k},\boldsymbol{q})\right|^2 \\ &\times\left[\delta\left(\varepsilon_{n\boldsymbol{k}}-\hbar\omega_{\nu\boldsymbol{q}}-\varepsilon_{m\boldsymbol{k}+\boldsymbol{q}}\right)\left(1+N^0_{\nu\boldsymbol{q}}-f^0_{m\boldsymbol{k}+\boldsymbol{q}}\right)\right. \\ &\left.+\,\delta\left(\varepsilon_{n\boldsymbol{k}}+\hbar\omega_{\nu\boldsymbol{q}}-\varepsilon_{m\boldsymbol{k}+\boldsymbol{q}}\right)\left(N^0_{\nu\boldsymbol{q}}+f^0_{m\boldsymbol{k}+\boldsymbol{q}}\right)\right], \end{aligned} \tag{6.9}$$

where $N^0_{\nu\boldsymbol{q}}$ are equilibrium Bose-Einstein phonon occupations. Note that since $\tau_{n\boldsymbol{k}}$ is an electron quasiparticle lifetime, it can be written equivalently as the imaginary part of the e-ph self-energy [20], $\tau^{-1}_{n\boldsymbol{k}}=2\mathrm{Im}\Sigma^{e\text{-ph}}_{n\boldsymbol{k}}/\hbar$.

In the RTA, we neglect the second term in Eq. (6.7) and obtain $\boldsymbol{F}_{n\boldsymbol{k}}=\tau_{n\boldsymbol{k}}\boldsymbol{v}_{n\boldsymbol{k}}$. In some cases, the second term in Eq. (6.7) cannot be neglected. In metals, a commonly used scheme to approximate this term is to add a factor of $(1-\cos\theta_{\boldsymbol{k},\boldsymbol{k}+\boldsymbol{q}})$ to Eq. (6.9), where $\theta_{\boldsymbol{k},\boldsymbol{k}+\boldsymbol{q}}$ is the scattering angle between $\boldsymbol{k}$ and $\boldsymbol{k}+\boldsymbol{q}$. The resulting so-called "transport relaxation time" is then used to compute the transport properties [20]. PERTURBO implements a more rigorous approach and directly solves Eq. (6.7) using an iterative method [21, 22], for which we rewrite Eq. (6.7) as

$$\boldsymbol{F}^{i+1}_{n\boldsymbol{k}} = \boldsymbol{F}^{0}_{nk} + \frac{\tau_{n\boldsymbol{k}}}{\mathcal{N}_{\boldsymbol{q}}} \sum_{m,\nu\boldsymbol{q}} \boldsymbol{F}^{i}_{m\boldsymbol{k}+\boldsymbol{q}} W^{\nu\boldsymbol{q}}_{n\boldsymbol{k},m\boldsymbol{k}+\boldsymbol{q}} \,. \tag{6.10}$$

In the iterative algorithm, we choose in the first step $\boldsymbol{F}^{0}_{nk} = \tau_{n\boldsymbol{k}}\boldsymbol{v}_{n\boldsymbol{k}}$, and then compute the following steps using Eq. (6.10) until the difference $|\boldsymbol{F}^{i+1}_{n\boldsymbol{k}} - \boldsymbol{F}^{i}_{n\boldsymbol{k}}|$ is within the convergence threshold.

Once $\boldsymbol{F}_{nk}$ has been computed, either within the RTA or with the iterative solution of the BTE in Eq. (6.10), the conductivity tensor is obtained as

$$\begin{aligned}\sigma_{\alpha\beta} &= \frac{1}{\Omega \boldsymbol{E}_{\beta}} \cdot \frac{S}{\mathcal{N}_{\boldsymbol{k}}} \sum_{n\boldsymbol{k}} -e\boldsymbol{v}^{\alpha}_{n\boldsymbol{k}} \cdot f^{1}_{n\boldsymbol{k}} \\ &= \frac{e^2 S}{\mathcal{N}_{\boldsymbol{k}}\Omega} \sum_{n\boldsymbol{k}} \boldsymbol{v}^{\alpha}_{n\boldsymbol{k}} \boldsymbol{F}^{\beta}_{nk} \left(-\frac{\partial f^{0}_{n\boldsymbol{k}}}{\partial \varepsilon_{n\boldsymbol{k}}} \right),\end{aligned} \tag{6.11}$$

where α and β are Cartesian directions, Ω is the volume of the unit cell, and S is the spin degeneracy. We also compute the carrier mobility tensor, $\mu_{\alpha\beta} = \sigma_{\alpha\beta}/(e\, n_c)$, by dividing the conductivity tensor through the carrier concentration n_c.

In our implementation, we conveniently rewrite Eq. (6.11) as

$$\sigma_{\alpha\beta} = e^2 \int dE(-\partial f^0/\partial E)\Sigma_{\alpha\beta}(E), \tag{6.12}$$

where $\Sigma_{\alpha\beta}(E)$ is the transport distribution function (TDF) at energy E,

$$\Sigma_{\alpha\beta}(E) = \frac{S}{\mathcal{N}_{\boldsymbol{k}}\Omega} \sum_{n\boldsymbol{k}} \boldsymbol{v}^{\alpha}_{n\boldsymbol{k}} \boldsymbol{F}^{\beta}_{nk} \delta(E - \varepsilon_{n\boldsymbol{k}}), \tag{6.13}$$

which is computed in PERTURBO using the tetrahedron integration method [23]. The integrand in Eq. (6.12) can be used to characterize the contributions to transport as a function of electron energy [12, 13]. The code can also compute the Seebeck coefficient $\boldsymbol{S}$ from the TDF, using

$$[\boldsymbol{\sigma}\boldsymbol{S}]_{\alpha\beta} = \frac{e}{T} \int dE(-\partial f^0/\partial E)(E - \mu)\Sigma_{\alpha\beta}(E), \tag{6.14}$$

where μ is the chemical potential and T is the temperature.

6.3 Capabilities and workflow

Code organization and capabilities

PERTURBO contains two executables: a core program `perturbo.x` and the program `qe2pert.x`, which interfaces the QE code and `perturbo.x`, as shown in

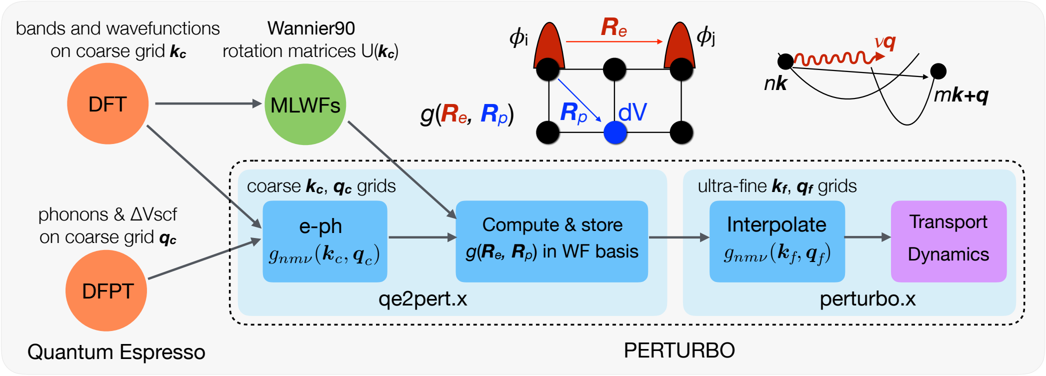

Figure 6.1: Workflow of the PERTURBO code. Before running PERTURBO, the user performs DFT calculations on the system of interest to obtain the Bloch states on a coarse $\boldsymbol{k}_c$-point grid and DFPT calculations to obtain the lattice dynamical properties and perturbation potentials on a coarse $\boldsymbol{q}_c$-point grid. The `qe2pert.x` executable of PERTURBO computes the e-ph matrix elements on coarse $\boldsymbol{k}_c$- and $\boldsymbol{q}_c$-point grids, from which the e-ph matrix elements in the localized Wannier basis are obtained with the rotation matrices from Wannier90. The core executable `perturbo.x` is then employed to interpolate the band structure, phonon dispersion, and e-ph matrix elements on ultra-fine $\boldsymbol{k}_f$- and $\boldsymbol{q}_f$-point grids, and to perform charge transport and carrier dynamics calculations.

Fig. 6.1. The current release supports DFT and DFPT calculations with norm-conserving or ultrasoft pseudopotentials, with or without SOC; it also supports the Coulomb truncation for 2D materials [41]. The current features include calculations of:

1 Band structure, phonon dispersion, and e-ph matrix elements on arbitrary BZ grids or paths.

2 The e-ph scattering rates, relaxation times, and electron mean free paths for electronic states with any band and $\boldsymbol{k}$-point.

3 Electrical conductivity, carrier mobility, and Seebeck coefficient using the RTA or the iterative solution of the BTE.

4 Nonequilibrium dynamics, such as simulating the cooling and equilibration of excited carriers via interactions with phonons.

Several features of PERTURBO, including the nonequilibrium dynamics, are unique and not available in other existing codes. Many additional features currently being developed or tested will be added to the list in future releases.

PERTURBO stores most of the data and results in HDF5 file format, including all the main results of `qe2pert.x`, the TDF and other files generated in the transport calculations, and the nonequilibrium electron distribution computed in `perturbo.x`. The use of the HDF5 file format improves the portability of the results between different computing systems and is also convenient for post-processing using high-level languages, such as Python and Julia.

Installation and usage of PERTURBO and an up-to-date list of supported features are documented in the user manual distributed along with the source code package, and can also be found on the code website [42].

Computational workflow

Figure 6.1 summarizes the workflow of PERTURBO. Before running PERTURBO, the user needs to carry out DFT and DFPT calculations with the QE code, and Wannier function calculations with Wannier90. In our workflow, we first carry out DFT calculations to obtain the band energies and Bloch wavefunctions on a coarse grid with points $\boldsymbol{k}_c$. A regular Monkhorst-Pack (MP) $\boldsymbol{k}_c$-point grid centered at Γ and Bloch states for all $\boldsymbol{k}_c$-points in the first BZ are required. We then construct a set of Wannier functions from the Bloch wavefunctions using the Wannier90 code. Only the rotation matrices $\mathcal{U}$ that transform the DFT Bloch wavefunctions to the Wannier gauge and the center of the Wannier functions are required as input to PERTURBO. We also perform DFPT calculations to obtain the dynamical matrices and e-ph perturbation potentials on a coarse MP grid with points $\boldsymbol{q}_c$. In the current version, the electron $\boldsymbol{k}_c$-point grid and phonon $\boldsymbol{q}_c$-point grid need to be commensurate. Since DFPT is computationally demanding, we carry out the DFPT calculations only for $\boldsymbol{q}_c$-points in the irreducible wedge of the BZ, and then obtain the dynamical matrices and perturbation potentials in the full BZ grid using space group and time reversal symmetries (see Sec. 6.4).

The executable `qe2pert.x` reads the results from DFT and DFPT calculations, including the Bloch states $|\psi_{n\boldsymbol{k}_c}\rangle$, dynamical matrices $D(\boldsymbol{q}_c)$ and e-ph perturbation potentials $\partial_{\boldsymbol{q}_c,\kappa\alpha}V$, and then computes the electron Hamiltonian in the Wannier basis [Eq. (1.3)] and the IFCs [Eq. (1.8)]. It also computes the e-ph matrix elements on coarse grids and transforms them to the localized Wannier basis using Eqs. (1.12)-(1.13). To ensure that the same Wannier functions are used for the electron Hamiltonian and e-ph matrix elements, we use the same DFT Bloch states $|\psi_{n\boldsymbol{k}_c}\rangle$ and $\mathcal{U}(\boldsymbol{k}_c)$ matrices for the calculations in Eqs. (1.3) and (1.12)-(1.13). Following these preliminary steps, `qe2pert.x` outputs all the relevant data to an HDF5 file, which is the main input for `perturbo.x`.

The executable `perturbo.x` reads the data computed by `qe2pert.x` and carries out the transport and dynamics calculations discussed above. To accomplish these tasks, `perturbo.x` interpolates the band structure, phonon dispersion, and e-ph matrix elements on fine $\boldsymbol{k}$- and $\boldsymbol{q}$-point BZ grids, and uses these quantities in the various calculations.

6.4 Technical aspects

e-ph matrix elements on coarse grids

As discussed in Sec. 1.2, we compute directly the e-ph matrix elements in Eq. (1.12) using the DFT states on a coarse $\boldsymbol{k}_c$-point grid and the perturbation potentials on a coarse $\boldsymbol{q}_c$-point grid. It is convenient to rewrite Eq. (1.12) in terms of lattice-periodic quantities,

$$\tilde{g}_{mn}^{\kappa\alpha}(\boldsymbol{k}_c, \boldsymbol{q}_c) = \left\langle u_{m\boldsymbol{k}_c+\boldsymbol{q}_c} \left| \partial_{\boldsymbol{q}_c,\kappa\alpha} v \right| u_{n\boldsymbol{k}_c} \right\rangle, \tag{6.15}$$

where $|u_{n\boldsymbol{k}_c}\rangle$ is the lattice periodic part of the Bloch wavefunction and $\partial_{\boldsymbol{q}_c,\kappa\alpha} v = e^{-i\boldsymbol{q}_c\cdot\boldsymbol{r}} \partial_{\boldsymbol{q}_c,\kappa\alpha} V$ is the lattice-periodic perturbation potential. Since we compute only $|u_{n\boldsymbol{k}_c}\rangle$ on the coarse grid of the first BZ, $|u_{m\boldsymbol{k}_c+\boldsymbol{q}_c}\rangle$ may not be available because $\boldsymbol{k}_c + \boldsymbol{q}_c$ may be outside of the first BZ. However, by requiring the $\boldsymbol{q}_c$-point grid to be commensurate with and smaller than (or equal to) the $\boldsymbol{k}_c$-point grid, we can satisfy the relationship $\boldsymbol{k}_c + \boldsymbol{q}_c = \boldsymbol{k}'_c + \boldsymbol{G}_0$, where $\boldsymbol{k}'_c$ is on the coarse grid and $\boldsymbol{G}_0$ is a reciprocal lattice vector. Starting from $|u_{m\boldsymbol{k}'_c}\rangle = \sum_{\boldsymbol{G}} c_{\boldsymbol{k}'_c}(\boldsymbol{G}) e^{i\boldsymbol{G}\cdot\boldsymbol{r}}$, we can thus obtain $|u_{m\boldsymbol{k}_c+\boldsymbol{q}_c}\rangle$ with negligible computational cost as

$$|u_{m\boldsymbol{k}_c+\boldsymbol{q}_c}\rangle = e^{-i\boldsymbol{G}_0\cdot\boldsymbol{r}} |u_{m\boldsymbol{k}'_c}\rangle = \sum_{\boldsymbol{G}} c_{\boldsymbol{k}'_c}(\boldsymbol{G}) e^{i(\boldsymbol{G}-\boldsymbol{G}_0)\cdot\boldsymbol{r}}. \tag{6.16}$$

The lattice-periodic perturbation potential $\partial_{\boldsymbol{q}_c,\kappa\alpha} v$ consists of multiple terms, and can be divided into a local and a non-local part [43]. The non-local part includes the perturbation potentials due to the non-local terms of pseudopotentials, which typically includes the Kleinman-Bylander projectors and SOC terms. The local part includes the perturbations to the local part of the pseudopotentials as well as the self-consistent potential contribution. The latter, denoted as $\partial_{\boldsymbol{q}_c,\kappa\alpha} v_{\text{sc}}(\boldsymbol{r})$, accounts for the change in the Hartree and exchange-correlation potentials in response to the atomic displacements. While the pseudopotential contributions, both local and non-local, can be evaluated efficiently for all $\boldsymbol{q}_c$-points with the analytical formula given in Ref. [43], the self-consistent contribution $\partial_{\boldsymbol{q}_c,\kappa\alpha} v_{\text{sc}}(\boldsymbol{r})$ is computed and stored in real space using expensive DFPT calculations. This step is the main bottleneck of the entire e-ph computational workflow.

To improve the efficiency, we compute the self-consistent contribution with DFPT only for $\boldsymbol{q}_c$-points in the irreducible BZ wedge, and then unfold it to the equivalent points $\mathcal{S}\boldsymbol{q}_c$ in the full BZ using symmetry operations [34, 44]. For non-magnetic systems, $\partial_{\boldsymbol{q}_c,\kappa\alpha} v_{\mathrm{sc}}(\boldsymbol{r})$ is a scalar function, so we can obtain the self-consistent contribution at $\mathcal{S}\boldsymbol{q}_c$ by rotating $\partial_{\boldsymbol{q}_c,\kappa\alpha} v_{\mathrm{sc}}(\boldsymbol{r})$ [34]:

$$\begin{aligned}\partial_{\mathcal{S}\boldsymbol{q}_c,\kappa\alpha} v_{\mathrm{sc}}(\boldsymbol{r}) = &\sum_{\kappa'\beta} e^{i\boldsymbol{q}_c\cdot\boldsymbol{\tau}_{\kappa'} - i\mathcal{S}\boldsymbol{q}_c\cdot\boldsymbol{\tau}_{\kappa}} \\ &\times \left[\mathcal{S}^{-1}\right]_{\beta\alpha} \partial_{\boldsymbol{q}_c,\kappa'\beta} v_{\mathrm{sc}}\left(\{\mathcal{S}|\boldsymbol{t}\}^{-1}\boldsymbol{r}\right),\end{aligned} \tag{6.17}$$

where $\{\mathcal{S}|\boldsymbol{t}\}$ is a space group symmetry operation of the crystal. A detailed derivation of Eq. (6.17) can be found in Appendix C of Ref. [34]. In addition to space group operations, time reversal symmetry is also used for non-magnetic systems via

$$\partial_{-\boldsymbol{q}_c,\kappa\alpha} v_{\mathrm{sc}}(\boldsymbol{r}) = [\partial_{\boldsymbol{q}_c,\kappa\alpha} v_{\mathrm{sc}}(\boldsymbol{r})]^*, \tag{6.18}$$

since the time reversal symmetry operator for a scalar function is the complex conjugation operator. We emphasize that Eq. (6.17) is only used to unfold the self-consistent contribution of the perturbation potential, while all the terms due to the pseudopotentials are computed directly, without using symmetry, for all the $\boldsymbol{q}_c$-points in the coarse grid.

An alternative approach to obtain the e-ph matrix elements in the full BZ starting from results in the irreducible wedge is to rotate the wavefunctions instead of the perturbation potential:

$$\begin{aligned}&\langle u_{m\boldsymbol{k}_c+\mathcal{S}\boldsymbol{q}_c}|\partial_{\mathcal{S}\boldsymbol{q}_c,\kappa\alpha} v|u_{n\boldsymbol{k}_c}\rangle = \\ &\qquad \langle u_{m\boldsymbol{k}_c+\mathcal{S}\boldsymbol{q}_c}|\mathcal{D}^{\dagger}_{\{\mathcal{S}|\boldsymbol{t}\}} \partial_{\boldsymbol{q}_c,\kappa\alpha} v \, \mathcal{D}_{\{\mathcal{S}|\boldsymbol{t}\}}|u_{n\boldsymbol{k}_c}\rangle,\end{aligned} \tag{6.19}$$

where $\mathcal{D}_{\{\mathcal{S}|\boldsymbol{t}\}}$ is the symmetry operator acting on the wavefunction. In this approach (not employed in PERTURBO), the perturbation potentials are needed only for $\boldsymbol{q}_c$ in the irreducible wedge [32]. It is important to keep in mind that the wavefunctions are spinors in non-collinear calculations, so the symmetry operators $\mathcal{D}_{\{\mathcal{S}|\boldsymbol{t}\}}$ should act both on the spatial coordinate and in spin space. Neglecting the rotation in spin space would lead to significant errors in the computed e-ph matrix elements, especially in calculations with SOC.

To benchmark our implementation, we compare the e-ph matrix elements obtained using symmetry operations to those from direct DFPT calculations. The absolute

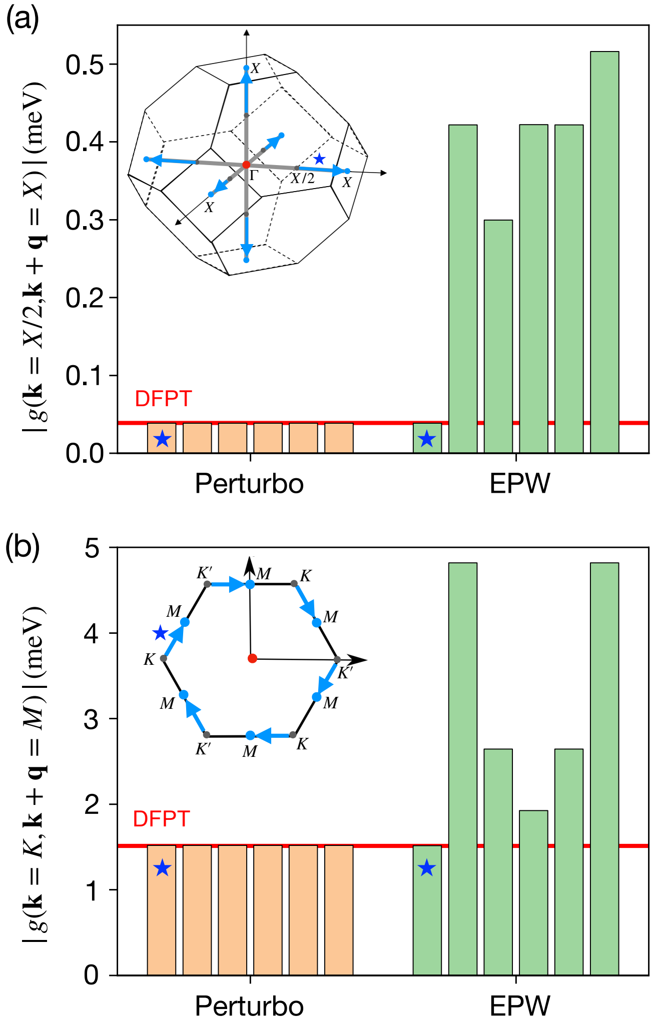

Figure 6.2: Absolute value of the gauge-invariant e-ph matrix elements, $|g\left(\boldsymbol{k}, \boldsymbol{q}\right)|$ in Eq. (6.20), computed with PERTURBO (orange) and EPW (green) in (a) silicon and (b) monolayer MoS_2. SOC is included in both cases. The six bars are $|g\left(\boldsymbol{k}, \boldsymbol{q}\right)|$ values for six equivalent $(\boldsymbol{k}, \boldsymbol{q})$ pairs connected by symmetry, which are shown as blue arrows in the inset. The result with $\boldsymbol{q}$ in the irreducible wedge (labeled with a blue star) is computed directly with the DFPT perturbation potential, while the others are obtained by applying symmetry operations either on the perturbation potentials (PERTURBO) or on the wavefunctions (EPW). The red horizontal line shows the benchmark values computed directly from DFPT for all $(\boldsymbol{k}, \boldsymbol{q})$ pairs.

value of the e-ph matrix elements, $|g\left(\boldsymbol{k}, \boldsymbol{q}\right)|$, is computed in gauge-invariant form for each phonon mode (with index ν) by summing over bands:

$$|g_{\nu}\left(\boldsymbol{k}, \boldsymbol{q}\right)| = \sqrt{\sum_{mn} |g_{mn\nu}\left(\boldsymbol{k}, \boldsymbol{q}\right)|^2 / N_b}, \tag{6.20}$$

where m, n are band indices for the selected N_b bands. We perform the comparison with direct DFPT calculations for silicon and monolayer MoS_2 as examples of a bulk and a 2D material, respectively. We include SOC in both cases. For silicon, we choose $\boldsymbol{k} = X/2$, $\boldsymbol{k} + \boldsymbol{q} = X$ and compute $|g\,(\boldsymbol{k}, \boldsymbol{q})|$ in Eq. (6.20) using the four highest valence bands; for monolayer MoS_2, we choose $\boldsymbol{k} = K$, $\boldsymbol{k} + \boldsymbol{q} = M$ and compute $|g\,(\boldsymbol{k}, \boldsymbol{q})|$ for the two lowest conduction bands with 2D Coulomb truncation turned off. For both silicon and monolayer MoS_2, we compute $|g\,(\boldsymbol{k}, \boldsymbol{q})|$ for all the six *equivalent* $(\boldsymbol{k}, \boldsymbol{q})$ pairs connected by space group and time reversal symmetry [see the inset of Fig. 6.2(a, b)]. As a benchmark, DFPT calculations are carried out to evaluate directly $|g\,(\boldsymbol{k}, \boldsymbol{q})|$ for all the six $(\boldsymbol{k}, \boldsymbol{q})$ pairs. The results shown in Fig. 6.2 are for the lowest acoustic mode, though the results for the other modes show similar trends. The $|g\,(\boldsymbol{k}, \boldsymbol{q})|$ values computed with DFPT are identical for the six equivalent $(\boldsymbol{k}, \boldsymbol{q})$ pairs (see the red horizontal line in Fig. 6.2), which is expected based on symmetry. In the PERTURBO calculation, only the $(\boldsymbol{k}, \boldsymbol{q})$ pair with $\boldsymbol{q}$ in the irreducible wedge is computed directly with the perturbation potential from DFPT, while results for the other five equivalent $(\boldsymbol{k}, \boldsymbol{q})$ pairs are obtained by rotating the self-consistent perturbation potential. The results obtained with this approach match to a high accuracy the DFPT benchmark results, which validates the perturbation potential rotation approach implemented in PERTURBO.

For comparison, we show in Fig. 6.2 the results from the alternative approach of rotating the wavefunctions, as implemented in the EPW code (version 5.2) [45]. Surprisingly, using the EPW code only the $|g\,(\boldsymbol{k}, \boldsymbol{q})|$ value for the $(\boldsymbol{k}, \boldsymbol{q})$ pair containing the irreducible $\boldsymbol{q}$-point agrees with the DFPT benchmark, while all other $|g\,(\boldsymbol{k}, \boldsymbol{q})|$ values for $\boldsymbol{q}$-points obtained using symmetry operations show significant errors. We stress again that all the results in Fig. 6.2 are computed with SOC. We have verified that, in the absence of SOC, both PERTURBO and EPW produce results in agreement with DFPT. The likely reason for the failure of EPW in this test is that in EPW the wavefunctions are rotated as scalars even in the presence of SOC, rather than as spinors as they should (that is, the rotation in spin space is missing). Further investigation of this discrepancy is critical, since the large errors in EPW for the coarse-grid e-ph matrix elements will propagate to the interpolated matrix elements on fine grids, giving incorrect results in calculations including SOC carried out with EPW [46].

Wigner-Seitz supercell for Wannier interpolation

As discussed in Sec. 1.2, the DFT Bloch states obtained at $\boldsymbol{k}_c$-points on a regular BZ grid are used to construct the Wannier functions. A discrete BZ grid implies a Born-von Karman (BvK) boundary condition in real space, so that an $N \times N \times N$ $\boldsymbol{k}_c$-point grid corresponds (for simple cubic, but extensions are trivial) to a BvK supercell of size $Na \times Na \times Na$, where a is the lattice constant of the unit cell. If we regard the crystal as made up by an infinite set of BvK supercells at lattice vectors $\boldsymbol{T}_e$, we can label any unit cell in the crystal through its position $\boldsymbol{T}_e + \boldsymbol{R}_e$, where $\boldsymbol{R}_e$ is the unit cell position in the BvK supercell. Because of the BvK boundary condition, the Bloch wavefunctions are truly periodic functions over the BvK supercell, and the Wannier function $|n\boldsymbol{R}_e\rangle$ obtained using Eq. (1.1) is actually the superposition of images of the Wannier function in all the BvK supercells. Therefore, we can write $|n\boldsymbol{R}_e\rangle = \sum_{\boldsymbol{T}_e} |n, \boldsymbol{R}_e + \boldsymbol{T}_e\rangle^0$, where $|n, \boldsymbol{R}_e + \boldsymbol{T}_e\rangle^0$ denotes the image of the Wannier function in the BvK supercell at $\boldsymbol{T}_e$. Similarly, the electron Hamiltonian computed using Eq. (1.3) can be expressed as

$$H_{nn'}(\boldsymbol{R}_e) = \sum_{\boldsymbol{T}_e} H^0_{nn'}(\boldsymbol{R}_e + \boldsymbol{T}_e). \tag{6.21}$$

The hopping matrix elements $H^0_{nn'}(\boldsymbol{R}_e + \boldsymbol{T}_e)$ usually decay rapidly as the distance between two image Wannier functions increases. The BvK supercell should be large enough to guarantee that only the hopping term between the two Wannier function images with the shortest distance is significant, while all other terms in the summation over $\boldsymbol{T}_e$ in Eq. (6.21) are negligible.

We use this "least-distance" principle to guide our choice of a set of $\tilde{\boldsymbol{R}}_e$ vectors for the Wannier interpolation. For each Hamiltonian matrix element labeled by $(n, n', \boldsymbol{R}_e)$ in Eq. (6.21), we compute the distance $d = |\boldsymbol{T}_e + \boldsymbol{R}_e + \boldsymbol{\tau}_{n'} - \boldsymbol{\tau}_n|$, with $\boldsymbol{\tau}_n$ the position of the Wannier function center in the unit cell, and find the vector $\boldsymbol{T}^0_e$ giving the minimum distance. The set of vectors $\tilde{\boldsymbol{R}}_e = \boldsymbol{R}_e + \boldsymbol{T}^0_e$ is then selected to construct the Wigner-Seitz supercell used in the Wannier interpolation. We compute $H_{nn'}(\tilde{\boldsymbol{R}}_e)$ using Eq. (1.3) and use it to interpolate the band structure with Eq. (1.4). Note that the same strategy to construct the Wigner-Seitz supercell is also used in the latest version of Wannier90 [26].

Similarly, we choose a set of least-distance $\tilde{\boldsymbol{R}}_p$ vectors for the interpolation of the phonon dispersion, and separately determine least-distance $\tilde{\boldsymbol{R}}_e$ and $\tilde{\boldsymbol{R}}_p$ pairs for the interpolation of the e-ph matrix elements in Eqs. (1.13)-(1.14).

Brillouin zone sampling and integration

Several computational tasks carried out by PERTURBO require integration in the BZ. Examples include scattering rate and TDF calculations, in Eqs. (6.8) and (6.13), respectively, and the iterative BTE solution in Eq. (6.10). In PERTURBO, we adopt different BZ sampling and integration approaches for different kinds of calculations. For transport calculations, we use the tetrahedron method [23] for the integration over $\boldsymbol{k}$ in Eq. (6.13). We sample $\boldsymbol{k}$-points in the first BZ using a regular MP grid centered at Γ, and divide the BZ into small tetrahedra by connecting neighboring $\boldsymbol{k}$-points. The integration is first performed inside each tetrahedron, and the results are then added together to compute the BZ integral. To speed up these transport calculations, we set up a user-defined window spanning a small energy range (typically ~0.5 eV) near the band edge in semiconductors or Fermi level in metals, and restrict the BZ integration to the $\boldsymbol{k}$-points with electronic states in the energy window. Since only states within a few times the thermal energy k_BT of the band edge in semiconductors (or Fermi energy in metals) contribute to transport, including in the tetrahedron integration only $\boldsymbol{k}$-points in the relevant energy window greatly reduces the computational cost.

To compute the e-ph scattering rate for states with given bands and $\boldsymbol{k}$-points, we use the Monte Carlo integration as the default option. We sample random $\boldsymbol{q}$-points in the first BZ to carry out the summation over $\boldsymbol{q}$ in Eq. (6.8) and obtain the scattering rate. One can either increase the number of random $\boldsymbol{q}$-points until the scattering rate is converged or average the results from independent samples. Note that the energy broadening parameter used to approximate the δ function in Eq. (6.9) is important for the convergence of the scattering rate, so the convergence with respect to both the $\boldsymbol{q}$-point grid and broadening needs to be checked carefully [12]. PERTURBO supports random sampling of the $\boldsymbol{q}$-points with either a uniform or a Cauchy distribution; a user-defined $\boldsymbol{q}$-point grid can also be specified in an external file and used in the calculation.

In the carrier dynamics simulations and in the iterative BTE solution in Eq. (6.10), the $\boldsymbol{k}$- and $\boldsymbol{q}$-points should both be on a regular MP grid centered at Γ. The two grids should be commensurate, with the size of the $\boldsymbol{q}$-point grid smaller than or equal to the size of the $\boldsymbol{k}$-point grid. This way, we satisfy the requirement in Eq. (6.10) that each ($\boldsymbol{k}$+$\boldsymbol{q}$)-point is also on the $\boldsymbol{k}$-point grid. To perform efficiently the summation in Eq. (6.10) for all the $\boldsymbol{k}$-points, we organize the scattering probability in Eq. (6.9) using ($\boldsymbol{k}$, $\boldsymbol{q}$) pairs. We first determine a set of bands and $\boldsymbol{k}$-points for states inside the energy window. We then find all the possible scattering processes in which both the initial and final states are in the selected set of $\boldsymbol{k}$-points, and the phonon wave vector connecting the two states is on the $\boldsymbol{q}$-point grid. The scattering processes are indexed as $(\boldsymbol{k}, \boldsymbol{q})$ pairs; their corresponding e-ph matrix elements are computed and stored, and then retrieved from memory during the iteration process.

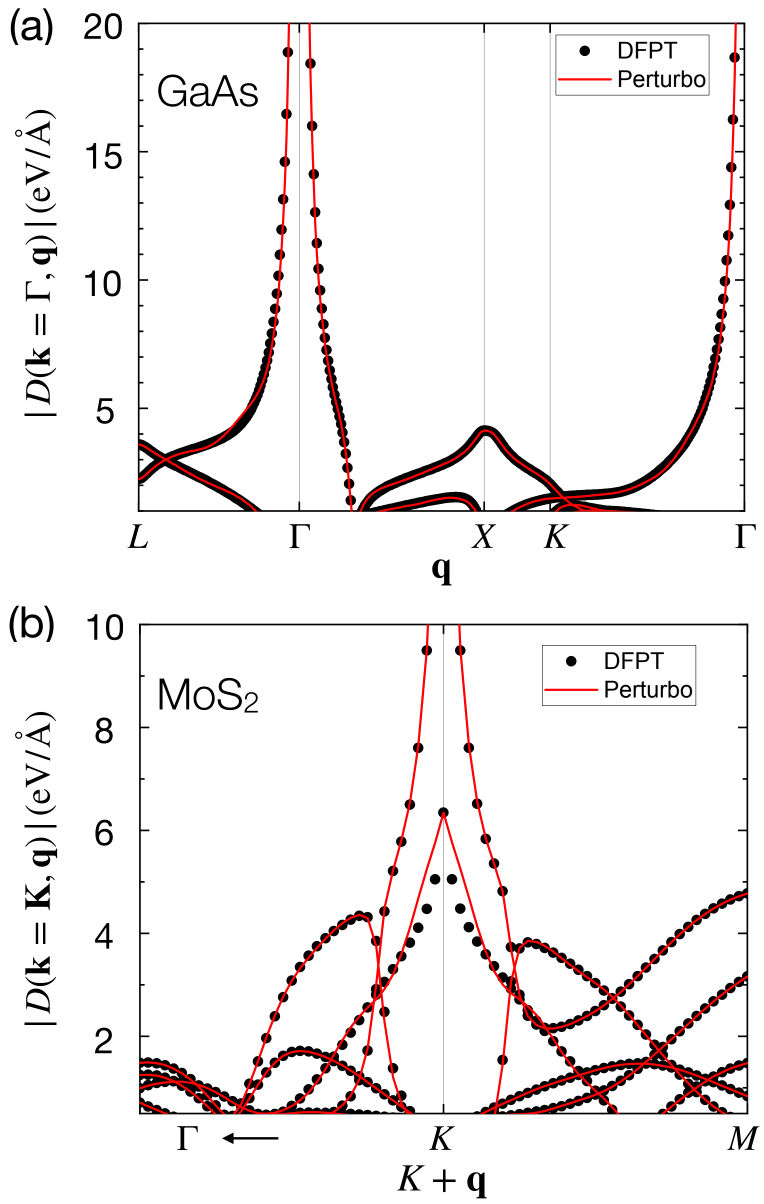

Figure 6.3: The e-ph deformation potential [see Eq. (6.22)] in (a) GaAs and (b) monolayer MoS_2 computed using PERTURBO and compared with direct DFPT calculations for benchmarking.

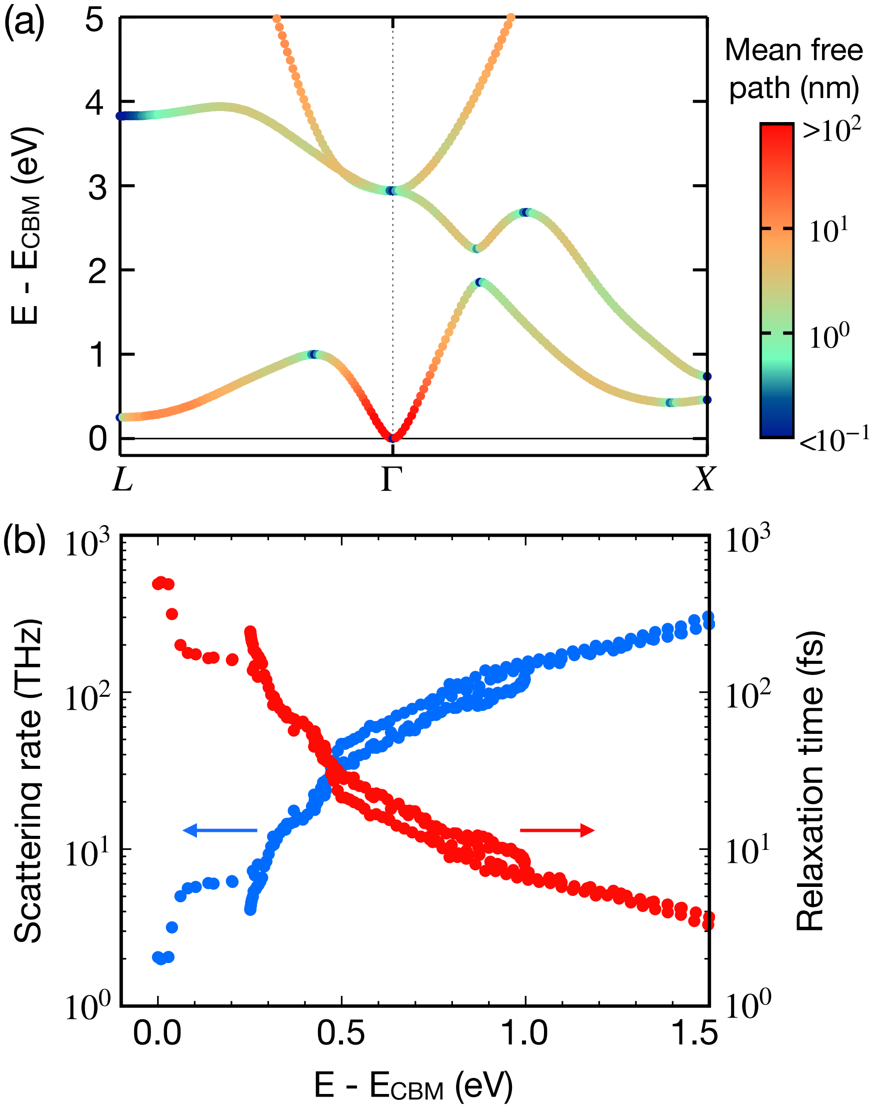

Figure 6.4: (a) Band structure of GaAs overlaid with a log-scale color map of the electron mean free paths computed at 300 K. (b) The *e*-ph scattering rates and their inverse, the relaxation times, for the electronic states in (a) given as a function of electron energy. The energy zero is the CBM.

6.5 Examples

In this section, we demonstrate the capabilities of the PERTURBO code with a few representative examples, including calculations on a polar bulk material (GaAs), a 2D material with SOC (monolayer MoS_2), and an organic crystal (naphthalene) with a relatively large unit cell with 36 atoms.

The ground state and band structure are computed using DFT with a plane-wave basis with the QE code; this is a preliminary step for all PERTURBO calculations, as discussed above. For GaAs, we use the same computational settings as in Ref. [12], namely a lattice constant of 5.556 Å and a plane-wave kinetic energy cutoff of 72 Ry. For monolayer MoS_2, we use a 72 Ry kinetic energy cutoff, an experimental lattice constant of 3.16 Å and a layer-normal vacuum spacing of 17 Å. All calculations are carried out in the local density approximation of DFT using norm-conserving pseudopotentials. For MoS_2, we use fully relativistic norm-conserving pseudopotentials from Pseudo Dojo [47] to include SOC effects.

Lattice dynamical properties and the e-ph perturbation potential [see Eq. (1.11)] are

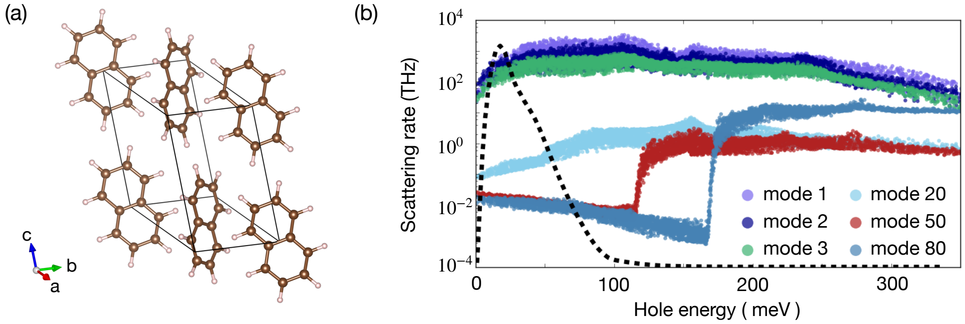

Figure 6.5: (a) Crystal structure of naphthalene, a prototypical organic molecular semiconductor with 36 atoms in the unit cell. (b) Mode-resolved e-ph scattering rates in naphthalene, computed at 300 K. Results are shown for three acoustic modes (1-3) associated with inter-molecular vibrations and three optical modes (20, 50, 80) associated with intra-molecular vibrations. The black dashed line represents the conductivity integrand in Eq. (6.12) and quantifies the relative contribution to transport as a function of electron energy. It is seen that only states within about 100 meV of the valence band maximum contribute to hole transport.

computed on coarse $\boldsymbol{q}$-point grids of $8\times8\times8$ (GaAs) and $24\times24\times1$ (MoS_2) using DFPT as implemented in the QE code. We use the 2D Coulomb cutoff approach in DFPT for MoS_2 to remove the spurious interactions between layers [39]. For naphthalene, we use the same computational settings as in Ref. [15] for the DFT and DFPT calculations. Note that we only perform the DFPT calculations for the irreducible $\boldsymbol{q}$-points in the BZ grid, following which we extend the dynamical matrices to the entire BZ grid using space group and time reversal symmetry [see Eq. (6.17)] with our `qe2pert.x` routines.

The Wannier90 code is employed to obtain localized Wannier functions in each material. Only the centers of the Wannier functions and the rotation matrices $\mathcal{U}$ [see Eq. (1.2)] are read as input by `qe2pert.x`. The Wannier functions for GaAs are constructed using a coarse $8\times8\times8$ $\boldsymbol{k}$-point grid and sp^3 orbitals centered at the Ga and As atoms as an initial guess. For MoS_2, we construct 22 Wannier functions using a coarse $24 \times 24 \times 1$ $\boldsymbol{k}$-point grid and an initial guess of d orbitals on Mo and s orbitals on S atoms, using both spin up and spin down orbitals. For naphthalene, we construct two Wannier functions for the two highest valence bands using a coarse $\boldsymbol{k}$-point grid of $4 \times 4 \times 4$. The selected columns of density matrix (SCDM) approach [48] is employed to generate an initial guess automatically.

Following the workflow in Fig. 6.1, we compute the e-ph matrix elements on the coarse $\boldsymbol{k}$- and $\boldsymbol{q}$-point grids and obtain the e-ph matrix elements in the localized Wannier basis using `qe2pert.x`.

Interpolation of the e-ph matrix elements

It is important to check the accuracy of all interpolations before performing transport and carrier dynamics calculations. PERTURBO provides routines and calculation modes to compute and output the interpolated band structure, phonon dispersion, and e-ph matrix elements, which should be compared to the same quantities computed using DFT and DFPT to verify that the interpolation has worked as expected. The comparison is straightforward for the band structure and phonon dispersion. Here we focus on validating the interpolation of the e-ph matrix elements, a point often overlooked in e-ph calculations. Since the e-ph matrix elements are gauge dependent, a direct comparison of $g_{mn\nu}(\boldsymbol{k},\boldsymbol{q})$ from PERTURBO and DFPT calculations is not meaningful. Instead, we compute the absolute value of the e-ph matrix elements, $|g_\nu(\boldsymbol{k},\boldsymbol{q})|$, in the gauge-invariant form of Eq. (6.20), and the closely related "deformation potential", which following Ref. [37] is defined as

$$D_\nu(\boldsymbol{k},\boldsymbol{q}) = \sqrt{2\omega_{\nu\boldsymbol{q}} M_{tot}}\, |g_\nu(\boldsymbol{k},\boldsymbol{q})| / \hbar, \tag{6.22}$$

where M_{tot} is the total mass of the atoms in the unit cell.

We show in Fig. 6.3 the deformation potentials for the bulk polar material GaAs and the 2D polar material MoS_2. For GaAs, we choose the Γ-point as the initial electron momentum $\boldsymbol{k}$, and vary the phonon wave vector $\boldsymbol{q}$ along a high-symmetry path, computing $D_\nu(\boldsymbol{k},\boldsymbol{q})$ for the highest valence band. For MoS_2, we choose the K-point as the initial electron momentum and vary the final electron momentum $K + \boldsymbol{q}$ along a high-symmetry path, computing $D_\nu(\boldsymbol{k},\boldsymbol{q})$ by summing over the two lowest conduction bands. In both cases, results are computed for all phonon modes. The respective polar corrections are included in both materials, which is crucial to accurately interpolate the e-ph matrix elements at small $\boldsymbol{q}$. The results show clearly that the e-ph interpolation works as expected, giving interpolated matrix elements in close agreement with direct DFPT calculations.

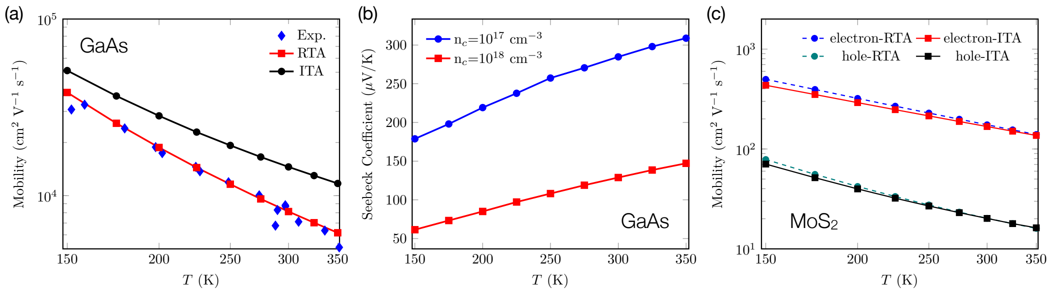

Figure 6.6: (a) Electron mobility in GaAs as a function of temperature, computed using the RTA and ITA methods and compared with experimental data [49, 50]. (b) Temperature dependent Seebeck coefficient in GaAs, computed for two different carrier concentrations. (c) Electron and hole mobilities in monolayer MoS_2 as a function of temperature, computed using the RTA and ITA.

Scattering rates and electron mean free paths

The `perturbo.x` routines can compute the e-ph scattering rate ($\Gamma_{n\boldsymbol{k}}$), relaxation time ($\tau_{n\boldsymbol{k}} = \Gamma^{-1}_{n\boldsymbol{k}}$), and electron mean free path ($L_{n\boldsymbol{k}} = \tau_{n\boldsymbol{k}} v_{n\boldsymbol{k}}$) for electronic states with any desired band and crystal momentum $\boldsymbol{k}$. Figure 6.4 shows the results for GaAs, in which we compute these quantities for the lowest few conduction bands and for $\boldsymbol{k}$-points along a high-symmetry path.

Carefully converging the scattering rate in Eq. (6.8) is important, but it can be far from trivial since in some cases convergence requires sampling millions of $\boldsymbol{q}$-points in the BZ. A widely applicable scheme is to sample random $\boldsymbol{q}$-points uniformly, and compute the scattering rates for increasing numbers of $\boldsymbol{q}$-points until the scattering rates are converged. However, uniform sampling can be nonoptimal in specific scenarios in which importance sampling can be used to speed up the convergence. For polar materials such as GaAs, the scattering rate for electronic states near the conduction band minimum (CBM) is dominated by small-$\boldsymbol{q}$ (intravalley) LO phonon scattering. In this case, importance sampling with a Cauchy distribution [12] that more extensively samples small $\boldsymbol{q}$ values can achieve convergence more effectively than uniform sampling. On the other hand, for electronic states in GaAs farther in energy from the band edges, the contributions to scattering are comparable for all phonon modes and momenta, so uniform sampling is effective because it avoids bias in the sampling. To treat optimally both sets of electronic states in polar materials like GaAs, we implement a polar split scheme in PERTURBO, which is detailed in Ref. [12]. The scattering rates shown in Fig 6.4(b) are obtained with this approach.

To analyze the dominant scattering mechanism for charge transport, it is useful to resolve the contributions to the total scattering rate from different phonon modes.

Figure 6.5 shows the mode-resolved scattering rates for holes in naphthalene computed at 300 K [15]. A unit cell of naphthalene includes two molecules, for a total of 36 atoms [see Fig. 6.5(a)] and 108 phonon modes. Figure 6.5(b) shows the contribution to the scattering rate from the three acoustic phonon modes (modes 1−3), which are associated with inter-molecular vibrations. The contributions from three optical modes (modes 20, 50, 80) associated with intra-molecular atomic vibrations are also shown. In the relevant energy range for transport, as shown by the dashed line in Fig. 6.5(b), the inter-molecular modes dominate hole carrier scattering. This analysis is simple to carry out in PERTURBO because the code can output the TDF and mode-resolved scattering rates.

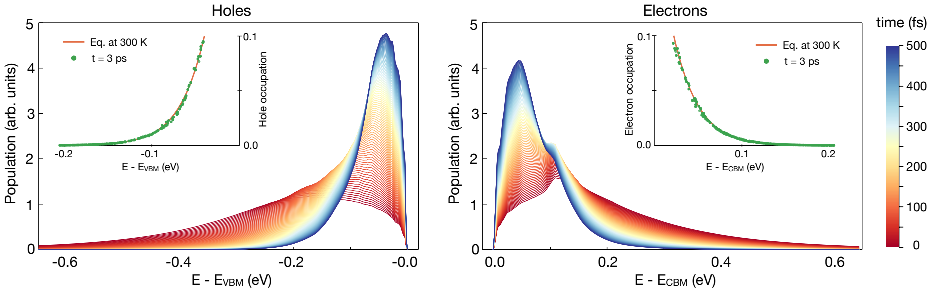

Figure 6.7: Hot carrier cooling simulation in silicon, for holes (left panel) and electrons (right panel). The time evolution of the carrier population $p(E,t)$ in Eq. (6.23) is shown, with the simulation time t color-coded. The carrier occupations $f_{n\boldsymbol{k}}(t)$ at $t = 3$ ps are compared in the inset with the equilibrium Fermi-Dirac distribution at 300 K (red curve) for the same carrier concentration.

Charge transport

We present charge transport calculations for GaAs and monolayer MoS_2 as examples of a bulk and 2D material, respectively. Since both materials are polar, the polar corrections to the e-ph matrix elements are essential, as shown in Fig. 6.3. For MoS_2, we include SOC in the calculation since it plays an important role. In MoS_2, SOC splits the states near the valence band edge, so its inclusion has a significant impact on the e-ph scattering rates and mobility for hole carriers. The transport properties can be computed in PERTURBO either within the RTA or with the iterative solution of the linearized BTE. In the RTA, one can use pre-computed state-dependent scattering rates (see Sec. 6.5) or compute the scattering rates on the fly during the transport calculation using regular MP $\boldsymbol{k}$- and $\boldsymbol{q}$-point grids. In some materials, the RTA is inadequate and the more accurate iterative solution of the BTE in Eq. (6.10) is required. PERTURBO implements an efficiently parallelized routine to solve the BTE iteratively (see Sec. 6.6).

Figure 6.6(a) shows the computed electron mobility in GaAs as a function of temperature and compares results obtained with the RTA and the iterative approach (ITA). The calculation uses a carrier concentration of $n_c = 10^{17}$ cm^{-3}; we have checked that the mobility is almost independent of n_c below 10^{18} cm^{-3}. We perform the calculation using an ultra-fine BZ grid of $600 \times 600 \times 600$ for both $\boldsymbol{k}$- and $\boldsymbol{q}$-points, and employ a small (5 meV) Gaussian broadening to approximate the δ function in the e-ph scattering terms in Eq. (6.9). To reduce the computational cost, we select a 200 meV energy window near the CBM, which covers the entire energy range relevant for transport. In GaAs, the ITA gives a higher electron mobility than the RTA, as shown in Fig. 6.6(a), and this discrepancy increases with temperature. The temperature dependence of the electron mobility is also slightly different in the RTA and ITA results. The RTA calculation is in better agreement with experimental data [49, 50] than results from the more accurate ITA. Careful analysis, carried out elsewhere [51], shows that correcting the band structure [52] to obtain an accurate effective mass and including two-phonon scattering processes [51] are both essential to obtain ITA results in agreement with experiment.

The Seebeck coefficient can be computed at negligible cost as a post-processing step of the mobility calculation. Figure 6.6(b) shows the temperature dependent Seebeck coefficient in GaAs, computed using the ITA at two different carrier concentrations. The computed value at 300 K and $n_c = 10^{18}$ cm^{-3} is about 130 μV/K, in agreement with the experimental value of $\sim$150 μV/K [53]. Our results also show that the Seebeck coefficient increases with temperature and for decreasing carrier concentrations (here, we tested $n_c = 10^{17}$ cm^{-3}), consistent with experimental data near room temperature [53, 54]. Note that the phonon occupations are kept fixed at their equilibrium value in our calculations, so the phonon drag effect, which is particularly important at low temperature, is neglected, and only the diffusive contribution to the Seebeck coefficient is computed. To include phonon drag one needs to include nonequilibrium phonon effects in the Seebeck coefficient calculation. While investigating the coupled dynamics of electrons and phonons remains an open challenge in first-principles calculations [22, 55], we are developing an approach to time-step the coupled electron and phonon BTEs, and plan to make it available in a future version of PERTURBO.

Figure 6.6(c) shows the electron and hole mobilities in monolayer MoS_2, computed for a carrier concentration of 2×10^{12} cm^{-2} and for temperatures between 150−350 K. A fine BZ grid of $180 \times 180 \times 1$ is employed for both $\boldsymbol{k}$- and $\boldsymbol{q}$-points.

Different from GaAs, the RTA and ITA give very close results for both the electron and hole mobilities, with only small differences at low temperature. The computed electron mobility at room temperature is about 168 cm^2/V s, in agreement with the experimental value of 150 cm^2/V s [56]; the computed hole mobility at 300 K is about 20 cm^2/V s.

Ultrafast dynamics

We demonstrate nonequilibrium ultrafast dynamics simulations using hot carrier cooling in silicon as an example. Excited (so-called "hot") carriers can be generated in a number of ways in semiconductors, including injection from a contact or excitation with light. In a typical scenario, the excited carriers relax to the respective band edge in a sub-picosecond time scale by emitting phonons. While ultrafast carrier dynamics has been investigated extensively in experiments, for example with ultrafast optical spectroscopy, first-principles calculations of ultrafast dynamics, and in particular of hot carriers in the presence of e-ph interactions, are a recent development [14, 19, 57, 58].

We perform a first-principles simulation of hot carrier cooling in silicon. We use a lattice constant of 5.389 Å for DFT and DFPT calculations, which are carried out within the local density approximation and with norm-conserving pseudopotentials. Following the workflow in Fig. 6.1, we construct 8 Wannier functions using sp^3 orbitals on Si atoms as an initial guess, and obtain the e-ph matrix elements in the Wannier basis using coarse $8 \times 8 \times 8$ $\boldsymbol{k}$- and $\boldsymbol{q}$-point grids.

Starting from the e-ph matrix elements in the Wannier basis, the electron Hamiltonian, and interatomic force constants computed by `qe2pert.x`, we carry out hot

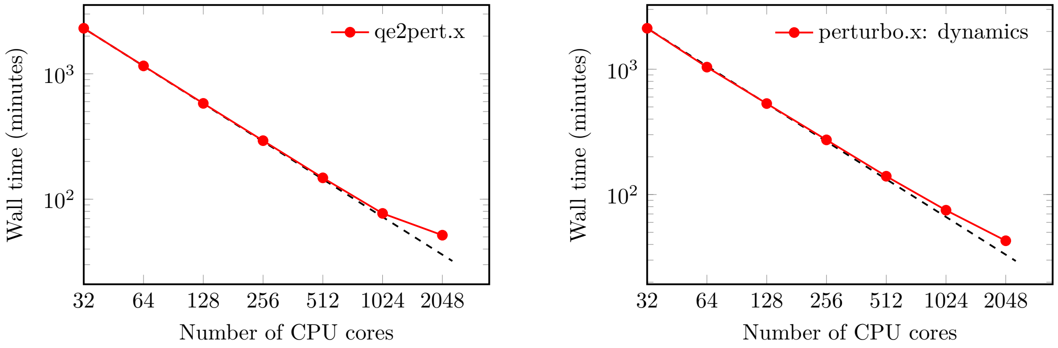

Figure 6.8: Performance scaling with the number of CPU cores of `qe2pert.x` and `perturbo.x`. The black dashed line indicates the ideal linear scaling. For `perturbo.x`, we show the performance of the carrier dynamics simulation, which is the most time-consuming task of `perturbo.x`.

carrier cooling simulations, separately for electron and hole carriers, using a fine $\boldsymbol{k}$-point grid of $100 \times 100 \times 100$ for the electrons (or holes) and a $50 \times 50 \times 50$ $\boldsymbol{q}$-point grid for the phonons. A small Gaussian broadening of 8 meV is employed to approximate the δ function in the e-ph scattering terms in Eq. (6.9). The phonon occupations are kept fixed at their equilibrium value at 300 K. We set the initial electron and hole occupations to hot Fermi-Dirac distributions at 1500 K, each with a chemical potential corresponding to a carrier concentration of 10^{19} cm^{-3}. We explicitly time-step the BTE in Eq. (6.4) (with external electric field set to zero) using the RK4 method with a small time step of 1 fs, and obtain nonequilibrium carrier occupations $f_{n\boldsymbol{k}}(t)$ as a function of time t up to 3 ps, for a total of 3,000 time steps. The calculation takes only about 2.5 hours using 128 CPU cores due to the efficient parallelization (see Sec. 6.6). To visualize the time evolution of the carrier distributions, we compute the BZ averaged energy-dependent carrier population,

$$p(E,t) = \sum_{n\boldsymbol{k}} f_{n\boldsymbol{k}}(t)\delta(\varepsilon_{n\boldsymbol{k}} - E), \tag{6.23}$$

using the tetrahedron integration method. The carrier population $p(E,t)$ characterizes the time-dependent energy distribution of the carriers.

Figure 6.7 shows the evolution of the electron and hole populations due to e-ph scattering. For both electrons and holes, the high-energy tail in the initial population decays rapidly as the carriers quickly relax toward energies closer to the band edge within 500 fs. The carrier concentration is conserved during the simulation, validating the accuracy of our RK4 implementation to time-step the BTE. The hole relaxation is slightly faster than the electron relaxation in silicon, as shown in Fig. 6.7. The sub-picosecond time scale we find for the hot carrier cooling is consistent with experiment and with previous calculations using a simplified approach [19]. Although the hot carriers accumulate near the band edge in a very short time, it takes longer for the carriers to fully relax to a 300 K thermal equilibrium distribution, up to several picoseconds in our simulation. We show in the inset of Fig. 6.7 that the carrier occupations $f_{n\boldsymbol{k}}$ at 3 ps reach the correct long-time limit for our simulation, namely an equilibrium Fermi-Dirac distribution at the 300 K lattice temperature. Since we keep the phonon occupations fixed and neglect phonon-phonon scattering, hot-phonon effects are ignored in our simulation. Similarly, electron-electron scattering, which is typically important at high carrier concentrations or in metals, is also not included in the current version of the code. Electron-electron scattering and coupled electron and phonon dynamics (including phonon-phonon collisions) are both under development.

6.6 Parallelization and performance

Transport calculations and ultrafast dynamics simulations on large systems can be computationally demanding and require a large amount of memory. Efficient parallelization is critical to run these calculations on high-performance computing (HPC) systems. To fully take advantage of the typical HPC architecture, we implement a hybrid MPI and OpenMP parallelization, which combines distributed memory parallelization among different nodes using MPI and on-node shared memory parallelization using OpenMP.

For small systems, we observe a similar performance by running PERTURBO on a single node in either pure MPI or pure OpenMP modes, or in hybrid MPI plus OpenMP mode. However, for larger systems with several atoms to tens of atoms in the unit cell, running on multiple nodes with MPI plus OpenMP parallelization significantly improves the performance and leads to a better scaling with CPU core number. Compared to pure MPI, the hybrid MPI plus OpenMP scheme reduces communication needs and memory consumption, and improves load balance. We demonstrate the efficiency of our parallelization strategy using two examples: computing e-ph matrix elements on coarse grids, which is the most time-consuming task of `qe2pert.x`, and simulating nonequilibrium carrier dynamics, the most time-consuming task of `perturbo.x`.

For the calculation of e-ph matrix elements on coarse grids [see Eq. (6.15)], our implementation uses MPI parallelization for $\boldsymbol{q}_c$-points and OpenMP parallelization for $\boldsymbol{k}_c$-points. We distribute the $\boldsymbol{q}_c$-points among the MPI processes, so that each MPI process either reads the self-consistent perturbation potential from file (if $\boldsymbol{q}_c$ is in the irreducible wedge) or computes it from the perturbation potential of the corresponding irreducible point using Eq. (6.17). Each MPI process then computes $g(\boldsymbol{k}_c, \boldsymbol{q}_c)$ for all the $\boldsymbol{k}_c$-points with OpenMP parallelization.

For carrier dynamics simulations, the $\boldsymbol{k}$-points on the fine grid are distributed among MPI processes to achieve an optimal load balance. Each process finds all the possible scattering channels involving its subset of $\boldsymbol{k}$-points, and stores these scattering processes locally as $(\boldsymbol{k}, \boldsymbol{q})$ pairs. One can equivalently think of this approach as distributing the $(\boldsymbol{k}, \boldsymbol{q})$ pairs for the full $\boldsymbol{k}$-point set among MPI processes. After this step, we use OpenMP parallelization over local $(\boldsymbol{k}, \boldsymbol{q})$ pairs to compute the e-ph matrix elements and perform the scattering integral. The iterative BTE in Eq. (6.10) is also parallelized with the same approach. This parallelization scheme requires minimum communication among MPI processes; for example, only one MPI reduction operation is required to collect the contributions from different processes for the integration in Eq. (6.10).

We test the parallelization performance of `qe2pert.x` and `perturbo.x` using calculations on MoS_2 and silicon as examples (see Sec. 6.5 for the computational details). We run the carrier dynamics simulation on silicon using the Euler method with a time step of 1 fs and a total simulation time of 50 ps, for a total of 50,000 steps. The tests are performed on the Cori system of the National Energy Research Scientific Computing center (NERSC). We use the Intel Xeon "Haswell" processor nodes, where each node has 32 CPU cores with a clock frequency of 2.3 GHz.

Figure 6.8 shows the wall time of the test calculations using different numbers of CPU cores. Both `qe2pert.x` and `perturbo.x` show rather remarkable scaling that is close to the ideal linear-scaling limit up to 1,024 CPU cores. The scaling of `qe2pert.x` for 2,048 CPU cores is less than ideal mainly because each MPI process has an insufficient computational workload, so that communication and I/O become a bottleneck. The current release uses the serial HDF5 library, so after computing $g(\boldsymbol{k}_c, \boldsymbol{q}_c)$, the root MPI process needs to collect $g(\boldsymbol{k}_c, \boldsymbol{q}_c)$ from different processes and write them to disk (or vice versa when loading data), which is a serial task that costs $\sim$14% of the total wall time when using 2048 CPU cores. Parallel I/O using the parallel HDF5 library could further improve the performance and overall scaling in this massively parallel example. We plan to work on this and related improvements to I/O in future releases.

6.7 Conclusions and outlook

In conclusion, we present our software, PERTURBO, for first-principles calculations of charge transport properties and simulation of ultrafast carrier dynamics in bulk and 2D materials. The software contains an interface program to read results from DFT and DFPT calculations from the QE code. The core program of PERTURBO performs various computational tasks, such as computing e-ph scattering rates, electron mean free paths, electrical conductivity, mobility, and the Seebeck coefficient. The code can also simulate the nonequilibrium dynamics of excited electrons. Wannier interpolation and symmetry are employed to greatly reduce the computational cost. SOC and the polar corrections for bulk and 2D materials are supported and have been carefully tested. We demonstrate these features with representative examples. We also show the highly promising scaling of PERTURBO on massively parallel HPC architectures, owing to its effective implementation of hybrid MPI plus OpenMP parallelization.

References

[1] F. Rossi, T. Kuhn, Theory of ultrafast phenomena in photoexcited semiconductors, Rev. Mod. Phys. 74 (3) (2002) 895–950.

[2] R. Ulbricht, E. Hendry, J. Shan, T. F. Heinz, M. Bonn, Carrier dynamics in semiconductors studied with time-resolved terahertz spectroscopy, Rev. Mod. Phys. 83 (2) (2011) 543–586.

[3] D. A. Egger, A. Bera, D. Cahen, G. Hodes, T. Kirchartz, L. Kronik, et al., What remains unexplained about the properties of halide perovskites?, Adv. Mater. 30 (20) (2018) 1800691.

[4] S. Baroni, S. de Gironcoli, A. Dal Corso, P. Giannozzi, Phonons and related crystal properties from density-functional perturbation theory, Rev. Mod. Phys. 73 (2) (2001) 515–562.

[5] P. Giannozzi, S. Baroni, N. Bonini, M. Calandra, R. Car, et al., QUANTUM ESPRESSO: a modular and open-source software project for quantum simulations of materials, J. Phys.: Condens. Matter 21 (39) (2009) 395502.

[6] P. Giannozzi, O. Andreussi, T. Brumme, O. Bunau, M. B. Nardelli, et al., Advanced capabilities for materials modelling with QUANTUM ESPRESSO, J. Phys.: Condens. Matter 29 (46) (2017) 465901.

[7] J. M. Ziman, Electrons and phonons: The theory of transport phenomena in solids, Oxford University Press, New York, 2007.

[8] J. Park, J.-J. Zhou, M. Bernardi, Spin-phonon relaxation times in centrosymmetric materials from first principles, Phys. Rev. B 101 (2020) 045202.

[9] I.-T. Lu, J.-J. Zhou, M. Bernardi, Efficient ab initio calculations of electron-defect scattering and defect-limited carrier mobility, Phys. Rev. Mater. 3 (2019) 033804.

[10] I.-T. Lu, J. Park, J.-J. Zhou, M. Bernardi, Ab initio electron-defect interactions using Wannier functions, npj Comput. Mater. 6 (1) (2020) 1-7.

[11] H.-Y. Chen, V. A. Jhalani, M. Palummo, M. Bernardi, Ab initio calculations of exciton radiative lifetimes in bulk crystals, nanostructures, and molecules, Phys. Rev. B 100 (2019) 075135.

[12] J.-J. Zhou, M. Bernardi, *Ab initio* electron mobility and polar phonon scattering in GaAs, Phys. Rev. B 94 (20) (2016) 201201(R).

[13] J.-J. Zhou, O. Hellman, M. Bernardi, Electron-phonon scattering in the presence of soft modes and electron mobility in $SrTiO_3$ perovskite from first principles, Phys. Rev. Lett. 121 (22) (2018) 226603.

[14] V. A. Jhalani, J.-J. Zhou, M. Bernardi, Ultrafast hot carrier dynamics in GaN and its impact on the efficiency droop, Nano Lett. 17 (8) (2017) 5012–5019.

[15] N.-E. Lee, J.-J. Zhou, L. A. Agapito, M. Bernardi, Charge transport in organic molecular semiconductors from first principles: The bandlike hole mobility in a naphthalene crystal, Phys. Rev. B 97 (11) (2018) 115203.

[16] M. Bernardi, First-principles dynamics of electrons and phonons, Eur. Phys. J. B 89 (11) (2016) 239.

[17] G. K. H. Madsen, D. J. Singh, BoltzTraP. A code for calculating band-structure dependent quantities, Comput. Phys. Commun. 175 (1) (2006) 67–71.

[18] G. Pizzi, D. Volja, B. Kozinsky, M. Fornari, N. Marzari, BoltzWann: A code for the evaluation of thermoelectric and electronic transport properties with a maximally-localized Wannier functions basis, Comput. Phys. Commun. 185 (1) (2014) 422–429.

[19] M. Bernardi, D. Vigil-Fowler, J. Lischner, J. B. Neaton, S. G. Louie, *Ab initio* study of hot carriers in the first picosecond after sunlight absorption in silicon, Phys. Rev. Lett. 112 (2014) 257402.

[20] G. D. Mahan, Many-particle physics, Springer US, 3rd edn., 2000.

[21] W. Li, Electrical transport limited by electron-phonon coupling from Boltzmann transport equation: An *ab initio* study of Si, Al, and MoS_2, Phys. Rev. B 92 (7) (2015) 075405.

[22] M. Fiorentini, N. Bonini, Thermoelectric coefficients of n-doped silicon from first principles via the solution of the Boltzmann transport equation, Phys. Rev. B 94 (8) (2016) 085204.

[23] P. E. Blöchl, O. Jepsen, O. K. Andersen, Improved tetrahedron method for Brillouin-zone integrations, Phys. Rev. B 49 (23) (1994) 16223–16233.

[24] N. Marzari, A. A. Mostofi, J. R. Yates, I. Souza, D. Vanderbilt, Maximally localized Wannier functions: Theory and applications, Rev. Mod. Phys. 84 (4) (2012) 1419–1475.

[25] A. A. Mostofi, J. R. Yates, G. Pizzi, Y.-S. Lee, I. Souza, D. Vanderbilt, N. Marzari, An updated version of wannier90: A tool for obtaining maximally-localised Wannier functions, Comput. Phys. Commun. 185 (8) (2014) 2309–2310.

[26] G. Pizzi, V. Vitale, R. Arita, S. Blügel, F. Freimuth, G. Géranton, M. Gibertini, D. Gresch, C. Johnson, T. Koretsune, et al., Wannier90 as a community code: new features and applications, J. Phys.: Condens. Matter 32 (16) (2020) 165902.

[27] X. Wang, J. R. Yates, I. Souza, D. Vanderbilt, Ab initio calculation of the anomalous Hall conductivity by Wannier interpolation, Phys. Rev. B 74 (2006) 195118.

[28] I. Souza, N. Marzari, D. Vanderbilt, Maximally localized Wannier functions for entangled energy bands, Phys. Rev. B 65 (3) (2001) 035109.

[29] J. R. Yates, X. Wang, D. Vanderbilt, I. Souza, Spectral and Fermi surface properties from Wannier interpolation, Phys. Rev. B 75 (19) (2007) 195121.

[30] M. Born, K. Huang, Dynamical theory of crystal lattices, Clarendon press, 1954.

[31] X. Gonze, C. Lee, Dynamical matrices, Born effective charges, dielectric permittivity tensors, and interatomic force constants from density-functional perturbation theory, Phys. Rev. B 55 (16) (1997) 10355–10368.

[32] F. Giustino, M. L. Cohen, S. G. Louie, Electron-phonon interaction using Wannier functions, Phys. Rev. B 76 (16) (2007) 165108.

[33] M. Calandra, G. Profeta, F. Mauri, Adiabatic and nonadiabatic phonon dispersion in a Wannier function approach, Phys. Rev. B 82 (16) (2010) 165111.

[34] L. A. Agapito, M. Bernardi, Ab initio electron-phonon interactions using atomic orbital wave functions, Phys. Rev. B 97 (23) (2018) 235146.

[35] X. Gonze, J.-C. Charlier, D. Allan, M. Teter, Interatomic force constants from first principles: The case of α-quartz, Phys. Rev. B 50 (1994) 13035(R).

[36] H. Fröhlich, Electrons in lattice fields, Adv. Phys. 3 (11) (1954) 325–361.

[37] J. Sjakste, N. Vast, M. Calandra, F. Mauri, Wannier interpolation of the electron-phonon matrix elements in polar semiconductors: Polar-optical coupling in GaAs, Phys. Rev. B 92 (5) (2015) 054307.

[38] C. Verdi, F. Giustino, Fröhlich electron-phonon vertex from first principles, Phys. Rev. Lett. 115 (17) (2015) 176401.

[39] T. Sohier, M. Calandra, F. Mauri, Two-dimensional Fröhlich interaction in transition-metal dichalcogenide monolayers: Theoretical modeling and first-principles calculations, Phys. Rev. B 94 (2016) 085415.

[40] T. Sohier, M. Gibertini, M. Calandra, F. Mauri, N. Marzari, Breakdown of optical phonons' splitting in two-dimensional materials, Nano Lett. 17 (6) (2017) 3758–3763.

[41] T. Sohier, M. Calandra, F. Mauri, Density functional perturbation theory for gated two-dimensional heterostructures: Theoretical developments and application to flexural phonons in graphene, Phys. Rev. B 96 (2017) 075448.

[42] The PERTURBO website, `https://perturbo-code.github.io`

[43] A. Dal Corso, Density-functional perturbation theory with ultrasoft pseudopotentials, Phys. Rev. B 64 (23) (2001) 235118.

[44] A. A. Maradudin, S. H. Vosko, Symmetry properties of the normal vibrations of a crystal, Rev. Mod. Phys. 40 (1) (1968) 1–37.

[45] S. Poncé, E. R. Margine, C. Verdi, F. Giustino, EPW: Electron–phonon coupling, transport and superconducting properties using maximally localized Wannier functions, Comput. Phys. Commun. 209 (2016) 116–133.

[46] G. Gaddemane, S. Gopalan, M. Van de Put, M. V. Fischetti, Limitations of ab initio methods to predict the electronic-transport properties of two-dimensional materials: The computational example of 2H-phase transition metal dichalcogenides, arXiv:1912.03795 [cond-mat.mtrl-sci] .

[47] M. J. van Setten, M. Giantomassi, E. Bousquet, M. J. Verstraete, D. R. Hamann, et al., The PseudoDojo: Training and grading a 85 element optimized norm-conserving pseudopotential table, Comput. Phys. Commun. 226 (2018) 39–54.

[48] A. Damle, L. Lin, L. Ying, SCDM-k: Localized orbitals for solids via selected columns of the density matrix, J. Comput. Phys. 334 (2017) 1–15.

[49] P. Blood, Electrical properties of n-type epitaxial GaAs at high temperatures, Phys. Rev. B 6 (6) (1972) 2257–2261.

[50] K. H. Nichols, C. M. L. Yee, C. M. Wolfe, High-temperature carrier transport in n-type epitaxial GaAs, Solid-State Electron. 23 (2) (1980) 109–116.

[51] N.-E. Lee, J.-J. Zhou, H.-Y. Chen, M. Bernardi, Next-to-leading order ab initio electron-phonon scattering, Nat. Commun. 11 (2020) 1607.

[52] J. Ma, A. S. Nissimagoudar, W. Li, First-principles study of electron and hole mobilities of Si and GaAs, Phys. Rev. B 97 (4) (2018) 045201.

[53] O. Madelung, U. Rössler, M. Schulz (Eds.), Semiconductors, vol. 41A1β, Springer, Berlin, 2002.

[54] G. Homm, P. J. Klar, J. Teubert, W. Heimbrodt, Seebeck coefficients of n-type (Ga,In)(N,As), (B,Ga,In)As, and GaAs, Appl. Phys. Lett. 93 (4) (2008) 042107.

[55] N. H. Protik, D. A. Broido, Coupled transport of phonons and carriers in semiconductors, arXiv:1911.02916 [cond-mat.mtrl-sci] .

[56] Z. Yu, Z.-Y. Ong, Y. Pan, Y. Cui, R. Xin, Y. Shi, et al., Realization of room-temperature phonon-limited carrier transport in monolayer MoS_2 by dielectric and carrier screening, Adv. Mater. 28 (3) (2016) 547–552.

[57] S. Sadasivam, M. K. Y. Chan, P. Darancet, Theory of thermal relaxation of electrons in semiconductors, Phys. Rev. Lett. 119 (2017) 136602.

[58] A. Molina-Sánchez, D. Sangalli, L. Wirtz, A. Marini, Ab initio calculations of ultrashort carrier dynamics in two-dimensional materials: Valley depolarization in single-layer WSe_2, Nano Lett. 17 (8) (2017) 4549–4555.

[59] J.-J. Zhou, M. Bernardi, Predicting charge transport in the presence of polarons: The beyond-quasiparticle regime in $SrTiO_3$, Phys. Rev. Res. 1 (2019) 033138.

[60] O. Hellman, P. Steneteg, I. A. Abrikosov, S. I. Simak, Temperature dependent effective potential method for accurate free energy calculations of solids, Phys. Rev. B 87 (10) (2013) 104111.

Chapter 7

SUMMARY AND FUTURE DIRECTIONS

In summary, this thesis provided a many-body first-principles framework for studying phonon-induced spin relaxation and decoherence in condensed matter, extended the current capability of *ab-initio* e-ph interaction by addressing quadrupolar interactions and correlated electron systems, and developed an open-source platform for investigating e-ph interactions from first principles.

In Chapter 2, we focused on spin-phonon interaction and relaxation. We first present a first-principles approach for computing the phonon-limited T_1 spin relaxation time due to the Elliott-Yafet mechanism. Our scheme combines fully-relativistic spin-flip electron-phonon interactions with an approach to compute the effective spin of band electrons in materials with inversion symmetry. We apply our method to silicon and diamond, for which we compute the temperature dependence of the spin relaxation times and analyze the contributions to spin relaxation from different phonons and valley processes. The computed spin relaxation times in silicon are in excellent agreement with experiment in the $50-300$ K temperature range. In diamond, we predict intrinsic spin relaxation times of 540 μs at 77 K and 2.3 μs at 300 K. We show that the spin-flip and momentum relaxation mechanisms are governed by distinct microscopic processes. Our work enables precise predictions of spin-phonon relaxation times in a wide range of materials, providing microscopic insight into spin relaxation and guiding the development of spin-based quantum technologies.

In Chapter 3, we developed a microscopic understanding of spin decoherence, which is essential to advancing quantum technologies. Electron spin decoherence due to atomic vibrations (phonons) plays a special role as it sets an intrinsic limit to the performance of spin-based quantum devices. Two main sources of phonon-induced spin decoherence, the Elliott-Yafet (EY) and Dyakonov-Perel (DP) mechanisms, have distinct physical origins and theoretical treatments. In this work, we show a rigorous theoretical framework: the spin-phonon Bethe-Salpeter equation to treat the two main spin decoherence mechanisms due to phonons on the same footing, and develop corresponding first-principles calculations. Our framework allows us to predict spin relaxation times in semiconductors with a high accuracy, without using any free or empirical parameters, and to shed new light on microscopic spin dynamics, such as the interplay between spin precession and relaxation. Our approach is general and applicable well beyond the examples in this work: it enables precise predictions of spin decoherence in systems of fundamental and technological relevance, including materials with band and localized spins, ions, heterostructures and nanostructures, and quantum dot qubits.

In Chapter 4, the thesis focused on the long-range quadrupolar e-ph interaction. Lattice vibrations in materials induce perturbations on the electron dynamics in the form of long-range (dipole and quadrupole) and short-range (octopole and higher) potentials. The dipole Fröhlich term can be included in current first-principles electron-phonon (e-ph) calculations and is present only in polar materials. The quadrupole e-ph interaction is present in both polar and nonpolar materials, but currently it cannot be computed from first principles. We have shown an approach to compute the quadrupole e-ph interaction and include it in *ab initio* calculations of e-ph matrix elements. Analysis of e-ph interactions for different phonon modes reveals that the quadrupole term mainly affects optical modes in silicon and acoustic modes in $PbTiO_3$, although the quadrupole term is needed for all modes to achieve quantitative accuracy. The effect of the quadrupole e-ph interaction on electron scattering processes and transport is shown to be important. Our approach enables accurate studies of e-ph interactions in broad classes of nonpolar, polar and piezoelectric materials.

In Chapter 5, the thesis focused on correlated electron systems. e-ph interactions are pervasive in condensed matter, governing phenomena such as transport, superconductivity, charge-density waves, polarons, and metal-insulator transitions. First-principles approaches enable accurate calculations of e-ph interactions in a wide range of solids. However, they remain an open challenge in correlated electron systems, where density functional theory often fails to describe the ground state. Therefore reliable e-ph calculations remain out of reach for many transition metal oxides, high-temperature superconductors, Mott insulators, planetary materials, and multiferroics. We have shown first-principles calculations of e-ph interactions in CES, using the framework of Hubbard-corrected density functional theory (DFT+U) and its linear response extension (DFPT+U), which can describe the electronic structure and lattice dynamics of many CES. We showcase the accuracy of this approach for a prototypical Mott system, CoO, carrying out a detailed investigation of its e-ph interactions and electron spectral functions. While standard

DFPT gives unphysically divergent and short-ranged e-ph interactions, DFPT+U is shown to remove the divergences and properly account for the long-range Fröhlich interaction, allowing us to model polaron effects in a Mott insulator. Our work establishes a broadly applicable and affordable approach for quantitative studies of e-ph interactions in CES, a novel theoretical tool to interpret experiments in this broad class of materials.

In Chapter 6, we have presented PERTURBO, a software package for first-principles calculations of charge transport and ultrafast carrier dynamics in materials. The current version focuses on electron–phonon interactions and can compute phonon-limited transport properties such as the conductivity, carrier mobility and Seebeck coefficient. It can also simulate the ultrafast nonequilibrium electron dynamics in the presence of electron–phonon scattering. Taken together, Perturbo provides efficient and broadly applicable ab initio tools to investigate electron–phonon interactions and carrier dynamics quantitatively in metals, semiconductors, insulators, and 2D materials.

Several future directions are possible for the newly enabled research areas discussed above. The workflow proposed in Chapter 2 can be adapted to different perturbation potentials, including perturbations from defects [1, 2], through which one could study spin-flip and other defect-induced spin scattering processes. Our approach can be applied broadly to study spin relaxation in materials for spintronics and magnetism, and in topological materials. It can also be extended to treat spin states localized at ions or defect, using calculations with large supercells that at present are still technically challenging.

The currently developed formalism of the phonon-dressed vertex in Chapter 3 is quite general; it can be readily applied to a broad range of systems as long as the operator expectation values and the e-ph interactions are known. Chapter 3 applied the formalism to spin decoherence, starting from the computational advancements made in Chapter 2, and computing simultaneously the spin vertex and e-ph interaction in the presence of SOC through joint interpolation of the e-ph matrix elements and spin matrices through Wannier functions [3]. The formalism extends well beyond spins, and our work opens the avenue for theoretical studies of linear response of the system to various external field in the presence of e-ph interactions, which includes charge transport including the effect of interband coherence, spin-current inter-conversion, and operator decoherence in systems of interest for spintronics, magnetism, in topological materials, and quantum information science.

The capabilities of PERTURBO in Chapter 6 can be significantly expanded. Many features are currently under development for the next major release, including spin-phonon relaxation times and spin dynamics [3], transport calculations in the large polaron regime using the Kubo formalism [4], and charge transport and ultrafast dynamics for coupled electrons and phonons, among others. As an alternative to Wannier functions, interpolation using atomic orbitals [5] will also be supported in a future release. We will extend the interface program to support additional external codes, such as the TDEP software for temperature-dependent lattice dynamical calculations [6].

In conclusion, the novel and computationally affordable methods presented in this thesis enable precise predictions of spin relaxation and decoherence, with broad implications for spin-based quantum technologies and for advancing microscopic understanding of spin dynamics in condensed matter. The advancements made in this thesis enable new avenues for computational research of e-ph interactions in both condensed matter physics and quantum technologies.

References

[1] I-Te Lu, Jin-Jian Zhou, and Marco Bernardi. Efficient *ab initio* calculations of electron-defect scattering and defect-limited carrier mobility. *Phys. Rev. Mater.*, 3(3):033804, 2019. doi: 10.1103/PhysRevMaterials.3.033804.

[2] Nguyen H. Long, Phivos Mavropoulos, Bernd Zimmermann, Swantje Heers, David S. G. Bauer, Stefan Blügel, and Yuriy Mokrousov. Spin relaxation and the Elliott-Yafet parameter in W(001) ultrathin films: Surface states, anisotropy, and oscillation effects. *Phys. Rev. B*, 87(22):224420, 2013. doi: 10.1103/PhysRevB.87.224420.

[3] Jinsoo Park, Jin-Jian Zhou, and Marco Bernardi. Spin-phonon relaxation times in centrosymmetric materials from first principles. *Phys. Rev. B*, 101(4):045202, 2020. doi: 10.1103/PhysRevB.101.045202.

[4] Jin-Jian Zhou and Marco Bernardi. Predicting charge transport in the presence of polarons: The beyond-quasiparticle regime in $SrTiO_3$. *Phys. Rev. Res.*, 1(3):033138, 2019. doi: 10.1103/PhysRevResearch.1.033138.

[5] Luis A. Agapito and Marco Bernardi. Ab initio electron-phonon interactions using atomic orbital wave functions. *Phys. Rev. B*, 97(23):235146, 2018. doi: 10.1103/PhysRevB.97.235146.

[6] Jin-Jian Zhou, Olle Hellman, and Marco Bernardi. Electron-Phonon Scattering in the Presence of Soft Modes and Electron Mobility in $SrTiO_3$ Perovskite from First Principles. *Phys. Rev. Lett.*, 121(22):226603, 2018. doi: 10.1103/PhysRevLett.121.226603.